Experimentelle Physik

Dissertationsthema:

Gas purification of the XENON dark matter search

Inauguraldissertation
zur Erlangung des Doktorgrades
der Naturwissenschaften im Fachbereich Physik
der Mathematisch-Naturwissenschaftlichen Fakultät
der Westfälischen Wilhelms-Universität

vorgelegt von

Stephan Rosendahl

aus Hesel-Kiefeld

- 2015 -

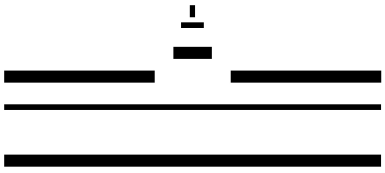

Westfälische
Wilhelms-Universität
Münster

Dekan:	**Prof. Dr. Christian Weinheimer**
Erster Gutachter:	**Prof. Dr. Christian Weinheimer**
Zweiter Gutachter:	**Prof. Dr. Alfons Khoukaz**
Tag der mündlichen Prüfung:	
Tag der Promotion:	

Zusammenfassung

Die Erforschung der dunklen Materie ist von essentieller Bedeutung sowohl für die Astrophysik und Kosmologie als auch für die Teilchenphysik. Astronomische Beobachtungen zeigen, dass unser Universum nur zu etwa 5% aus baryonischer Materie besteht, welche sich mit dem Standardmodel der Teilchenphysik beschreiben lässt. Den größten Anteil zur Energiedichte des Universums trägt mit etwa 70% die dunkle Energie bei, über die sich bisher wenig aussagen lässt. Die übrigen 25% der Energiedichte des Universums wird der dunklen Materie zugeschrieben. Diese nicht-baryonische Materie wirkt gravitativ und beinflusst die Bewegung von Sternen und Galaxien. Ihr Wirken lässt sich bis in den kosmischen Mikrowellenhintergrund hinein nachweisen und die verschiedensten Evidenzen erlauben es die Eigenschaften dieser unbekannten Materie abzuleiten. Daher gibt es, im Gegensatz zur dunklen Energie, für die dunkle Materie verschiedene Modelle zur Erweiterung des Standardmodells der Teilchenphysik, welche die Existenz von nicht-baryonischen Teilchen postuliert, die als dunkle Materie in Frage kommen. Ein Kandidat für die dunkle Materie ist das *WIMP*, ein "weakly-interacting massive particle". Der Nachweis des *WIMP* ist das Ziel verschiedener Experimente, welche die Interaktion mit normaler Materie ausnutzen. Die in einem *WIMP*-Kernrückstoß übertragene Energie äussert sich in Form von Szintillation, Ionisation und Phonon-Anregung des Mediums, welche nachgewiesen werden könnte. Die Verwendung von Edelgasen, insbesondere Xenon, hat in diesem Feld Einzug gehalten und die sensitivsten Experimente auf diesem Gebiet waren in den letzten Jahren das XENON100 Experiment und das LUX Experiment, welche jeweils eine Zwei-Phasen Zeit-Projektions Kammer (TPC) gefüllt mit Xenon verwenden, um nach *WIMP*-Kern Interaktionen zu suchen. Bei einer Anregung des Xenons durch einfallende Strahlung werden sowohl primäres Szintillationslicht (S1) als auch freie Elektronen erzeugt, welche durch Stöße mit gasförmigem Xenon ein zweites Lichtsignal (S2) erzeugen. Beide Signale werden mit Photomultipliern detektiert. Das XENON100 Experiment erreichte eine Sensitivität für den Spin-unabhängigen Wirkungsquerschnitt in einer elastischen Streuung von 2×10^{-45} cm^2 bei einer *WIMP* Masse von 55 GeV und einer statistischen Sicherheit von 90%. Die sensitive Masse während der Messdauer von über einem Jahr belief sich auf 34 kg. Das LUX Experiment erreichte mit einer höheren sensitiven Masse von 118 kg sogar noch bessere Grenzen mit einem Minimum von $\sigma_{SI} = 7.6 \times 10^{-46}$ cm^2 bei 33 GeV/c^2, ebenfalls bestimmt mit einer statistischen Sicherheit von 90%. Das Nachfolgeexperiment von XENON100, genannt XENON1T, ist für eine Gesamtmasse von 3.5 t ausgelegt und strebt ein sensitives Volumen von einer Tonne Material an. Die projezierte Sensitivität liegt bei $\sigma_{SI} \approx 2 \times 10^{-47}$cm^2 nach zwei Jahren Messzeit. Um die gewünschte Sensitivität zu erreichen, ist die Reinheit des verwendeten Xenons von entscheidender Bedeutung. Dabei sind zwei verschiedene Aspekte zu beachten: Zum einen muss das Xenon von sogenannten elektronegativen Elementen, z.B. Sauerstoff oder Wasser, gereinigt werden, um eine optimale Lichtausbeute und Ladungsdrift zu gewährleisten. Zu diesem Zweck wurde für das XENON1T Experiment ein neues Gasreinigungssystem konzipiert, welches als Kernstück einen auf Zirkonium basierten Gasreiniger (Getter) verwendet, um das Xenon zu säubern. Im Rahmen dieser Dissertation wurde ein Prototyp dieses Systems entworfen und gebaut, um die verschiedenen Komponenten, wie Getter, Gasförderpumpe und Ventile auf ihre Tauglichkeit für das XENON1T Experiment zu testen. Es konnte mit Hilfe eines laser-basierten Analysators gezeigt werden, dass die Konzentration von Wasser in Xenon auf ein Level von $H_2O/Xe < 0.2$ ppb reduziert werden konnte, wobei die Designvorgabe bei $H_2O/$ Xe <1 ppb liegt. Weiterhin muss das Xenon von intrinischen radioaktiven Verunreinigungen gesäubert werden, welche als radioaktiver Untergrund die Sensitivität verringern. Insbesondere der β-Zerfall des ^{85}Kr beeinflusst die Suche nach dunkler Materie erheblich, weshalb das Xenon im Vorfeld gereinigt werden muss. Für XENON1T wird eine Konzentration von Krypton in Xenon von $^{\mathrm{nat}}\mathrm{Kr/Xe} < 0.5 \cdot 10^{-12}$ benötigt. Für die Reinigung wurde eine kryogene Destillationssäule entworfen und gebaut. Weiterhin wurde im Rahmen dieser Dissertation ein Tracer Verfahren entwickelt, welches radioaktives $^{83\mathrm{m}}$Kr verwendet, um die Separationseigenschaften der Destillationssäule zu bestimmen. Während der Inbetriebnahme konnte gezeigt werden, dass die Anlage unter den Designvorgaben thermodynamisch stabil operiert und die vorgesehene Durchlaufgeschwindigkeit von 3 kg/h sogar noch übertroffen werden konnte. Weiterhin konnte mit verschiedensten Messmethoden nachgewiesen werden, dass Konzentrationen von $^{\mathrm{nat}}\mathrm{Kr/Xe} < 0.1 \cdot 10^{-12}$ erreicht werden können und das die Destillation geeignet ist, die gewünschte Reinheit für XENON1T herzustellen. Auf Basis der gewonnenen Erkenntnisse ist in einer weiteren Ausbaustufe der Trennfaktor maximiert worden, sodass sogar hochgradig verunreinigtes Xenon verarbeitet werden kann. Die Gasreinigung des Xenons konnte sowohl für elektronegative Elemente wie auch für das Edelgas Krypton erfolgreich demonstriert werden, sodass beide Systeme am XENON1T Experiment zum Einsatz kommen werden.

Abstract

The study of dark matter is of crucial importance for the astrophysics and cosmology as well as for the particle physics. Astronomical observation showed, that only 5% of our universe is made from baryonic matter, which can be explained by the standard model of particle physics. The major contributor to the energy density of the universe is with 70% the dark energy, which is the biggest mystery in nowadays. The remaining 25% is caused by dark matter. This non-baryonic matter interacts gravitationally with ordinary matter and influences the movement of stars and galaxies. Its influence is even detectable in the cosmic-microwave background and the different observations allows to derive the characteristics of this unknown matter. Hence, there exist different models to explain the dark matter in contrary to the dark energy problem. Different models to enhance the standard model of particles have been developed, which introduce new particles that might be the dark matter. One candidate is the *WIMP*, the weakly interacting massive particle. Its detection is the goal of different experiments around the world, using the interaction between *WIMP*s and ordinary matter. An elastic *WIMP*-nucleon scattering is supposed to transfer energy to the nucleus of an atom, producing scintillation light, ionization and phonon excitation, which might be detectable. The usage of rare gases in this field increased in the recent years and especially xenon got very important, and the most sensitive results have been produced by the XENON100 and the LUX experiment. Both of them use a dual phase time projection chamber, filled with liquid xenon to search for *WIMP*-nucleon interactions. The excitation of xenon by incoming particles produces primary scintillation light (S1) as well as free electrons, whereat the electrons produce a second light signal (S2) by collisions with gaseous xenon. Both signals are detected with photomultiplier tubes. The XENON100 experiment reached a sensitivity for the spin-independent WIMP-nucleon cross section of 2×10^{-45} cm^2 at 55 GeV and 90% confidence level, using a fiducial volume of 34 kg during a runtime of more than a year. The LUX experiment, using a fiducial mass of 118 kg, even reached a higher sensitivity with a minimum of 7.6×10^{-46} cm^2 at 33 GeV and 90% confidence level. The successor of the XENON100 experiment, called XENON1T, aims for one ton fiducial mass with a projected sensitivity of 2×10^{-47} cm^2 after 2 years measurement time. In order to achieve the desired sensitivity, the purity of the xenon is of crucial importance, whereat different aspects have to be taken into account. The xenon has to be cleaned from electronegative impurities, like oxygen or water, to achieve a good light collection and charge drift. Hence, a new gas purification system for the XENON1T system has been developed, using a zirconium-based gas purifier (getter) to clean the xenon. In the context of this thesis, a demonstrator setup has been designed and constructed in order to test the performance characteristics of different components, like the getter, circulation pumps and valves and to find the proper components for the final setup. It has been shown, using a laser-based moisture analyzer, that it was possible to reduce the water contamination in the xenon to $H_2O/Xe < 0.2$ ppb while the requirement for the experiment was calculated to be $H_2O/Xe < 1$ ppb. Beside the electronegative contaminations, it is important to purify the xenon from radioactive impurities as well. In particular, the β-decay of ^{85}Kr is one of the major background components in the experiment and spoils its sensitivity. Therefore, it has to be removed once in advance. For the XENON1T experiment a concentration of natural krypton in xenon of $^{\mathrm{nat}}\mathrm{Kr}/\mathrm{Xe} < 0.5 \cdot 10^{-12}$ is necessary. For the separation of krypton and xenon, a cryogenic distillation column has been designed and constructed. In the context of this thesis also a new tracer method has been developed, using radioactive $^{83\mathrm{m}}$Kr, which allows to investigate the separation characteristics of the distillation column. During the commissioning of the column the thermodynamic stability under the design conditions have been demonstrated. The intended process speed of 3 kg/h has even been outreached. Additionally it has been shown, that very low concentrations of $^{\mathrm{nat}}\mathrm{Kr}/\mathrm{Xe} < 0.1 \cdot 10^{-12}$ can be achieved and that the technique of cryogenic distillation is feasible for the requirements of the XENON1T experiment. Due to these performance studies, further improvements could be made and additional separation stages were added to the setup, in order to further enhance the performance and which even allow to process highly contaminated xenon. Finally, after the purification of xenon for electronegative impurities and krypton were demonstrated, the final systems for the XENON1T system were constructed and will be used at the experiment.

Contents

1 Dark Matter

The infinite wideness of the universe and the objects on the sky are fascinating the human race for many thousand years now. With improving technologies over the centuries, the understanding of how our universe is structured and composed also improved. In the last 100 years the capabilities for astronomic observation is getting to such precision, that the development of models for the evolution of our universe, based on reliable experimental data, has been performed extensively. Due to this development in technology, several observations have been made, which can not be explained by the actual standard models of cosmology and particle physics. One of this open questions in the field of astro-physics is the nature of dark matter.

In this chapter, the different astronomic observations are presented that are indicating the existence of dark matter (section 1.1). From these evidences, the characteristics of the dark matter are derived, leading to possible explanations for the dark matter by particle physics. The introduction of new particles that fulfill the requirements from the observations will be discussed in section 1.2.

1.1 Evidence for dark matter

It was in 1933, when the German expression "dunkle Materie" [Zwi33] - in English: dark matter, appeared in a work of Fritz Zwicky about the redshift of extragalactic nebular [Zwi33]. Zwicky presented measurements of the peculiar velocities of eight galaxies in the coma cluster, which were larger than expected. By using the virial theorem

$$\begin{aligned} \overline{E}_{kin} &= -\frac{1}{2}\overline{U}_{pot} \\ \overline{E}_{kin} &\propto \overline{v}^2 \\ \overline{U}_{pot} &\propto \frac{M^2}{R} \end{aligned} \tag{1.1.1}$$

with $\overline{E}_{kin}$ being the kinetic energy, which is proportional to the velocity squared $\overline{v}^2$ and $\overline{U}_{pot}$ being the potential energy. For the latter, a gravitational potential is assumed, which is proportional to the total mass of the cluster squared M^2 and inverse proportional to the

radius R of the cluster. He concluded, that there has to be much more matter, than only the visible, to explain the velocities in the cluster. Since it was not visible he called it dark matter.

It took more than 40 years until a different type of observations indicated the existence of dark matter on the scale of galaxies as well. In the 1970's and 1980's it was Vera Rubin et al., who measured the rotation curves of several different galaxies. From the assumption, that the center of mass of a galaxy is following the luminous mass distribution, it can be expected, that the velocity of stars is decreasing, following the Kepler motion (analog to the motion of planets) with increasing distant from the center of the galaxy:

$$\frac{mv_{rot}^2}{r} = G\frac{mM(r)}{r^2} \Longrightarrow v_{rot} \propto r^{-\frac{1}{2}} \tag{1.1.2}$$

In contrary, they found that the rotational curves are approximately flattening out for increasing distances from the galactic center [Rub78]. To explain this discrepancy between the measurement and the expectation, the model of the mass distribution of the galaxies was modified, by adding a halo of dark matter [Beg91]. The result is shown in figure 1.1. The measured data is presented together with a model function to explain the dynamics, which consists of contributions from the visible components, gas and a halo made from dark matter. From these observations, some characteristics of the dark matter can be derived: It has to be non-luminous and interacting gravitationally. The density of dark matter and the halo core radius are essential free fit parameters together with the mass to light ratio (M/L) of the visible matter.

A different possible explanation for the rotational curves came from a modified Newtonian dynamics (MOND) theory, which suggested to change the equation of motion in a gravitational potential, claiming, that the established law of gravity might not be correct on larger scales. This attempt is also presented in the same work [Beg91] to compare the two approaches. In fact, in the early 1990's, the MOND theory was favored against the dark matter explanation. This changed in the following years due to additional astronomical observations.

Among others, the studies of the cosmic microwave background (CMB) are of crucial importance to understand the composition of our universe and to get further hints on the properties of dark matter. The existence of the CMB has been proven in the 1960's by A. Penzias and R.W. Wilson. They got the Nobel prize in physics for the discovery in 1978 [Nob78]. The CMB is a relic from the early universe. During this period, the photons are in thermal equilibrium with the baryons (protons preferably) and the electrons:

$$\gamma + \mathrm{e}^- \longleftrightarrow \gamma + \mathrm{e}^- \tag{1.1.3a}$$

$$\gamma + p \longleftrightarrow \gamma + p \tag{1.1.3b}$$

$$\mathrm{e}^- + p \longleftrightarrow {}^1\mathrm{H} + \gamma \tag{1.1.3c}$$

Around 380.000 years after the big bang the universe got too cold so that the dissociation of the hydrogen atoms (1.1.3c) could not happen anymore and the free electrons and

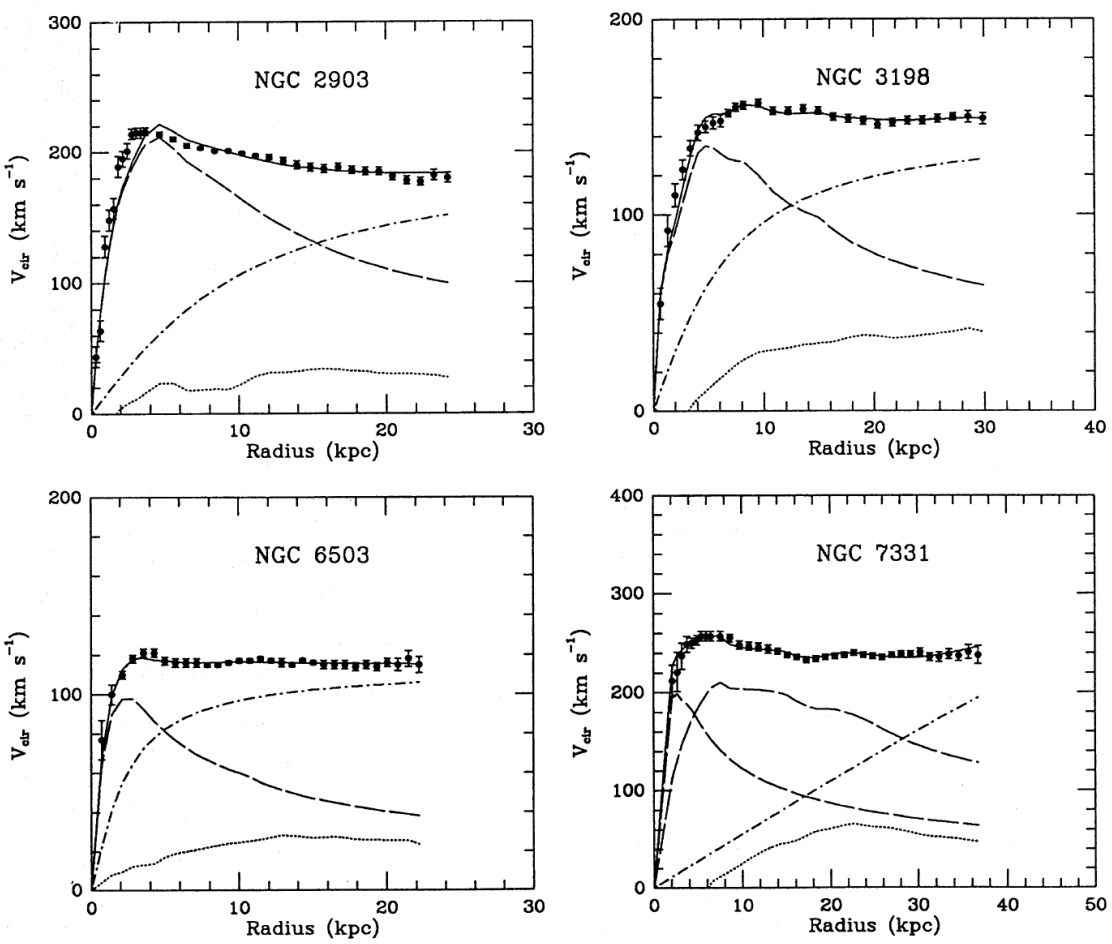

Figure 1.1: **Fit to rotation curves including a dark matter halo.** These plots show a three-parameter fit to the rotation curves of four galaxies. The solid curve shows the total fit, while the different components are also shown: The dashed curves are representing the visible matter, the doted curves the gas, the dash-dotted curves are indicating the dark matter halo. The plots are taken from [Beg91].

protons disappeared. Thus, the photons decoupled from the matter and the universe got transparent for the photons. Due to the further expansion of the universe the photon spectra, observable in nowadays, is a nearly perfect black body spectrum with a maximum of $T = (2.72548 \pm 0.00057)\,K$ determined from different experiments, e.g. COBE(FIRAS), WMAP [Fix09].

Although the temperature of the CMB is very uniform in all observed directions, further investigations with the satellite experiments COBE (1989-93), WMAP (2001-2010) and Planck (2009-2013) have been carried out, at which the Planck satellite performed the most precise measurements of the CMB, observing $\approx$ 93% of the sky in several frequency bands between 25 GeV and 1000 GHz, realized by 74 different detectors [Ade14]. The full sky map of the first 9 month of operation is shown in figure 1.2. This sky map illustrates, that several different objects on the sky have to be taken into account, strongly influencing the measurement of the CMB. There are sources of microwave radiation from the galactic plane of the milky way

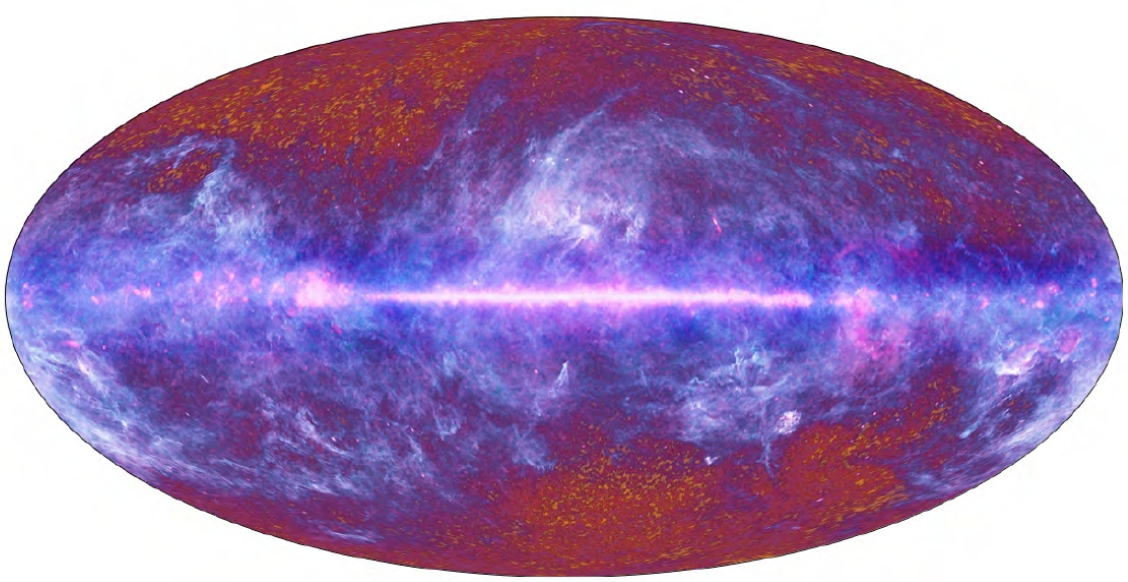

Figure 1.2: **Temperature fluctuations of the full sky image, measured by the PLANCK satellite.** This picture shows a composed map of the temperature fluctuations of the full sky, using observation from different frequencies. For this map, the first nine month of data have been used. The picture was released in 2010 and is taken from [Ade14].

as well as from extragalactic sources. These so called foregrounds can be disentangled, by measuring at different frequencies and looking for characteristic power laws. Furthermore, there exist dipole effects, which are related to the movement of the earth-sun system relative to the CMB, that have to be addressed. The corrected full sky map of the CMB is shown in figure 1.3.

As already proven and investigated with COBE and WMAP, there exist very small anisotropies on the μK scale in the CMB map, that are related to density fluctuations in the plasma from the time of the decoupling. These anisotropies carry a lot of different information about the curvature of our universe as well as the matter- and energy content. With the Planck observatory, these anisotropies have been investigated with higher sensitivities than the previous experiments.

For the further analysis, the projection of the temperature fluctuations into surface spherical harmonics is performed [Gru05]:

$$T(\theta,\phi) = \sum_{\ell=0}^{\infty} \sum_{m=-\ell}^{\ell} a_{\ell m} Y^{\ell m}(\theta,\phi) \tag{1.1.4}$$

with

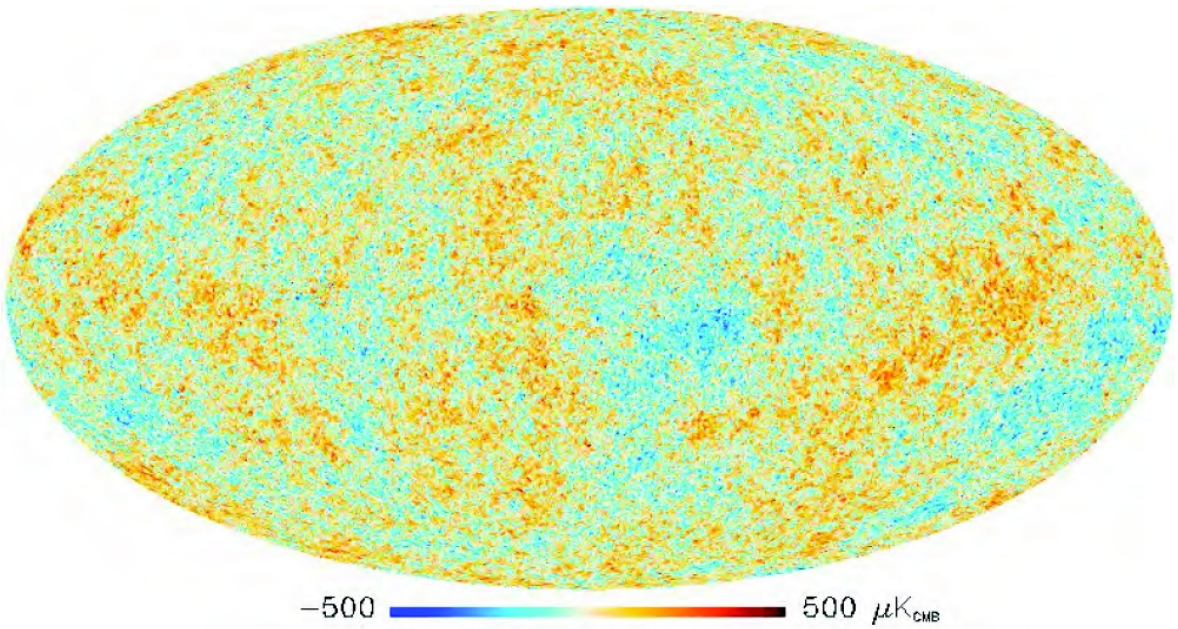

Figure 1.3: **Temperature fluctuations of the full sky CMB image, measured by the PLANCK satellite.** This picture shows the CMB map of the full sky after corrections and is taken from [Ade14].

$$C_\ell := \frac{1}{2\ell+1} \sum_{m=-\ell}^{\ell} \mid a_{\ell m} \mid^2 . \tag{1.1.5}$$

In figure 1.4, the intensity $D_\ell = \ell(\ell+1)C_\ell/2\pi$ is plotted against the multipole moment ℓ, which is related to the angular scale. The power spectrum has a dominant peak at $\ell \approx 200$ or $\theta \approx 1°$, respectively. In general, these peaks are referred to as acoustic peaks. They are produced in the early universe in the photon-baryon plasma before the decoupling of the photons. During this period small fluctuations occurred in the density of the plasma, which further grew, due to the attractive gravitational force. In contrary, the radiation pressure of the photons destroyed again the clumping. Therefore the plasma started to oscillate. After the decoupling of the photons from the plasma, these oscillations also froze out and are still visible in the CMB today.

For the further interpretation of the data, it is important to describe the kinematics of the universe: The first cosmological principle implied, that the universe is isotropic and homogeneous on large scales. As consequence, the universe has a constant curvature and the Robertson-Walker metric can be applied to translate Einstein′s field equation to the Friedman-LeMaître equations:

$$H^2 = \left(\frac{\dot{R}}{R}\right)^2 = \frac{8\pi G\rho}{3} - \frac{kc^2}{R^2} + \frac{\Lambda c^2}{3} \tag{1.1.6}$$

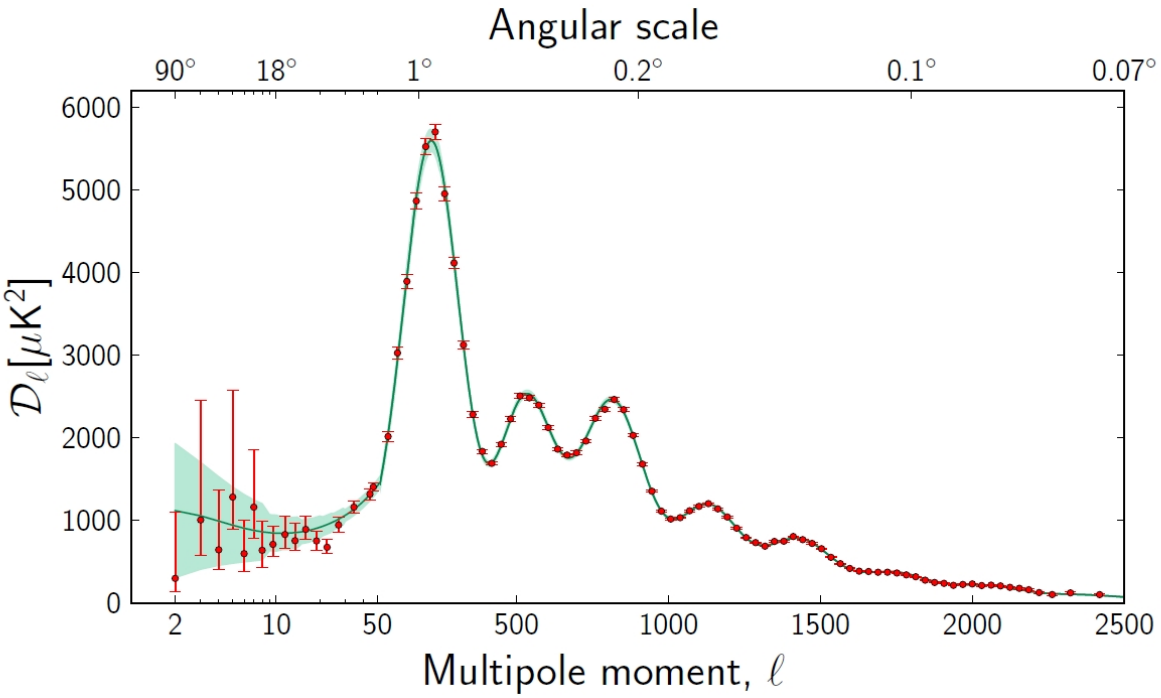

Figure 1.4: **Angular power spectrum of the CMB.** This plot shows the angular power spectrum, obtained from a projection of the temperature fluctuation into spherical harmonics taken from [Ade14].

$$2\left(\frac{\ddot{R}}{R}\right)^2 = -\frac{8\pi G\rho}{c^2} - \frac{kc^2}{R^2} + \Lambda c^2 - \left(\frac{\dot{R}}{R}\right)^2 \tag{1.1.7}$$

With R, representing a scale parameter (can be seen as the radius of the universe), G being the gravitational constant and ρ is the matter density. Λ is called the cosmological constant and k denotes the curvature of the space-time. The energy density of the universe is usually described in dimensionless variables $\Omega_i = \rho_i/\rho_c$, where $\rho_c = 3H_0^2/8\pi G$ is the critical density of the universe as function of the Hubble parameter of nowadays H_0 and $\rho_\Lambda = \Lambda c^2/8\pi G$ defining the vacuum energy density. Using this, equation 1.1.6 can be expressed with the scale parameter R_0 of nowadays like:

$$\frac{kc^2}{R_0^2 H_0^2} + 1 = \Omega_m + \Omega_\Lambda = \Omega_{Tot} \tag{1.1.8}$$

Distinguishing between three different scenarios:

- $k < 0$ or $k = -1 \rightarrow \Omega_{Tot} < 1$: Negative curvature, open universe
- $k = 0 \rightarrow \Omega_{Tot} = 1$: No curvature, flat universe
- $k > 0$ or $k = +1 \rightarrow \Omega_{Tot} > 1$: positive curvature, closed universe

Furthermore, the total matter density Ω_m can be divided into a fraction for baryonic matter Ω_b and dark matter Ω_c:

$$\frac{kc^2}{R_0^2 H_0^2} + 1 = \Omega_b + \Omega_c + \Omega_\Lambda = \Omega_{Tot} \tag{1.1.9}$$

The measurement of the CMB and the analysis in spherical harmonics give access to several of these values, some of them as parameters in the fit function. In tabular 1.1 the most important parameters, relevant for the characterization of the dark matter and determined by the WMAP and the Planck satellite are collected:

Table 1.1: **Selected cosmological parameters, determined from WMAP and Planck satellite mission.** In this tabular, some of the parameters, that are obtained from observations of the CMB are collected. While the WMAP results are related to a maximum likelihood analysis (ML), the Planck results are best fit values. In the literature, the values for Ω_b and Ω_c are usually given in terms of the Hubble parameter h with $H_0 = 100\ h$ km s^{-1} Mpc^{-1}. Additionally, CMB data are often combined also with data sets from different experiments e.g. from baryonic acoustic oscillation (BAO), super-nova observations (SN) or big bang nucleosynthesis (BNN) which is in agreement with SN observations. For further information see the references: WMAP results from [Kom09] and preliminary Planck results from [Ade14].

	WMAP (ML)	WMAP+BAO +SN (ML)	Planck (CMB+ lensing)	Planck+WMAP pol.+ BAO+high ℓ exp.
$\Omega_b h^2$	0.02268	0.02262	0.022242	0.022161
$\Omega_c h^2$	0.1081	0.1138	0.11805	0.11889
Ω_Λ	0.751	0.723	0.6964	0.6914
H_0	72.4	70.2	68.14	67.77
Age/Gyr	13.69	13.72	13.784	13.798

It is obvious, that the matter content in our universe is dominated by non-baryonic dark matter, although the WMAP and the Planck results are not fully consistent. Their differences are highly discussed in the astro-physics community and are focus of up-to-date research.

The combination of the different observations, e.g. coming from the CMB, the bayonic acoustic oscillations, lensing experiments or the observation of super-nova at large distances show that the universe is dominated by dark energy and dark matter. The baryonic matter only makes a tiny fraction of $\approx 5\%$ of the energy density, which means that we can explain only this fraction by the standard model of particle physics (SM). Further investigations showed, that cold and warm dark matter (non-relativistic at structure formation) are essential for the formation of the structures in the universe which are observed. Hot dark matter in the early universe would destroy small scale structures and prohibited the formation of galaxies at that time, which is in contradiction to the observations of a hierarchical structure formation (often called as “bottom-up” scenario).

To explain the missing $\approx 95\%$ of the energy density, the standard model of particle physics has to be enhanced by adding new symmetries and mechanisms. This is often referred to as "Physics beyond the standard model". This thesis is contributing to the experimental search for cold dark matter particles and therefore, I will focus on this research.

1.2 Candidates for dark matter

First attempts to explain the dark matter by massive compact halo objects (MACHOs), e.g. brown dwarfs or black holes, failed. Although their existence has been proven by the usage of micro-lensing techniques, their relative abundance is to small to explain dark matter [Alc00]. As already explained in the previous chapter, the physics beyond the standard models of cosmology and particle physics has to be investigated to understand the nature of dark matter.

From the wide variety of observation, it is deduced, that the dark matter has to be non-baryonic, non-relativistic during structure formation (cold or warm dark matter), non-luminous, massive and interacts only gravitationally and maybe on the scale of weak interaction.

Since the dark matter has been found to be a non-baryonic compound, the standard model of particle physics provides no candidate to fulfill all requirements. Even light neutrinos, which are non-luminous and weak interacting particles, are not matching to the profile. They have been ultra-relativistic in the early universe, which is not in agreement with observations of the structure formations [Pri00]. The light neutrinos belong to the hot dark matter and only make a small fraction to the energy content of the universe.

To explain the dark matter problem by particle physics, additional particles are postulated to enhance the standard model. Three very popular candidates will be introduced: Axions, sterile neutrinos and WIMPs. The latter one is of particular importance for several detection experiments (see the following chapter 2) and will be explained in more detail.

The Axion

The axion is a hypothetical particle, and originates from trying to solve the strong CP problem in quantum-chromo-dynamics by introducing a new symmetry as a minimal extension to the standard model. This global and chiral symmetry, named after Robert Peccei and Helen Quinn who proposed it in 1977, is spontaneously broken. Therefore, the existence of a new Goldstone boson is assumed, which is named as axion. Initially, the axion-mass-windows covered several orders of magnitude from $10^{-12}\,\mathrm{eV}$ to $10^{6}\,\mathrm{eV}$. But several astronomical observations reduced the mass-window down already in the late 1980′s to $10^{-6}\,\mathrm{eV} < m_a < 10^{-3}\,\mathrm{eV}$ and $2\,\mathrm{eV} < m_a < 5\,\mathrm{eV}$ for hadronic axions. [Tur90]

One experiment, among others, searching for solar QCD axions is the CAST experiment. The axions can transform into photons and vice versa in a strong electromagnetic field, which is called the Primakoff effect. Therefore the sun is supposed to be a strong axion source. A

so called axion helioscope is used by the CAST collaboration to search for axions produced in the sun. Inside the device, a strong magnetic field of $\approx 9\,\mathrm{T}$ is induced, where the solar axions are supposed to transform back into real photons (inverse Primakoff effect), that can be detected. The different phases of the CAST experiment are sensitive for axion masses of $m_a < 1.15\,\mathrm{eV}$. Up to now, only limits on the photon-axion coupling have been set. [Zio05], [Ari11]. Another experiment searching for axions making the dark matter is the Axion Dark Matter eXperiment, ADMX also using the Primakoff effect in a rf-cavity but looking for axions as dark matter in the galactic halo [Asz04].

Sterile Neutrinos as dark matter candidates

As already mentioned before, the light neutrinos are not good candidates for cold dark matter. In the standard model of particle physics, originally, the neutrinos are meant to be massless. But observation of neutrino oscillation from one flavor into another, implies that neutrinos do have mass [Kay08].

But there exist extensions of the neutrino model, that introduce new, heavy neutrinos [Dod93]. By adding right-handed neutrinos to the existing model, these neutrinos would not participate to the weak interaction (therefore, called sterile neutrinos), but are mixed as the active neutrinos $(\nu_e, \nu_\mu, \nu_\tau)$ to the mass eigenstates. This leads to additional effects in the neutrino oscillation and to the coupling of these sterile neutrinos to the observable particles. Furthermore, they interact gravitationally to baryonic matter, hence being a good dark matter candidate. Their existence, the number of additional sterile neutrinos and the masses are unknown, but different experiments are going to proof the existence and investigate their properties. The possibility of finding a signature from sterile neutrinos in ultra-precise measurement of the tritium β-decay with KATRIN experiment is discussed in [Ste13, Mer15]. Also baseline reactor experiments, like Double Chooz, Daya bay and Reno, can at least test the sterile neutrino hypothesis [Esm13] although these sterile neutrinos with the mass of $\sim$ eV are no candidates for the cold or warm dark matter. In addition, a short distance neutrino oscillation experiment using the Borexino detector at Gran Sasso and artificial neutrino sources is discussed. Even x-rays, produced by the decay of sterile neutrinos in other galaxies are possible and first evidences showed up recently [Bul14].

In general, a sterile neutrino with mass on the keV-scale would be an interesting candidate for the warm dark matter.

The WIMP and super-symmetric models

The WIMP (*weakly interacting massive particle*) can be seen as a class of particles with certain properties. As already mentioned in the name, they are supposed to be massive (typical masses in the GeV to TeV scale) and interacting only very weakly with ordinary matter. Usually it is also assumed that they are non-baryonic and stable or at least long-lived compared to the age of the universe. [Jun96]

The most prominent candidate for the WIMP is provided by super-symmetric (SUSY) theories, namely the neutralino χ. Since the theory of super-symmetry is very complex due to the existence of several different models, only a brief overview of some selected models will be presented, using [Ber05], [Jun96] and [Fen10], if not cited differently.

There are different reasons for introducing the super-symmetry as extension of the standard model of particle physics. Although the SM is a very successful theory, there are several aspects, beside the dark matter problem, that leads to the conclusion, that it is not complete. E.g. the "gauage hierarchy problem", which deals with the difference in the electro-weak energy scale and the Planck energy scale, is one of the main arguments for introducing super-symmetry. The mass difference of SM-neutrino compared to other fermions as well as the strong-CP problem are additional open questions in the framework of the SM. Finally the super-symmetry can be seen as one step to a grand unification of the forces in an overall theory.

In the super-symmetric enhancements of the SM, new, yet undiscovered particles are introduced: Every SM particle gets a super-symmetric partner with almost the same quantum numbers and gauge interactions. They only differ by the spin of 1/2. Some of the new particles are good WIMP or dark matter candidate. There exist different SUSY models with varying amounts of parameters and assumptions. One simplified model is called "Minimal Supersymmetric Standard Model" (MSSM), containing the minimal set of field enhancements to get access to all of the SM properties. One possibility for such kind of model is given in [Ber05]. For all the gauge bosons (gluons, $W^{+/-}$ and B) new fermionic partners are introduced (called gluino, wino and bino), while the quarks and leptons are associated with their SUSY partners (called squarks and sleptons). Furthermore, additional Higgs-fields are implemented, with a Higgsino doublet linked to the SM Higgs bosons. To complete the model, a new quantum number, the R- parity appears, which is $R = +1$ for SM particles and $R = -1$ for the partner particles. If the R-parity is conserved (not necessary in all SUSY models), this would lead to the fact, that the lightest super-symmetric particle (LSP) is supposed to be stable and thus being a perfect dark matter candidate if it is neutral.

The collection of new particles is shown in tabular 1.2, including the SM particles together with the minimal super-partners. As indicated, there are four neutral super-symmertric partners, the wino $\widetilde{W}_3$, the bino $\widetilde{B}$ and higgsinos $\widetilde{H}_1^0$, $\widetilde{H}_2^0$, that are mixing to four mass-eigenstates, called neutralino $\widetilde{\chi}_{1,2,3,4}^0$.

Usually they are ordered by the mass with $\widetilde{\chi}_1^0$ is chosen to be the lightest and stable one (LSP), being a linear combination of the neutral super-partners as shown in equation 1.2.1. This $\widetilde{\chi}_1^0 \equiv \chi$ is a WIMP candidate.

$$\chi = a_1\widetilde{W}_3 + a_2\widetilde{B} + a_3\widetilde{H}_1^0 + a_4\widetilde{H}_2^0 \tag{1.2.1}$$

Although the MSSM is already simplified, further assumptions on couplings and mixing angles are necessary to study the properties of the MSSM, leading to different scenarios, that are not discussed here. For the detection of the χ, the self-interaction (annihilation) and the interaction with SM particles (e.g. elastic scattering) are important and will be briefly discussed in chapter 2.

Table 1.2: **Particles in the Standard Model and in MSSM.** This tabular collects all the particles from the standard model and its super-partners from MSSM. The tabular is taken from [Ber05].

Standard Model particles and fields		Supersymmetric partners			
		Interaction eigenstates		Mass eigenstates	
Symbol	Name	Symbol	Name	Symbol	Name
$q = d, c, b, u, s, t$	quark	$\tilde{q}_L$, $\tilde{q}_R$	squark	$\tilde{q}_1$, $\tilde{q}_2$	squark
$l = e, \mu, \tau$	lepton	$\tilde{l}_L$, $\tilde{l}_R$	slepton	$\tilde{l}_1$, $\tilde{l}_2$	slepton
$\nu = \nu_e, \nu_\mu, \nu_\tau$	neutrino	$\tilde{\nu}$	sneutrino	$\tilde{\nu}$	sneutrino
g	gluon	$\tilde{g}$	gluino	$\tilde{g}$	gluino
$W^\pm$	W-boson	$\tilde{W}^\pm$	wino	$\tilde{\chi}^\pm_{1,2}$	chargino
H^-	Higgs boson	$\tilde{H}_1^-$	higgsino		
H^+	Higgs boson	$\tilde{H}_2^+$	higgsino		
B	B-field	$\tilde{B}$	bino	$\tilde{\chi}^0_{1,2,3,4}$	neutralino
W^3	W^3-field	$\tilde{W}^3$	wino		
H_1^0	Higgs boson	$\tilde{H}_1^0$	higgsino		
H_2^0	Higgs boson	$\tilde{H}_2^0$	higgsino		
H_3^0	Higgs boson				

Beside the neutralino, there are other potential WIMP candidates, for example Kaluza-Klein particles. This approach is introducing extra dimensions, where new particles exist and could make the dark matter. Sometimes in literature also sneutrinos or fourth generation (sterile) neutrinos are counted to the WIMP candidates.

Of course it is reasonable to assume, that the dark matter might be composed out of different particles or having a complete different origin, without any possibility to detect it with the current technology. Therefore, the investigation on candidates is started with well-motivated and promising candidates, to constrain the properties of the dark matter furthermore. This thesis is written in the context of the direct WIMP detection and in the following I will focus on the detection of neutralinos.

1.3 Outline of the thesis

This thesis is structured as following:

In chapter 2 an overview of the different approaches for the dark matter search is given, before the XENON100 and the XENON1T experiment are introduced in dedicated sections 2.2 and 2.3. Since the major topics of this thesis are related to the XENON1T project, the different purity and background requirements for the detector materials and the xenon gas are explained in this chapter as well.

Chapter 3 introduces the design and the construction of a gas purification system to remove electronegative impurities from xenon gas. The system has been set-up to investigate the

proper design for the XENON1T purification system. Different performance studies on the key components are presented.

The following chapter 4 addresses the design of a cryogenic distillation column to separate krypton from xenon. ^{85}Kr is one of the major backgrounds in xenon dark matter searches and has to be removed. The common theoretical model to design a distillation column, the McCabe-Thiele method is used to evaluate the optimal technical realization of a new type of distillation facility to separate krypton and xenon. The model as well as the constrains related to the special demands for XENON1T are also presented in this chapter.

In order to investigate the separation performance of the new setup, different techniques have been developed. Beside the measurement of the krypton concentration using a cold-trap enhanced residual gas analyzer, the performance has been tested using a novel ^{83m}Kr tracer method. Both techniques, will be presented in chapter 5.

In chapter 6 the separation performance of a single stage distillation setup is determined, using the ^{83m}Kr tracer method, investigating whether cryogenic distillation at very low concentrations is feasible at all.

Chapter 7 summarizes the commissioning of a package-type distillation column using 1 m package material, the so called Phase-1 column. The thermodynamic stability of the system and the determination of the separation performance will be presented.

Finally chapter 8 gives a summary of the work and an outlook for the enhancement of the column, using 3 m package material (Phase-2 column) and for the usage of the systems at the XENON1T experiment.

Detection of Dark Matter 2

There exist several approaches to investigate the existence of WIMPs and its properties. In this section the different detection techniques for the dark matter search are presented, with giving an introduction to direct and indirect detection methods before the XENON Project and its requirements are presented in more detail.

2.1 Direct and indirect dark matter detection and searching with particle colliders

The different detection methods, which are presented in the following, have in common that the neutralino is supposed to interact to some extend with standard model matter, producing measurable signatures in collisions (energy transfer), annihilation products as well as missing mass or momentum signatures in collider experiments when they are produced.

WIMP search with particle colliders

In dedicated models of super-symmetric enhancements of the standard model of particle physics, the neutralino χ is allowed to be produced in the collisions of standard model particles (SMP):

$$SMP + SMP \rightarrow SMPs + \chi\chi \tag{2.1.1}$$

This is investigated in collider experiments at e.g. LHC, where proton-proton collisions are used for producing super-symmetric particles. By comparing the energy and momentum in the initial state to the final state, weakly interacting particles can be identified by missing energy and momentum. The model-independence regarding cosmological parameters (e.g. WIMP density, velocity distribution, explained in more detail later in this chapter) is one of the advantages against indirect and direct detection technique. [Mit14]

Results from the ATLAS experiment, searching for dark matter production in proton-proton collisions have been presented in [Aad13]. The ATLAS detector is a multi-purpose detector,

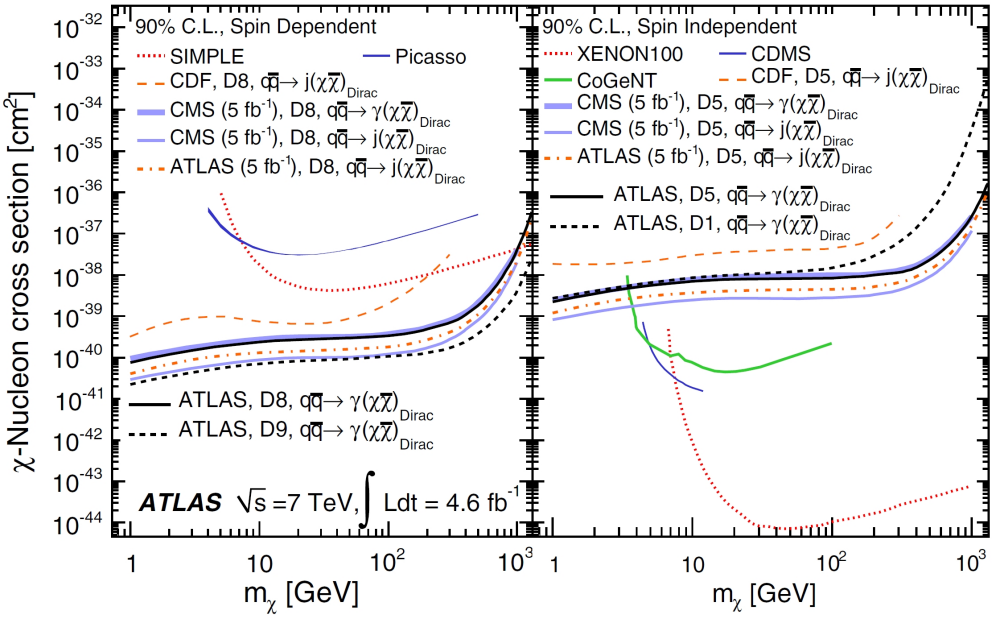

Figure 2.1: **Limits on the WIMP-nucleon cross section from collider experiments:** This picture shows the exclusion curves on the spin-dependent and spin-independent WIMP-nucleon cross section, measured with the ATLAS detector, in comparison with other experiments. The figure is taken from [Aad13].

located at the large hadron collider (LHC) at CERN. The results, that are presented, have been extracted from proton-proton collision at an energy of $\sqrt{s} = 7\,\text{TeV}$, taken in 2011, looking for missing transverse momentum in a mono-photon final state. The observation showed good agreement with SM predictions. Therefore only exclusion limits on the WIMP-nucleon cross sections are given, illustrated in connection to possible WIMP masses m_χ between $\approx 1\,\text{GeV}$ and $\approx 1\,\text{TeV}$ (see figure 2.1). In comparison to direct detection techniques, the sensitivity regarding lighter WIMPs is better, which is related to the energy transfer in direct-detection experiments.

Indirect WIMP search: detection of annihilation and decay products

Another approach is to investigate the self-interaction of dark matter particles. The WIMPs should be allowed to annihilate or even to decay to standard model particles:

$$\chi + \chi \rightarrow SMPs \qquad \text{and} \qquad \chi \rightarrow SMPs \tag{2.1.2}$$

The annihilation reaction can only takes place in regions with a very high local WIMP density. It is expected, that these reactions can take place in the center of the galaxy or even the sun, where the dark matter should be accumulated, due to the gravitational potential.

The particles, produced in these processes, like $e^{-/+}$, γs or neutrinos might be visible as special signature (sometimes referred as "smoking gun") in the cosmic particle flux and are objects of ongoing research. E.g. the Pamela experiment, a satellite experiment, was investigating the flux of charged cosmic particles in a range of 100 MeV up to several hundred GeV, searching for WIMP annihilations signatures in the cosmic anti-particle flux (mainly positrons and anti-protons) [Moc11]. The observation of 500 days in space, presented in [Men13], show an increase in the positron fraction with increasing energy. Although this signature might be caused by the annihilation or the decay of dark matter, as allowed in different models, there exist also known astrophysical accelerators, that can explain the excess, like nearby pulsars. Another experiment, investigating the flux of anti-matter is the AMS-2 detector, located on the international space station (ISS) [Agu13]. The AMS-2 experiment also detected a rise of the positron/electron fraction to even higher higher energies up to 500 GeV [Acc14], confirming the PAMELA results with higher precision. As already mentioned, different astrophysical background models and new sources (e.g. pulsars) can be used to explain the excess.

A different approach is to search for neutrinos from WIMP annihilation using earth bound detectors like IceCube or to search for special γ-signatures with Cerenkov-telescopes like H.E.S.S. or with satellite experiments like FERMI LAT.

In summary, up to now the annihilation and decaying processes of dark matter have not been confirmed so far. Although different observation are in agreement with theoretical models for dark matter interactions, additional studies on the background components are needed.

Direct detection of WIMPS

The direct detection technique aims to measure the energy transfer usually in the elastic scattering of WIMPs from the cosmic halo on a nucleus (N) inside an earth-bound detector. The recoil of the nucleus in the detector is defining the signal:

$$\chi + N \rightarrow \chi + N + \mathrm{E_{Recoil}} \tag{2.1.3}$$

These interactions usually produces ionization, scintillation light and phonon excitation inside the target material, that can be detected. The different experiments around the world usually take advantage of two signal channels to search for a WIMP-nucleon interaction. It allows for discrimination between nuclear recoils and electronic recoils, which is one tool for background suppression (see chapter 2.2). The CDMS experiment is using ultra pure semiconductor crystals (silicon and germanium) at cryogenic temperatures of $\approx 40\,\mathrm{mK}$ to measure the charge and the heat signal [Agn13], while the CRESST experiment is using $CaWO_4$ crystals at $\approx 10\,\mathrm{mK}$ to measure the heat and the light signal [Ang14]. Several experiments using liquid noble gases, e.g. the XENON project uses liquid xenon, while the DarkSide experiment is using a liquid argon detector [Ale13]. These detectors are sensitive to the light and the charge signal.

In general the interaction can be distinguished between spin-dependent and spin-independent WIMP-nucleon coupling (as already presented in figure 2.1). This is also reflected in the cross section for the wimp-nucleon interaction, defining the interaction probability for the two cases. In addition to the cross section, also the WIMP-mass and its local density in our solar system, together with their velocity distribution are of crucial importance: The Rate R measured at the detector can be written as an integral over all possible recoil energies (starting with the energy threshold of the detector E_T) of the differential rate dR/dQ:

$$R = \int_{E_T}^{\infty} \frac{dR}{dQ} dQ. \tag{2.1.4}$$

The differential rate is further connected to the WIMP O-nucleus cross-section σ_0, to the local WIMP density ρ_0, to the mass of the WIMP m_χ and the reduced mass of the WIMP-nucleus system $m_r = m_\chi m_N/(m_\chi + m_N)$. Furthermore, v_0 is the circulation speed of the sun around the galactic center of $\approx 220\,\mathrm{km/s}$, while T(Q) is giving the velocity distribution of the WIMP-wind (compare figure 2.2). Finally the form-factor $F^2(Q)$ carries the properties of the nucleus in the interaction [Jun96]:

$$\frac{dR}{dQ} = \frac{\sigma_0 \rho_0}{\sqrt{\pi} v_0 m_\chi m_r^2} F^2(Q) T(Q). \tag{2.1.5}$$

This formalism carries several unknown parameters. Some of them can be derived from observations, while others are provided from theoretical calculations, as explained in the following: The local WIMP density is usually set to $0.3\,\mathrm{GeV/cm^3}$, estimated from rotation velocities of our home galaxy, and usually the WIMP mass range between 1 Gev to the TeV scale is observed. The velocity distribution of the WIMPs $T(Q)$ is expressed by:

$$T(Q) = \frac{\sqrt{\pi}}{2} v_0 \int_{v_{min}}^{\infty} \frac{f_1(v)}{v} dv. \tag{2.1.6}$$

where $f_1(v)$ is the velocity distribution, integrated to take all possible velocities for a defined recoil energy Q into account. The structure of $f_1(v)$ is unknown, but usually a Maxwellian velocity distribution is applied and also the motion of the sun and the earth is taken into account. The earth motion around the sun on an inclined orbit of $\approx 60°$ with respect to the galactic plane (illustrated in figure 2.2) is expected to produce an annual modulation of the signal rate. Typically, these values are used by the community and in literature to make the results from different experiments comparable.

Beside the astrophysical quantities, also the characteristics of the WIMP-nucleus scattering has to be taken into account, addressed in $F(Q)$ and σ_0: In general, the elastic scattering properties of a WIMP to a nucleus is defined by the WIMP interaction with the quarks and the gluons inside the nucleons. Therefore also the distribution of quarks and gluons in the nuclei are important in order to understand the scattering process. The WIMP-quark coupling is rather unknown and the mechanism and coupling strength depend on the underlying super-symmetric model, inserting a strong model-dependency during this step into the calculation. Whenever possible, limits on the allowed parameter space by using experimental data

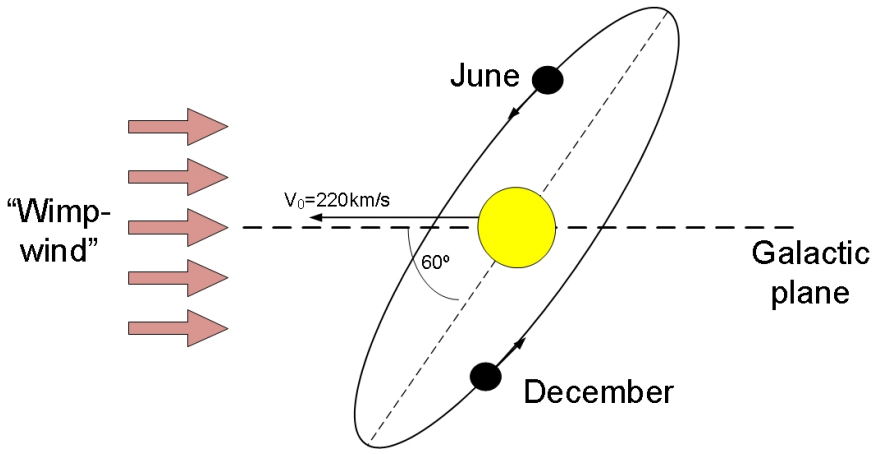

Figure 2.2: **Movement of the solar system through the galaxy.** The earth is moving around the sun, while the latter one is traveling with $\approx 220\,\mathrm{km/s}$ around the galactic center. Assuming a non-rotating WIMP halo and considering the inclination of the earth orbit with respect to the galactic plane, the effective "WIMP-wind" on earth would be different for different seasons.

from collider experiments are set. In a second step, the microscopic interactions are taken and transfered onto the bigger scale of the nucleons, using the nuclear matrix element of the quark and gluon structure in a nucleon, extracted from scattering experiments. In this step, the different coupling types are getting important: scalar, pseudo-scalar, vector, axial-vector and tensor couplings. Finally the nucleon operators are transported into a global matrix element to describe the WIMP-nucleus cross section, which depends on the transfered momentum. This is done by coherently adding up all the scalar and vector contributions of the single nucleons. During this step the form-factor $F(Q)$ for the interaction of the constituents is introduced.

The scattering of WIMPs on a nucleus takes place in an un-relativistic regime, which means that the energy transfer (or the momentum transfer) is small. Supposing, that the neutralino is a majorana fermion, the calculations are simplified and only spin-spin (axial vector coupling between quark and χ) and scalar couplings contribute, where the latter one couples to the mass of nucleus.

For the axial-vector coupling, it can be assumed, that the interaction is translated between the quark and the neutralino by a virtual Z^0 or squark $\widetilde{q}$ exchange. In the "odd-group" model, the spin of the nucleus is dominated by the amount of neutrons or protons and which group is mostly unpaired. Finally, the cross section for spin-dependent couplings depends on the total angular momentum J of the nucleus: $\sigma_{0,Spin} = \sigma_{0,Spin}(J)$.

The scalar coupling is different from the axial-vector coupling. There exist more possible interactions to the nucleus content, e.g. the χ-quark interaction via squark $\widetilde{q}$ or Higgs (H, h) exchange, but also couplings to the gluons which contribute to the scattering process. Therefore, the scalar interaction might be dominant for heavy nuclei, compared to the spin-coupling, with the cross section for spin-independent coupling $\sigma_{0,Scalar} \propto A^2 \sim m_N^2$.

As already mentioned before, in this formalism, a lot of uncertainties are implemented, starting from cosmological parameters like WIMP density or velocity profiles going to scattering parameters and interaction properties that strongly depend on the used models. Therefore, transferring a signal rate in a detector to physical properties of the dark matter might lead to miss-interpretations. In the following, the direct detection of dark matter with the XENON100 experiment is presented together with the latest results from the dark matter search. Afterwards the XENON1T project is introduced, which is the next generation dark-matter experiment.

2.2 The XENON100 Experiment

The XENON project has been a very successful campaign in the recent years, searching for dark matter. Although no discovery has been made yet, very strong restrictions on the interaction cross section with ordinary matter are claimed. Especially the XENON100 experiment was the most sensitive experiment world-wide up to autumn 2013. In this section, the technology of the XENON100 detector is explained, before its follower, the XENON1T experiment is introduced, which is working on the same principle, but with more target material and improved background suppression to achieve higher sensitivity. Some of the requirements and the technical realization will also be introduced in the following chapters.

Advantages of xenon for dark matter detection

The physical properties of xenon make it very feasible for the direct dark matter search [Apr10a]: The high atomic number (Z=54) in combination with the high density of liquid xenon ($\rho = 2.9\,\mathrm{g/cm^3}$ at $\mathrm{T} = -100°\mathrm{C}$ and $\mathrm{p} = 1.6\,\mathrm{bar}$) provide good stopping performance for incoming particles. E.g. photons get absorbed and electrons are stopped after a few centimeter and therefore the inner region of the detector is shielded against radioactive radiation coming from the walls of the detector by the xenon itself (self-shielding). The xenon isotopes have even and odd numbers of nucleons, which makes it interesting for studies of both spin-independent and spin-dependent WIMP-nucleon interactions. Furthermore, there is only one, so far confirmed, long-lived radioactive xenon isotope. The ^{136}Xe undergoes a $2\nu\beta\beta$ decay with a half-live of $\mathrm{T}_{1/2}^{2\nu\beta\beta} \approx 2 \times 10^{+21}\,\mathrm{yr}$ [Exo14a] and is a candidate for neutrino-less double beta decay, whereas it has not been observed so far [Exo14b]. Due to the long half-lives, the decays from ^{136}Xe are of minor importance for dark matter search experiments.

As already pointed out in the previous chapter, the expected signal rate in the detector is directly related to the characteristics of the target nuclei. One can calculate the expected rate for different targets, as shown in figure 2.3. In general the expected recoil energies E_r are rather low, in this calculation up to 200 keVr. In combination with the low expected rate of the order $\approx 10^{-5}$ events/kg/day/keVr, the used detector has to provide a low threshold to measure the deposited energy in combination with very low background rate. These two constrains are mandatory for xenon detectors and other detectors as well. Furthermore, it is shown in figure 2.3, that the expected rate for low recoil energies is enhanced for

xenon, compared with other detector materials because of the A^2-dependence of the scalar interaction until the form factor reduces the sensitivity. This enhances the possibility of detection for these rare events.

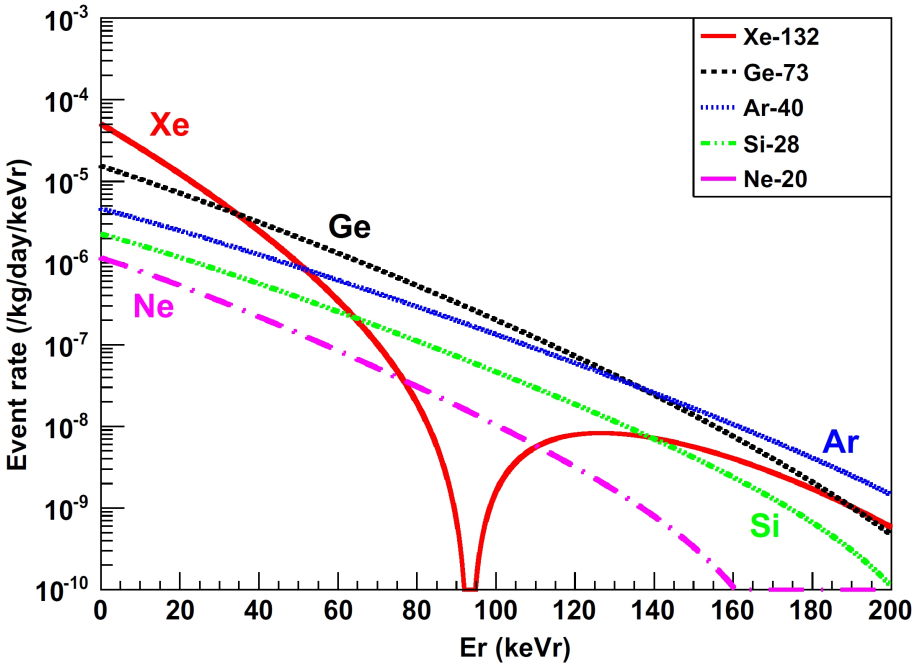

Figure 2.3: **Calculated nuclear recoil spectrum of WIMPs on different target materials.** This plot shows the differential recoil spectrum for different target materials for a WIMP with a mass of 100 GeV. The vanishing event rate at a recoil energy of $\sim$ 94 keV for xenon is caused by the Form factor $F(Q)$. the picture is taken from [Ari12].

Another, more technical advantage of xenon is the moderate, cryogenic temperature, needed for the liquefaction of the xenon (T = -100°C at 1.6 bar). The up-scaling to higher target masses is simply achieved by increasing the cooling power, using additional commercial available cryo-coolers.

The dual-Phase time projection chamber of XENON100

The XENON100 detector is constructed as a dual phase time projection chamber (TPC), filled with liquid xenon at an operating temperature of -91°C. The working principle is shown in figure 2.4 (left) and is also explained in more detail in [Apr10c] and [Apr12a]: An incoming particle is interacting with the liquid xenon and is producing primary scintillation light of 178 nm wavelength, called S1, as well as free electrons. The S1 light is detected by special photomultiplier tubes, optimized for this wavelength. The produced electrons are prevented from recombination with the ionized xenon by drifting in an electric field of 0.53 kV/cm between cathode and gate grid towards the gaseous phase. In a second electric

field between the gate grid and the anode, which is with $\approx 12\,\mathrm{kV/cm}$ much stronger, the electrons are extracted from the liquid phase, accelerated and produce proportional scintillation light, called S2, which is also detected with PMTs.

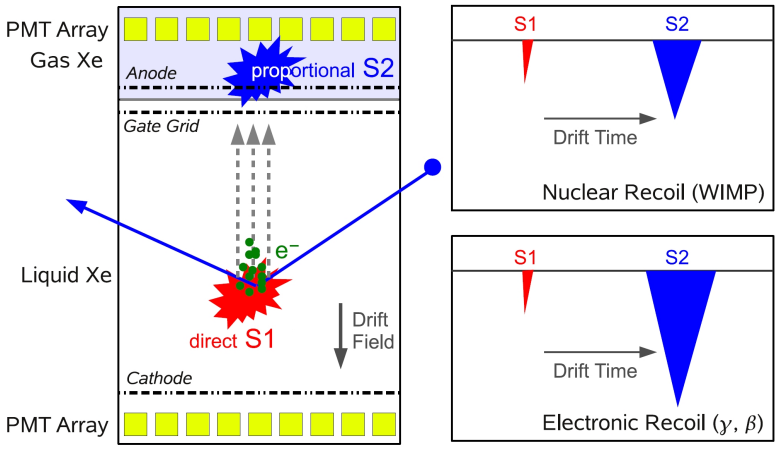

Figure 2.4: **Schematics of the XENON dual phase TPC.** This picture shows the working principle of the XENON100 TPC, using scintillation light and charge readout together with two arrays of photomultiplier tubes (PMTs) for the position reconstruction. The picture is taken from [Apr12a].

The 3D position reconstruction is realized by using the distribution of the S2 light hit pattern, detected by the different PMTs of the top array, to calculate the interaction place in the horizontal plane. The vertical position can be calculated by the time difference between the S1 and the S2 signal (see figure 2.4, right). Due to the self-shielding properties of the xenon many interactions are identified by the 3D position reconstruction to take place near the wall of the detector. Hence, it is a successful technique to define a background reduced detector volume, the so called fiducial volume, where the contamination coming from the walls do not spoil the dark matter search.

To distinguish between events, produced by WIMPs and standard model particles, e.g. electrons or photons, the spectral shape of the S1 relative to the S2 signal for the individual event is used. As already mentioned in chapter 1.2, it is expected that the neutralino is transferring the energy by interactions with the neutrons and protons of the xenon nucleus (nuclear recoil). In contrary, electrons, positrons or gammas transfer their energy mainly to the electron cloud, referred to as electronic recoils. Although the number of of created charges is almost equal in the two cases, the ionization density in the first reaction is much higher. As consequence, more ions can recombine and the number of free electrons is lower for nuclear recoils than for electronic recoils (so called quenching). Since the number of initial electrons is related to the amplitude of the S2 signal, the ratio S1/S2 is used to discriminate between signal and background events (see figure 2.4, right picture).

In figure 2.5, two calibration measurements are presented to illustrate the effect. The electronic recoil band is calibrated by using a ^{60}Co source, which emanates β-electrons with an endpoint energy of $E_\beta = 0.3\,\mathrm{MeV}$ and γ radiation with $E_\gamma \approx 1.1\,\mathrm{MeV}$ and $E_\gamma \approx 1.3\,\mathrm{MeV}$

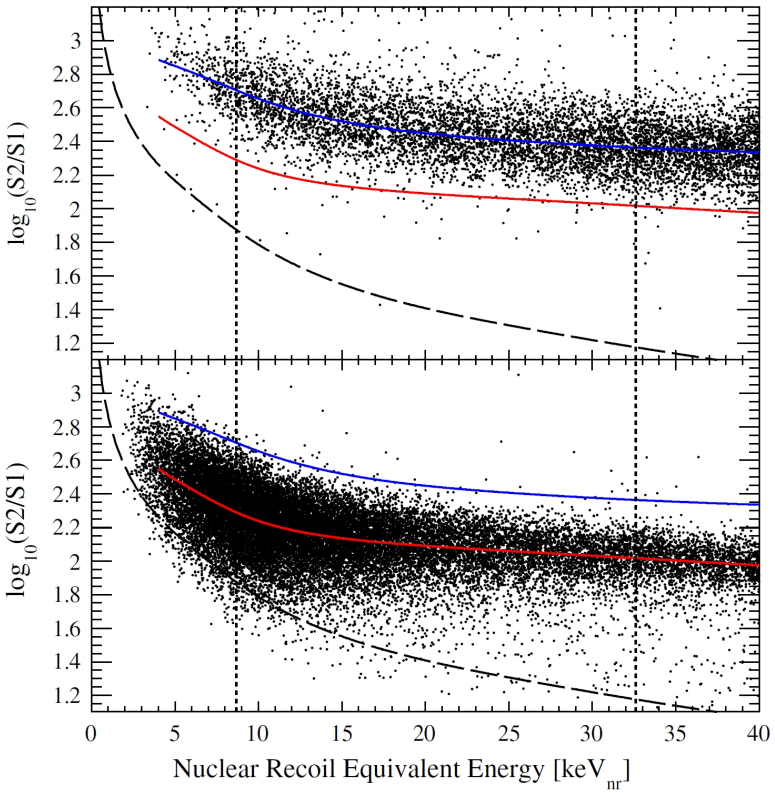

Figure 2.5: **Response of the XENON100 TPC to different calibration sources.** This plot shows two different calibrations, performed at the XENON100 detector. The ratio of S2 to S1 is plotted against the nuclear recoil equivalent energy, derived from the S1 signal. Top: calibration with ^{60}Co to define the electronic recoil band. Bottom : AmBe-calibration, to get the response to nuclear recoils. The vertical dashed lines are indicating the WIMP search window, while the long-dashed line indicates a S2 software threshold. The medians of nuclear- and electronic recoil bands are indicated by the red and the blue lines, respectively. The figure is taken from [Apr10c].

[Nuc14], whereas only the high energy γ radiation can penetrate deeply through the whole detector, producing electronic recoils via Compton scattering. Although the discrimination probability for electronic recoil events is very high ($> 99\%$ at 50% nuclear recoil acceptance, [Apr11]), a small fraction of electronic-recoil events can pass the data quality cut and are interpreted as nuclear-recoil events (leakage events). The nuclear recoil band is calibrated using neutrons from (α,n)-reactions in an americium-beryllium (^{241}AmBe) source. Neutrons also deposit their energy by nuclear recoils which make them a good calibration source but also a major contributor to the background in direct dark matter searches. These aspects are of crucial importance for the design of the experiment. All radioactive sources, contributing to the background, have to be reduced to a minimum.

The XENON100 experiment has been collected data for several years now, but unfortunately no dark matter has been found so far. The results on the spin-independent search with 225 live-days of data in 2012 have been published in [Apr13a] and are briefly reviewed: In total

224.6 live days of data with a fiducial volume of 34 kg have been collected. The blind analysis shows no evidence for WIMP-nucleon interaction. Two candidate events have been detected, which is consistent with a background expectation of (1.0 ± 0.2) events in the region of interest. Therefore an exclusion curve has been plotted, shown in figure 2.6.

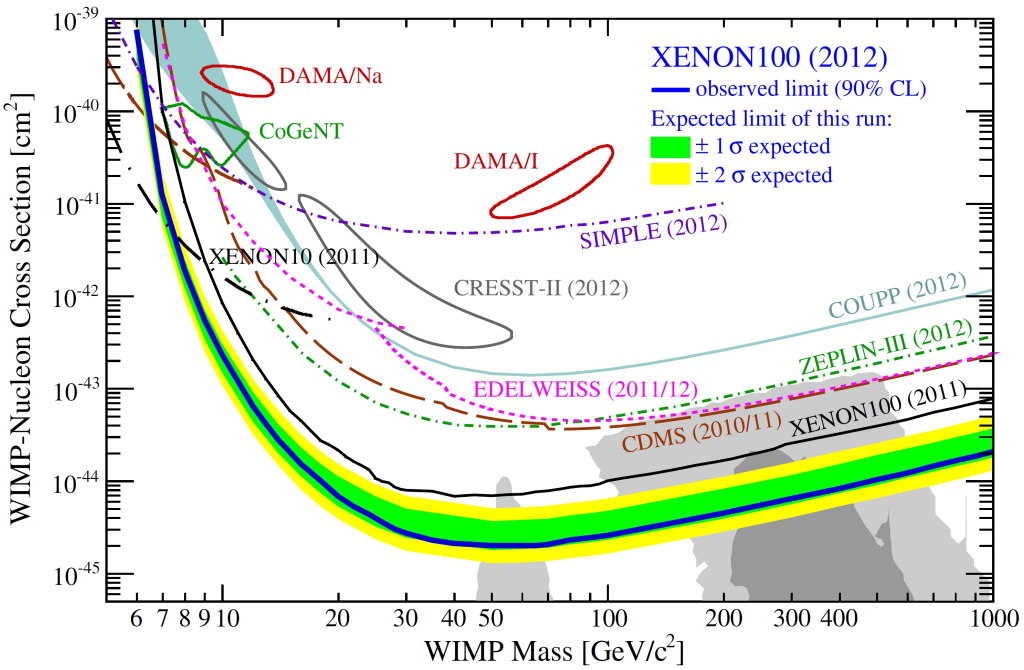

Figure 2.6: **Limits on the spin-independent WIMP-nucleon cross-section.** In this plot the limits for spin-independent WIMP-nucleon cross section as function of a hypothetical WIMP mass from the XENON100 experiment is shown, taking 225 live-days of data with a fiducial volume of 34 kg. For comparison, the results from competitors are shown as well. The calculated exclusion line is shown in blue, while the expected sensitivity of the XENON100 experiment is marked as green and yellow bands. The shadowed area is the region that is predicted by super-symmetric models. The figure is taken from [Apr13a].

The minimum of the curve is reached at 55 GeV with an elastic, spin-independent WIMP-nucleon cross section of 2×10^{-45} cm^2 at 90% confidence level. The XENON100 experiment was the most sensitive experiment for spin-independent WIMP-search from 2012 up to autumn 2013.

Further investigations on that data sample also for spin-dependent couplings have been performed and are presented in [Apr13b]. The data showed no indication for an axial-vector interaction with ^{129}Xe and ^{131}Xe. Therefore, upper limits have been set, the most stringent ones for WIMP-neutron coupling with a minimal cross section at 3.5×10^{-40} cm^2 for a WIMP mass of 45 GeV (90% confidence level), shown in figure 2.7 (left). Since xenon has an even number of protons, the spin-dependent coupling is much weaker than for the neutron. Therefore the latter channel has the much higher sensitivity and gives the most stringent limits.

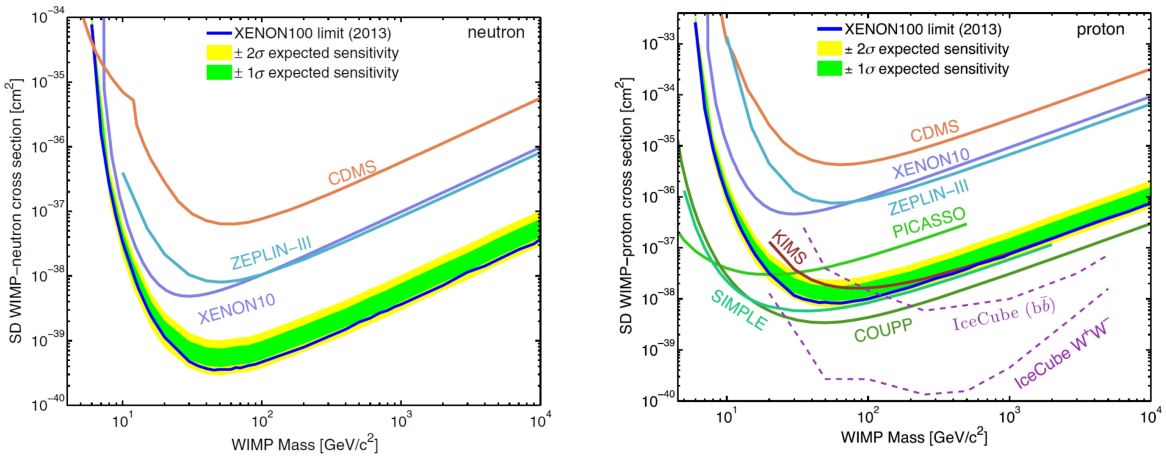

Figure 2.7: **Limits on the spin-dependent WIMP-nucleon cross-section as function of the hypothetical WIMP mass.** Here, the exclusion plots for spin-dependent couplings to neutrons (left) and protons (right) achieved with the XENON100 experiment are shown in comparison with other experiments. The figure is taken from [Apr13b].

Further investigation also on solar axions and axion-like particles (ALP) have been performed and are presented in [Apr14a]. The electron-axion coupling is investigated, setting the most stringent limits up-to-date. For further information, please see the associated publication.

To summarize, the XENON100 experiment has been the most sensitive dark matter detector until it is surpassed in sensitivity by the LUX experiment, which confirmed the XENON100 result and set the most stringent limits at a minimal spin-independent WIMP-nucleon cross section of $\sigma_{SI} = 7.6 \times 10^{-46}$ cm^2 at 33 GeV/c^2 with 90% confidence level [Ake14]. The LUX experiment is also using a dual-phase xenon TPC, realizing a fiducial volume of 118 kg to achieve a better sensitivity. This shows the advantages of xenon TPCs in dark matter search. The XENON100 detector has reached the final sensitivity. Further data collecting in 2013 and 2014 have been performed to enlarge the data sample for an annual modulation analysis. Furthermore, the XENON100 experiment is used for testing new technologies, needed for the XENON1T experiment, e.g. new calibration sources or active radon removal.

The XENON1T detector, is the next step for the XENON collaboration to gain better sensitivity by enlarging the target mass and reducing the background. In the following the XENON1T project is introduced and also its requirements, before the main topics of this thesis will be presented.

2.3 The XENON1T Experiment

The XENON1T experiment is designed as the next step after the very successful XENON100 experiment and aims for a much higher sensitivity down to a spin-independent WIMP-nucleon cross section of $\sigma_{SI} \approx 2 \times 10^{-47}$cm^2 after two years of operation [Apr12b]. The projected sensitivity in comparison with the latest resuts from LUX and XENON100 is

shown in figure 2.9. Beside the upscaling of the target mass, it is also necessary to reduce the background by a factor of 100 compared to the XENON100 experiment.

The XENON1T experiment has been described in a technical design report [Apr10b], while a more actual overview of the experiment has been presented in [Pla14] and will be briefly summarized here: The XENON1T design is based on the same principles than its predecessor and will be located at Hall B in the Gran Sasso Underground Laboratory in Italy.

Figure 2.8: **Illustration from the XENON1T experiment at LNGS.** This picture shows a photo composition of the XENON1T experiment, with the CAD drawing of the detector inside the water shield and some part of the service building next to it. In the back it also shows the Grans Sasso Mountain where the underground lab is located, together with an Overview of Hall B (left), where XENON1T will be placed. This picture has been provided by Donato Orlandi from LNGS to the XENON collaboration

It is constructed as dual phase TPC with ≈ 3.3 tons of xenon as total target mass, aiming for a fiducial volume of 1.3 tons. The TPC will be equipped with 248 PMTs (Hamamatsu, type R11410-21), which provide high quantum efficiency of $Q_e \approx 36\%$ at the xenon scintillation wavelength. The TPC is encapsulated by a double-walled cryostat vessel, made from special low-radioactive stainless steel. The TPC is further mounted inside a water tank of 9.6 m diameter and 10 m height, which is used for shielding against radioactive background from the outside and as active muon veto. The latter aspect will be described in more detail in chapter 2.5.1. The xenon inside the TPC is permanently circulated through a purification system to clean the xenon from electronegative impurities, mounted outside of the water tank in a service building. The design of the purification system is done by the Institut für Kernphysik in Münster together with colleagues from the Columbia University, USA and since summer 2014 from Rensselaer Polytechnic Institute, USA. The design and the construction of a prototype of this purification system is done in Münster and is one of the

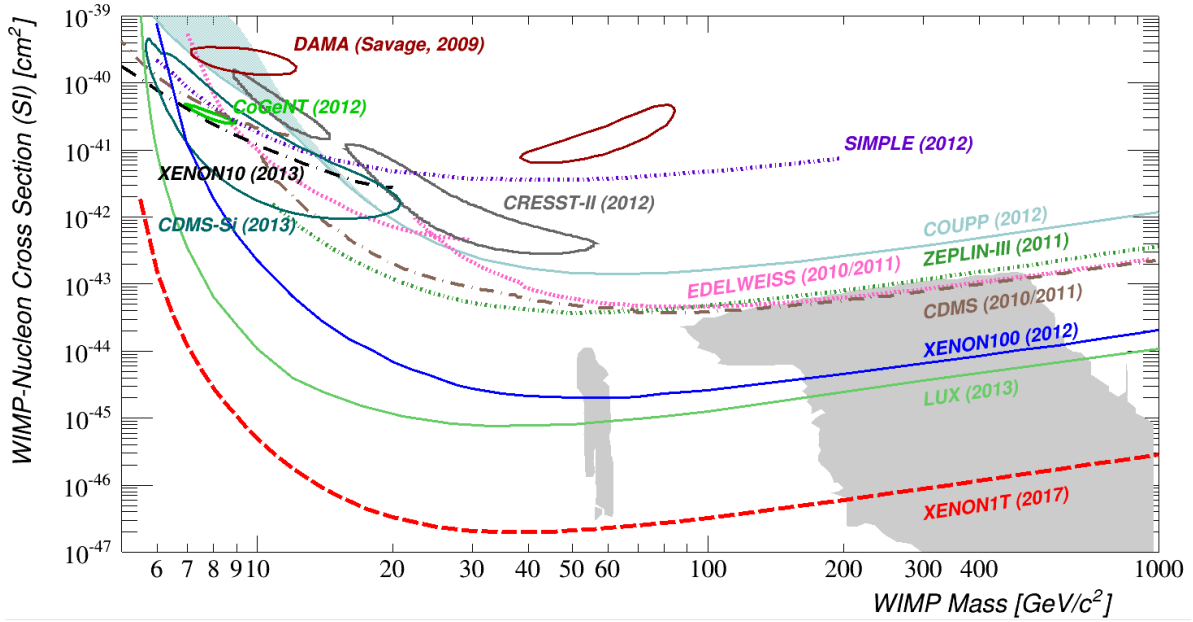

Figure 2.9: **Projected sensitivity of the XENON1T experiment.** This plot contains the projected sensitivity of the XENON1T experiment for an exposure of two years and a fiducial volume of 1 ton of xenon in comparison with other experiments. XENON1T is supposed to probe a significant fraction of the area, favored by super-symmetric models (grey shaded region) and is aiming to be the most sensitive experiment in the next years. The plot is kindly provided by the XENON collaboration.

topics in this thesis, discussed in the following chapter 3.1. Inside the service building the xenon recovery and storage system (Restox) is mounted, which allows to store about 7.6 tons of xenon in a high pressure, vacuum insulated and with liquid nitrogen cooled sphere. This vessel is used for storing the xenon until it is used inside the detector and also as emergency recovery system, in case that the cryogenic system of the TPC fails. The cryogenic system, as well as all the electronics for the data acquisition and the high voltage is also housed in the service building. Furthermore, a distillation column will be mounted to clean the xenon from krypton before it is used in the experiment. The Institut für Kernphysik in Münster is responsible for the development and the construction of the distillation column. The design, the construction and the commissioning of a test setup called Phase-1 distillation column is the major topic, that is presented in this work. The final distillation column for the XENON1T experiment will be presented in [Mur18].

In the following, the requirements for the xenon purity as well as the handling for radioactive contaminations is explained, which are important aspect to achieve the goal of the XENON1T experiment.

2.4 Purity requirements of the xenon gas for the XENON1T experiment

Due to the working principle of the TPC, the purity of the xenon is of crucial importance for the performance of the detector. Since the vacuum-ultra-violet (vuv) scintillation light of xenon can be absorbed by different kind of impurities, e.g. water, the level of these impurities has to be extremely low, in order to achieve the maximum in light yield. In addition, the electrons produced in the interaction and drifted in the electric field can react with the electronegative impurities e.g. water or oxygen as well to form negative ions:

$$e^- + S \rightarrow S^- \tag{2.4.1}$$

Hence, the concentration of impurities [S] in mol/l is directly related to the concentration of free electrons that are drifted in the liquid xenon reservoir and have to be sufficiently low [Apr10a]:

$$d[e^-]/dt = -k_s \cdot [S] \cdot [e^-] \tag{2.4.2}$$

where k_s in $l/(mol \cdot s)$ is called attachment rate constant, which varies for the different impurities and depending on the impurities also in the applied electric filed strength. Solving the differential equation gives the exponential time evolution of the electron concentration $e^-(t) = e(0) \cdot \exp(-k_s \cdot [S] \cdot t)$ with $\tau_e = 1/(k_s \cdot [S])$ is being called as electron lifetime.

Since the concentration [S] is usually unknown, it is more practicable to measure the electron lifetime directly in the experiment. This can be achieved by measuring the exponential decrease in time over the integrated, collected charge. Any kind of interaction of drifting electrons would lead to a decrease in collected charge. In the XENON100 experiment, the electron lifetime is determined by regularly calibration with a radioactive ^{137}Cs source. During the commissioning and the first science run in 2010, electron lifetimes of $\tau_e = 556\,\mu s$ have been measured according to [Apr12a] and even higher values of $\tau_e = 611\,\mu s$ have been achieved in the science run of 2011 and 2012 [Apr13a].

Since the electron mobility is strongly influenced by the electric field, usually the attenuation length is defined:

$$\lambda_{att} = \mu \mathrm{E} \tau = v_d \tau \tag{2.4.3}$$

with E being the electric field, μ the electron mobility and v_d the electron drift velocity. This will be used for the estimation of the purity that is needed for the XENON1T TPC. Since the strength of the electric field has been specified to be $\approx 1\,\mathrm{kV/cm}$ [Apr10b], the values for k_s and v_d can be found in literature (see figures 2.10 and 2.11).

The drift velocity v_d has been determined in different experiments and calculations summarized in figure 2.10, giving the velocity $W = v_d$ as function of the reduced electric field strength E/N in the unit Townsend Td. The latter one is defined as the ratio of field strength

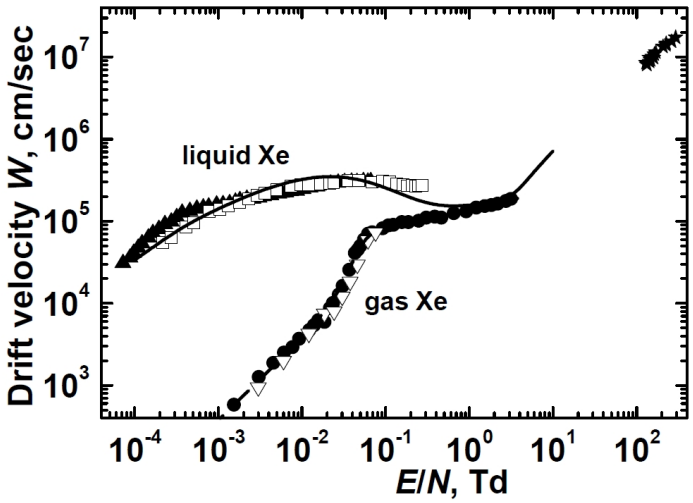

Figure 2.10: **Electron drift velocity for increasing electric field strength.** This picture shows the result of several measurements of the electron drift velocity for different field strength (dots), parameterized in units of the reduced electric field strength Td ($1\,\mathrm{Td} = 1 \cdot 10^{-17}\,\mathrm{Vcm}^2$) together with a calculation (line) presented in [Atr05].

E and particle density N with $1\,\mathrm{Td} = 1 \cdot 10^{-17}\,\mathrm{Vcm}^2$. At the given conditions for the field strength $E \approx 1\,\mathrm{kV/cm}$ and the particle density in liquid xenon $N \approx 1.3 \cdot 10^{22}\,\mathrm{particles/cm}^3$, the reduced field strength is calculated to $E/N = 8.5 \cdot 10^{-3}\,\mathrm{Td}$. Comparing with figure 2.10 gives an estimation on the drift velocity $v_d \approx 2 \times 10^5 \mathrm{cm/s}$. Furthermore, it is shown, that the drift velocity is rather constant in this regime, which implies, that changes in the field strength only cause a small impact on the velocity. The attachment rate constant strongly depends on the electric field strength and on the element or molecule. Since oxygen is one of the dominant impurities, the value at the given field strength is obtained from figure 2.11 to be $k_s \approx 7 \times 10^{10}\, l/(mol \cdot s)$

For a liquid xenon reservoir of one meter height and requesting the same length as attenuation length ($\lambda_{att} = 100\,\mathrm{cm}$), which is the drift length of the electrons in the XENON1T TPC and a liquid xenon density of $21.9\,mol/l$ (at 2 bar and $-98°\mathrm{C}$), $[\mathrm{S}]_{oxygen}$ is calculated to be

$$\lambda_{att} = v_d \tau = \frac{v_d}{k_s \cdot [S]_{oxygen}} \rightarrow [S]_{oxygen} = \frac{v_d}{k_s \cdot \lambda_{att}} = 2.9 \times 10^{-8} mol/l \approx 1.3\,\mathrm{ppb}^1 \qquad (2.4.4)$$

This estimation shows, that a technique is needed to reduce the concentration of oxygen and other electronegative impurities below the 1 ppb level to ensure a proper charge collection inside the TPC. The chosen technique and further requirements for the removal of electronegative impurities will be presented together with the experimental setup in chapter 3.

[1] $1\,\mathrm{ppb} = 1 \cdot 10^{-9}\,\mathrm{mol/mol}$

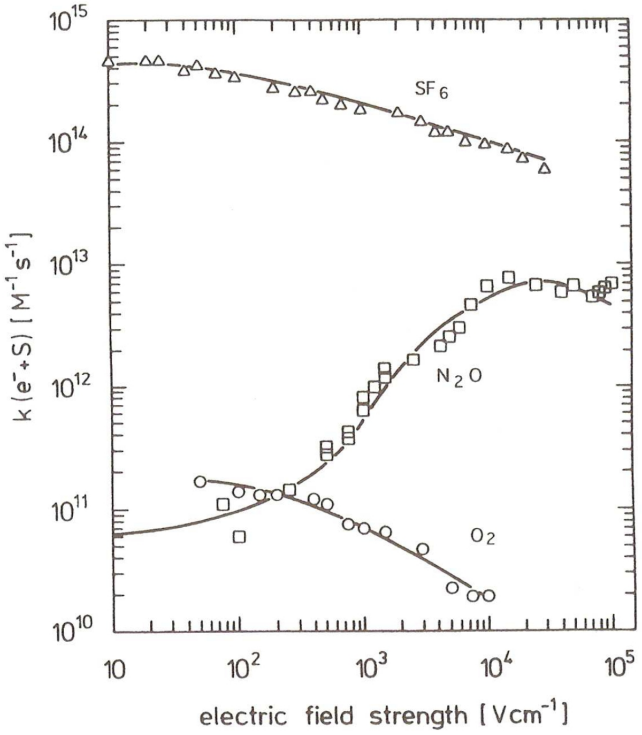

Figure 2.11: **Attachment rate constant of different molecules and field strength in liquid xenon.** The attachment rate constant k_s for SF_6, N_2O and O_2 is given for different field strengths. k_s is plotted in units of the molar concentration $[M] = [mol]/[l]$. The picture is taken from [Bak76].

2.5 Background requirements for the XENON1T experiment

Beside the purity requirements for electronegative contaminations, to get a proper light and charge collection inside the TPC, the radioactive background inside the detector can also be treated to some extend with dedicated cleaning and purity standards. In general, the sources of background are divided into electronic background, produced by electronic recoils (ER) and neutron generated background, produced by nuclear recoils (NR).

The background from neutrons, that are produced by cosmic muons and by (α, n)-reactions, and its reduction will be explained in the next chapter 2.5.1, while the ER background, that is consisting of γ-rays and electrons from β-decay, has different origins (intrinsic and internal backgrounds). The latter ones will be described together with the reduction techniques in chapter 2.5.2.

2.5.1 Neutron background in the XENON1T experiment

Although this thesis deals with xenon purity, the handling of the neutron background is briefly introduced, to give a full overview, about the different components of background inside the detector.

As already mentioned in chapter 2.2, one crucial background for the WIMP search is coming from neutrons, that produce WIMP-like nuclear recoil events [Apr13c]. Since neutrons are expected to scatter also multiple times with the xenon target, these signals can be selected from the data, using quality cuts (the WIMP is expected to perform single scatter events only). Hence, the background of single-scatter neutrons has to be treated differently.

There are two major origins for the neutrons: either from (α, n)-reactions or spontaneous fission and from reactions with cosmic muons in the surrounding materials and give rise to neutrons with typical energies in the MeV range. The (α, n)-reactions and spontaneous fission takes place in the surrounding materials. All the parts of the detector (stainless steel, PTFE, copper,....) are containing small amounts of radioactive impurities, e.g. ^{238}U, ^{235}U, and ^{232}Th. The amount of neutrons, produced by these contaminations can be reduced, by careful screening campaigns to find materials with a minimal content of radioactive impurities. The results of the screening is also used in Monte-Carlo studies to predict the background inside the detector. In addition, this screening campaign is also reducing the ER background, since the noted processes are usually coupled to the emission of γ rays. Furthermore, these (α, n)-reactions and spontaneous fission are taking place in the rock of the underground lab as well, which also contains naturally the noted elements. The background, caused by these neutrons is reduced by a shielding of the detector with water, moderating and stopping the incoming neutrons. The background coming from reactions of cosmic muons[2], with the material is handled by implementing an active muon veto inside the water shield. For the XENON1T experiment, the detector is mounted inside a cylindric steel vessel of $\approx 10\,\mathrm{m}$ diameter and height, filled with purified water. The volume is equipped with PMTs to detect Cerenkov radiation inside the water as indicator for a muon interaction with the water [Apr14b]. The detection of the muon track allows to select coincided events inside the detector, related to the muon, as background.

The construction of the vessel had been finished early 2014 and filling test with water confirmed the leak tightness. The construction of support structure and the mounting of first elements of the TPC (support tube and cryostat vessel) have been done until November 2014. The muon veto system with PMTs, cabling and a special reflector foil will follow.

2.5.2 Radioactive background and intrinsic radioactive contaminations of xenon with radon and krypton

As already mentioned in the previous section, a big part of the electronic recoil background, is coming from unstable isotopes in the detector material itself (internal contaminations), which is treated by proper material selection to get very radio-pure materials inside the

[2]cosmic muons have a broad energy spectrum with a mean energy at ground of $\approx 4\,\mathrm{GeV}$ [Oli14].

Figure 2.12: **Water shield for the XENON1T experiment:** The pictures show the water tank for the XENON1T experiment, after the construction in HALL B at LNGS was finished. Next to the vessel, the service building is placed which will contain the different sub-system, like purification, Restox and distillation column. Further pictures from the construction phase are available on the XENON1T homepage: http://www.xenon1t.org/.

detector. Furthermore the self-shielding properties of xenon in combination with position reconstruction inside the TPC are used to reduce this kind of background furthermore.

An other source of radioactive background is coming from intrinsic contaminations of the xenon itself. Although the xenon has no long-lived isotopes (as pointed out in section 2.2), other radioactive elements are mixed with the xenon producing severe background signals. This type of contamination cannot be treated by shielding or fiducialisation since they are expected to be homogeneously distributed inside the liquid xenon reservoir. Hence, they have to be removed actively. There exist different types of impurities with different origins: While trace contaminations from radioactive components, like ^{14}C bound in carbon dioxide or methane, released from the detector material (e.g. stainless steel), is treated by the purification system for electronegative elements, there are radioactive isotopes of the noble gases krypton and radon inside the xenon that produce a severe radioactive background which can not be taken out by the purification system.

The radon isotopes ^{219}Rn , ^{220}Rn and ^{222}Rn originating from the actinium, thorium and

uranium decay chains are released from the surfaces inside the detector into the xenon. Furthermore, they are continuously emanated from different devices in the gas purification system. Although their half-lives are very short ($\approx 4\,\mathrm{s}$, $\approx 56\,\mathrm{s}$ and $\approx 4.8\,\mathrm{days}$ respectively), the concentration in the system is reaching an equilibrium between decay and emanation processes. Consequently, the amount of radon in the xenon does not decrease with time, but staying constant. The radon decay chains are producing several long-lived radioactive daughter nuclei, which spoil the sensitivity of the experiment. A dedicated campaign of emanation measurements for different materials and devices is performed together with the development of special surface treatment in order to reduce the radon contamination inside the detector. Furthermore, active removal techniques, like charcoal-adsorption or cryogenic distillation are investigated. This is the task of a dedicated working group at the Max Planck Institut für Kernphysik in Heidelberg.

For krypton, there is only one radioactive isotope which contributes to the background of the experiment, which is ^{85}Kr. With a half-live of $\mathrm{T}_{1/2} = 10.7\,\mathrm{a}$ the ^{85}Kr is a rather long-lived β-emitter. The decay scheme is shown in figure 2.13. The ^{85}Kr decays with a branching ratio of $\approx 99.6\,\%$ directly into the stable ^{85}Rb with an endpoint energy of 687 keV. Due to the continuous shape of the β-spectrum, the low energy part of the spectrum is of particular interest to understand the contribution of ^{85}Kr to the intrinsic background.

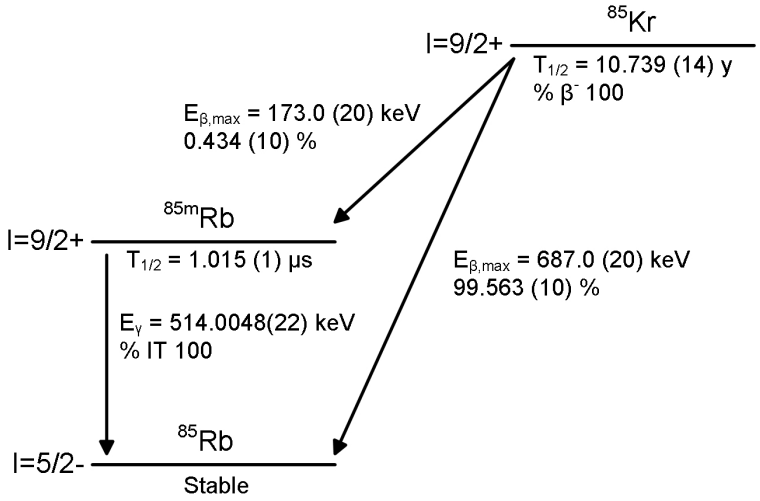

Figure 2.13: **Decay scheme of ^{85}Kr.** The ^{85}Kr is a β emitter with a half life of $\approx 10.7\,\mathrm{a}$ and decays directly to stable ^{85}Rb with a branching ratio of $\approx 99.6\,\%$, while in $\approx 0.4\,\%$ percent decays into a metastable $^{85\mathrm{m}}$Rb before changing by isomeric transition (IT) into the stable ground state. The scheme is based on data from the National Nuclear Data Center, Brookhaven National Laboratory [Nuc14], [Sin14].

In contrary to the radon isotopes, the ^{85}Kr is not emanated continuously from the detector materials, it is mixed inside the xenon during the fabrication process. Since xenon is gained from air, the xenon is containing trace amounts of other elements, including krypton. The majority of ^{85}Kr in the atmosphere is produced during the first above-ground nuclear bomb tests and is enriched furthermore from nuclear waste management and reprocessing

plants. The natural production mechanism from interaction of ^{84}Kr with cosmic rays is negligible. The abundance of ^{85}Kr related to the most abundant krypton isotope is very small: $^{85}\mathrm{Kr}/^{\mathrm{nat}}\mathrm{Kr} \approx 2 \cdot 10^{-11}$ mol/mol. Commercial available xenon has a krypton concentration in the ppb to ppm[3] range, therefore a concentration of $^{85}\mathrm{Kr/Xe} < 10^{-17}$ inside the commercial xenon can be expected. Although, this seems very low, it is not feasible for the experiment and an active krypton removal has to take place before the xenon is filled into the TPC.

The number of expected background events inside the fiducial volume for a certain concentration of natural krypton in xenon can be estimated by calculating the activity $A_{^{85}Kr}$ in 1 ton xenon using the average lifetime τ:

$$A_{^{85}Kr} = \frac{N_{^{85}Kr}}{\tau} = \frac{N_{Xe} \cdot c_{^{85}Kr}}{\tau} \approx 3100\,\mathrm{decays/ton/yr} \tag{2.5.1}$$

With N_{Xe} being the number of xenon atoms, calculated from the molar mass of 1 ton xenon and the Avogadro number and $c_{^{85}Kr}$ being the concentration of ^{85}Kr. For this calculation, $^{\mathrm{nat}}\mathrm{Kr/Xe} = 0.5$ ppt has been used. The average lifetime $\tau \approx 15.5$ yr is obtained from figure 2.13[4]. As already mentioned before, the dual-phase TPC technique allows to discriminate between nuclear recoil events and electronic recoil events. Expecting a S2/S1 discrimination of 99.5%, the rate of leakage events R_{Leak} is calculated to be $R_{Leak} = 16\,\mathrm{evts/ton/yr}$. Due to the continuous shape of the beta spectrum, only a small fraction of the electrons are depositing the correct amount of energy in the region of interest for the dark matter search. In an internal study by the XENON collaboration it has been investigated, that only 3% of the electrons from the ^{85}Kr decay produce an energy deposit in the region of [2,15] keV$_{\mathrm{ee}}$ [Sel12]. This gives a background rate of $R_{Back} = 0.47\,\mathrm{evts/ton/yr}$.

The calculation of background events for different concentrations of natural Krypton in xenon is shown in figure 2.14. Since the abundance of ^{85}Kr in natural krypton is small, the concentration of krypton in xenon is usually referred to $^{\mathrm{nat}}$Kr. A concentration of $^{\mathrm{nat}}\mathrm{Kr/Xe} = 1$ ppt[5] corresponds to a background of ≈ 1 event/ton/year. To reach the design sensitivity of the XENON1T experiment, a concentration of $^{\mathrm{nat}}\mathrm{Kr/Xe} < 0.5$ ppt is needed. Hence, any separation device needs a reduction factor of $\approx 10^4 - 10^5$ to reach 0.5 ppt. the reduction factor can be defined as the ratio of the concentrations in the in-gas $\mathrm{c(Kr)_{in\text{-}gas}}$ sample related to the purified sample $\mathrm{c(Kr)_{pur}}$:

$$\mathrm{F_{Red}} = \frac{\mathrm{c(Kr)_{in\text{-}gas}}}{\mathrm{c(Kr)_{pur}}} \approx 10^4 - 10^5 \quad \text{to reach } 0.5\,\mathrm{ppt} \tag{2.5.2}$$

To determine the absolute concentration of natural krypton inside the detector, which is important for the background estimation, different techniques are used and developed. In section 5, the different techniques to measure trace amounts of natural krypton in xenon are presented. But also the decay of ^{85}Kr inside the TPC can be used, to directly estimate the background. As presented in figure 2.13, the decay of ^{85}Kr into the metastable $^{85\mathrm{m}}$Rb and

[3] 1 ppm = 10^{-6} mol/mol
[4] The average life time and the half-live are directly related: $\tau = T_{1/2}/ln\,2$
[5] 1 ppt = 10^{-12} mol/mol

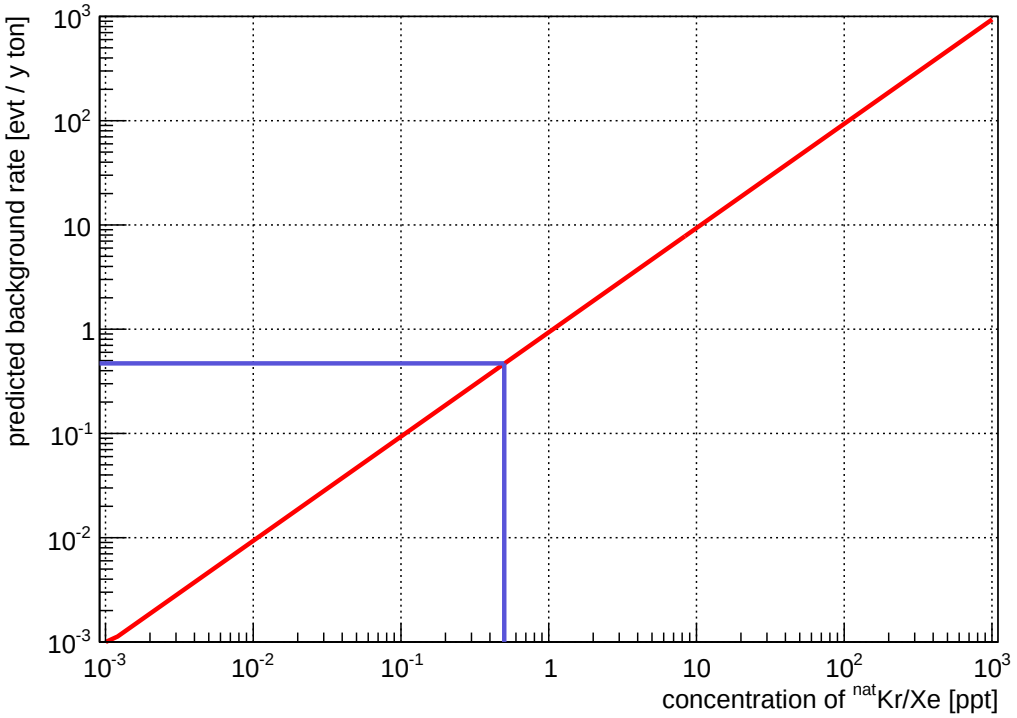

Figure 2.14: **Background rate from intrinsic ^{85}Kr contamination.** The event rate inside the XENON1T TPC produced by ^{85}Kr is calculated for different concentration of natural krypton (^{nat}Kr) in xenon. The blue lines are indicating the XENON1T requirement of $^{nat}\mathrm{Kr/Xe} < 0.5\,\mathrm{ppt}$.

the second short-lived γ-transition occurs with a branching ratio of $\approx 0.4\%$. By searching for this β-γ coincidence signature in the TPC data, the concentration of the ^{85}Kr inside the detector can directly be measured. This method is complementary to direct detection of natural krypton in xenon as stated in [Apr13a].

The main topic of this thesis is the design and the construction of a cryogenic distillation column to separate krypton and xenon, in order to fulfill the requirements for the XENON1T experiment. From chapter 4 on, the development and the construction will be presented.

Removal of electronegative impurities from xenon 3

In order to clean the xenon from electronegative impurities to a ppb level as explained in chapter 2.4, the process of adsorption can be used. The adsorption belongs to the thermal cutting processes and is used to separate dedicated components from a fluid (in this case xenon) by chemical or physical bondings to a solid phase material [Loh07a].

In the XENON100 experiment, a commercial gas purifier (SAES, type MonoTorr PS3-MT3-R/N-1/2) is used to clean the xenon from electronegative impurities down to the 1 ppb level [Apr12a]. The purifier cartridge is made from a special, patent-registered zirconium-based alloy, which is operated at T = 400°C by constant heating. Thus, the impurities can diffuse inside the material, instead of just use the surface for adsorption, with the advantage of increased performance and lifetime [SAE10]. Due to out-gassing processes inside the detector, the cleaning of the xenon has to be done in a continuous mode to guarantee a stable electron lifetime. Therefore, xenon is extracted from the TPC, cleaned in the getter and guided back inside the detector with a certain process speed, to keep the level of impurities constantly low over the whole runtime of the experiment. In the XENON100 experiment the recirculation flow rate q was chosen to be $q \approx 5\,\mathrm{slpm}$.

The good experience, made with these type of getters during the operation of XENON100 led to the decision to use this technology in XENON1T as well. The design and the construction of the gas purification system for XENON1T is done at the University of Münster in collaboration with the Columbia University, USA and since summer 2014 with the Rensselaer Polytechnic Institute, USA. Performance tests of different devices, like pumps and getters are done at locations in Münster and Columbia. Further measurements on the radio-purity, especially on the radon emanation, is done at the Max Planck Institut für Kernphysik in Heidelberg and is of crucial importance as it has been pointed out in the chapter 2.5.2.

3.1 Prototype of a gas purification system for the XENON1T experiment

The gas purification system for the XENON1T system has to fulfill different requirements. The whole xenon inventory of 3.3 tons has to be circulated at a high circulation speed in

order to clean the xenon after the initial filling of the detector and furthermore, to keep it clean during the operation. With the design value of 100 slpm, one cleaning cycle of the complete inventory takes about four days. Therefore, all components, like the piping as well as additional devices like flow controllers, gas circulation pumps and getters have to be able to support this flow rate. Furthermore it has to be a very leak tight system, to avoid contaminations of the xenon with ambient air. The system will be connected to a dry turbo-molecular pumping station that allows to evacuate the whole system before the initial filling. In addition the system should be bakeable as much as possible, to remove contaminations during the initial evacuation. Since XENON1T is a more complex experiment than XENON100, the whole experiment is planed to be remotely controlled by a slow control system, that also allows to regulate the gas routing.

Before the design of the XENON1T purification system has been fixed, a demonstrator setup was designed and built in the context of this thesis, to investigate the characteristics of different components and to find the proper hardware for the XENON1T system.

The flowchart of the demonstrator system is shown in figure 3.1. The whole system is designed as gas purification and routing system, which supplies different sub-systems with xenon.

The gas is stored in a series of special aluminum bottles, mounted to the wall with load cells to monitor the weight of the bottles in order to control the amount of xenon (see figure 3.2). The mounting of the bottles allows to cool down single bottles to 77 K by immersing them into dewar vessels, filled with liquid nitrogen, to transfer the xenon by cryogenic pumping from the different setups back into the bottles (recuperation). For safety reasons, this operation is only possible with those aluminum bottles, that are equipped with stainless steel valves, which are specified for low temperatures.

The xenon bottles are connected to the circulation system with a pressure regulator (GCE, AP1010S 4PW FV4 FV4 40 H HF), in figure 3.1 labeled as PR1 to reduce the pressure from ≈ 50 bar down to $\approx$ 2-3 bar. Furthermore, this section is equipped with pressure sensors P1 and P2 (Swagelok, PTU-S-AC100-31AD) with a range up to 100 bar to monitor the pressure in the bottles and with a flow controller (labeled FC3, MKS, 1579A) that is used during the recuperation procedure to control the amount of xenon filled into the single bottle.

The main circulation loop, is equipped with ultra-clean stainless steel bellows-sealed valves (Swagelok, SS-8BG-VCR) which are either hand-driven, manual valves labeled as MV1-MV20 or pneumatic-driven valves labeled as PV1-PV17. The latter ones are opened by using an actuator pressure of 5-10 bar (normally closed by design) and allow to control the gas routing remotely by the slow control system as it is requested for XENON1T. These pneumatic valves have the advantage to be designed for ultra-clean gas handling. They are made from electro-polished stainless steel and are mounted and packed under clean-room conditions. Furthermore, they show excellent leak-tightness and are bake-able up to $+150°C$. The actuator pressure is supplied from a standard nitrogen bottle and controlled with magnetic valves. Several ports have been implemented in the gas system to achieve a high flexibility and to connect the different sub-systems, as it will be also the case in the XENON1T experiment (see section 3.6). During the startup of the system, the circulation has been driven by a membrane gas circulation pump (KNF, type N143AN.12E) and later

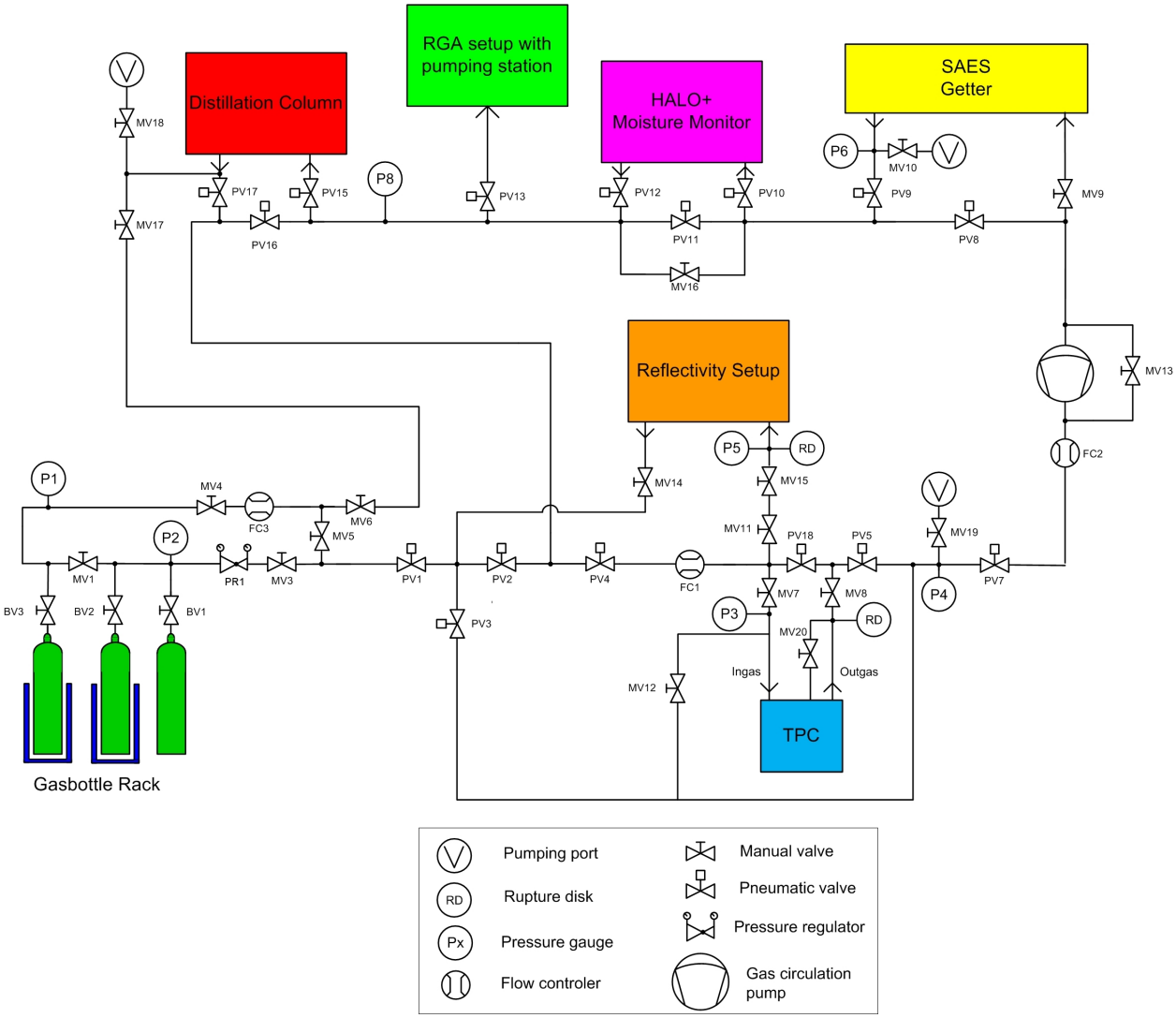

Figure 3.1: **Flowchart of the xenon purification system in Münster.** This picture shows the flowchart of the complete gas system as it is used in this thesis. It also includes other experimental setups like the TPC and the reflectivity setup, which are explained in more detail in [Bro15] and [Lev14], respectively.

by a special custom-made magnetic driven pump (Chart-Inc, type QDrive). The latter one is designed for the XENON1T purification system to achieve high flow rates and leak tightness. The working principle and the performance tests of the QDrive, carried out in Münster, will be presented in section 3.5.

For the process monitoring, the setup is equipped with several mass flow controllers (FC2-FC4) which allow to measure the flow (fully open mode) or even to regulate it. This depends strongly on the type of pump that is used. While the membrane pump runs at full circulation speed at all times, the flow has to be controlled separately. In contrary, the QDrive allows to regulate the circulation directly by the applied voltage and frequency (see chapter 3.5). At different locations of the system, pressure sensors for a range up to 10 bar are implemented (Swagelok, PTU-S-AC9-31AD and MKS, Baratron 121A). Although both sensor types are

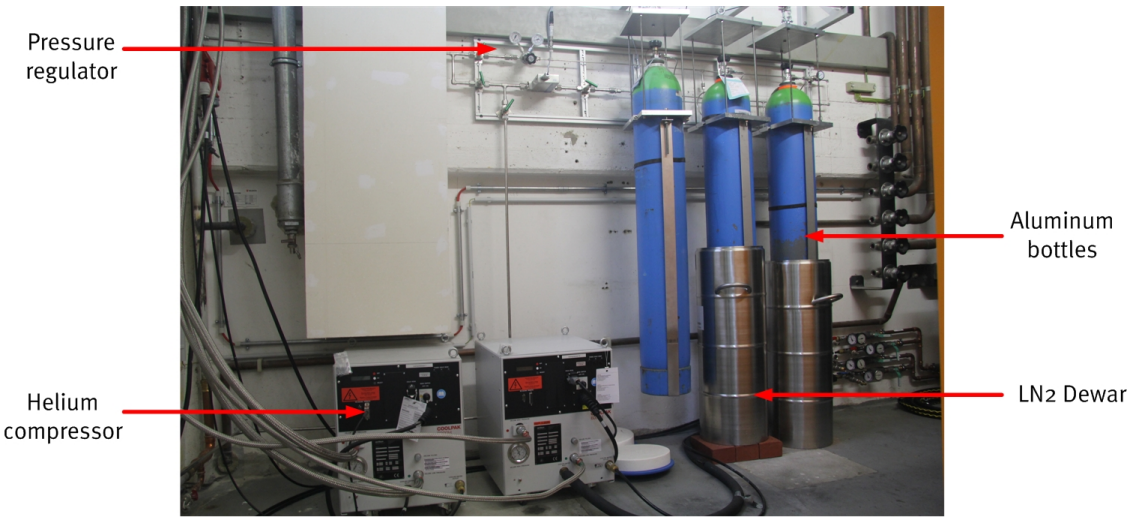

Figure 3.2: **Xenon storage rack.** This picture shows the bottle storage room, where the xenon is kept in bottles until it is used in the different setups. Two bottles are equipped with Dewar vessels, that allow to transfer the xenon back to the storage bottles by cryogenic pumping.

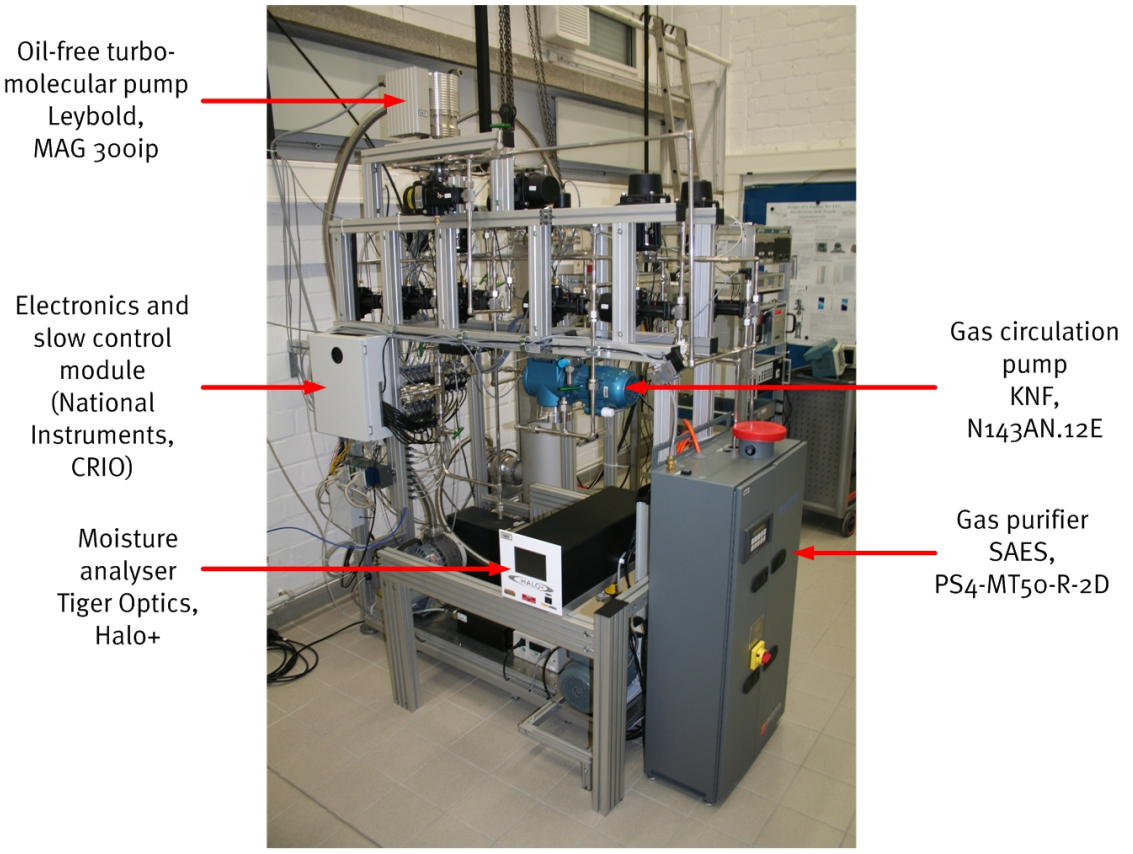

Figure 3.3: **Gas purification system.** This picture shows the gas purification system, constructed at IKP Münster as prototype for the XENON1T purification system.

capacitive manometers, working independently of the type of gas and designed for ultra-clean environments, they differ in sensitivity and operation conditions. While the PTU-series is less accurate in the measurement than the Baratron and also not bake-able (the Baratron is bake-able up to 200°C without removing the electronics) it is less expensive and well suited for process observations. The Baratron, instead, is more suitable for analytic application, where higher accuracy is needed (compare chapter and 4.4 and 5.1).

The getter, that is implemented in the gas system, is made from the same material as the one used in XENON100, but allows to clean the xenon with higher flow rates up to 75 slpm down to less than 1 ppb for different impurities, as shown in table 3.1. The performance and characteristics of this type of getter (SAES, type PS4-MT50-R-2D) has been tested in several facilities in Münster, New York and Heidelberg and will be presented later on.

Table 3.1: **Performance of getter type PS4-MT50-R** This tabular collects the achievable concentrations for different impurities with the purifier of the type PS4-MT50-R, stated by the manufacturer [SAE10].

Impurities removed	Concentration in purified gas
H_2O	< 1 ppb
CO	< 1 ppb
CO_2	< 1 ppb
O_2	< 1 ppb
N_2	< 1 ppb
H_2	< 1 ppb
Total hydrocarbons	< 1 ppb

All the pipings as well as all VCR-fittings and valves are out of electro-polished, stainless steel (316L). The connections between the tubes and the fittings have been done using the orbital welding technique (Orbitec) to procure leak-tight and clean weld-seams. Finally, the pipes have been cleaned following an ultra sonic cleaning procedure, consisting of several cleaning steps with Almeco and deionized water.

The control system is based on an industrial real-time controller (National Instruments, Compact Rio), programmed in Labview, which is equipped with different modules, that allow to control all the pneumatic valves and flow controllers in combination with the read-out of all relevant sensor signals. The compact rio (CRIO) system consists of a backplane with integrated controller (model NI-CRIO-9074), where the different modules are plugged to the designated slots. The controller is equipped with two Ethernet connections, where one port is used for communication with a temperature controller (Lakeshore, model 336) used at the TPC and the other port for communication with the lab-PC for programming and data-storage. The backplane is equipped with an analog input module (NI-CRIO-9205) which allows to measure the analog voltage of the different pressure and flow sensors. Furthermore an analog output module is used to produce the auxiliary voltage that is needed to adjust the flow set-point at the flow controllers (set-point voltage). Finally, two digital modules are implemented to control and read-out the actuator pressure for the pneumatic valves. In the software also the controlling of the TPC via the temperature controller is implemented, giving

access to the measured temperatures inside the TPC and allows to control the temperature inside the system by using one of the PID[6] control circuits of the Lakeshore. While the slow-control program is executed on the CRIO controller, it is visible and controllable via the lab-PC due to the Ethernet connection. Furthermore, the slow-control values are stored on the lab-PC in time interval of 5 s. Finally a status- and alarm-system is implemented, sending status reports 3 times a day, containing all relevant parameters and comparing the measured values with pre-defined safety-values. In case an indicated value is out of the safety margin, an alarm is send via sms and e-mail to the different responsible people. Thus, the system is self-controlling and allows for fast response by the operator in case of a failure. Especially for cryogenic applications where severe amounts of expensive xenon is stored, such a system is of crucial importance.

In the following, the different components are tested in oder to fulfill the requirements for the XENON1T experiment. A laser-based moisture analyzer (chapter 3.2) is tested, which is supposed to observe the gas quality in the system and later in XENON1T. Furthermore, the performance of a high flow getter and a new gas circulation pump is investigated as well as the cryogenic distillation the krypton distillation column, which is the major topic of this thesis and presented in the chapters 4 and 7. Additional systems are a dual phase TPC (details can be found in [Bro15]) and the reflectivity setup. The latter one allows to investigate the reflections of vacuum ultra-violet (VUV) light on PTFE[7] in a liquid xenon environment (for details see [Lev14]).

3.2 Gas quality measurement with a laser-based moisture analyzer

Although the TPC itself can be used as purity monitor, it has one disadvantage: The purity can only be measured during dedicated calibration runs (e.g. ^{137}Cs calibration in XENON100, see chapter 2.4), which does not show instant changes in the gas quality. Therefore, it has been decided to use a laser-based moisture analyzer (Tiger Optics, type Halo+), implemented in the purification system, to monitor continuously the water content in the xenon, coming from the getter. Although the device is only designed for the detection of water, it is feasible for usage inside the gas stream to perform continuous measurements (expect for regular calibration on a month time scale) without any loss of sample gas.

3.2.1 Working principle of the Halo+ moisture analyzer

The Halo+ moisture analyzer determines the water content in the sample gas by the so called "Cavity Ringdown Spectroscopy" [Tig06], which is based on absorption spectroscopy with infra-red light on the water molecules. Main components of the system, shown in figure 3.4 are a continuous wave diode laser, the absorption cell (cavity), equipped with ultra-high

[6] PID: The Proportional - Integral - Derivative algorithm is widely used in industry, consisting of three terms, which allow for fast and reliable regulation of a given parameter to a set-point value, e.g. Temperature.
[7] Polytetrafluoroethylene

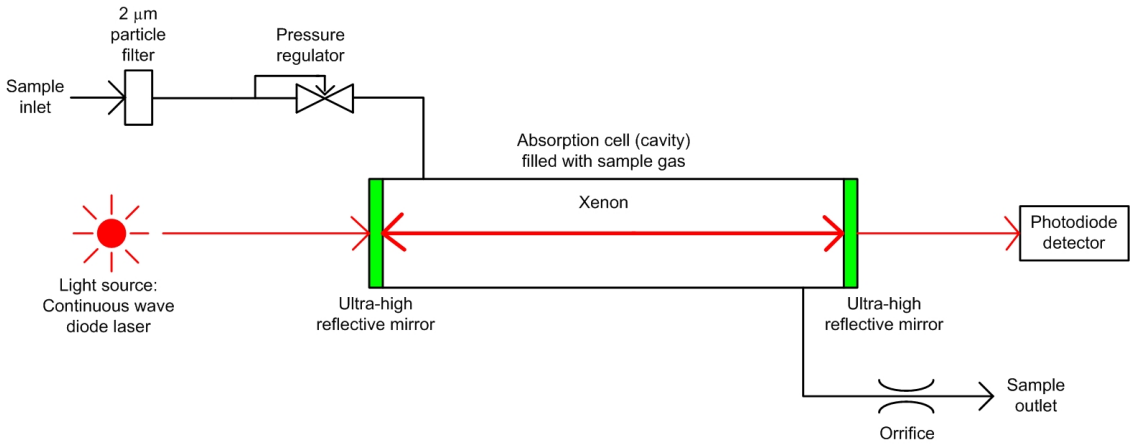

Figure 3.4: **Working principle of the Halo+ moisture analyzer.** The picture shows the schematic working principle of the Halo+ moisture analyzer from Tiger Optics. The so called "Cavity Ringdown Spectroscopy" is based on absorption of infrared light by water molecules and measuring the intensity of their de-excitation over time. The decrease in intensity is directly related to the water content in the sample gas. The sketch is based on the information in the user manual [Tig06].

reflectivity mirrors and a photo-diode detector. The laser is emitting light in the infrared wavelength at $\lambda = 1392.5\,\text{nm}$, where an absorption peak of water occurs (see figure 3.5).

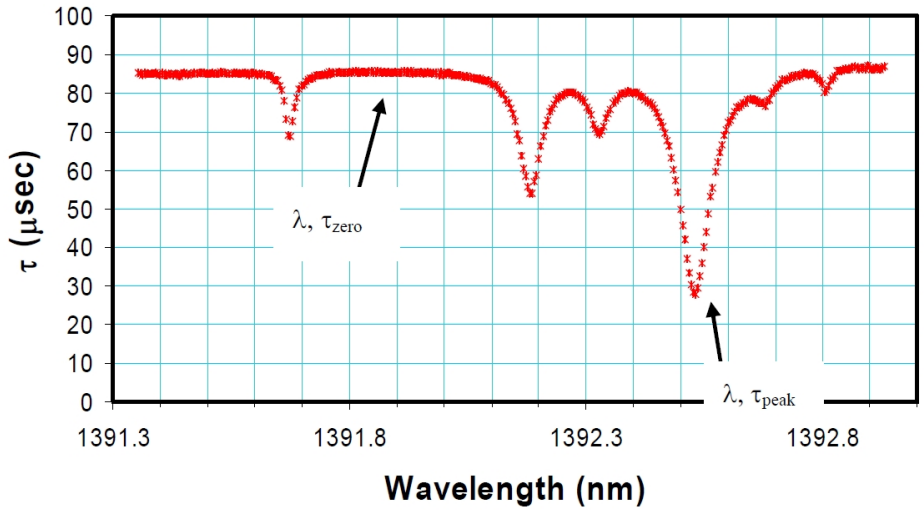

Figure 3.5: **Absorption spectrum of water.** The Halo+ moisture analyzer uses the adsorption of infrared laser light by water to determine the concentration in the sample. The intensity in the absorption peak at the wavelength of $\lambda = 1392.5\,\text{nm}$, shown in this picture, is compared to the intensity at a wavelength without adsorption to calculate the ring-down time (τ_{zero}). The figure is taken from [Tig06].

The light is passing the mirror into the cavity, filled with the sample gas, where it is reflected back and forth and excites the water molecules. These start to de-excite after some time and

a small fraction of the light is decoupled from the cavity and is measured by the photo-diode detector. After a certain level of light intensity is achieved, the laser is turned of and the light intensity, measured with the diode decreases due to losses from the mirror but also from the de-excitation of the excited water molecules. An example is shown in figure 3.6. The measurement at t = 0 is started, when the laser is shuttered. The intensity of the de-excitation I_{out} is following an exponential decay function, it "rings down" [Tig06]:

$$I_{out} = I_0 e^{-t/\tau} \tag{3.2.1}$$

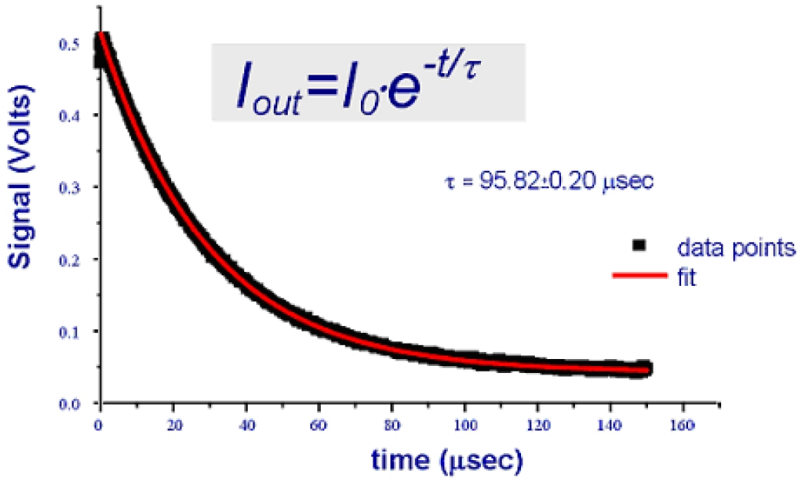

Figure 3.6: **Intensity of absorption light inside the cavity.** This plot illustrates the measurement process. The light intensity is measured in units of voltage as function of time and the exponential fit gives the time constant τ which is related to the concentration (figure taken from [Tig06]).

The concentration N of water in the sample is given by [Tig06]:

$$N = \frac{1}{c \cdot \sigma(\nu)} \cdot \left(\frac{1}{\tau(\nu)} - \frac{1}{\tau_{zero}}\right) \tag{3.2.2}$$

with c being the speed of light and $\sigma(\nu)$ the absorption cross section. The concentration is calculated by the measurement of the ring-down time $\tau(\nu)$ in comparison with a reference time τ_{zero}, that has been measured by adjusting the laser wavelength to a point without absorption peak (see figure 3.5). Furthermore, τ_{zero} and $\tau(\nu)$ are also depending on the geometry of the cavity: $\tau_{zero} = \frac{d}{c \cdot (1-R)}$ and $\tau(\nu) = \frac{d}{c \cdot ((1-R)+\sigma(\nu)Nd)}$, with R as reflectivity of the mirrors and d being the cell length.

3.2.2 Implementation of the Halo+ to the gas purification system

The Halo+ moisture analyzer is designed for loss-free measurements in-line of a gas-routing system under certain conditions. The inlet of the Halo+ is equipped with a pressure regu-

lator, that is adjusting the pressure inside the cavity to be constant at $p_{Cav} = 2.4\,\text{bar}$ (see figure 3.4).

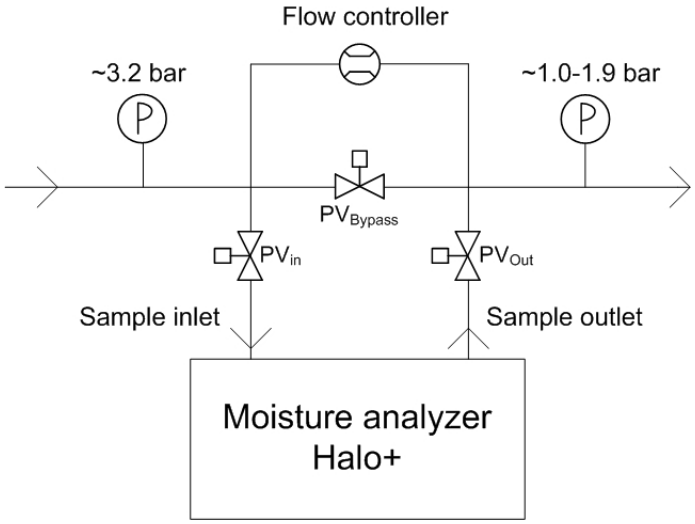

Figure 3.7: **Flow chart of the implementation of the Halo+ moisture analyzer into the gas purification system:** The Halo+ is mounted together with a mass flow controller, which allows to realize the pressure difference that is needed for the operation and to use the analyzer in high-flow applications.

In order to induce a mass flow through the sample cell, it is requested that the inlet pressure has to be higher than this, but is not allowed to exceed $p_{Max,In} = 9.6\,\text{bar}$. At the outlet an orifice is mounted which regulates the outgoing flow, recommending a maximal pressure of $p_{Max,Out} = 1.15\,\text{bar}$ at the outlet, specified by the company. Due to the requirements of the purification system, it has been used with higher pressures up to $p_{Out} = 1.9\,\text{bar}$ at the outlet, after consulting the company. For a proper performance of the analyzer, a certain flow rate of 0.5-2.0 slpm through the cell has to be achieved, which is realized as long as the output pressure is below the cell pressure. With higher pressure at the outlet, the flow rate inside is reduced, but this effect can be compensated by calibration of the device under this condition.

Since the flow rate through the Halo+ is not higher than 0.5-2 slpm, it is necessary to use the device in a bypass mode, as shown in figure 3.7, in order to achieve flow rates up to 100 slpm in the XENON1T system. When running the analyzer, the pneumatic valve PV_{Bypass} is closed, while the other valves PV_{In} and PV_{Out} are open. The major part of the flow is passing the flow controller, while only a small fraction of gas is passing through the Halo. The flow controller is also used to keep the inlet pressure during operation constant at $p_{In} \approx 3.2\,\text{bar}$. In figure 3.1 the Halo+ is connected to PV10 and PV12, with PV11 being the bypass valve.

In figure 3.8 two initial test measurements with dry xenon, cleaned by the getter, are shown. The system shows an unstable behavior on the 22.02.2012 due to not optimized pressure difference. The flow through the Halo+ was interrupted, which can be seen directly in the measured data. The humidity increases immediately when the flow breaks down due

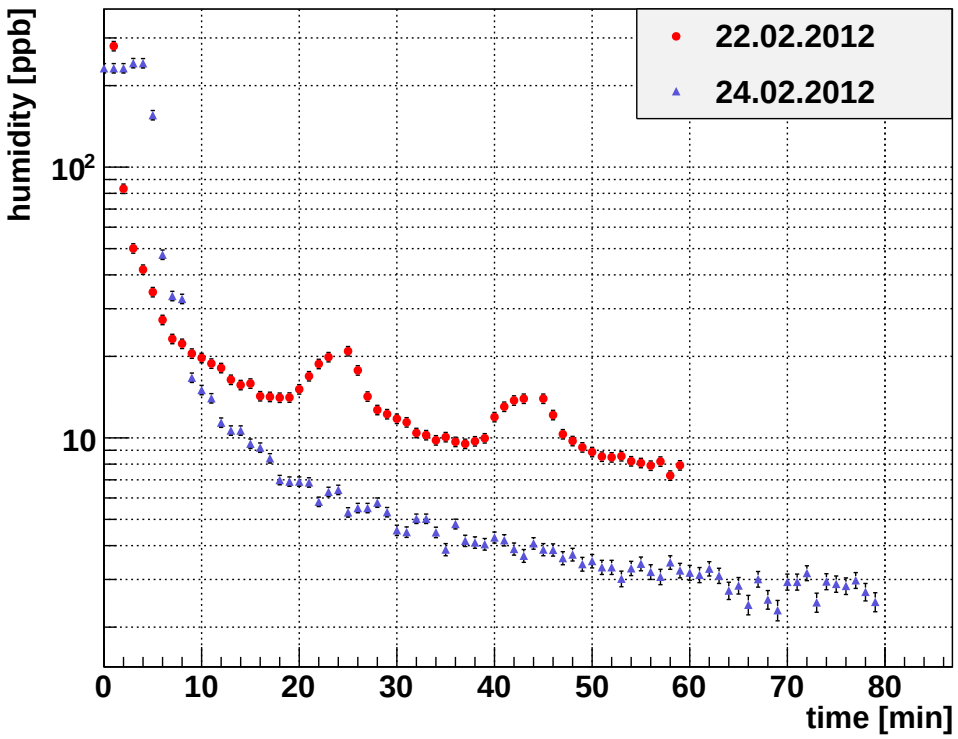

Figure 3.8: **Performance test of the HALO+ moisture analyzer.** In this plot, two measurements from the initial start-up of the Halo+ with xenon, cleaned by the getter, are shown. While the measurement from the 22.02.12 (red dots) shows instabilities due to non-optimized flow through the cavity, the measurement from the 24.02.12 shows a much smoother response, profiting from an optimized flow balance.

to desorption of water from the walls of the cavity. As soon as the flow is stabilized, like realized for the 24.02.2012, the humidity inside the cell decreases smoothly. During this test a humidity of less than 2 ppb is reached after $\approx$ 80 min. Due to these out-gassing processes, it is always necessary to measure for some time before the proper result is given, especially for very dry sample gases (see previous chapter 3.3).

The Halo+ is further used to characterize the performance of the getter as explained in the following chapter 3.3.

3.3 Characteristics of high flow getters: PS4-MT50-R

The impedance of the getter cartridge and the gas quality of the xenon after passing the device are the most important quantities for the design of the purification system. Unfortunately, the TPC was under commissioning, thus, only the Halo+ was available to check the gas quality at the outlet of the getter.

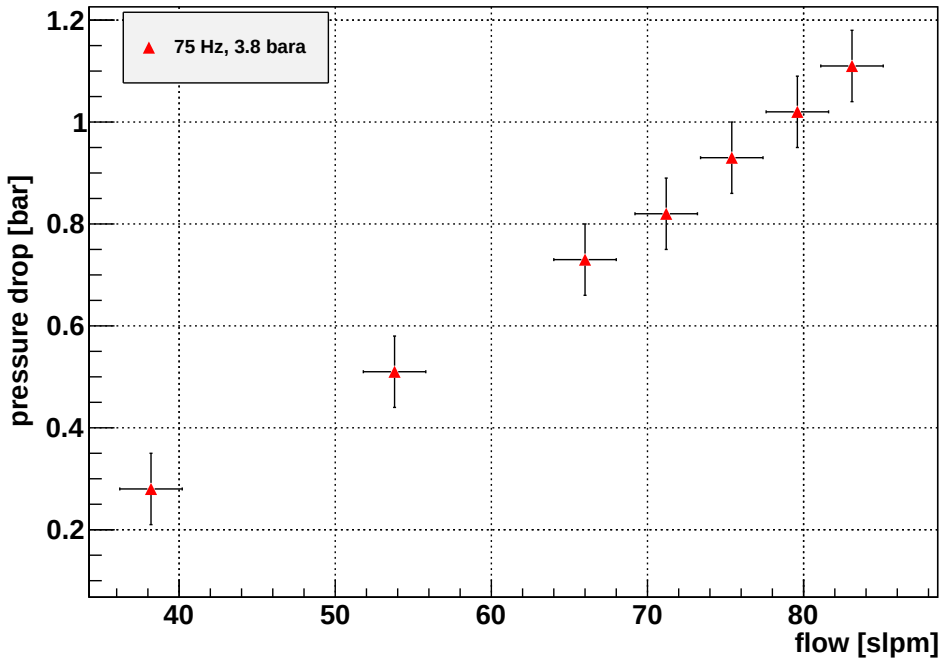

Figure 3.9: **Pressure drop along the getter:** The pressure drop at the getter has been measured for different flow rates up to $\approx 83\,\text{slpm}$.

The impedance of the getter is influencing the gas-stream and is checked by measuring the pressure before and after the getter for different flow rates. The result is shown in figure 3.9. For very high flow rates ($Q > 80\,\text{slpm}$) the pressure drop at the getter is greater than 1 bar.

The sensitivity in the measurement is limited by the flow controller and the pressure reading. The accuracy of the flow controller is limited to 1% of the full scale, which is 200 slpm ($\Delta Q = \pm 2\,\text{slpm}$), while the accuracy of the pressure reading is limited to $\Delta p = \pm 50\,\text{mbar}$. The measurement has been performed at an initial pressure of 3.8 bar in the system, while the pumping speed of the circulation pump (QDrive) has been increased stepwise until the maximal possible flow has been reached (see also section 3.5 for detailed information on the circulation pump). The conductance for the maximal flow rate C_{Max} can be calculated from the pressure drop $p_d = 1.1\,\text{bar}$ and the flow rate $Q = 83\,\text{slpm}$ [Jou06]:

$$Q = C_{Max} \cdot p_d \qquad \rightarrow \qquad C_{Max} = \frac{Q}{p_d} = (1.3 \pm 0.1)\,\frac{\ell}{s} \tag{3.3.1}$$

In general, for high flow rates, the turbulent regime is reached, which can be calculated using the Reynolds number R_e and compare it with the critical Reynolds number R_{crit}. For circular shaped pipings, the turbulent regime starts when $R_e > R_{crit} = 4000$ is realized [Jou06]:

$$R_e = \frac{\rho \cdot \nu \cdot d}{\eta} \tag{3.3.2}$$

While the xenon gas density $\rho = 22.1\,\mathrm{kg/m^3}$ at 4 bar and 20°C is obtained from the NIST database, η and ν, which are the dynamic viscosity and the average flow velocity respectively, can be calculated. With $\eta = 2.89 \cdot 10^{-5}\,\frac{\mathrm{kg}}{\mathrm{m \cdot s}}$ for the given conditions and $\nu = 4.3\,\mathrm{m/s}$, calculated from the flow rate $Q = 83\,\mathrm{slpm}$ and the inner diameter of a quarter inch tube ($d \approx 10\,\mathrm{mm}$, one gets $R_e(4\,\mathrm{bar}) = 33606 > R_{crit} = 4000$.

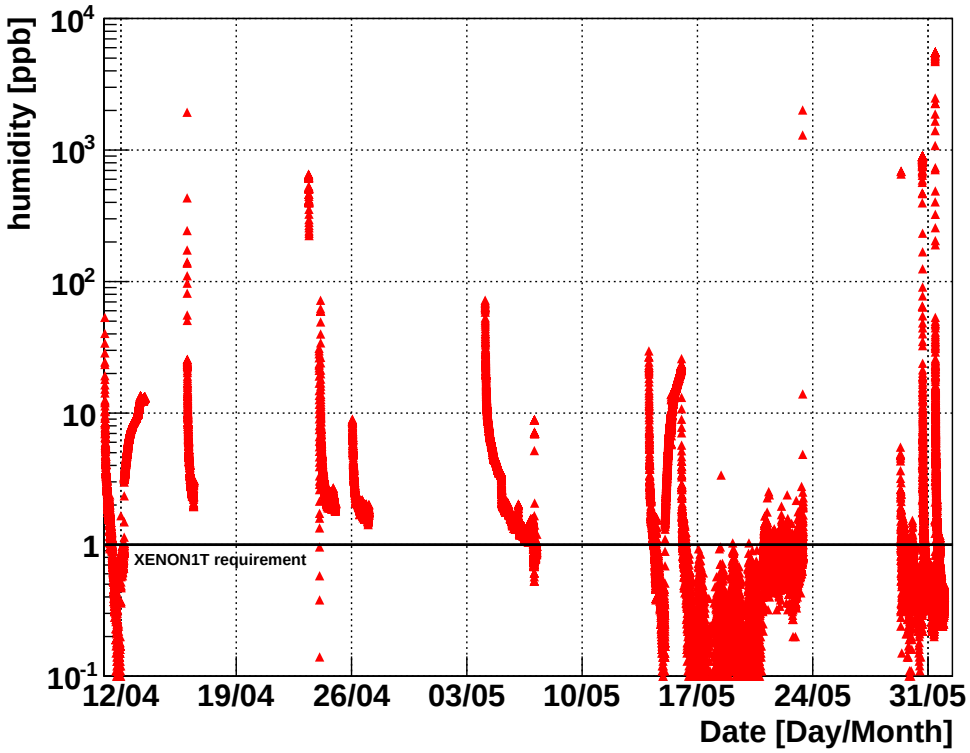

Figure 3.10: **Humidity measurements at the gas system in 2012.** In this plot the different measurements with the Halo+ in spring 2012 are collected. There are several interruptions and the humidity in the system increases when some tests are conducted, e.g. after filling of the TPC. The humidity always decreases rapidly when using the getter.

The getter has provided clean xenon for several investigations on the TPC and the distillation column. Therefore, no longterm behavior of the purity outcome has been performed, using the Halo. In figure 3.10 the measured humidity of two months is shown. In many of the cases, the humidity was raising several times up to the ppm regime due to the introduction of uncleaned xenon or a bypassed getter. Furthermore, the analyzer was not running all the time causing interruptions in the time evolution. One measurement of the humidity (from the 31st of May) is shown in more detail in figure 3.11. In this measurement, the xenon was circulating through the gas system and the TPC, while the latter one was filled with

≈ 3.5 kg of xenon. The initial humidity has been measured to be ≈ 5500 ppb, circulating with a bypassed getter. When routing the flow through the heated getter, the humidity decreased by two orders of magnitude in about 100 s, indicating that the heated getter immediately cleans the xenon and is further decreasing down to 0.4 ppb, which is the sensitivity limit of the device. I would like to note, that this measurement is just accounting for the humidity in the xenon after passing the getter and is not equal to the impurity concentration inside the TPC. It further shows, how much flushing time with cleaned gas is needed (9 hours in this example) before a reliable measurement with Halo+ near the sensitivity limit can be performed without desorption effects from the measurement cell.

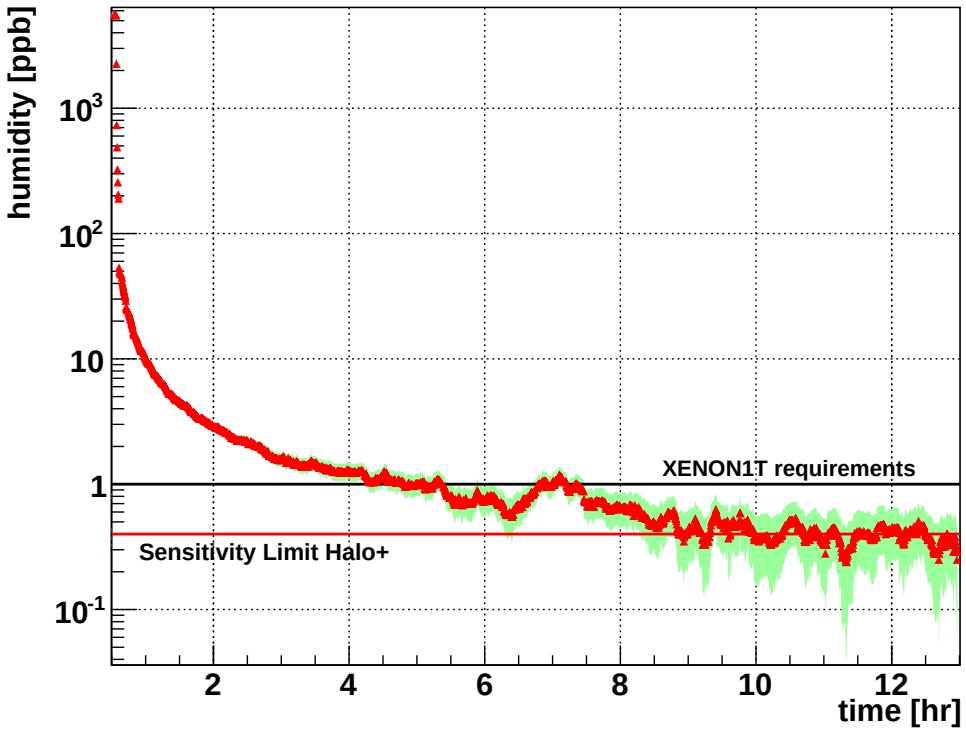

Figure 3.11: **Humidity measurement with the getter.** This plot shows a measurement of the humidity inside the gas circulation system and the TPC. After the xenon passes the getter, the humidity decreases below 1 ppb (XENON1T limit, black line) and reaches the sensitivity level of the analyzer (red line). The data points are marked in red, while the green band corresponds to the systematic error of the device.

Further studies of the getter performance have been done at the Columbia University, using a dual phase xenon TPC to probe electron drift length of one meter for the final XENON1T TPC.

In addition to these efforts, the emanation of radioactive radon isotopes from the heated getters have been measured at the Max Planck Institut für Kernphysik (MPIK) in Heidelberg. The getter, tested and used in Münster, has been measured to emanate (1.34 ± 0.1) mBq

[Lin13]. The amount of radon, that is emanated, is related to the radio-purity of the getter material and thus, similar types of cartridges can give different emanation rates. Therefore each getter will be screened before it is used for XENON1T.

3.4 Venting of the KATRIN main spectrometer with ultra-clean argon using XENON1T purification techniques

The described purification technique is also interesting for other experiments. It has been used during the first commissioning phase of the KATRIN main spectrometer in 2013 for the venting of the spectrometer vessel with ultra-clean argon. Detailed information about the main spectrometer system, including the vacuum components and the argon-venting procedure can be found in [Wol14]. In the context of this thesis, the argon purification system has been constructed and commissioned at the KATRIN experiment. In the following, the KATRIN experiment will be introduced briefly, before the venting procedure and the design of the system will be summarized.

The KATRIN experiment aims for direct detection of the mass of the electron-anti-neutrino $\overline{\nu}_e$ by measuring the endpoint of the tritium-β spectrum [Kat04, Fra11, Dre13]. The experimental setup is shown in figure 3.12. The electrons are produced in the windowless gaseous tritium source (b) and are guided over magnetic field lines to the spectrometer section, while the tritium is pumped away in the differential (c) and cryogenic pumping sections (d). The spectrometer section consists of two single spectrometers, where both are working as electrostatic energy filters (MAC-E filter type), that only electrons of a certain energy can pass. The pre-spectrometer (e) is filtering all electrons with low energies, that only electrons with an energy near the tritium endpoint can enter in the main spectrometer (f). The electrons that can pass the potential barrier of the main spectrometer are finally counted by the detector system. With this setup, the endpoint region of the tritium-β spectrum can be measured with high precision and the information on the neutrino mass can be extracted.

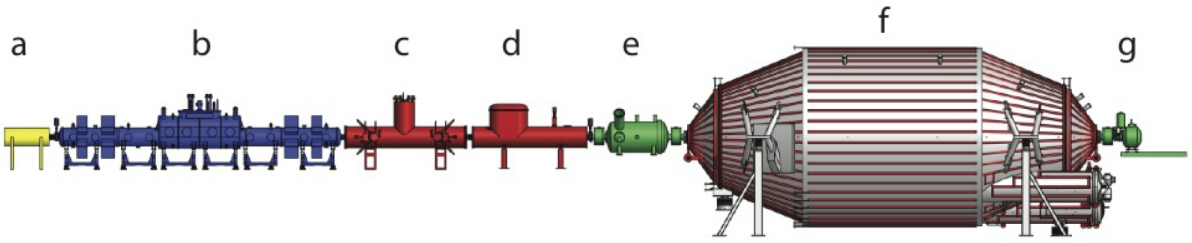

Figure 3.12: **Scheme of the KATRIN experiment.** This picture shows the different segments of the KATRIN experiment, a) the calibration and monitoring section, b) the window-less gaseous tritium source, b) the differential pumping section, c) the cryogenic pumping section, d) pre-spectrometer, e) main spectrometer and g) electron detector system. Figure taken from [Fra11].

One of the key components of the ≈ 70 m long setup is the main spectrometer. With a length of 23.4 m, a diameter of 10 m and a weight of ≈ 200 tons it is the largest ultra-high vacuum vessel in the world, aiming for a residual pressure of $\approx 10^{-11}$ mbar over the whole runtime of the experiment. To achieve this goal, a cascaded pumping system, consisting of scroll- and turbo-molecular pumps as well as huge NEG[8] pumps is used

During the first commissioning phase, it was necessary to open the vacuum vessel, after the initial pump-down and baking procedure, due to a miss-aligned gasket in a shutter valve. Without the valve the connection to the detector system was not possible, since the spectrometer would be vented. It has been decided to vent the spectrometer with ultra-clean argon instead of air for the repairing. This had two main reasons:

- The activated NEG getter pumps are not spoiled with ambient air and can further be used, without activating them again.
- Venting with dry argon prohibits against a new water contamination of the spectrometer. Therefore, a second baking baking phase, which takes several weeks is not necessary.

Previous calculations showed, that commercial available argon of quality 6.0 is still containing to much impurities, e.g. water, oxygen or nitrogen, for the venting procedure and would saturate the NEG getters. Therefore, a venting and purification system has been designed to further clean the argon to quality 9.0 before flushing it into the spectrometer. The scheme of the system can be seen in figure 3.13.

For the venting procedure $\approx 1200\,\mathrm{m}^3$ of argon was needed until the main spectrometer reaches ambient pressure, which is stored in 11 bundles of $12 \times 50\,\ell$ bottles with a pressure of ≈ 220 bar. The system is designed, so that two bundles are always connected. One of them is opened to the purification system until it gets empty. When reaching a certain pressure level, the empty bundle is closed and the other one is opened, to not interrupt the venting procedure. The empty bundle is than replace by a full one. A pressure regulator with two separate input lines is used to switch between the two bundles. When connecting a new set of bottles, the associated line is pumped and afterwards flushed several times via V-1x and V-1a to avoid any contamination of the argon with ambient air.

The pressure regulator is reducing the pressure from ≈ 220 bar down to 4.5-5.0 bar to have the optimal inlet pressure for the purification system. The getter is the most important component of the system. It is the same device, SAES, PS4-MT50-R, than described in chapter 3.3. Since it is specified for rare gases in general, it is feasible to use it for the argon venting procedure. Its designed maximum flow rate for xenon of 75 slpm at a minimum inlet pressure of 2.8 bar, would allow to flush the vessel in less than 10 days. The flow as well as the pressure before and after the getter are measured using a flow controller (MKS, 1579A) and capacitive pressure sensors (Swagelok PTU-S-AC9-31AD) respectively.

To avoid any contaminations, the system has been evacuated over the pump station 2 and furthermore, the gas lines had been flushed several times over the pressure relief valve. In addition, all connections on the low pressure side have been done by VCR- and Conflat

[8]NEG: non-evaporable getter

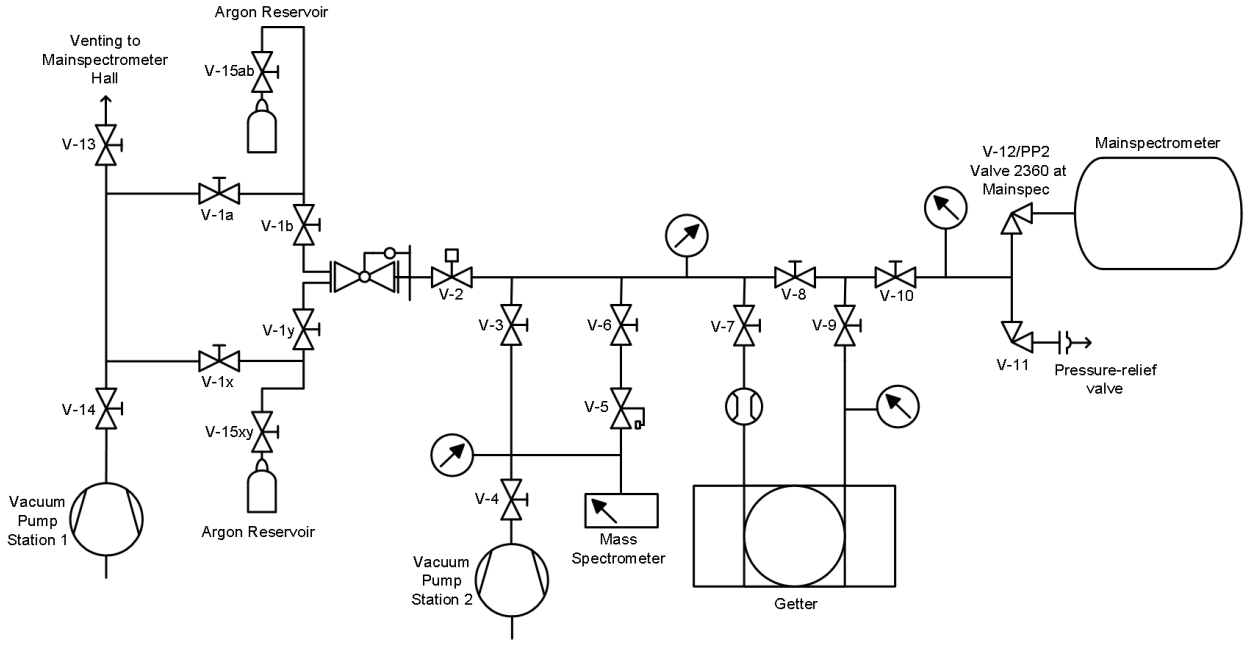

Figure 3.13: **Flowchart of the venting System.** This picture shows the flowchart of the system, used for venting the KATRIN main spectrometer with ultra clean argon. Key component of the system is the high flow gas purifier SAES-PS4-MT50-R. The picture is taken from [Wol14].

connections in combination with orbital-welding technique to achieve extreme leak-tightness. This has been confirmed by helium leak checks, measuring a leak-rate of $< 10^{-9}\,\mathrm{mbar}\cdot\ell/\mathrm{s}$.

After the vessel had been flushed, the maintenance of the damaged gasket has been performed and a new pump-down was initiated. It took about 24 days from starting the venting until reaching ultra-high vacuum again. The pressure before and after the venting was around $1\cdot10^{-10}\,\mathrm{mbar}$, demonstrating that the NEG getters were still working after the operation and indicating the successful flushing with ultra-clean argon. Finally, it was possible to perform the first studies on the electrostatic characteristics of the main spectrometer.

3.5 Performance test of a new gas circulation pump (QDrive)

The performance of the XENON1T TPC crucially depends on the flow rate of 100 slpm for the purification of the xenon. Furthermore, the pump has to be very clean, leak tight and reliable for the whole runtime of the experiment. Membrane pumps have been investigated by collaboration partners at the Columbia University and were found to not be able to fulfill these criteria. Their membranes produces abrasion that contaminates the system and they tend to break, therefore having a limited life time of less than 8000 hrs. Furthermore the leak rate is limited to $\approx 10^{-7}\,\mathrm{mbar}\cdot\ell/\mathrm{s}$, which is not feasible for the XENON1T requirements.

Therefore, a new custom magnetic driven pump has been produced by the company Chart, Inc, which was promised to match the design criteria. One of the two ordered pumps was delivered to Münster and is shown in figure 3.14, while the second one is tested at Columbia University.

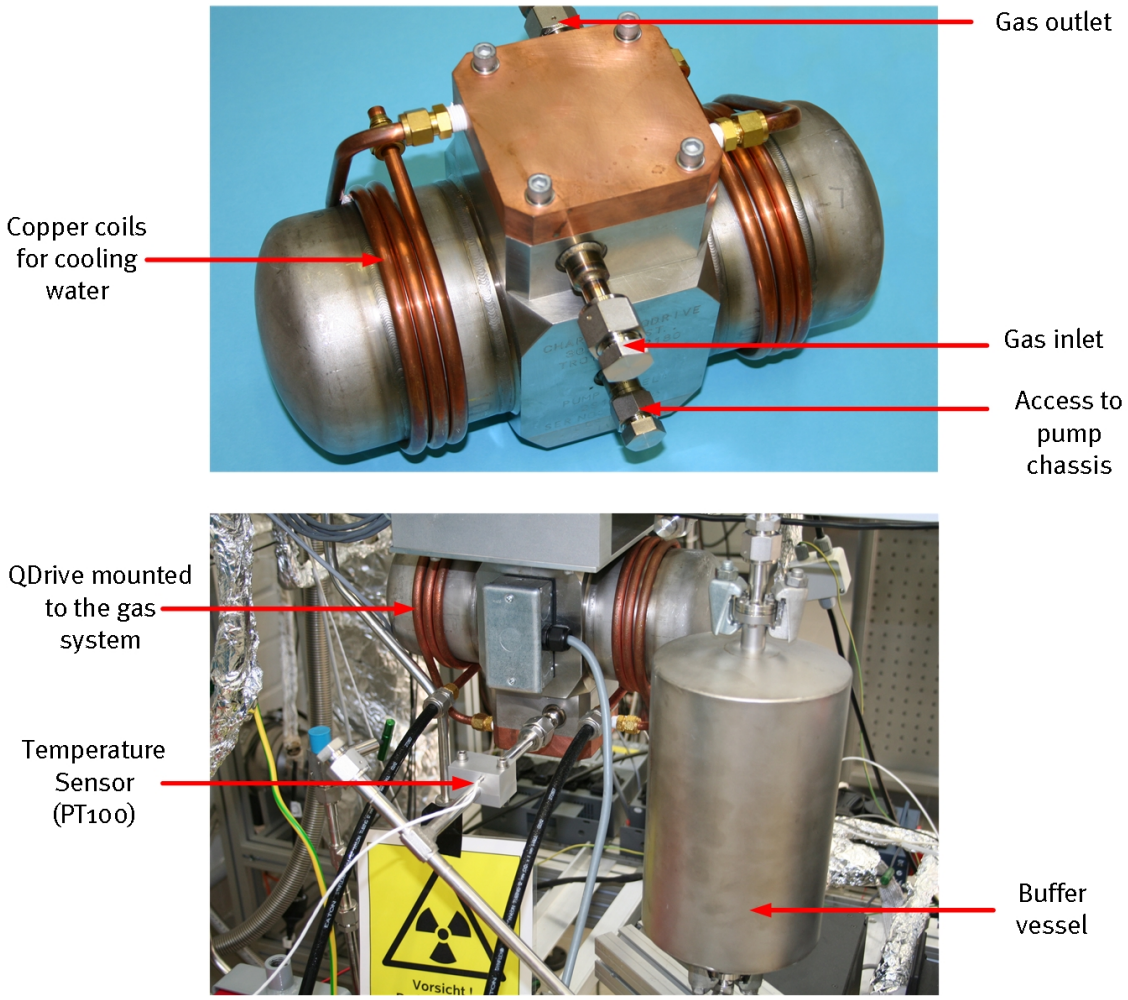

Figure 3.14: **The QDrive and its integration to the Münster gas system.** In these pictures the QDrive is shown (top picture) and how it is mounted together with a buffer volume to the gas purification system in Münster (bottom picture).

The QDrive is pumping the process gas, by linear motion of a piston in a compression volume induced by an electro-magnetic drive via solenoids. The gas is fed by an inlet reed valve and exhausted at the discharge reed valve. All parts inside the pump (piston, valves, e.t.c.) are not lubricated to be feasible for ultra-clean applications. The company tested the QDrive with argon gas only, achieving a thermally stable flow rate of 92 slpm with an inlet pressure of 2 bar and an average charge pressure of 3.3 bar [Cha12]. The data from this performance test is shown in figure 3.15.

To confirm the results of the performance-tests, carried-out by the manufacturer, further investigations have been performed in Münster as well as in New York using xenon gas. This was of crucial importance since argon and xenon, although both noble gases, have

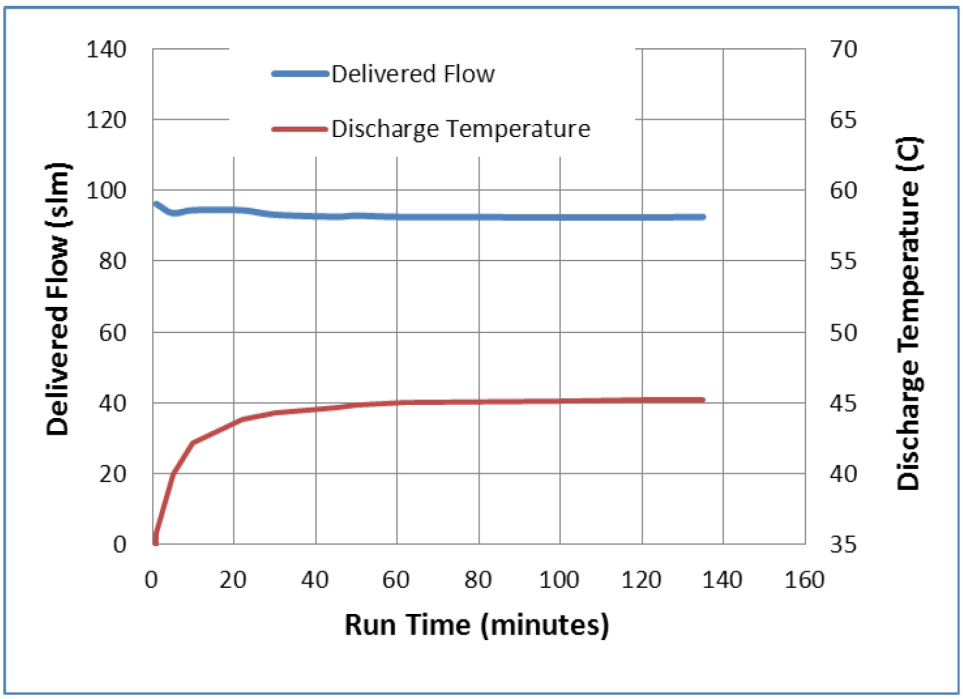

Figure 3.15: **Performance test of the QDrive carried out by Chart, Inc.** This plot shows the results of a performance test carried out by the company Chart, Inc. A thermally stable operation at a maximum flow rate of 92 slpm at an inlet pressure of 2.0 bar has been achieved. The test has been carried out for argon only [Cha12].

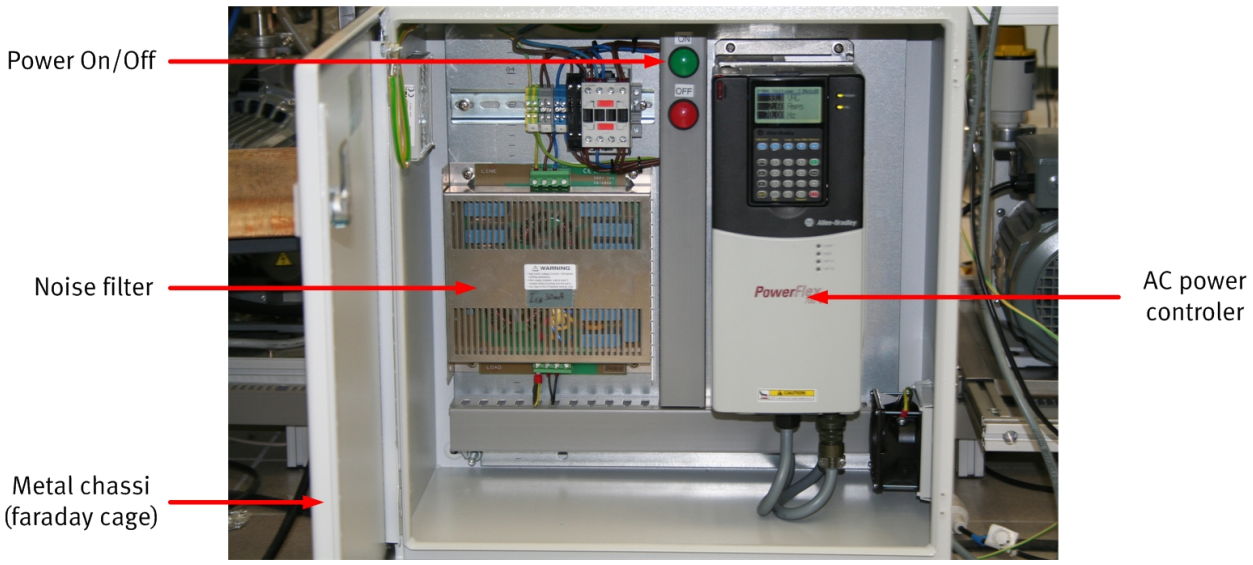

Figure 3.16: **Installation of the AC Power Drive.** This picture shows the cabinet that houses the AC Power Drive and a noise filter to prevent nearby electronics from electromagnetic nuisance.

different flow characteristics due to their difference in atomic mass. While argon has an atomic weight of 39.948(1) u, the xenon has an atomic weight of 131.293(6) u, being more than three times heavier [Iup13]. This has a direct impact on the characteristics of the gas transmission. For XENON1T the average pressure can be assumed to be $p = 2\,\mathrm{bar}$ and the gas temperature T at the inlet of the purification system to about $T = 20°\mathrm{C}$, which allows to calculate the average path length [Jou06]:

$$\bar{l} = \frac{k \cdot T}{\sqrt{2} \cdot \pi \cdot d^2 \cdot p} \approx 25\,\mathrm{nm} \tag{3.5.1}$$

with d being the diameter of the particle (here the Van der Waals diameter for xenon is used). For a half-inch tube of a diameter $d_T \approx 0.012\,\mathrm{m}$, the ratio $\bar{l}/d_T \approx 10^{-6} \ll 1$, which somehow defines the viscous flow[9]. In this regime an internal friction in the gas is produced, which leads to a friction force in the opposite direction than the flow. The viscosity η is related to the particle mass $\eta \propto \sqrt{m_P}$. Furthermore the specific heat capacity is related to the atomic mass and is influencing the heat transfer inside the gas. Summing up, the investigation with xenon instead of argon is absolutely necessary to give the proper performance characteristics of the QDrive and thus, the maximal achievable flow rate.

The QDrive is mounted to the gas lines of the purification system via half inch VCR connectors. It is supplied with cooling water of 15°C-20°C at a flow of greater than $5\,l/\mathrm{min}$ (2 ,l/min requested by manufacturer). The pump is powered by an adjustable frequency AC Drive (Bradley Allen, type PowerFlex 700) which allows the user to modify the voltage and the frequency which is applied to the pump and therefore, to regulate the pumping speed directly. The AC Drive is supplied with 230 V and 50 Hz.

To prevent the electricity network in the lab from high frequency noise coming from the AC Power Drive, a three phase 500 V 16 A Main Filter (Roxburgh EMC, type MIF-316) has been installed, which is also recommended by the manufacturer. The AC Power Drive together with a filter and switches for turning the power on and off have been mounted inside a lockable metal cabinet (figure 3.16), which is connected to the ground circuit connector of the lab. Before running the pump, it is necessary to prepare the electric circuit of the lab for high current on the ground return (greater 50 mA), which is too high with respect to German standards (30 mA). Therefore, it was necessary to use an insulating transformer to run the pump, otherwise the fuse would break all the time. This high current seems to be a known problem, since the manufacturer of the pump recommended to use an adjustable RCD, type B or an insulating transformer (see [Cha12]) to run the QDrive. For the installation at LNGS one has to consider this problem.

The QDrive has been tested by filling the gas purification system with xenon and circulate the gas inside the closed loop under different conditions. In total four sets of measurements have been performed at different pressures: 2.0 bar, 2.8 bar, 3.3 bar and 3.8 bar, where the frequency and the voltages have been varied to measure the flow rate, the temperature and the pressure drop along the getter (which already has been presented in figure 3.9). The

[9] In literature, the viscosity is defined by a fluid between two parallel plates with the distance x to be $\bar{l}/x \ll 1$. Here the diameter of the pipe is used to estimate the regime.

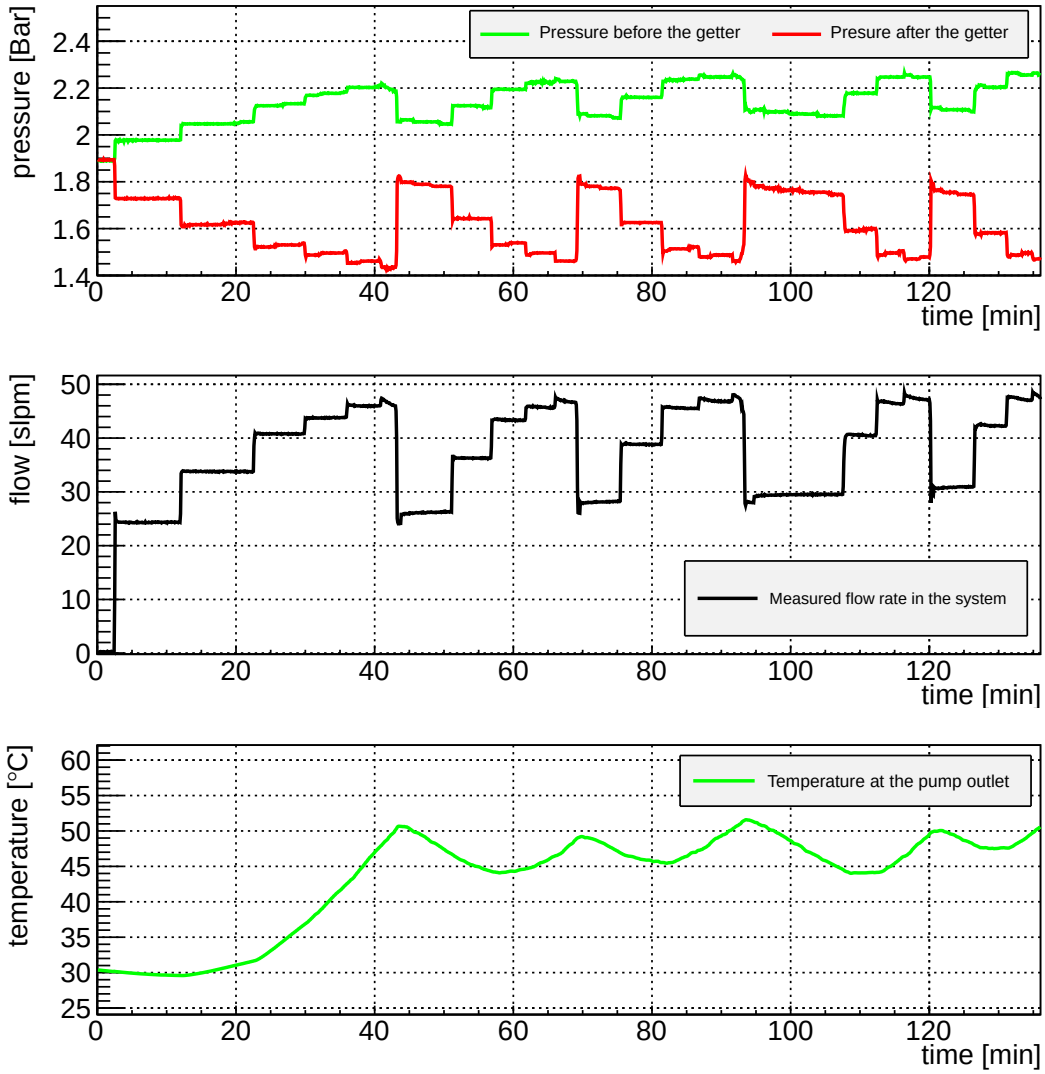

Figure 3.17: **Slow control data of the first test at 2.0 bar.** These plots show the most important sensor signals, the pressure before and after the getter (top), the related flow rate inside the system (middle) and the temperature at the gas-outlet of the pump (bottom). The data has been collected during the first performance test at a system pressure of $\approx$ 2.0 bar.

sensor output of the first measurement is shown in figure 3.17. The measurement is started at $t \approx 2.5$ min by turning on the pump with a frequency of 60 Hz and a voltage of 30 V.

The pump stabilizes rapidly to almost 25 slpm. After a few minutes of stabilization, the voltage is increased to 50 V, keeping the frequency constant. As consequence, the flow rate rises up to almost 35 slpm. This procedure is repeated several times, up to 100 V before the frequency has been changed from 60 Hz to 65 Hz and than to 70 Hz and 75 Hz. The maximum voltages for the different frequency steps, have been adjusted in order to keep the temperature at the gas-out line below 50°C and to limit the current in the pumps, as requested in the manual.

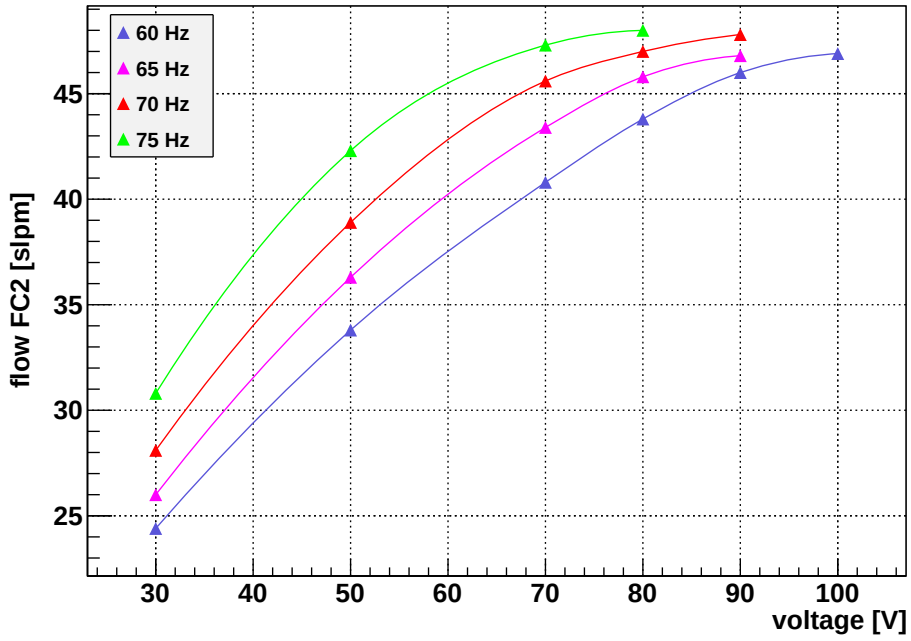

Figure 3.18: **Achieved flow rates for different voltages at 2.0 bar.** This plot collects the different flow rates, as a function of the applied voltage. The system pressure started with about 2 bar.

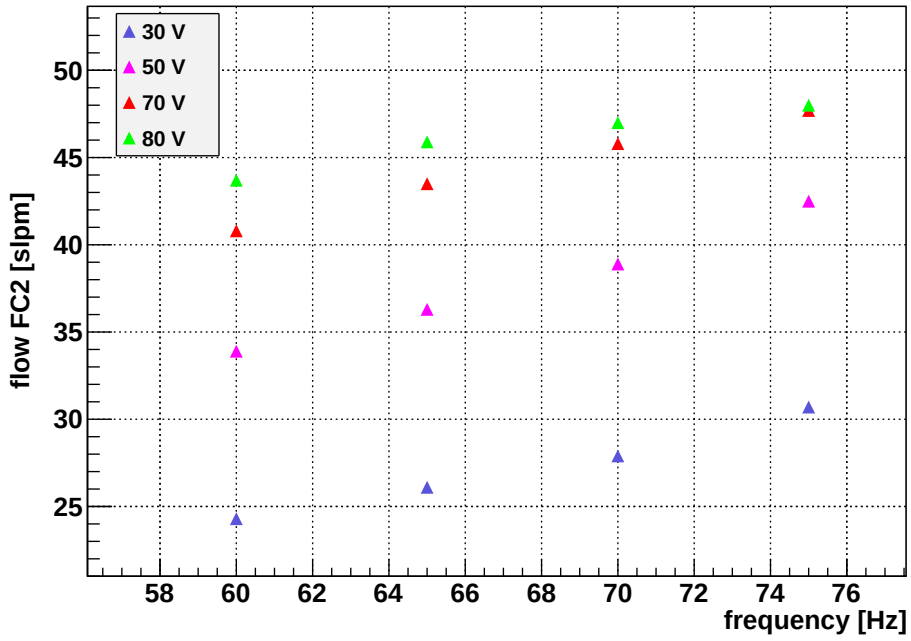

Figure 3.19: **Achieved flow rates for different frequencies at 2.0 bar.** This plot collects the different flow rates, that have been achieved as function of frequency. The system pressure started with about 2 bar.

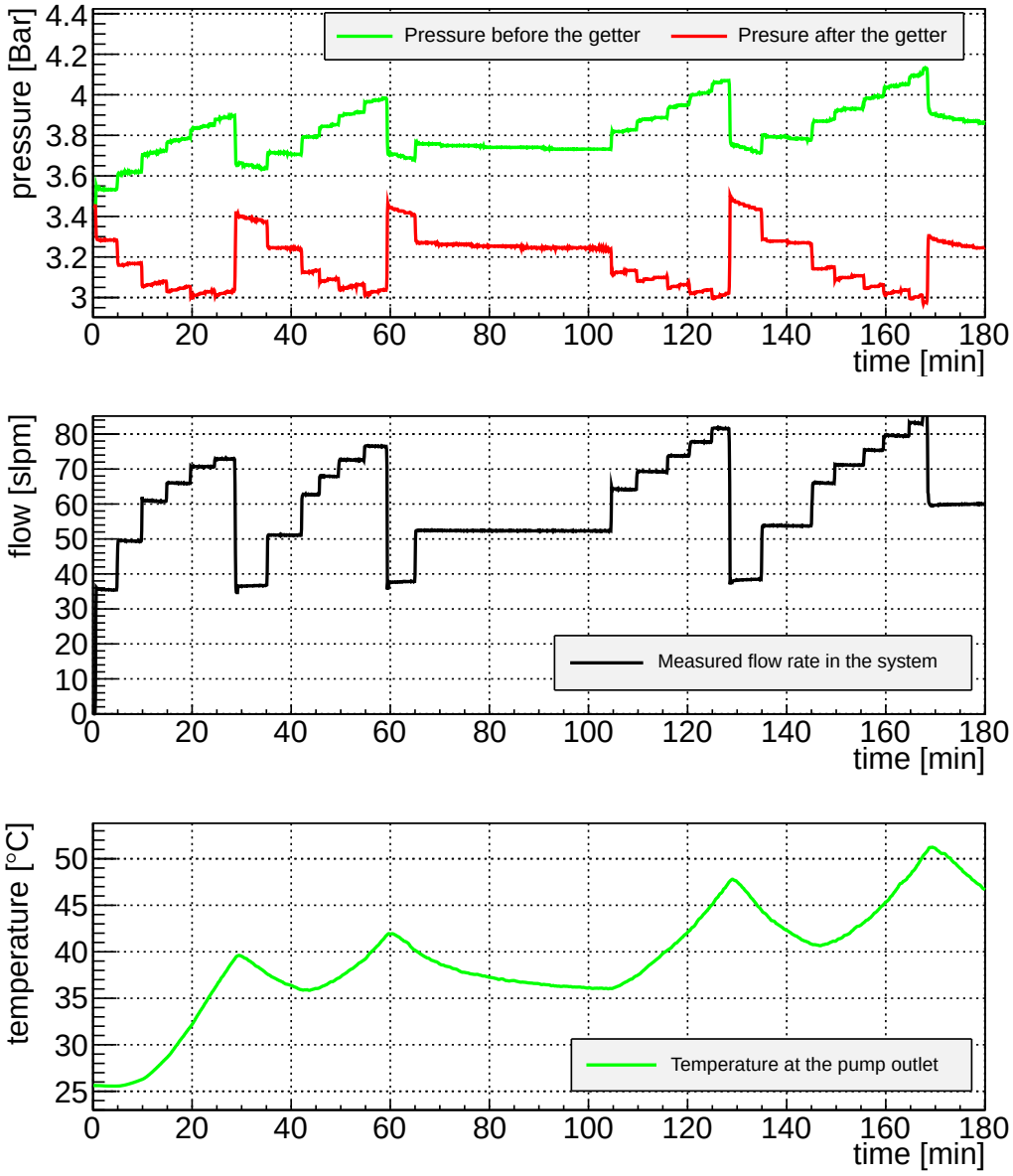

Figure 3.20: **Slow control data of the first test at 3.8 bar.** These plots show the most important sensor signals, the pressure before and after the getter (top), the related flow rate inside the system (middle) and the temperature at the gas-outlet of the pump (bottom). The data has been collected during the first performance test at a system pressure of $\approx$ 3.8 bar.

In figure 3.18, the achieved flow rates as function of the applied voltage for different frequencies are shown. The error bars in the y-axis have been removed, for clarity reasons. For these measurements the same thermal-based flow controllers as introduced in section 3.1 are used, producing the same error of 2 slpm. The lines in the graph are connecting lines only. As already mentioned, we use the controller in the fully-open mode, to not control the gas stream, but just to monitor it. Beside the systematic uncertainty of $\pm$2.0 slpm, the

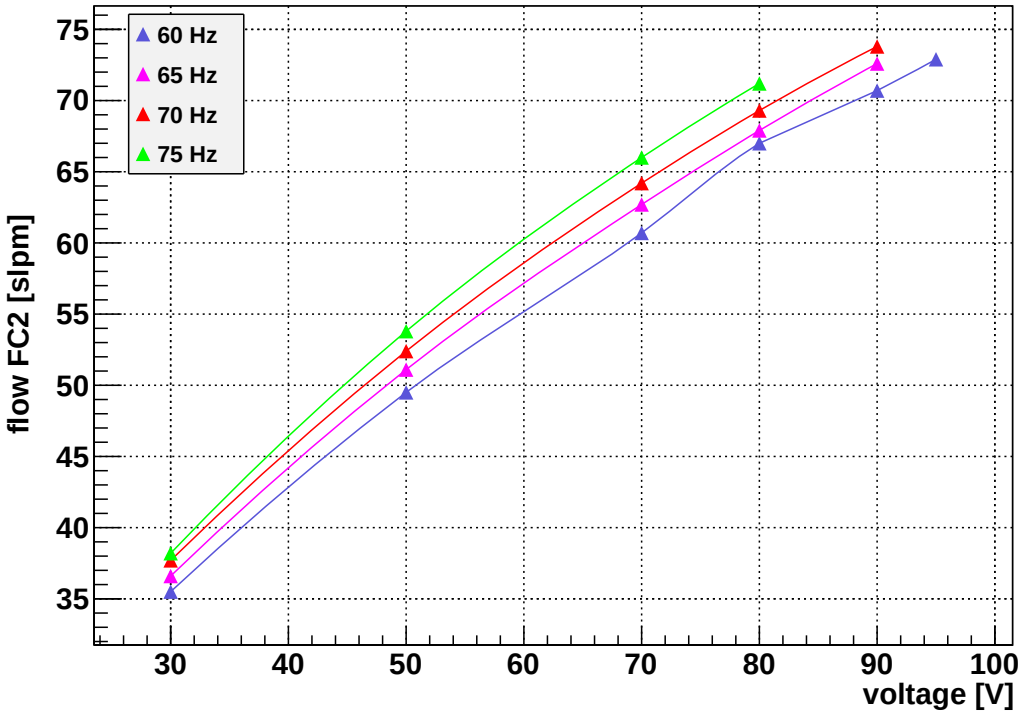

Figure 3.21: **Achieved flow rates for different voltages at 3.8 bar.** This plot collects the different flow rates, as a function of the applied voltage. The system pressure started with about 3.8 bar.

statistic fluctuation of the average flow for each voltage and frequency condition has been calculated and is varying between 0.1 - 0.3 slpm. Nevertheless, the first test shows immediately that a flow rate of 100 slpm for xenon is not achievable under these conditions. The last measurement with the highest initial pressure of 3.8 bar is also shown in figures 3.20, 3.21 and 3.22. It is directly shown in figure 3.20, that for high flow rates, up to 80 slpm, the temperature at the gas outlet is increasing beyond the safety specification. An active cooling of the gas in the outlet line would be one solution. Nevertheless, even with higher system pressure, the maximal achievable flow is limited and far of from reaching the 100 slpm. The best performance is achieved at frequencies between 70 Hz and 75 Hz. Higher frequencies were not supported by the corresponding AC Power Drive. In a second step, the longterm behavior of the QDrive has to be investigated, to ensure that the performance is stable over time, which is of crucial importance for the experiment.

The final stability test has been performed over $\approx$ 51 h, referred to as mid-term stability test, due to the limited time before the QDrive had to be shipped to MPIK, Heidelberg to perform the radon emanation measurements. The result of the 51 hr-circulation test is shown in figure 3.23.

The pump has been operated at a system pressure of 3.8 bar with a frequency of 70 Hz and a voltage of $\approx$ 55 V. These conditions were chosen to stabilize the temperature of the system to

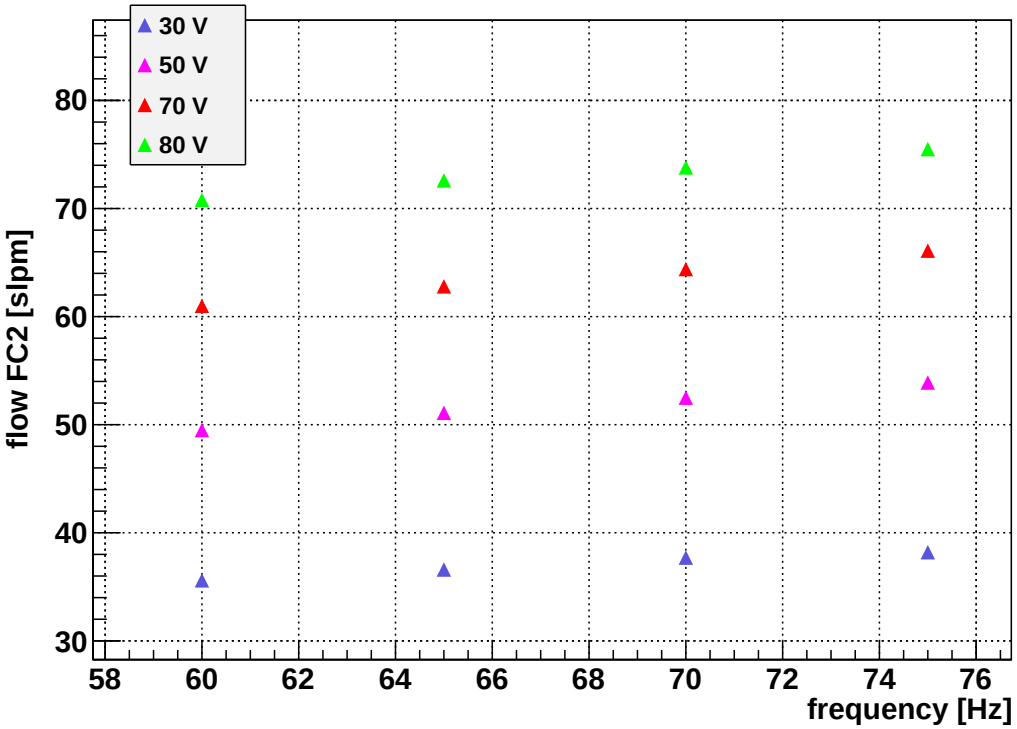

Figure 3.22: **Achieved flow rates for different frequencies at 3.8 bar.** This plot collects the different flow rates, that have been achieved as function of frequency. The system pressure started with about 3.8 bar.

a proper value. As one can see in figure 3.23, the flow is in average 54.1 slpm with a standard deviation of 0.1 slpm. The margin between the minimal and maximal flow rate during the measurement time is about 0.6 slpm (about 1.1% of the average flow). This indicates, that the QDrive is working rather stable. The modulation of the flow and temperature measurements might be caused by changing in the temperature of the colling water, which is not recorded. Nevertheless, the QDrive showed good stability on a mid term run. Further tests on the performance and the stability of the second QDrive have been carried out at the Columbia University, showing a rather similar behavior in the maximal achievable flow rate.

Regarding the purity in terms of radon emanation, it has been measured by colleagues at MPIK, Heidelberg, that the pump, tested in Münster is releasing a severe amount of radon. The first screening campaign gave values for its activity of $A(^{222}\mathrm{Ra}) > 1\,\mathrm{mBq}$, so that additional investigations have been carried out. In cooperation with the company it was tried to find the proper materials in order to construct the next pumps with less emanation rate.

In summary, the QDrive seems not to be the ideal pump for the needs of XENON1T, regarding the achievable flow rates. But it is by far better in terms of leak tightness, cleanliness and performance than membrane pumps of comparable strength. Therefore it has been decided by the collaboration to use the QDrive further on but to work with the company to find

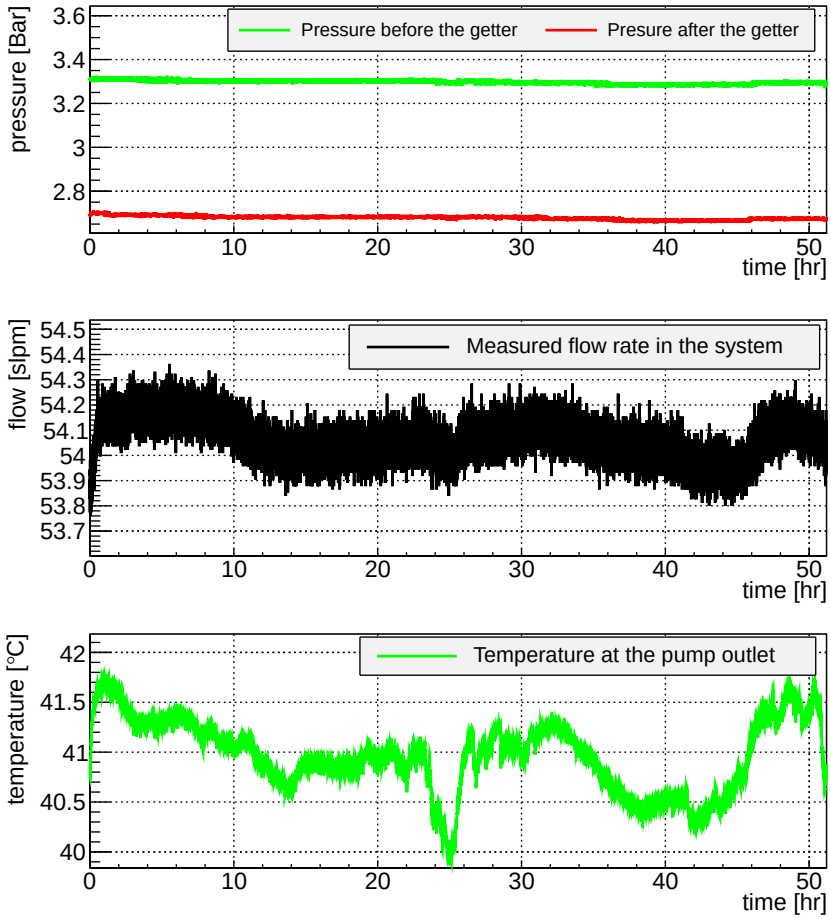

Figure 3.23: **Stability test of the QDrive.** This plot shows the slow control data for a measurement at high flow rates over more than 50 hours, with a system pressure of 3.8 bar at a frequency of 70 Hz and a voltage of ≈ 55 V.

better materials for less radon emanation. Due to the performance of the QDrive and since the getters are also only rated for circulation speeds of 75 slpm it has been decided to design the gas purification system in a way to use at least two pumps and getters in parallel to achieve higher flow rates.

3.6 The XENON1T gas purification system

The sum of the different tests with the demonstrator setup influenced the design of the XENON1T purification system. As already mentioned, the system will be build to use multiple pumps together with multiple getters in parallel. Beside the limited flow rate of the QDrives, there are further reasons to build a redundant system. In case of a regularly maintenance or even in case of a system malfunction in one of the parallel branches, the affected lines can be closed and the damaged parts can be exchanged, without stopping the whole circulation and hopefully without interrupting the detector operation. This depends

whether a proper electron lifetime at a temporary reduced circulation speed is preserved. Furthermore the load on the single devices is reduced, which allows for longer lifetimes of the components. Similar to the demonstartor setup in Münster, the XENON1T system will be the interface for gas distribution and connects all the different subsystems (see figure 3.24).

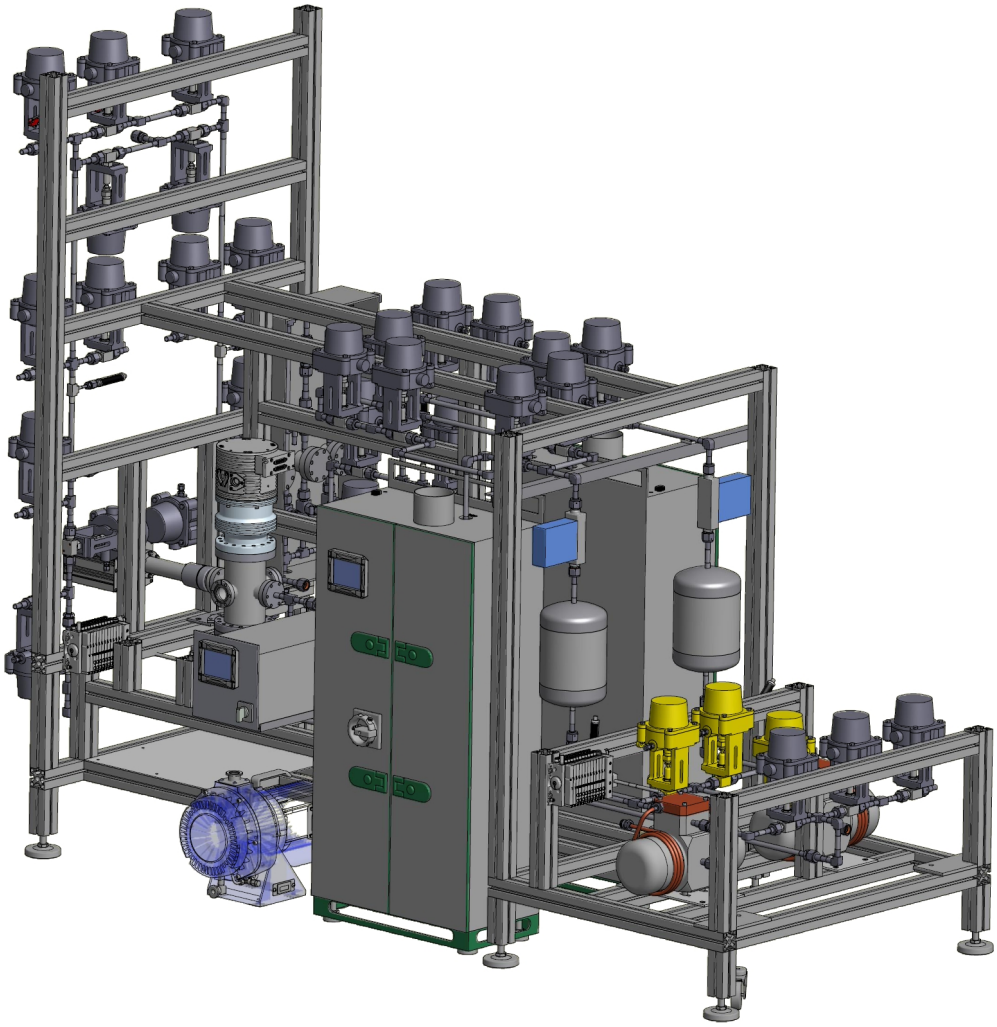

Figure 3.24: **CAD drawing of the XENON1T gas purification system.** The XENON1T gas purification system has been designed as a modular system, consisting of two pumps and two getters, which allow to achieve the flow rate of 100 slpm, that is needed. Furthermore it is equipped with several ports to connect analyzing devices (HALO+) or calibration sources. On the left side the distribution manifold is integrated, in order to connect the system with al the other sub-systems. Furthermore, the system is designed in a way to install additional getters and pumps on a second layer on top of the existing one to reach even higher flow rates of 200 slpm, to be prepared for a possible upgrade to XENONnT after 2017. The design and the sketch are courtesy provided by Dipl.-Ing. Christian Huhmann, Institut für Kernphysik, Universität Münster.

The same type of valves and pressure sensors will be used, while other components have been replaced to improve the performance of the system, e.g. the distribution of pressurized air has been upgraded. Although the slow control, based on components from National Instruments is working properly, it has been decided by the collaboration to use a different hard- and software platform, provided by General Electrics, for the slow control of the whole XENON1T experiment. The design and the software development for the overall XENON1T setup is done by a dedicated working-group, organized and led by the Weizmann institute, Israel and the Coimbra University, Portugal in close collaboration with all other groups, that deliver hardware to the experiment. The design and the construction of the setup will be explained in a dedicated master thesis [Sch15] and is not part of this work. Nevertheless in figure 3.24 the CAD design of the system is shown.

Currently the system has been constructed and already shipped to LNGS. It is placed in the third floor of the XENON1T service building in hall B and is going to be integrated in the experiment.

A cryogenic distillation column for the XENON1T Experiment 4

Since krypton as a noble gas is unaffected by the getter cleaning procedure, a different technique has to be used to reduce the amount of krypton in xenon. There are several approaches to separate krypton and xenon. The technique of gas-chromatography with special charcoal material is used by the LUX collaboration, achieving a concentration of natural krypton in xenon of 4 ppt [Ake14], with a calculated reduction factor of $F_{Red} \approx 32500$. An other method is the cryogenic distillation, which uses the distinction in the boiling points of krypton and xenon to perform the separation. This has been applied for the XENON100 experiment, achieving a concentration of $^{Nat}Kr/Xe \approx 1$ ppt [Lin13]. Generally, it is expected, that ^{85}Kr is behaving chemically in the same manner than the other krypton isotopes, and can be separated although its concentration is many orders of magnitudes less. It has been shown, by comparing the β-γ coincidence analysis with the direct measurement of the ^{84}Kr concentration, that this assumption is valid for the concentrations down to 19 ppt [Apr13a].

As it has been discussed in chapter 2.5.2 the fraction of natural krypton in xenon has to be below 0.5 ppt and a reduction factor of $\approx 10^4 - 10^5$ is needed. Furthermore the xenon inventory of 3.3 tons has to be cleaned in a feasible timescale of several weeks. The design value has been set to 3 kg/h, which allows to purify all the xenon in about seven weeks of continuous distillation. The amount of krypton enriched off-gas, which can not be used for the dark matter search, is restricted to 1%.

4.1 Cryogenic distillation and cryogenic separation

In general, the technique of distillation is using the different boiling points of the single components in a mixture to separate them. The most volatile components are evaporated first and are enriched in higher concentration in the steam. Hence, the distillation process is usually treated as an enrichment procedure. The different vapor pressures for krypton and xenon are shown in figure 4.1, pointing out that krypton has the higher vapor pressure and thus being the more volatile component.

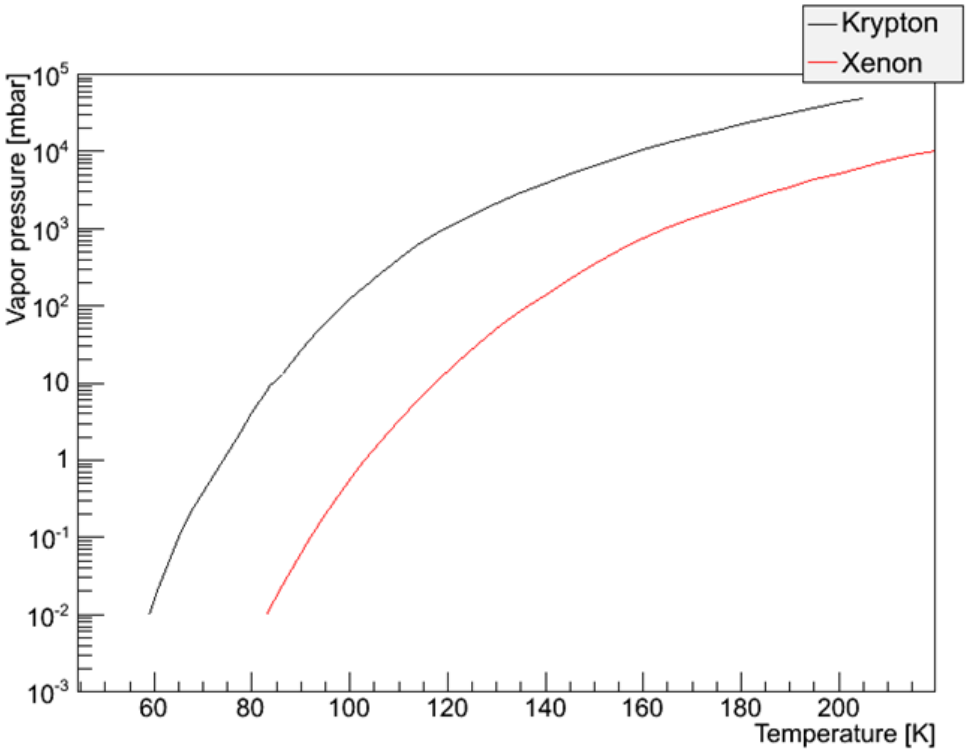

Figure 4.1: **Vapor pressures of krypton and xenon.** The vapor pressure of krypton is much higher for the whole temperature range compared with xenon, hence, being the more volatile component in a binary mixture. The plot is taken from [Bro13] and bases on data from [Lid06].

The distillation is a method widely used in industry, for example in fractional distillation of air to extract the technical gases or in oil refinery plants. It has been demonstrated to be feasible for mass-production, allowing for high process speeds. However, for industrial processes the separation is performed at concentrations up to the percent level. The concentration of krypton in xenon, required for the XENON1T experiment is several orders of magnitude lower. The theory to describe the separation has only been developed for high concentrations and has not been tested in this regime before. For a pressure of 2.0 bar, the boiling point of xenon is at $-95.3°C$, which would lead to a krypton vapor pressure of ≈ 20.7 bar. For trace concentrations far below the vapor pressure, the major amount of krypton particles should stay in the gas phase when the xenon is liquefied. For the XENON100 experiment concentrations of natural krypton in xenon of ~ 1 ppt have been achieved with a cryogenic distillation column. This value has been determined by dedicated measurements [Lin13], showing that the separation works but also that measurable amounts of krypton atoms are still contained in the xenon. Lower concentrations have not been reached so far. As consequence, additional effects have to be considered that are influencing the distillation process. At very low concentrations the separation might not be treated as a classic distillation process anymore, single atom processes which have been neglected so far become more important at this regime. The trapping of single krypton atoms into xenon droplets, which can be seen as an absorption of single krypton atoms to the liquid xenon is a possible process to obtain a certain amount of krypton in the purified xenon. Additionally, the

trapping of krypton atoms at the walls and its release into the purified liquid xenon might contribute to the final concentration in the outcome. The question remains, whether there exist a natural separation limit due to any kind of process, that prohibits the usage of cryogenic distillation to achieve the desired purity. In addition, the technical implementation has to accommodate for the design goal. Already small leakages in the system can spoil the cleaning procedure. Surface contamination can influence the phase transition, prohibiting the optimal separation.

Although there existed several open questions at the design phase of this custom cryogenic distillation column, the classic McCabe-Thiele method for cryogenic distillation of mixtures with high concentrations has been used as a start.

4.2 Design of a distillation column using the McCabe-Thiele method

In this section, the design of a distillation plant is described, using the common McCabe-Thiele model, as it is described in [Loh07] and [McC05].

In the simple case, the technique of cryogenic distillation uses the different vapor pressure of the two components of a binary mixture. In this particular case, it is valid to use this approach, because the xenon is cleaned from electronegative impurities with hot getter material beforehand (see chapter 3.1). For a closed, single distillation stage under constant pressure and temperature at the boiling point of xenon, the concentration of krypton in the gaseous phase (y_{Kr}) is compared to the concentration in the liquid phase (x_{Kr}) to quantify the separation. This is done by using Raoults law for ideal liquid mixtures and Daltons Law for an ideal gas mixture. Raoults law gives the relation between the partial pressure p_{Kr} and the vapor pressure P^0_{Kr} in an ideal, pure composition of krypton and xenon in the liquid: $p_{Kr} = x_{Kr} \cdot P^0_{Kr}$, while Daltons law relates the partial pressure to the total pressure p_{tot} for an ideal gas mixture: $p_{Kr} = y_{Kr} \cdot p_{tot}$. Both laws are used to describe the phase equilibrium between the gas and the liquid phase:

$$\frac{y_{Kr}}{x_{Kr}} = \frac{P^0_{Kr}}{p_{tot}} \qquad \text{and} \qquad \frac{y_{Xe}}{x_{Xe}} = \frac{P^0_{Xe}}{p_{tot}} \tag{4.2.1}$$

The relative volatility α is further defined as the ratio of the vapor pressures of the two components:

$$\alpha = \frac{y_{Kr}/x_{Kr}}{y_{Xe}/x_{Xe}} = \frac{P^0_{Kr}}{P^0_{Xe}} \tag{4.2.2}$$

In a closed system the vapor pressure is related to the probability that an atom changes from liquid into gas phase. For a single-stage distillation system in equilibrium it is expected, that the krypton concentration in the vapor is enriched by $\alpha = 10.8$ at T $= -98$°C compared to the liquid. In order to reach the high separation efficiency that is needed for the XENON1T experiment, in combination with a nearly loss-free performance, a cascade of distillation

stages (so called rectification) with a partial reflux is used (a schematic is shown in figure 4.2). Consequently, the number of distillation stages is directly influencing the separation efficiency of the distillation plant and has to be calculated for the design.

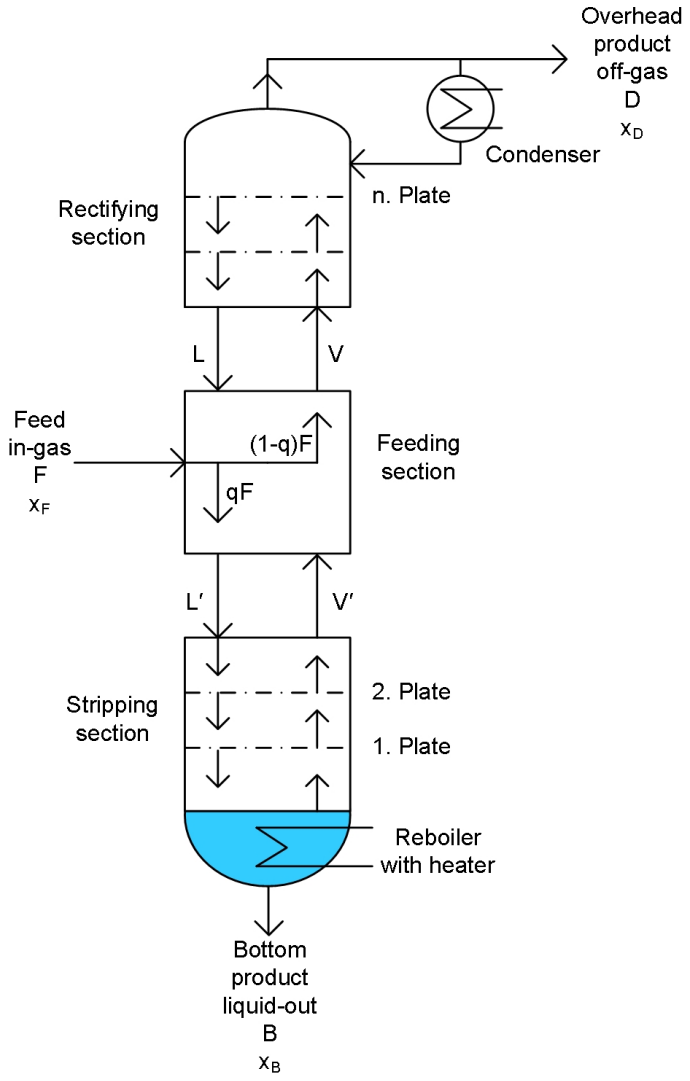

Figure 4.2: **Mass balance inside the distillation column.** This scheme shows the different flows F, B, D that are entering or leaving the column. L and L' are the liquid flows downward the column while V and V' are the vapor streams to the top of the column.

In the reboiler, a certain amount of the krypton-xenon mixture is evaporated. As described before, the high volatile krypton is enriched in the up-streaming gas. In the ideal case, the total amount of material is condensed again on the first distillation stage. Consequently, the liquid on this stage has the same krypton concentration as the evaporated steam coming from the reboiler stage. Hence, the concentration of krypton in this liquid is higher compared to the starting mixture. Further evaporation lead to the same result, the up-streaming gas contains a higher concentration of krypton, which gets liquefied on the following distillation stage. The evaporation and liquefaction on a cascade of several distillation plates (theoretical

stages) lead to an increase of the krypton concentration from the bottom to the top of the distillation column. While most of the up-streaming gas is condensed again at the top-condenser and flowing back to the system (partial reflux), a small fraction of krypton enriched gas is extracted (in our case $\approx 1\%$). The amount of liquid xenon that is fed back into the column is also influencing the distillation performance and can be calculated as well (see below).

The number of theoretical stages which is needed to achieve a certain concentration is obtained by drawing the different compositions for the gaseous and liquid phases in an equilibrium diagram based on the McCabe-Thiele method. This method is relied on the equilibrium of the binary mixture in connection with the mass-flow inside the column. As indicated in figure 4.2, a rectifying column is generally characterized by a division of the column in three different sections. These are the feeding section, the rectifying section and the stripping section, where different flow rates of gas and liquid xenon have to be considered. The design specifications allow to draw the so called operating lines for the different sections of the column, leading to the number of theoretical stages.

The determination of the total mass balance is one important step in the calculation. The incoming flow F (in-gas) in equilibrium is equal to the outgoing flows at the reboiler B (purified xenon, liquid-out) and at the condenser D (krypton enriched xenon, off-gas), giving the total mass-balance:

$$F = D + B \tag{4.2.3}$$

This can also be written in terms of krypton particles, using the different concentrations of krypton in the feed c_F, in the off-gas c_D and in the liquid-out c_B:

$$F \cdot c_F = D \cdot c_D + B \cdot c_B \tag{4.2.4}$$

F and D have been defined to 3 kg/h and 0.03 kg/h, respectively [Ros14b]. Therefore, B is fixed at 2.97 kg/h due to mass conservation. For an input concentration of $c_F = 100\,\text{ppb}$ and a pre-defined output concentration of $c_B = 0.5\,\text{ppt}$, the concentration in the off-gas can be calculated for the given flows to $c_D = 10\,\text{ppm}$.

In the rectifying section, the more volatile component is enriched and the unknown krypton concentration on a theoretical plate $y_{Kr,n+1}$ in the vapor stream V can be calculated using the krypton particle balance to get the operating line (rectifying line), with L being the liquid xenon flux in the rectifying section:

$$V \cdot y_{Kr,n+1} = L \cdot x_{Kr,n} + D \cdot c_D \qquad \rightarrow \qquad y_{Kr,n+1} = \frac{R}{R+1} \cdot x_{Kr,n} + \frac{c_D}{R+1} \tag{4.2.5}$$

R is called reflux ratio and describes the amount of xenon that is fed back as liquid (L) from the top, related to the flow of extracted off-gas D:

$$R = \frac{L}{D} \tag{4.2.6}$$

For a good separation performance, a high reflux ratio is needed to support the enrichment of the more volatile component in the up-streaming vapor. The minimum reflux ratio is related to the rectifying line with the minimum slope and can be calculated using the Underwood equation [Loh07b]:

$$R_{min} = \frac{1}{\alpha - 1} \cdot \left(\frac{c_D}{c_F} - \alpha \cdot \frac{1 - c_D}{1 - c_F}\right) = 9.1 \tag{4.2.7}$$

With $c_D = 10\,\text{ppm}$, $c_F = 10\,\text{ppb}$ and $\alpha = 10.8$. This equation is only valid under special feed configuration, namely a pure, saturated liquid feed. The different feeding conditions are explained in the following (see also figure 4.3). For the column at the XENON100 experiment the reflux ratio is $R = 191$ [Abe09]. Therefore, we aim to achieve the same value, since $R = 191 > 9.1 = R_{min}$ for our system.

Thereby, the liquid xenon flux L is calculated $L = R \cdot D = 5.73\,\text{kg/h}$. These design criteria also define the amount of cooling power that has to be provided by the top condenser (calculated later in this section).

The stripping line for the stripping section is determined by the liquid and gaseous flow rates in this part of the system L' and V', respectively:

$$L' \cdot x_{Kr} = V' \cdot y_{Kr} + B \cdot c_B \qquad \rightarrow \qquad y_{Kr} = \frac{R'}{R' - 1} \cdot x_{Kr} + \frac{c_B}{R' - 1} \tag{4.2.8}$$

With R' being the reflux ratio of gas evaporated from the reboiler, defined as:

$$R' = \frac{L'}{B} \tag{4.2.9}$$

For the determination of R' the flow rate of down streaming liquid L' has to be calculated. As shown in figure 4.2, L' is a combination of liquid from the rectifying section and also from the feeding section:

$$L' = L'(L, F) = L + q \cdot F \tag{4.2.10}$$

In the feeding section, the down-streaming liquid flow and the up-streaming gaseous flow depend on the thermal state of the feed. Different feed configurations are possible, influencing drastically the mass flow along the column. To describe the feeding condition in the mass balance, the caloric factor q is defined as:

$$q = \frac{L' - L}{F} \tag{4.2.11}$$

The difference in the down streaming liquid L and L' is related to the amount of injected material. Hence, different feed configurations are possible and illustrated in figure 4.3.

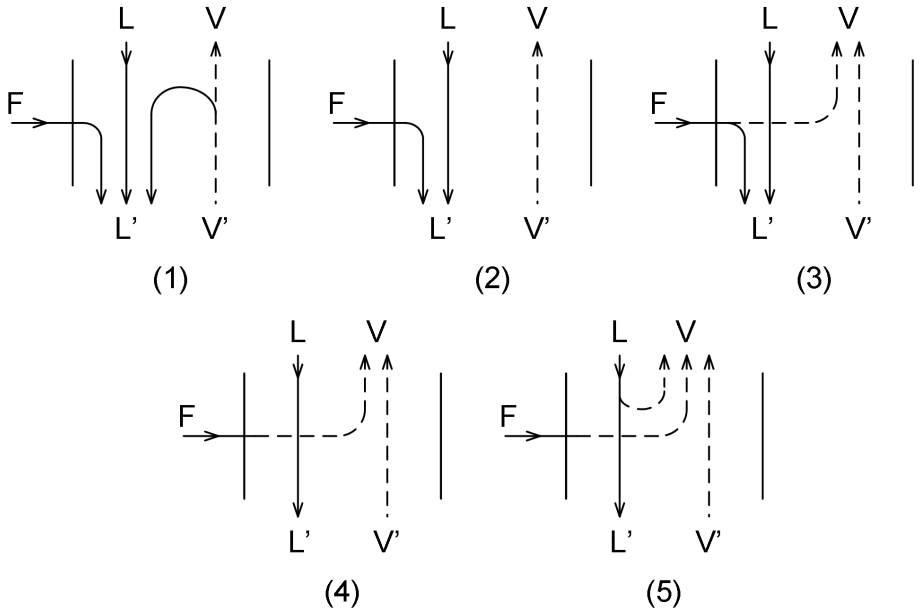

Figure 4.3: **Different feed conditions.** This figure illustrates the flow at the feeding section for different conditions. (1) cold liquid, (2) saturated liquid, (3) partially vaporized, (4) saturated vapor, (5) superheated vapor. Figure taken from [McC05].

1. **Cold liquid feed** ($q > 1$)**:** When injecting very cold liquid, a fraction of up-streaming gas V' is liquefied and enhancing L'.

2. **Saturated liquid feed** ($q = 1$)**:** Injecting in liquid feed at the boiling point does not affect the vapor stream and is directly added to L and becomes L'.

3. **Partially vapor** ($1 < q < 1$)**:** A mixture of gas and liquid is injected to column. While the gas is going up, contributing to V, the liquid fraction is going down, contributing to L'.

4. **Saturated vapor** ($q = 0$)**:** The vapor becomes directly part of the up-streaming vapor V.

5. **Superheated vapor** ($q < 0$)**:** Feeding with super-heated gas influences the down streaming xenon, as some of it is vaporized and enhancing V.

For the new system, the design foresees a liquid feed ($q = 1$), which allows to calculate $L' = L + F = 8.73\,\mathrm{kg/h}$ and $R' = 2.94$, used for the calculation of the stripping line.

Finally, the equilibrium line is constructed, depending on the volatility α, thus, the krypton concentration for very low concentrations of krypton in xenon ($x_{Kr} \cdot (\alpha - 1) \ll 1$) in the gas phase is defined as:

$$y_{Kr} = \frac{P_{Kr} \cdot x_{Kr}}{P_{Kr} \cdot x_{Kr} + P_{Xe} \cdot x_{Xe}} = \frac{\alpha \cdot x_{Kr}}{1 + (\alpha - 1) \cdot x_{Kr}} \approx \alpha \cdot x_{Kr} \tag{4.2.12}$$

By using the operation lines in conjunction with the so called equilibrium line for a krypton-xenon mixture and the design values, one can draw the McCabe-Thiele diagram, as shown in figure 4.4. The diagram has been made for a pure liquid feed ($q = 1$), indicated by the intersection line and a starting concentration of $^{\mathrm{nat}}\mathrm{Kr/Xe} = 100\,\mathrm{ppb}$. The different stages in the diagram are drawn by taking the liquefaction processes and the related vapor composition into account. A liquid mixture with the krypton content x_{Kr} has a vapor phase above with an enhanced krypton concentration y_{Kr}, which is streaming up to the next stage (vertical line), where it gets liquefied again (horizontal line). From this calculation, 9 theoretical stages are needed to reach the sub-ppt range.

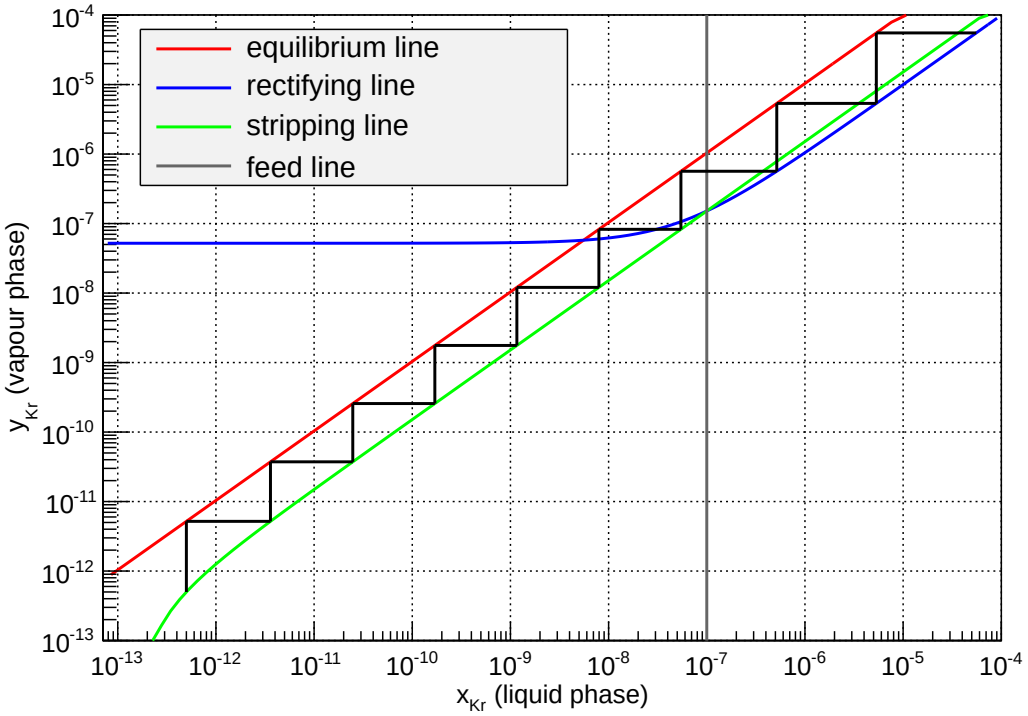

Figure 4.4: **McCabe-Thiele diagram to achieve a concentration of krypton in xenon to the sub-ppt scale.** This figure shows the McCabe-Thiele diagram, for a certain input concentration of $^{nat}\mathrm{Kr/Xe} = 100\,\mathrm{ppb}$ and the designed flow rates. In this example a liquid-only feed ($q = 1$) has been assumed.

4.3 Estimation on the cooling and heating power

From the reflux ratio and the designated flow rates the required heating and cooling power can be calculated. The cooling power, needed at the top condenser P_{Top} is equal to the heat flow $\dot{Q}_{Top}$ and can be calculated by using the down streaming flow rate $L = 5.73\,\mathrm{kg/h}$ and the difference in enthalpy between gaseous and liquid xenon of $\Delta h_{\nu,Xe} = 92.6\,\mathrm{kJ/kg}$ (at the boiling point for 2 bar):

$$P_{Top} = \dot{Q}_{Top} = L \cdot \Delta h_{\nu,Xe} = 147.4\,W \tag{4.3.1}$$

For a pure liquid feed ($q = 1$), the heating power at the reboiler can also be calculated:

$$P_{Reb} = \dot{Q}_{Reb} = V' \cdot \Delta h_{\nu,Xe} = (L' - B) \cdot \Delta h_{\nu,Xe} = 148.2\,W \tag{4.3.2}$$

P_{Reb} depends on the feeding condition. For a saturated liquid feed with$L' = L + F = 8.73\,\mathrm{kg/h}$ the heating power is calculated to be almost equal to the cooling power at the top condenser. For a gaseous feed this value is reduced to $P_{Reb,gas} \approx 70\,W$, since L' is reduced to $5.73\,\mathrm{kg/h}$.

These values are idealized, neglecting any kind of losses from heat radiation or thermal connections. In chapter 7 the achieved process variables will be compared to the design values.

In order to procure saturated liquid feed the incoming xenon, usually stored in gas bottles or other adequate vessels (Restox system, see chapter 2.3), has to be cooled down from room temperature ($\mathrm{T_{Room}} = +20°\mathrm{C}$) down to the liquefying temperature of $\mathrm{T_{Liq}} = -95.3°\mathrm{C}$ at a pressure of 2 bar. The required cooling power is calculated, by taking the power for the cool down process $P_{CD} = \dot{Q}_{CD}$ as well as the power for phase transition $P_{PT} = \dot{Q}_{PT}$ into account:

$$P_{Liq} = P_{CD} + P_{PT} = F \cdot c_P \cdot \Delta T + F \cdot \Delta h_{\nu,Xe} \tag{4.3.3}$$

The specific heat capacity for constant pressure c_P for xenon has been taken from the NIST database [Nis14a] and is rather constant until it reaches the boiling point (compare figure 4.5). By using the data, the cooling power for the cool down is calculated to $P_{CD} = 16.3\,W$.

In addition, the power needed for the liquefaction is calculated to $P_{PT} = 77.2\,\mathrm{W}$, summing up to a total cooling power of $P_{Liq} = 93.5\,\mathrm{W}$. This value is important for the design of the input condenser, as it will be described in the following chapter.

4.4 Setup of a package-type distillation column

For the technical realization of a rectification column, different technical approaches can be used, depending on the realization of an adequate, volume related interphase. This can be achieved either by dispersion of the liquid film to droplets and the gas stream to bubbles or by providing a large surface area, where the phase-transition can take place. The first attempt is used in plate columns, constructed out of special prepared plates, that allow the liquid and the gas to pass the plate through special holes or valves to produces droplets and bubbles. For the second approach, the column is filled with material, where the liquid is rinsed over a large surface, which acts as interphase, realized in so called package columns.

One advantage of package columns is the easy construction and therefore, the lower costs compared to plate columns. Furthermore, the pressure drop along the package is lower and the operation is less complex. The main problem of the package column is to provide a good

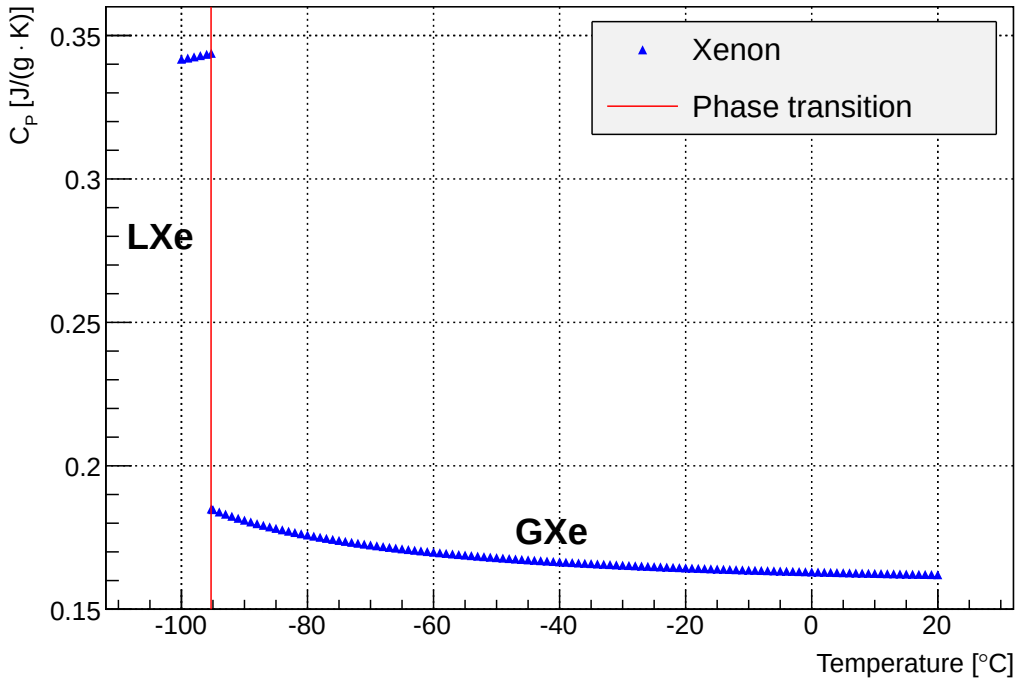

Figure 4.5: **Specific heat capacity of xenon.** This plot shows the specific heat capacity of xenon at constant pressure of 2 bar, which is needed for the calculation of the required cooling power. The data is taken from [Nis14a].

liquid distribution inside the package material. This is of crucial importance especially for long package tubes. It has been decided to use stainless steel, structured package material (Sulzer, type EX) for the XENON1T column, which has the advantage that the streaming liquid is guided due to the geometry of the package. As consequence, the danger of collecting liquid droplets due to blocking is minimized (as it can happen in unstructured packing material) but still a certain hold-up of the liquid is achieved. The manufacturer quotes a high separation efficiency in combination with a low pressure drop. Furthermore, it is available for small diameters (d_p), which is related to small gas load of a laboratory column, compared to industrial facilities. The package material, that is used, is produced in cylindrical shaped segments of ≈ 40 mm diameter and a length of 55 mm (see figure 4.6).

The load of the package tube is of crucial importance for the diameter and also for the operation of the column. The comparison of the liquid velocity to the gas velocity defines the operation regime. The flood point is the upper load limit of a package column. The up-streaming xenon with the velocity u_G is influencing the liquid, rinsed down along the package material with the velocity u_L. For a certain-gas velocity u_G, the liquid is hindered from streaming down anymore ($u_L \rightarrow 0$) and is collected in the package, prohibiting the rectification process. The flood-point can be determined experimentally by measuring the differential pressure along the package tube for different gas velocities u_G. The latter one can be controlled by the applied heating power in the reboiler. It is recommended to work

close below the flood point to achieve the optimal mass transfer.

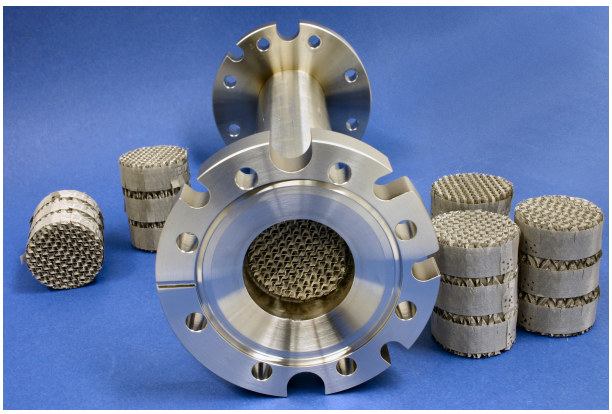

Figure 4.6: **Package material and tubing.** The stainless steel package material (type EX, Sulzer) is delivered in cylindrical segments of 55 mm length and a diameter of 40 mm. They are mounted in series inside a stainless steel tube, where the distillation process takes place [Ros14b].

The conversion from the number of theoretical stages into the amount of package material is done by the so called HETP-value, the height equivalent of one theoretical plate. This value has to be determined experimentally and strongly depends on the structure of the package as well as on the chemical properties of the components in the mixture and also on the operating conditions. The company Sulzer specifies a HETP of 30 mm (tested with standard non-xenon mixtures), which would lead to total column height of $\approx$30 cm, expecting 10 theoretical stages. The experience with the column at the XENON100 experiment, using a similar package material (Sulzer, type DX [Abe09]), showed that these HETP values are to small and not matching for xenon with trace amounts of krypton. Hence, more package material is needed to achieve the designated separation efficiency, but the total amount is unknown, due to the uncertainty of the HETP value. To investigate the separation efficiency for this special application in more detailed, it has been decided to construct a column with $\approx$1 m package material and to test its separation performance (Phase-1). In a second step an upgrade of the system to fulfill the XENON1T requirements can be done (Phase-2). The usage of a small amount of package material in the Phase-1 column allows for faster thermodynamic stabilization, to perform different studies of the characteristics on a shorter time-scale. Any possible upgrade to Phase-2 just requires to enhance the amount of package material, while the other components, e.g. reboiler and condensing stations, are supposed to be further used.

4.5 Design of the Phase-1 column

The column is designed, following the standard descriptions for these kind of systems, presented in literature [Loh07] and [McC05]. In addition, high purity requirements and leak tightness, usually associated to ultra-high vacuum systems have been adopted in order to avoid any influence on the distillation process and to achieve the required purity level

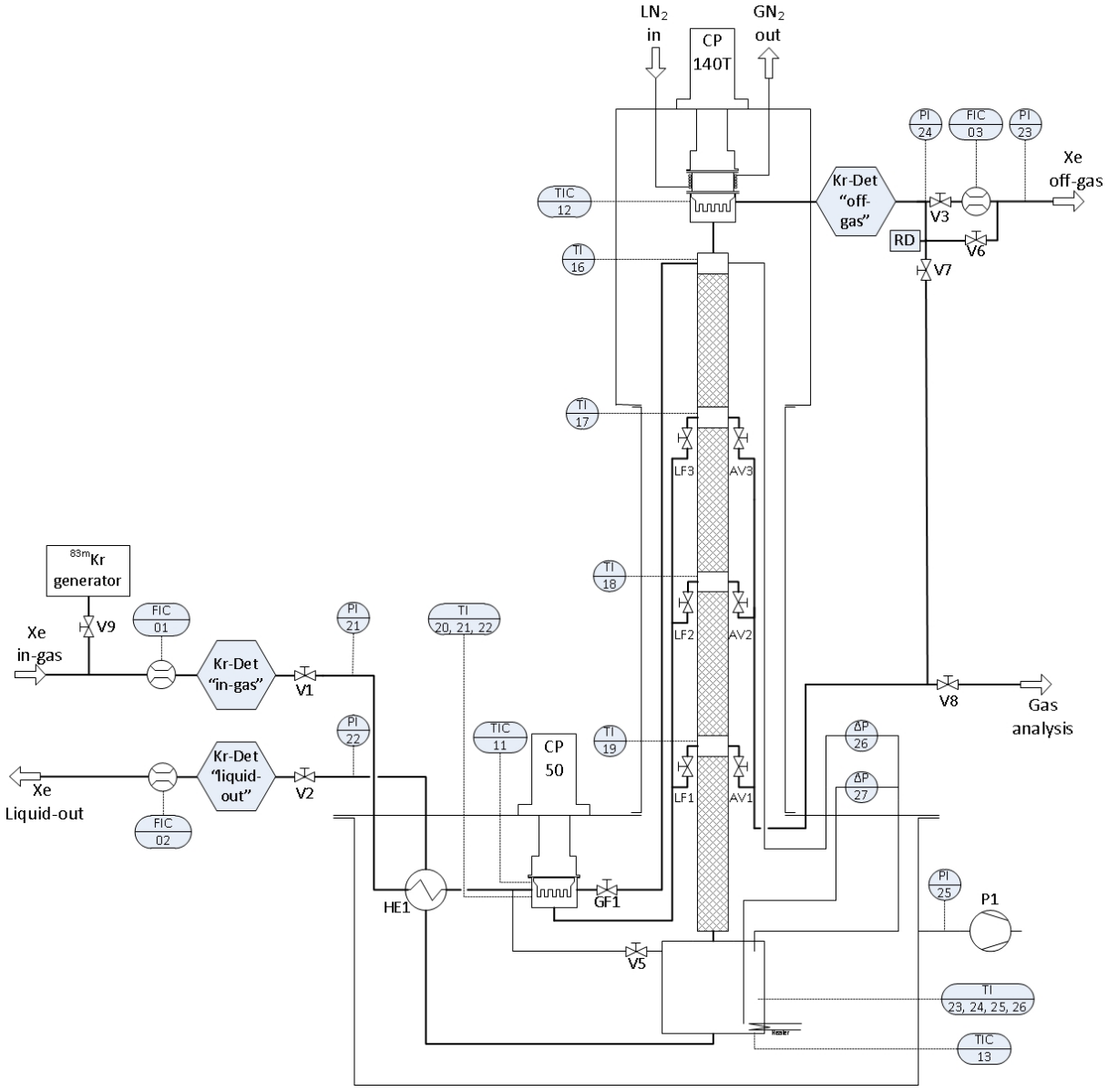

Figure 4.7: **Flowchart of the Phase-1 column.** The pictures shows the gas routing and the key components of the distillation column. The incoming xenon is liquefied in the first condensing station and injected to the package tube, where the distillation takes place. The whole setup is mounted in a vacuum insulation vessel.

[Ros14b]. The system has been designed in close collaboration with Dr. Ion Cristescu from the Tritium Laboratory Karlsruhe at the KIT, who is responsible for the cryogenic distillation at the ITER fusion project. Dr Cristescus long-year experience in cryogenic distillation and his advices were of crucial importance for the different phases of the project.

In figure 4.7 the flow chart of the system is shown. The incoming xenon is passing a heat exchanger (HE1) before it enters a condensing chamber, where the first liquefaction takes

place. The in-gas flow is regulated with a flow controller (MKS, 1479B, labeled FIC01[10]), rated for a maximum flow of 20 slpm and the pressure is measured with a capacitive manometer (Swagelok, PTU-S-AC9-31AD, labeled PI21[11]). The condensing chamber is made from

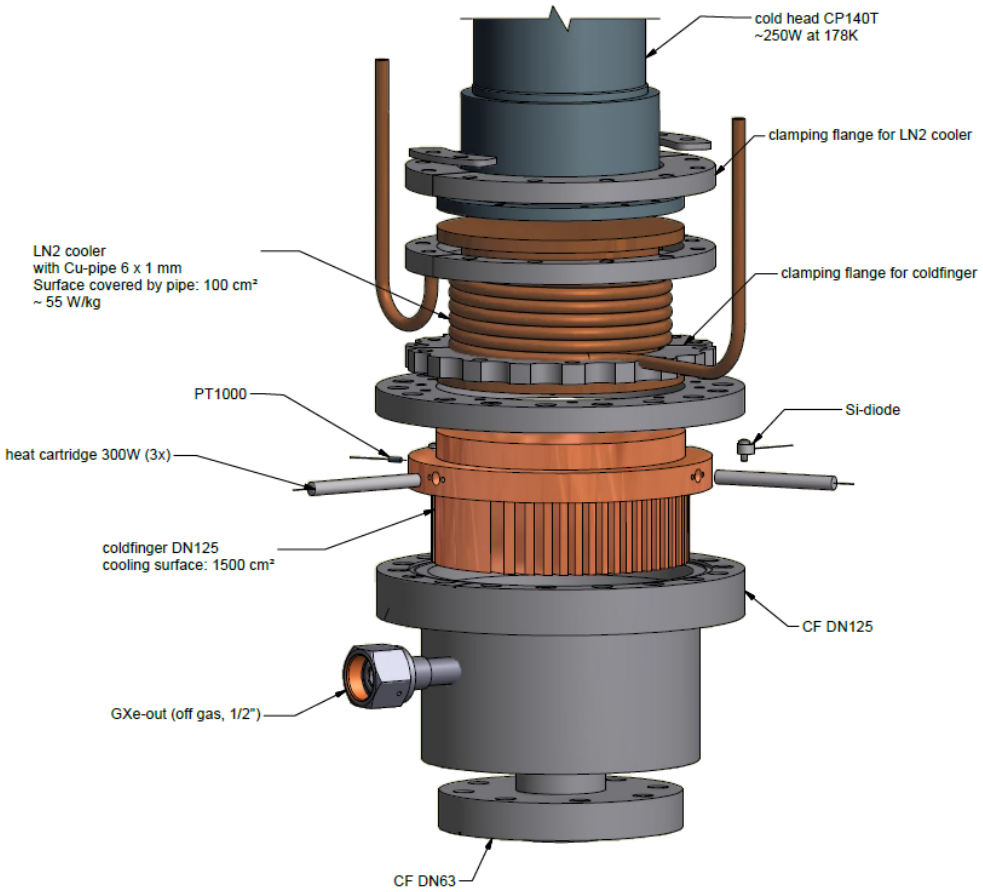

Figure 4.8: **Schematic drawing of the top condensing station.** The CAD drawing shows to design of the top condensing station, which consists of a copper cooling block, connected to a cryo cooler and a collection vessel made from stainless steel.

a stainless steel vessel (316L) and a copper block (OFHC), where cooling fins have been milled to the copper to provide a large surface area for the liquefaction of the xenon (see figure4.8). Additionally, the copper itself is also used as gasket to seal the vessel (compare figure 6.2). This condenser station is connected by dedicated clamping flanges to a cryo-cooler (Oerlikon-Leybold Vacuum, type CP50), that provides ≈ 100 W of cooling power at -98°C, in accordance to the required initial cooling power, calculated beforehand (see chapter 4.3). The temperature is measured with a silicon diode (TIC11[12]) and kept constant by a heater cartridge connected to a temperature controller (Lakeshore, model 336). Two outgoing lines of quarter inch diameter are welded to the vessel which allow to extract the xenon. While

[10]FIC stands for flow index control, indicating a flow read-out in combination with an active control of the process variable.

[11]PI stands for pressure index, denotes a pressure read-out

[12]TIC stands for temperature index control, which is not only a temperature read-out, but also a control variable for the distillation process.

one is located at the bottom of the reservoir and allows for collecting the liquid, the other line is located at the top of the vessel and is foreseen to extract gaseous xenon above the liquid surface. The liquid line is connected to the package tube at three different positions, using custom cold valves (labeled LF1 to LF3, see chapter 7.1), in order to control the flow into the package at different heights. The package tube is made from a stainless steel tube with an inner diameter of $\approx 45\,\mathrm{mm}$ containing the package material. It is segmented in four pieces, where each piece is of 27.5 cm length, containing 5 pieces of package material. Hence, the Phase-1 column contains 110 cm package material.

In the top, the package tube is connected to the condensing station (see figure 4.8) which is constructed very similar to the first one, but with larger diameter and equipped with a much stronger cryo cooler (Oerlikon-Leybold Vacuum, CP140MT), providing $\approx 250\,\mathrm{W}$ of cooling power at -98°C according to the manufacturer. Furthermore, the top condensing station is equipped with an extra copper block, which allows to use liquid nitrogen cooling to enhance the cooling power in additionally. The xenon gets liquefied and the krypton enriched off-gas is extracted. At the bottom, the package tube is mounted to the reboiler, which is connected with four threaded rods to the insulating vacuum vessel, supporting the load of the structure. The reboiler is made from a cylindrical vessel with 250 mm inner diameter, also sealed with copper gaskets (CF) and equipped with four cartridge heaters of 150 W each, to provide the required heating power. During normal operation it is foreseen, that two cartridges are connected to the power source while the other two are turned off in order to have a redundant system. The purified liquid xenon is extracted as liquid from the reboiler and evaporated in the heat exchanger. This allows to cool down the incoming xenon and to achieve higher efficiency in the performance of the system.

The CAD drawing of the complete setup is shown in figure 4.9. All the inner parts are made from electro-polished stainless steel or copper and sealed with metal gaskets (VCR and Conflat) or by orbital welding technique. As already mentioned before, the construction fulfills ultra-high vacuum standards in order to avoid any contamination with ambient air and to guarantee clean process conditions. hence, the package tube is equipped with a heating tape which allows to bake the inner part of the system. The outer vacuum vessel, made from stainless steel, is sealed with elastomer gaskets and is laid-out for a vacuum of the order $10^{-5}\,\mathrm{mbar}$, produced by a pumping station of turbo-pump (Oerlikon-Leybold Vacuum, Turbovac 361) and a rotary vane pump (Oerlikon-Leybold Vacuum, Trivac D16B) to procure a good thermal insulation.

In order to understand the processes inside the column, the setup is equipped with several temperature- and pressure sensors (labeled as TIx, PIx and ΔPIx), that are read-out with a Labview-based control system, which will be introduced in chapter 7.

For characterizing the separation performance, the column is equipped with several ports to extract gas samples. Each feeding port is equipped with an extraction port (AV1 to AV3), which can be closed using a custom cold valve of the same type than used for the liquid feeding ports. Additional ports have been implemented to the in-gas, the liquid-out and the off-gas lines. Furthermore two methods have been developed at IKP, Münster, allowing to determine the separation characteristics. These methods will be described in the following chapter.

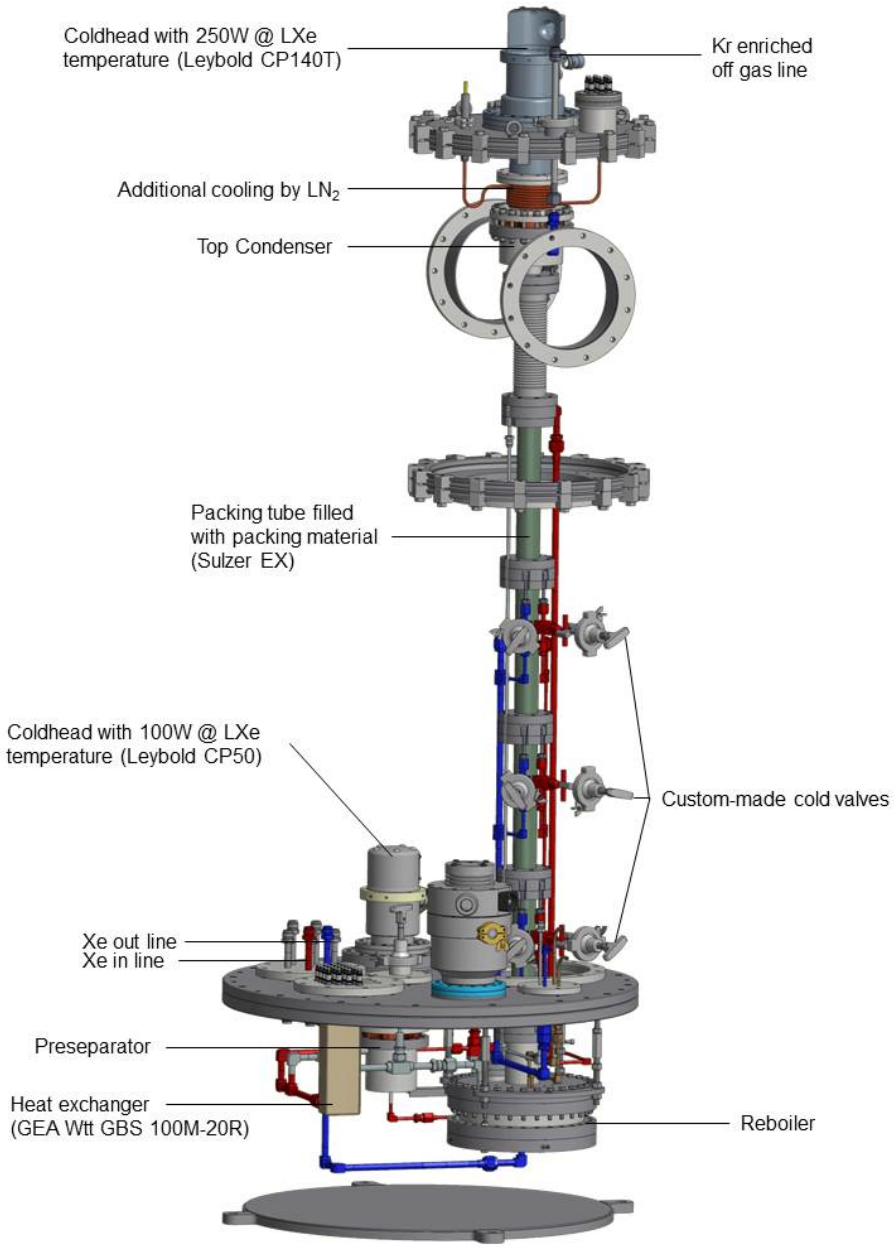

Figure 4.9: **CAD drawing of the Phase-1 distillation column.** The picture shows the technical design of the Phase-1 column without the vacuum insulation vessel, which has been partly removed, in order to give a look at the inner components and their arrangement. The segmented package tube is connected in the bottom to the reboiler and in the top to the condensing station. The drawing has been provided by Dipl.-Ing. Christian Huhmann.

Diagnostics for measuring the distillation performance of the Phase-1 system 5

For the determination of the separation efficiency, different techniques are developed in the XENON collaboration. Two techniques have been set-up in Münster, which will be presented here. A residual gas analyzer based on a quadrupole mass-filter with a cold-trap enhanced sensitivity is used to measure the krypton concentration at the different locations of the system. The setup is explained in section 5.1. An other approach is to use a radioactive krypton isotope as a tracer and to detect its decay. This technique can be used to study the distillation performance on the sub-ppt scale, since we only dope the xenon with tiny amounts of radioactive krypton. This technique is explained in more detail in section 5.2 before separation tests of a single stage distillation system are presented in chapter 6. The different approaches have the following characteristics:

RGA-system with cold-trap

1. The RGA system measures the krypton content of the most abundant isotopes ^{84}Kr, ^{86}Kr, ^{82}Kr, ^{83}Kr and ^{80}Kr, which allows to determine the absolute concentration after calibration of the system.
2. One measurement cycle takes about 30-45 minutes. Only one sample is measured at a time (no dynamic observation of the system).
3. The RGA system consumes tiny amounts of xenon for the measurement (no performance without loss).

^{83m}Kr tracer method

1. ^{83m}Kr tracer method allows the detection of the radioactive decay with custom-made detectors.
2. The usage of several detectors at different locations, allows for simultaneous measurement at different locations.
3. Since one measures decay rates continuously, it is further possible to perform dynamic studies of he system.
4. No determination of absolute krypton concentration.

5. Loss-free performance, without contaminating the xenon with long-lived radioactive isotopes.

As one can see, both methods are complementary, covering absolute concentration determination and dynamic observations. In addition to the methods, developed in Münster, two other techniques have been introduced by collaboration partners. A RGMS system, developed at Max Planck Institut für Kernphysik in Heidelberg and the ATTA system, designed at the Columbia University, USA. Both systems are designed to measure absolute krypton concentrations to the sub-ppt level.

The RGMS system has also been used to measure the separation efficiency the Phase-1 column, which is one of the crucial parameters. The system is introduced within this chapter (see section 7.6.2), while the measurements and results of the Phase-1 column will be explained in chapter 7.6. The ATTA system has not been used for the characterization of the distillation column so far, but is an important tool for upcoming performance tests. Hence, the working principle is only briefly introduced: The ATTA system allows to count single krypton atoms for the determination of the concentration. The injected gas is excited to meta-stable atoms $^{84}Kr^*$ through a RF discharge and after laser-cooling in a Zeeman-slower, the excited atoms are trapped in a magneto-optical trap. The fluorescence light, measured with an avalanche photo diode, is related to the number of $^{84}Kr^*$ in the gas sample. Further information about the system are presented in [Apr13d].

5.1 Measurement of natural krypton in xenon, using a sensitivity enhanced residual gas analyzer

This technique has been developed over the last years as topic of different Bachelor- Master- and Diploma theses [Ket12], [Sch12] and [Fie14]. Furthermore, it has been publicized in [Bro13]. Within this thesis, the design and the construction of two different systems (called RGA-1 and RGA-2) were supported, which are briefly introduced in the following.

Commercial available RGA systems are widely used to measure concentrations down to the ppm level. For the sub-ppb level or even lower concentrations (sub-ppt, as required for XENON1T) the sensitivity of the single devices is not sufficient. To enhance the sensitivity of a commercial residual gas analyzer based on a quadrupole mass filter, a liquid nitrogen cooled cold-trap can be used. This technique was originally presented in [Leo10] for the detection of nitrogen, oxygen and methane and later adopted for krypton in xenon [Dob11]. In contrary to the work presented by Leonard and Dobi et al., our system has been modified to use only a small and restricted gas volume instead of a steady high flow rate. One system has been set-up directly connected to the gas purification system (RGA-1). In addition, a second portable version for the usage at the XENON100 and XENON1T experiment has been constructed (RGA-2). Both systems are based on the same principles and they only differ in small technical details. Finally, both the RGA-1 and the RGA-2 system have been used to determine the separation performance of the column as it will be presented in chapter 7.6.

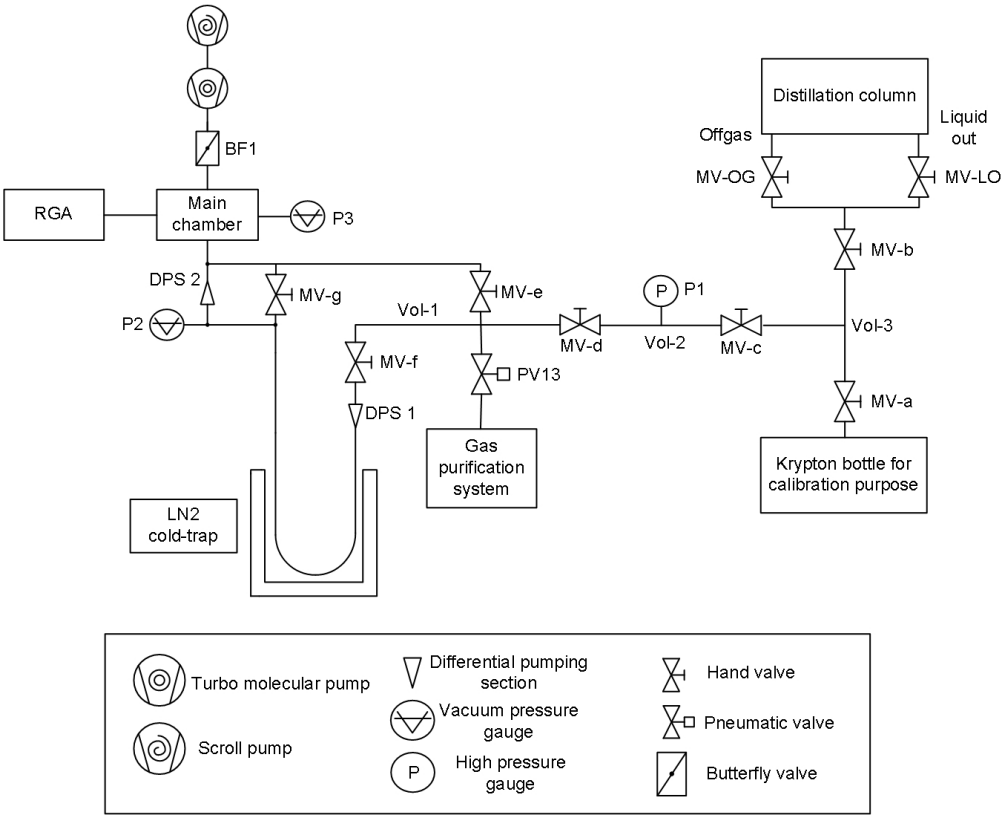

Figure 5.1: **Flowchart of the RGA-1 system.** This scheme shows the gas routing of the RGA-1 system, designed to measure trace amounts of krypton in xenon and its connection to the gas purification system and the distillation column. The gas is routed through two differential pumping sections (DPS1 and DPS2) and a liquid nitrogen cold-trap into the analyzing chamber which is equipped with a RGA. A butterfly valve (BF1) to the turbo-molecular pump allows to reduce the pumping speed. The scheme is similar to the one presented in [Bro13], but with several extensions.

In order to measure low concentrations of krypton in the dominant carrier gas xenon, an enhancement of the tracer component has to be performed beforehand. The enrichment of the krypton related to the xenon in a sample allows to measure the trace impurities with commercial mass filters. Due to this enhancement, a higher sensitivity can be achieved. The basic principle of the technique is given by the vapor pressures of krypton and xenon at liquid nitrogen temperature (see figure 4.1). While xenon has a vapor pressure of about $P^0_{Xe,LN_2} \approx 2.4{\cdot}10^{-3}$ mbar [Leo10] at liquid nitrogen temperature ($-196°$C), the vapor pressure of krypton is $P^0_{Kr,LN_2} \approx 2.0$ mbar at that temperature, being about three orders of magnitude higher. In a xenon sample of 1 bar, the partial pressure for a certain concentration, e.g. ^{nat}Kr/Xe = 1 ppb, can be calculated with Daltons law to $p_{Kr} \approx 1 \cdot 10^{-6}$ mbar $<< P^0_{Kr,LN_2}$. Therefore, after the injection of the sample gas into the cold-trap, the xenon is frozen out down to the vapor pressure while the krypton is staying in the gas phase unaffected and is enriched above the solid xenon phase.

The flowchart of the RGA-1 is shown in figure 5.1. The system has been mounted as inherent

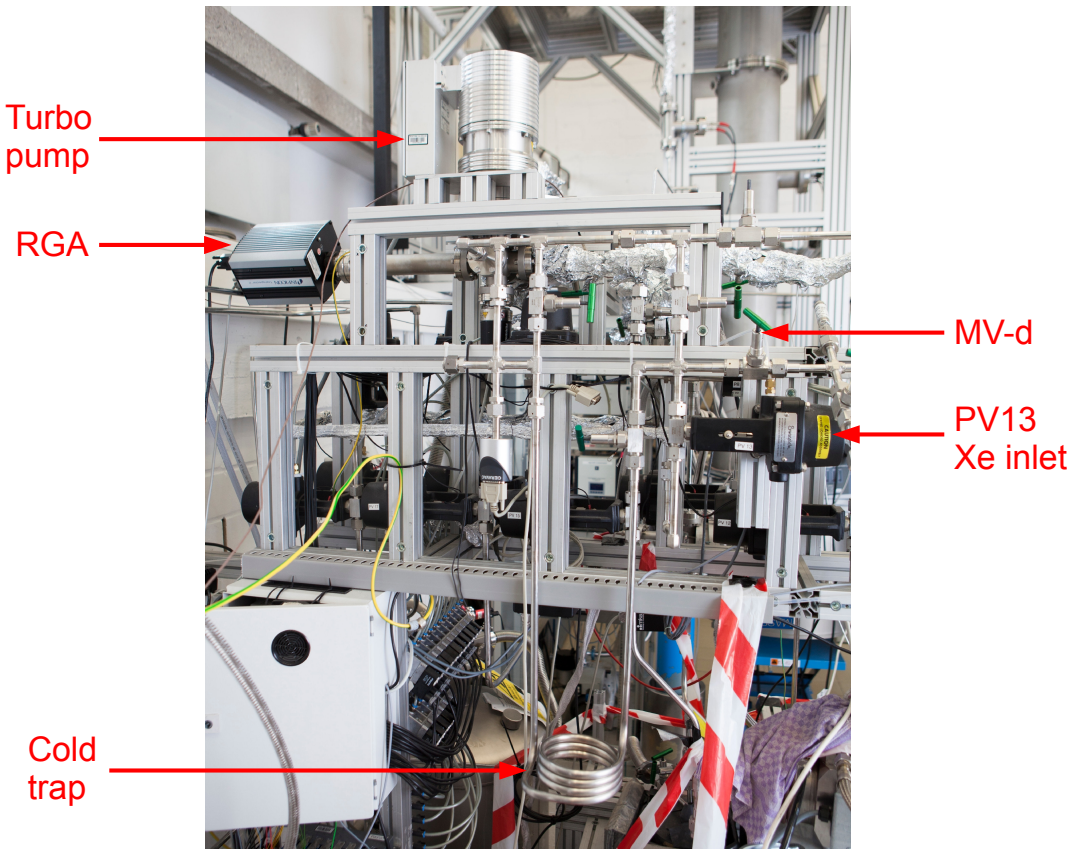

Figure 5.2: **RGA-1 system mounted to the gas purification system.** The RGA-1 system with cold-trap, measurement chamber and RGA is inherent part of the gas purification system, connected via PV13. But it is also connected to the distillation column via MV-d.

part of the gas purification system, which has been shown already in figure 3.1. The xenon is transfered into a sample volume (Vol-1) of a fixed size by opening PV13. The sample is expanded to Vol-2 by opening of MV-d, which is of rather similar size and equipped with a pressure gauge, in order to measure the pressure drop during the measurement to apply flow corrections in the analysis of the data. The sample is than passed through MV-f and the first differential pumping section (DPS1) to reduce the pressure before it enters the cold-trap. The DPS1 is made out of a capillary with 0.1 mm diameter and a length of 10 mm, laser-welded to a VCR gasket (see figure 5.3, right one). The cold-trap is a stainless-steel coil, made from a half-inch, electro-polished tube, which is connected with VCR connectors to the system. It is cooled down by immersing the coil into a dewar filled with liquid nitrogen.

The krypton enriched gas, after freezing out a substantial part of the xenon, is passing the second differential pumping section (DPS2) into the main chamber, where the sample is analyzed with the RGA (Transpector-2, H200M, Inficon). The chamber is pumped with an oil-free vacuum pumping station, consisting of a magnetic bearing turbo-molecular pump (MAG 300iP, Oerlikon-Leybold Vacuum) and an oil-free fore-pump (Scrollvac SC15D, Oerlikon-Leybold Vacuum).

Figure 5.3: **Differential pumping sections DPS1 and DPS2.** This picture shows the two differential pumping sections. The DPS1 (right one) is made out of a stainless steel capillary of 0.1 mm diameter welded into a VCR gasket, while the DPS2 (left one) is a piece of steel with a hole of 0.5 mm welded to the gasket.

A key feature of this setup is a custom-made butterfly-valve (BF1) between the main chamber and the turbo-pump (see figure 5.4), which allows to reduce the effective pumping speed S_{eff} of the pump to enhance the pressure inside the chamber to a value still feasible for the RGA. Due to this reduction of the pumping speed, the sensitivity of the setup increases, since the amount of krypton atoms in the analyzing chamber is increased.

The RGA-1 system is part of the gas system, but also connected to the liquid-out line and the off-gas line of the distillation column to measure the krypton concentration in the both outlets, while the in-gas is measured over PV13 (compare figure 5.1). The RGA-1 system is meant to determine directly the separation performance of the column. The RGA-2 system is connected to the analysis line of the distillation column via V8 (compare figure 4.7). Hence, it is used for measuring the concentration profile along the column and can also be used to measure the off-gas.

For the calibration of the system a dedicated procedure has been developed, which is based on mixing and dilution of xenon with natural krypton to produce different concentrations (see [Fie14]). Therefore a gas bottle, filled with krypton can also be connected to Vol-3. The analysis of the data is briefly reviewed, (based on [Fie14]) in chapter 7.6, introducing also the measurements at the Phase-1 column.

The RGA-2 system (see figure 5.5) has been designed for the usage at the XENON100 and XENON1T experiment and is a portable version of the RGA-1 system, but with some additional features. Beside additional blind-ports for the connection of additional components (Pipettes) and additional shutter valves to improve the cleanliness of the system during idle states, the technical realization of the butterfly valve slightly changed. As shown in figure 5.4, the butterfly of the RGA-1 is of ≈ 40 mm diameter, mounted to a CF-100 distance flange. The butterfly valve of the RGA-2 setup is of ≈ 100 mm diameter, mounted directly inside a custom made vacuum chamber. This design change was motivated to increase the effective pumping speed, in order to reduce the background before the measurement started. Finally, a third orifice which bypasses the cold-trap has been foreseen, which allows to run the system without cold-trap, just as a standard gas analyzing system, without enhanced sensitivity. This is important for investigation of other components inside the xenon that

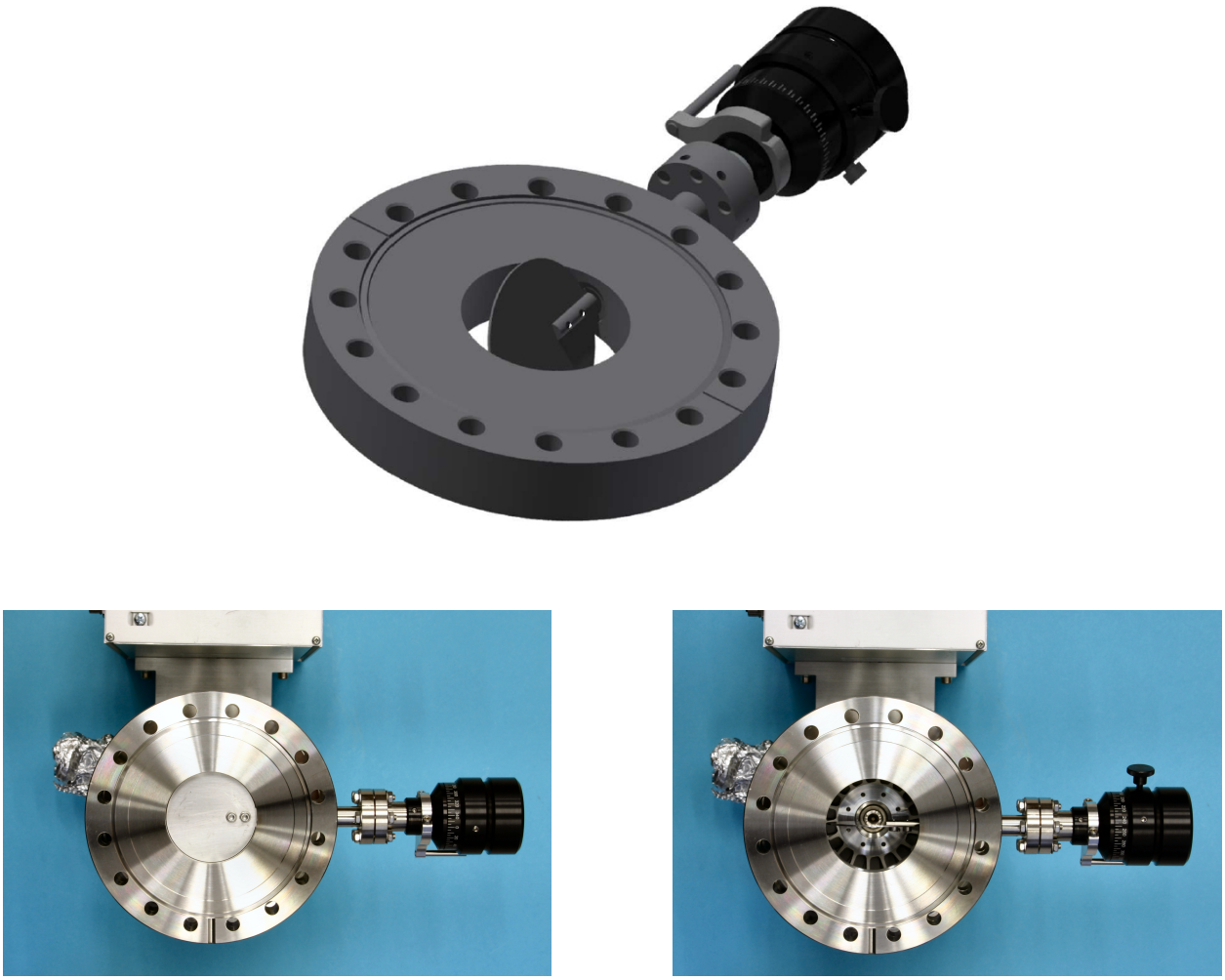

Figure 5.4: **Custom-made butterfly valve.** Top: CAD drawing of the butterfly valve, mounted to a CF-100 flange. Bottom right: Butterfly valve attached to the turbo-pump with orifice open. Upper left: Butterfly valve attached to the turbo-pump with orifice closed. The rotating vacuum feed-through with scale allows to reproduce the position of the valve.

are also freezing out in the cold-trap, but is still under investigation and has not been used in this work. Naturally, a calibration has been performed using the same technique than for the calibration of the RGA-1 system. The results, together with the detailed design are also presented in [Fie14].

5.2 A radioactive ^{83m}Kr tracer method

The method of using radioactive elements as tracer is widely applied in medical imaging, e.g. in positron emission tomography (PET). It allows to study biochemical processes inside the living organism and is therefore, called functional imaging. Transferring this principle

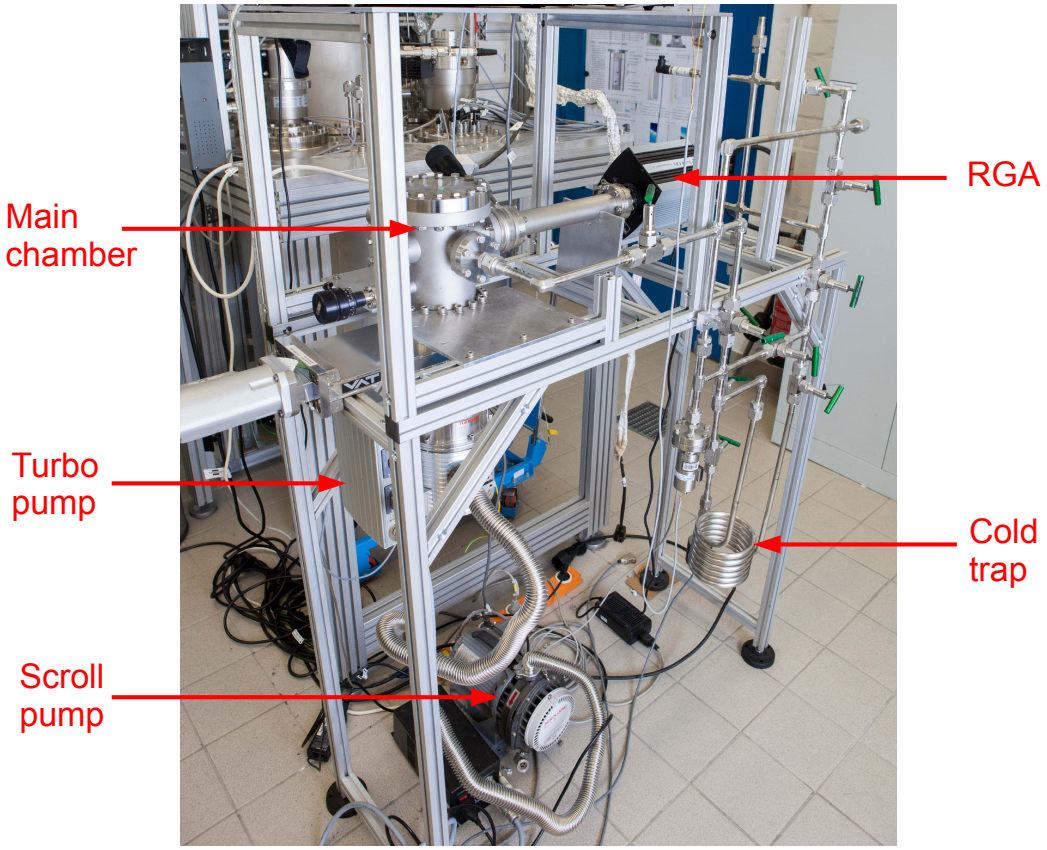

Figure 5.5: **RGA-2 system mounted to the distillation column.** This picture shows the portable RGA-2 setup, used for the measurements of the concentration profile along the Phase-1 column. The key components are the RGA, connected with the main chamber with the butterfly valve inside and the LN_2 cold-trap. The camber is pumped with a dry turbo-molecular pumping station, while the xenon can be injected via the cold-trap before it is analyzed.

to the investigation of separation performance, by using a radioactive krypton tracer, might allow to study the dynamics of the separation process. The radioactive krypton isotope, that will be used in the further investigations is ^{83m}Kr. The development of the mixing and the detection of ^{83m}Kr in xenon, explained in this thesis has been published with other coauthors in Journal of Instrumentation (JINST) [Ros14a] with the author of this PhD thesis as first and corresponding author. This sub-chapter 5.2 of the PhD thesis was also used as the first draft for the publication in JINST, which is in full agreement with the copyright rules of JINST. Therefore there are quite some similarities between the text of this sub-chapter of this thesis and the publication. The corresponding plots, of which some are made by coauthors are cited from the JINST publication.

The number of applications of the isomer ^{83m}Kr , produced by the decay of ^{83}Rb ($T_{1/2}$ = 86.2 d) via electron capture (see [Nuc14]), in nuclear, particle and astro-particle physics has increased in recent years. Since it produces mono-energetic conversion electrons from the highly converted gamma transitions of $E_{\gamma,1} = 32.2\,\text{keV}$ and $E_{\gamma,2} = 9.4\,\text{keV}$, it has been used as a calibration source in neutrino mass experiments at Los Alamos, Mainz, Troitsk [Rob91],

[Pic92] ,[Bor03], [Ase00] and in KATRIN [Kat04], [Zbo13], [Erh14]. The isomer ^{83m}Kr has been applied for the calibration of the time projection chamber (TPC) of the ALICE detector at CERN, which is the world largest TPC with a volume of about 90 m^3 [Alm10]. The first studies also demonstrated excellent suitability of ^{83m}Kr for single-phase and dual-phase xenon detectors [Kas09], [Man10]. ^{83m}Kr does not contaminate low-background detectors, since it has short half-life ($T_{1/2}$ = 1.83 h) and decays into the stable ground state ^{83}Kr. Furthermore, the time behavior for the mixing of ^{83m}Kr into a liquid xenon TPC has been investigated in [Kas10] and shows efficient distribution inside the detector volume. It has been, therefore, introduced as an internal calibration source in direct dark matter experiments using liquid noble gases (e.g. LUX [Ade14], DarkSide-50 [Ale13]) and it is planned as a calibration source for XENON1T [Apr12b].

Another ^{83m}Kr application as a tracer in xenon gas is presented in the following: Emanating from a ^{83}Rb generator, ^{83m}Kr is mixed into xenon gas. The ^{83m}Kr decay in the xenon gas is detected with a simple detector system measuring the xenon scintillation light with a photomultiplier tube (PMT). As already mentioned before, standard analytic techniques to measure the concentration of krypton in xenon are not suitable for dynamic studies of distillation systems, since they are not rapid enough due to time required for both sample preparation and analysis itself, what makes continuous monitoring of operation very difficult. We, therefore, developed a method of doping the gas with trace amounts of radioactive ^{83m}Kr and measured its decay using photomultiplier tubes with quartz windows and a special bi-alkali photo-cathode optimized for the scintillation light from gaseous xenon at 171 nm [Tak83]. Our measuring procedure should also be feasible for other noble gases like argon or neon, however, introducing wavelength shifters or specialized photomultipliers will be necessary.

In the following sections, the ^{83m}Kr-mixing method and the detector setup to measure the ^{83m}Kr-decay rate in xenon gas is introduced, before the working principle is demonstrated by the characterization of a xenon gas system. In section 6, the mixing and detection technique is applied to study the efficiency of a single stage cryogenic distillation system for removal of krypton from xenon. Finally, the technique is used in chapter 7.6 to investigate the performance of the Phase-1 column.

5.2.1 ^{83m}Kr decay

The isomeric state ^{83m}Kr at an excitation energy of 41.534 keV is populated by the electron capture of ^{83}Rb with a branching ratio of 77.9 %, from which it decays to the ground state of ^{83}Kr by two highly converted transitions. The intermediate state at 9.4058 keV has a very short half-life of 154.4 ns. Therefore, the half-life of 1.83 h of the isomeric state governs decay kinetics. Figure 5.6 displays the decay scheme. Significant advantage of using ^{83m}Kr is that the half-life of 1.83 hours is short enough to produce a rather high signal rate in the decay detectors, as well as still long enough for ^{83m}Kr distribution inside of gas and distillation systems. Furthermore, this isomer decays solely via isomeric transition to its stable ground state ^{83}Kr, so there is no risk of contamination of xenon with long-lived decay products. The only potential risk of radioactive contamination represents the mother nuclide ^{83}Rb with half-life of 86. 2 d, however, this contamination can be efficiently prevented (see below).

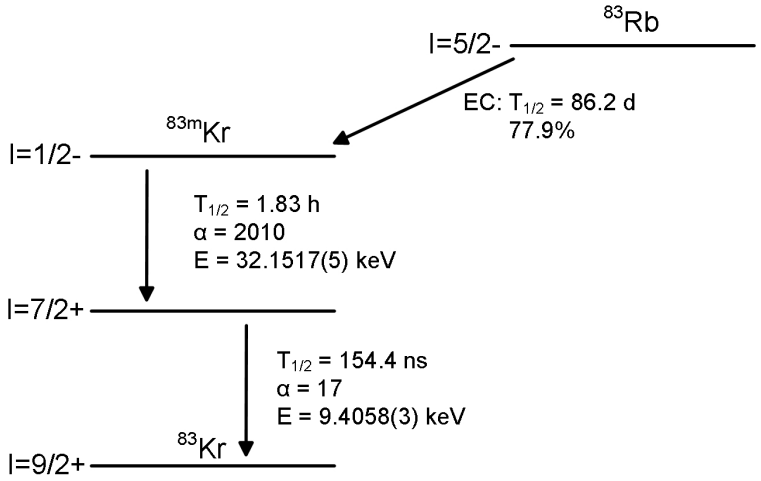

Figure 5.6: **Decay scheme of ^{83}Rb to ^{83}Kr.** The simplified decay scheme of ^{83}Rb to ^{83m}Kr, which further decays via two highly converted transitions (total conversion coefficients $\alpha = 2010$ and $\alpha = 17$ respectively) into the stable ^{83}Kr. The scheme is based on [Nuc14], [Ven06] and [Sle12] and published in [Ros14a].

5.2.2 Doping of xenon gas with ^{83m}Kr

The ^{83}Rb was produced at the Nuclear Physics Institute, Academy of Sciences of the Czech Republic, using a cyclotron (U-120M). A pressurized natural krypton gas target at 13 bar is irradiated by a 26 MeV proton beam with an intensity of 15 μA, generating the ^{83}RbȦfterwards, the rubidium isotopes were washed out and finally a fraction of the ^{83}Rb solution with a certain activity was absorbed in zeolite beads of 2 mm diameter having 0.5 nm pores, which were dried for 2 h at 350°C to get rid of the solvent [Ven05].

The structure and ion-exchange properties of the zeolite allow efficient emanation of ^{83m}Kr, while ^{83}Rb is strongly trapped. The possible release of ^{83}Rb from the beads has been investigated in [Han11], but no detectable traces of ^{83}Rb were observed (less than 1 mBq after 2 weeks measurement of a 1.8 MBq source). The ^{83m}Kr generator based on ^{83}Rb adsorbed on zeolite can be, therefore, used in low count rate experiments like XENON100 or KATRIN without the contamination risk. The emanation efficiency of ^{83m}Kr from zeolite depends on time and the environment around the source. A freshly prepared source emanates about 80% of ^{83m}Kr from the ^{83}Rb decay. The emanation efficiency drops to ca 15% within 3-5 days when the source is exposed to air. Inside a vacuum system with a pressure of 10^{-2} mbar or better, the ^{83m}Kr emanation efficiency increases to about 70% and stays constant for more than a week. Since the emanation efficiency has not been investigated in a xenon atmosphere and emanation efficiency of 70% is assumed.

The zeolite beads were placed into a stainless steel container linked by a VCR connector to a xenon gas system. A PTFE membrane filter with a pore size of 220 nm and a grid, closing the stainless steel container, prevent the potential release of zeolite microparticles from entering the system, while allowing easy transport of ^{83m}Kr . The ^{83m}Kr atoms are mixed with the xenon gas by diffusion. When xenon gas is circulating in the system, the ^{83m}Kr atoms follow the circulation as well (see also section 5.2.5).

5.2.3 Detection of the ^{83m}Kr in-gaseous xenon

The radioactive decay of ^{83m}Kr to ^{83}Kr can be detected by the interaction of the decay products (conversion, shake-off and Auger electrons as well as X- and γ-rays) with gaseous xenon that produces scintillation light of 171 nm wavelength (VUV light). The scintillation light in-gaseous xenon is produced by the de-excitation of xenon dimers that are formed by the recombination of an excited xenon atom with another Xe atom in the ground state [Apr10a]. The scintillation light can be detected by photomultiplier tubes (PMTs) with a quartz window and a special bi-alkali photo-cathode adapted to this wavelength. The measured rate is proportional to the ^{83m}Kr density in xenon gas.

Figure 5.7 shows the mass attenuation coefficient of X- and γ-rays and the CSDA range of electrons in-gaseous xenon. For typical energies of up to 30 keV, the range of electrons is less than 1 cm in xenon gas at a pressure of 1 bar and the mean free path of the X- and γ-rays ranges from 20 cm for 30 keV to 1 cm at 10 keV. This defines the necessary size of a ^{83m}Kr decay detector, based on the detection of scintillation light in-gaseous xenon.

5.2.4 The detector design

To detect the scintillation light formed in xenon, a custom detector has been constructed: An 1 inch photomultiplier tube (PMT, type R8520-06-AL, Hamamatsu, Japan) is mounted perpendicularly to a stainless tube of 40 mm diameter to monitor the xenon that passes through the line (see figure 5.8 left). The same type of PMT is also used in the XENON100 experiment and is also designed for the stable operation at liquid xenon temperature. The bialkali photocathode of the PMT provides a quantum efficiency of ≥ 30 % at $\lambda = 178$ nm. A Polytetrafluoroethylene (PTFE) foil inside the stainless steel tube enhances the reflectivity of the walls [Sil10] in order to increase number of scintillation photons detected by the PMT. The PMT is surrounded by a holding structure made out of PTFE to protect the sensitive detector and also to hold it in a defined position. It is attached to a CF-40 flange with threaded rods (see figure 5.8 right). The flange contains two SHV feedthroughs for a high voltage supply to the PMT (+800 V) and for a read out of the PMT signals. The casing of the PMT is at ground potential. The CF-40 flange is then mounted to a CF-40 T-piece on the outgoing line, while xenon can be flushed through the straight end. The detector is connected to the gas system by using half inch VCR connectors.

Our measurements revealed necessity, in order to achieve high light collection efficiency, to clean the xenon gas by a zirconium-based hot getter (type Monotorr, SAES) from impurities that absorb the scintillation light. We continuously run the xenon gas through the getter and gas purity was monitored by measuring xenon humidity with use of a moisture analyzer (type HALO+, Tiger Optics). In order to minimize the impurities that are introduced to the xenon, most of the parts have been cleaned in an ultrasonic bath using an alkaline degreaser (p3-almeco, Henkel) followed by deionized water. The parts that cannot be cleaned in the ultrasonic bath, like cables or bases, have been rinsed with pure ethanol.

The tubing volume, monitored by the PMT, is of cylindrical shape with length of $\approx$10.5 cm. Since the energy is well deposited on short distances, one can estimate the number of scintil-

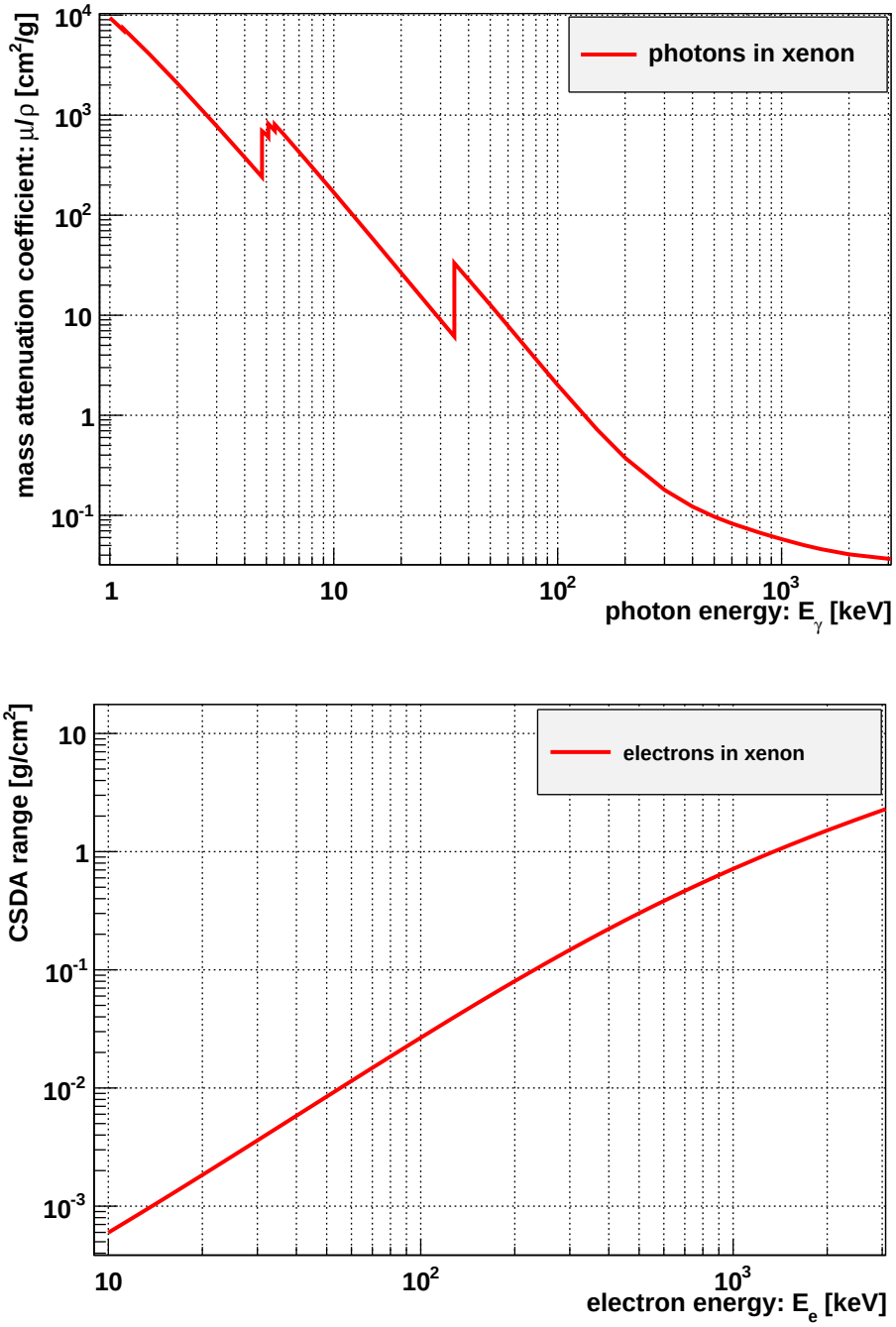

Figure 5.7: **Mass attenuation coefficients of photons and CSDA range of electrons in xenon.** Top: Mass attenuation coefficient μ/ρ for photons with energies up to 3 MeV, taken from [Hub04]. Bottom: CSDA range of electrons in xenon for energies up to 3 MeV, data taken from [Nis14b]. The xenon gas density at room temperature is 5.3 mg/cm^3, while liquid xenon density at T=−100°C and p=1.6 bar is 2.8 g/cm^3. The plots have been presented in [Ros14a] as well.

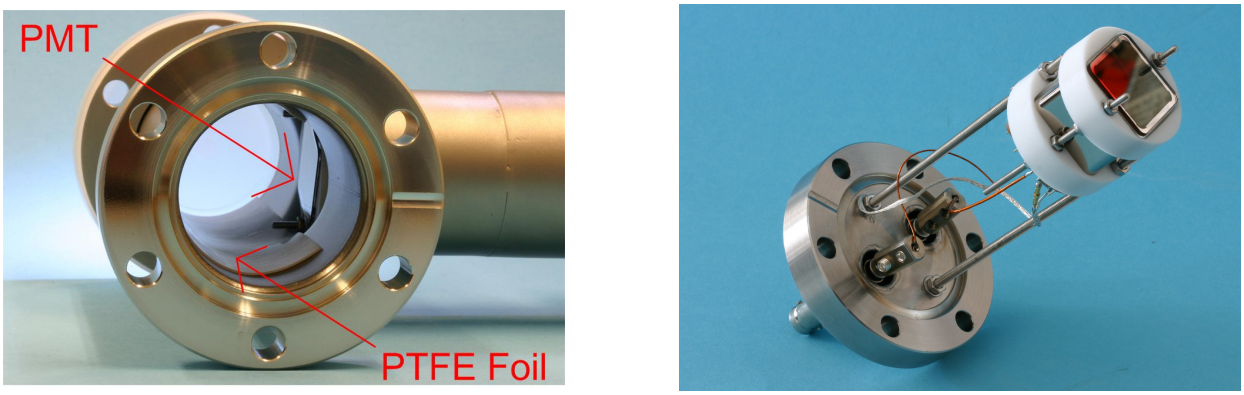

Figure 5.8: **Custom-made ^{83m}Kr decay detector.** Left: PMT mounted inside a CF-40 T-piece and the arrangement of the PTFE reflector foil. Right: PMT mounted on the CF-40 flange with feed-throughs. The mounting of the PMT with the teflon holder to the CF-40 flange is displayed. The flange is equipped with high voltage and signal feed-throughs to operate the PMT. Already shown in [Ros14a].

lation photons produced in xenon due to single ^{83m}Kr decay. The average energy deposition necessary for formation of one electron-ion pair is $W = 22.0\,\text{eV}$ for gaseous xenon [Pla61] and [Apr10a]. The average number of photons N_γ can be estimated as the fraction of deposited energy E_0 and the average energy per electron-ion pair W. For the I=1/2- to I=7/2+ transition with 32.2 keV energy difference, $N_{\gamma,32keV}=E_0/W_{xenon} = 1460$ and for the I=7/2+ to I=9/2+ transition with 9.4 keV, $N_{\gamma,9keV} = 427$. In liquid xenon it has been observed that the number of photons on the latter decay is partly enhanced due to the ionization following the first decay [Apr12c]. About 1900 emitted photons are expected from the sum of the two decays (≈41 keV).

The PMT signals are acquired using an eight channel flash analog to digital converter (FADC) (type SIS3320, Struck Innovative Systeme) without any fast amplifiers (see figure 5.9). The FADC provides a 12 bit resolution and was used with 100 MHz sampling rate. It can be readout by a VME interface connected to the lab PC with a custom acquisition program. For the PMT supply voltage of +800 V a NIM module (type N470, CAEN) was used.

Since scintillation light pulses in xenon are very fast, it is possible to resolve the two transitions in the ^{83m}Kr decay. A typical waveform of a ^{83m}Kr decay event is shown in figure 5.10. The pulse heights of the two transitions are different due to the different energies of the decay steps (see figure 5.6).

5.2.5 Characterizing the mixing of ^{83m}Kr in a xenon gas system

The ^{83}Rb source, emanating ^{83m}Kr, and the ^{83m}Kr decay detector were attached to a xenon gas system, which allowed for circulating the gaseous xenon. The scheme of the setup is shown in figure 5.11. This system has been set up as a demonstrator for a gas distribution and purification system for the dark matter experiment XENON1T.

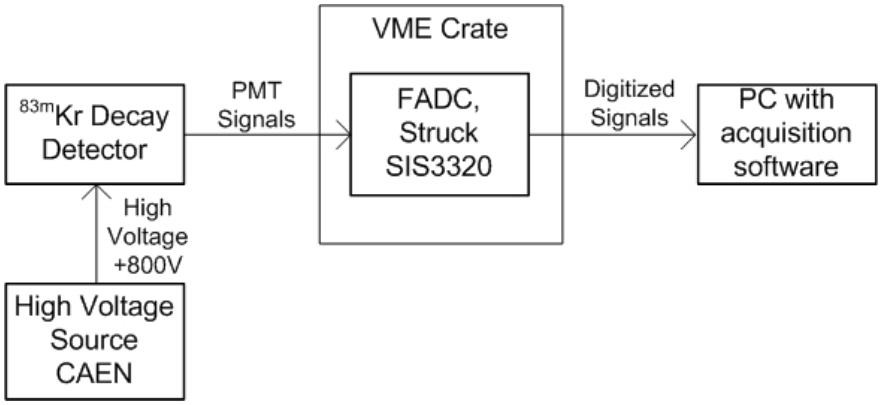

Figure 5.9: **Schematic of the data acquisition system.** The PMT is supplied with high voltage, while the raw signals are acquired with a FADC and processed by a PC using a VME interface to the digitizer. Scheme from [Ros14a].

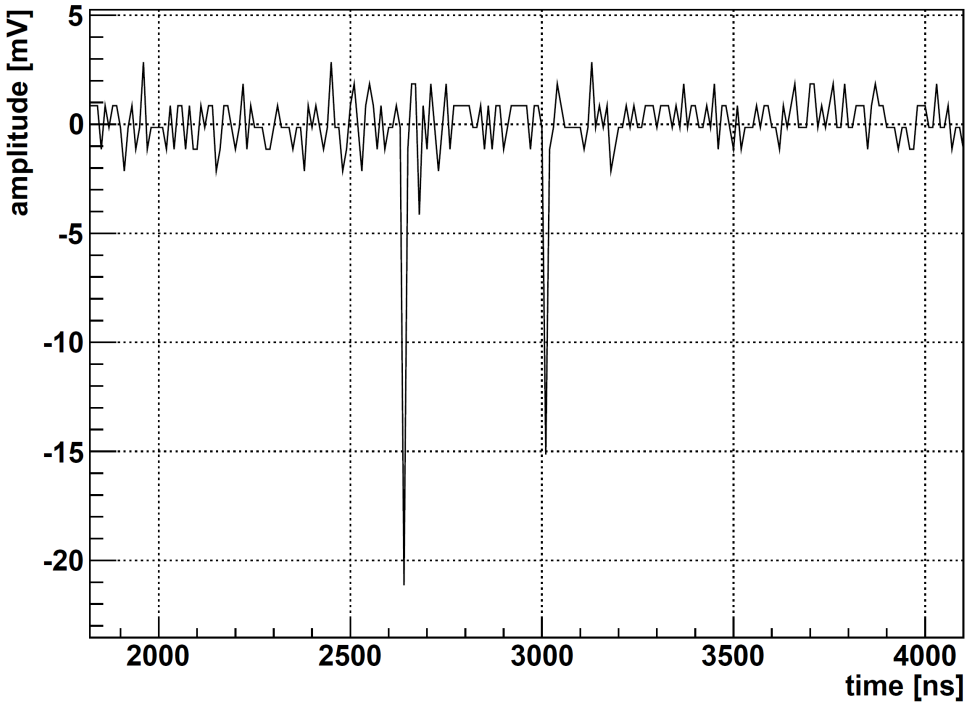

Figure 5.10: **Example of a double coincidence waveform.** This plot shows the waveforms that are acquired with a sampling rate of 100 MHz from the ^{83m}Kr decay detectors. In this waveform, the double coincidence signal represents the two resolved transitions in the ^{83m}Kr decay. Plot taken from [Ros14a].

The gas circulation through electro-polished stainless steel lines of half-inch outer diameter is driven by a membrane pump (type N143AN.12E, KNF) and controlled with a mass flow controller (type 1579A, MKS), calibrated for xenon. The pressure inside the system is measured at several locations by using capacitance manometer (type 121A, MKS). The routing of the gas is controlled with bellow-sealed valves, either remotely controlled, pneu-

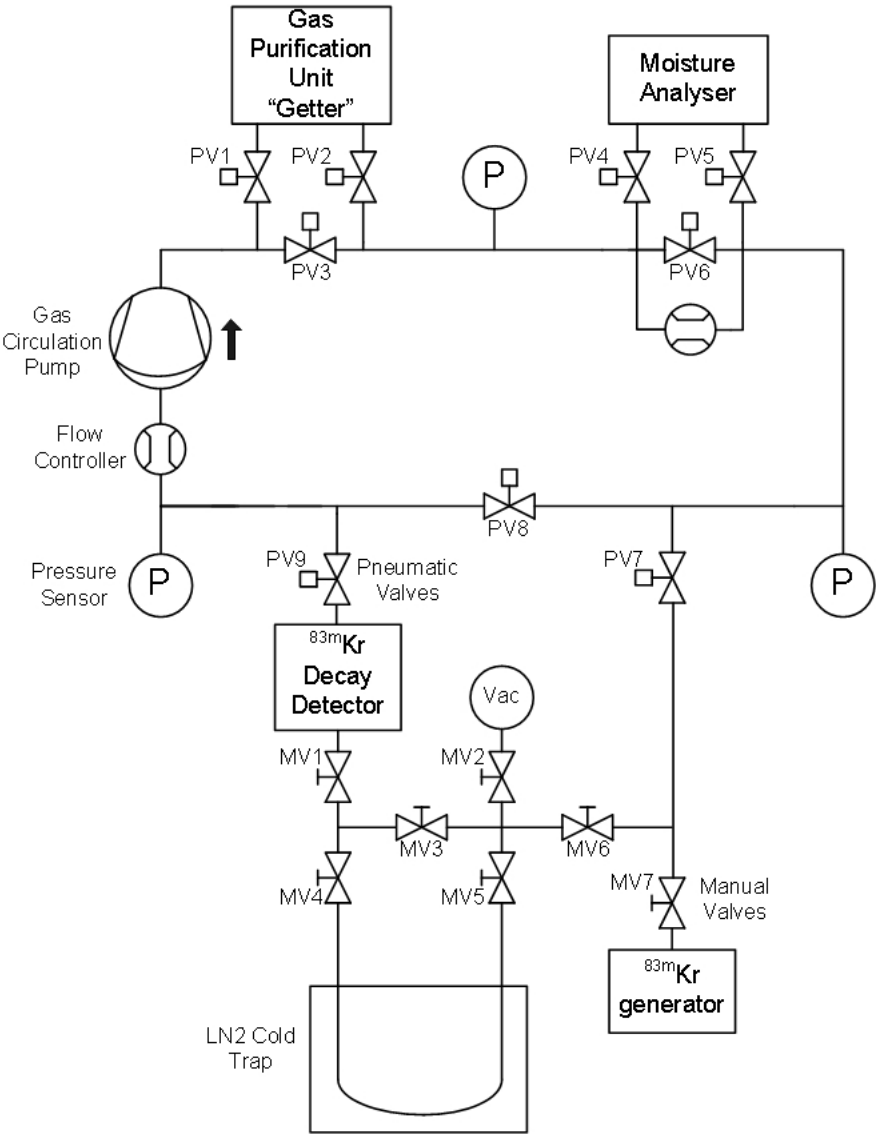

Figure 5.11: **Flowchart of the gas circulation system.** The simplified scheme of the gas circulation system, set up at IKP Münster. For the clear arrangement of the scheme, several additional ports to other subsystems, which have been closed during the measurements, have been neglected. The black arrow indicates the direction of the gas flow. Flowchart taken from [Ros14a].

matic valves (type SS-8BG-VCR-5C, Swagelok, in figure 5.11 denoted by PV1 to PV9) or manually operated valves (type SS-8BG-VCR, Swagelok, in figure 5.11 denoted by MV1 to MV7). The gas can be routed through the getter (PV3 closed, PV1 and PV2 open), while the moisture analyzer is mounted to a bypass after the getter (PV6 closed, PV4 and PV5 open) and allows to measure the fraction of water in xenon down to 200 ppt. Since the device needs a very low flow rate of ≈1 slpm of xenon, compared to the flow rate of 8 slpm during normal operation, the majority of the gas passes the analyzer through the flow controller.

The valves MV3 - MV5 allow the gas routing to the ^{83m}Kr decay detector either directly,

or via a tube, immersed in a liquid nitrogen bath. The latter one can be used to test the temperature dependence of the krypton collection efficiency. The source also has an additional valve (MV7) to separate it completely from the system. This section of the system is also connected to a vacuum pump (Vac) by the valve MV2 which allows for the evacuation of these volumes independently from the rest of the circuit.

The pneumatic valves PV7 and PV9 were closed, while PV8 remained open and xenon was circulating through the closed circuit and the getter. Before the collection was started, the volume above the ^{83}Rb containing zeolite beads was evacuated to $\approx 3{\cdot}10^{-3}$ mbar, by opening MV2-MV6, while MV1 and MV7 remained close. For the collection, MV3-MV6 remained open. MV2 was closed, while MV7 was opened and ^{83m}Kr, emanating from the beads, was collected in the section for 6 hours.

After the collection, the valve to the source MV7 was closed. The pneumatic valves PV7 and PV9 as well as MV1 were opened and PV8 was closed. The ^{83m}Kr then mixed with the circulating xenon, which was routed past the detector. On figure 5.12, the time evolution of a measurement of the first 800 s is shown. After the opening of the valve the signal rate peaks to a maximum of ≈ 500 cps and than decreases in a damped oscillation until it reaches a constant rate of ≈ 160 cps on the detector. The oscillation is a function of the xenon circulation flow rate. Since the krypton cloud is transported by the xenon flow around the closed loop, it forms a bolus in the beginning that diffuses with time and asymptotically approaches a uniform ^{83m}Kr concentration in xenon circuit, while slowly decaying.

We see the ^{83m}Kr-decays in the detector when the ^{83m}Kr passes by for the first time at $t_0 \approx 118$ s. Its decay gives rise to a very sharp Gaussian peak with a variance σ_0^2. After having cycled one time through the setup, the ^{83m}Kr passes by the ^{83m}Kr-decay detector at $t_0 + T_{per} \approx 155$ s. Now the time distribution already has a Gaussian shape with a width $\sigma = \sqrt{\sigma_0^2 + \sigma_1^2}$ due to diffusion of the ^{83m}Kr in the xenon. In fact, the process that is described here, is a diffusion process in a turbulent gas stream, driven by the circulation pump. To describe the data, we assume a further Gaussian broadening by σ_1 and a further delay of the peak by T_{per} per cycle. The overall rate is multiplied by an exponential function to describe the radioactive decay of ^{83m}Kr, see the definition of the function $f(t)$ in equation 5.2.1. We fit this function $f(t)$ to the data from the first Gaussian peak on, see figure 5.12, whereas the first peak is damped with a correction factor C_{DT}, that takes the dead time of the data acquisition for the high rate of the first transit of the ^{83m}Kr into account.

$$f(t) = a + b\left(\frac{C_{DT}}{\sqrt{2\pi}\sigma_0} \cdot e^{-\frac{(t-t_0)^2}{2\cdot\sigma_0^2}} + \sum_{n=1}^{N} \frac{1}{\sqrt{2\pi}\sqrt{\sigma_0^2 + n\sigma_1^2}} \cdot e^{-\frac{(t-(t_0+n\cdot T_{per}))^2}{2\cdot(\sigma_0^2+n\sigma_1^2)}} \cdot e^{-t/\tau}\right) \qquad (5.2.1)$$

From the fit, the period of the oscillation has been determined to be $T_{per} = (36.9 \pm 0.1)$ s, which is the time needed by gas particles to perform one circle. This value can be compared to the measurement of the gas circulation by the flow controller. The volume of the system has been estimated to be $\approx 3000\,\mathrm{cm}^3$ (with an uncertainty of 6%) by using a known volume of gas and measuring the pressure decrease after expanding it to the system. With a forced gas flow of (8 ± 2) slpm and a gas pressure of 1 bar xenon, the time for one cycle can be calculated

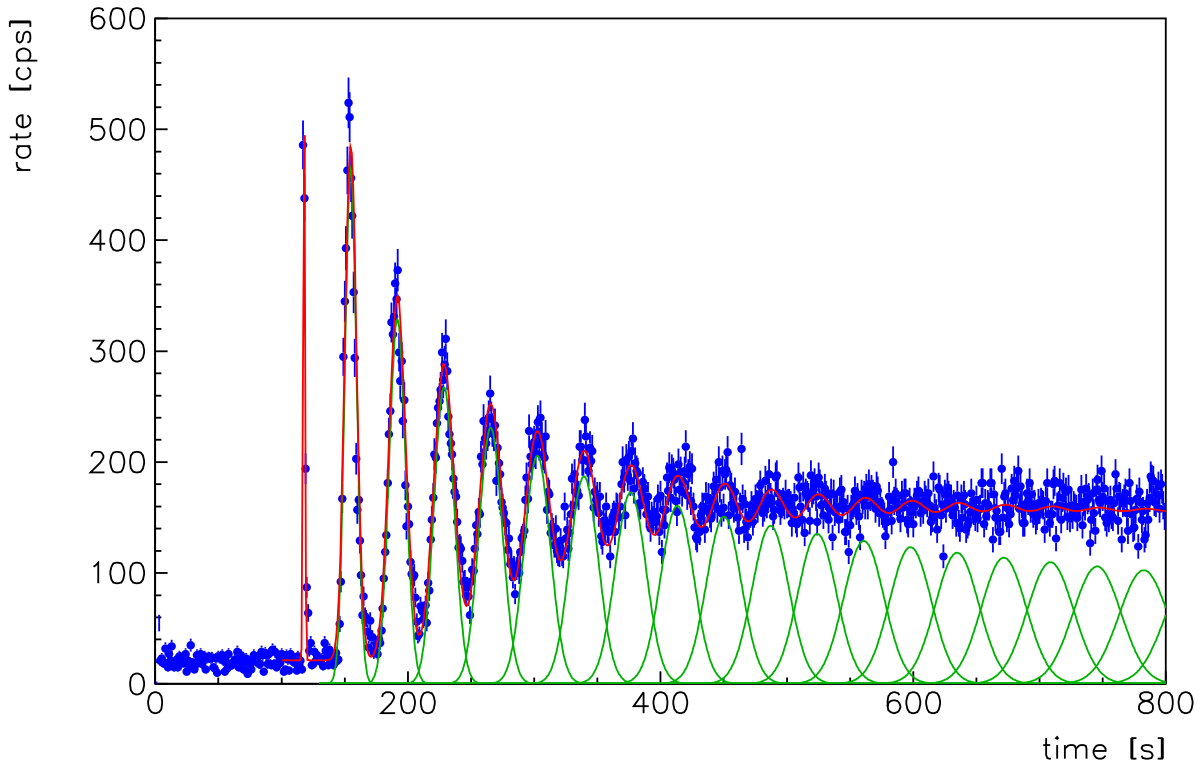

Figure 5.12: **^{83m}Kr decay rate in closed loop after injecting ^{83m}Kr at $T = 118$ s.** The fit described in equation 3.1 is shown in red, while the individual single Gaussian terms of equation 3.1 are displayed in green. Plot taken from [Ros14a].

to (22.5 ± 5.6) s. The uncertainty of the measurement is dominated by the accuracy of the flow controller. Since this device is specified for high flow rates up to 200 slpm, its accuracy at low flow rates is limited. The company is claiming an accuracy of $\pm 1\%$ of full scale [MKS06], i.e. 2 slpm. That gives a relative uncertainty of 25% at 8 slpm on the reading of the flow. Furthermore, the last calibration of the device by the company has been done almost two years before the measurements are performed. It, therefore, is very likely outdated and both effects can lead to the total discrepancy of $\approx 40\%$ related to T_{per}. As consequence, the ^{83m}Kr decay allows for a renewal of the calibration, assuming that the measurement of the gas volume is correct.

Since the valve to the ^{83}Rb source was closed, the amount of ^{83m}Kr particles inside the xenon decreases with the half-life of ^{83m}Kr. From the fit of the function $f(t)$, the ^{83m}Kr half-life was calculated to be (1.56 ± 0.04) h. In the figure 5.13, the complete evolution of the detector signal in time is shown. The measured half-life is lower compared to the published value of (1.83 ± 0.02) h [Nuc14]. One systematic uncertainty is introduced by only fitting the background in the beginning, neglecting the evolution of the background over time. But the main reduction of the effective half-life is coming from losses of ^{83m}Kr by diffusion into the parts of the system, where no circulation takes place, and by ^{83m}Kr adsorption at the system walls. The former can happen for example at pipes that lead to other subsystems.

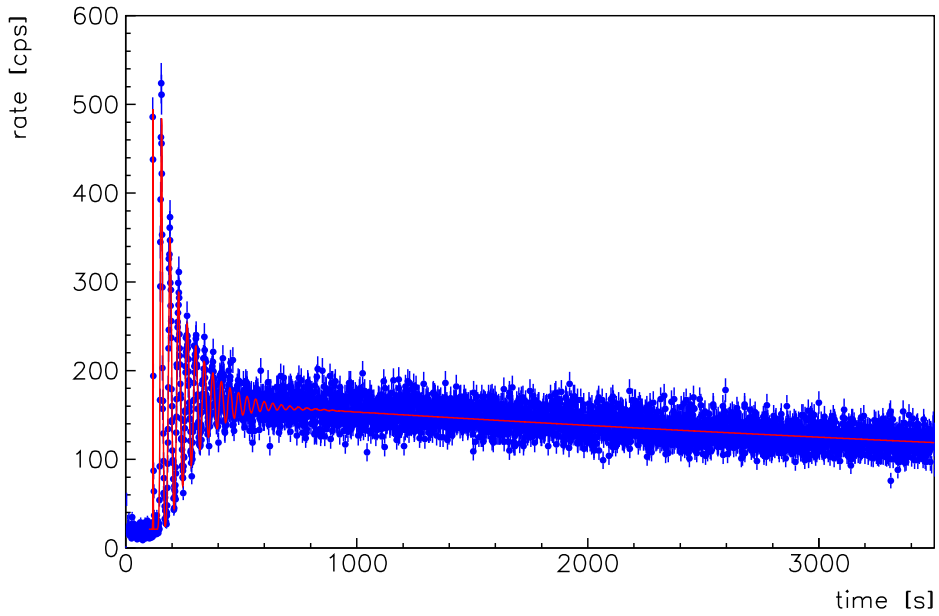

Figure 5.13: **^{83m}Kr decay rate in closed loop after injecting ^{83m}Kr source at t≈ 118 s.** The experimental data points are shown in blue, while the described fit is shown in red. The broadening of the Gaussians for each passing of the ^{83m}Kr by the detector due to diffusion results finally in a purely exponential decrease of the count rate in the ^{83m}Kr-decay detector [Ros14a].

Besides the time evolution of the rate, we could also determine energy spectra by integrating the signals and distinguishing between the two decay transitions of the ^{83m}Kr. After integrating the main signal, we identified and integrated the signal of the second transition as well. The result is shown in the figure 5.14.

The black distribution is related to the first transition of $E_{\gamma,1} = 32.2\,\text{keV}$ while the red distribution is related to the second transition at $E_{\gamma,2} = 9.4\,\text{keV}$. From figure 5.14 the mean of the first transition has been determined to $m_{\gamma,1} = (453.6 \pm 0.4)\,\text{mV·ns}$. The peak maximum is at 350 mV·ns with a left (right) half width (HWHM) of 50% (73%). With an anode readout resistor of 50 Ω and a photomultiplier gain of $\approx 2 \cdot 10^6$ the mean value corresponds to ≈ 28.4 detected photo electrons (0.88 pe/keV). The detector efficiency amounts to about $\varepsilon_{\gamma,1} = 1.9\%$ considering the 1460 expected scintillation photons for the first transition (see chapter 5.2.4).

For the second transition with $E_{\gamma,2} = 9.4\,\text{keV}$ the mean has been determined to be $m_{\gamma,2} = (188.0 \pm 0.3)\,\text{mV·ns}$. The peak maximum is at 120 mV·ns with a left (right) half width (HWHM) of 65% (87%). The mean value corresponds to ≈ 11.8 detected photo electrons (1.25 pe/keV). Compared to the 427 expected scintillation photons for the second transition (see chapter 5.2.4) the corresponding detection efficiency amounts to $\varepsilon_{\gamma,2} = 2.8\%$.

As one can see, the energy resolution is rather poor: the peaks are very wide, which is also reflected by the resolution for the two distributions. Both distributions are overlapping

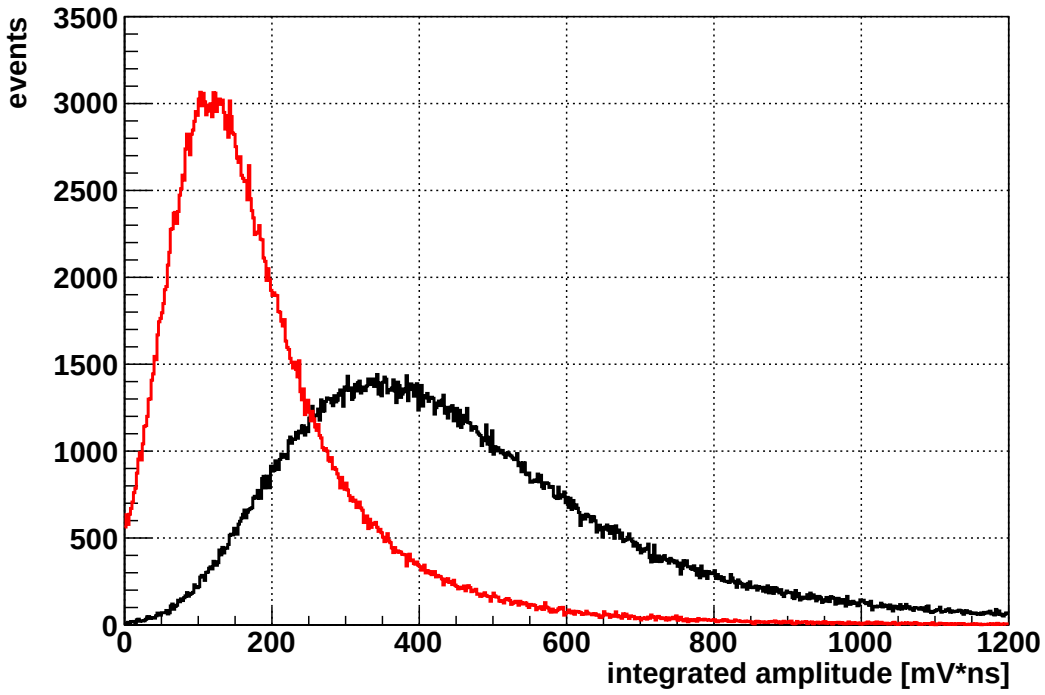

Figure 5.14: **Integrated spectrum of the double coincidence signals.** The pulses of the first and second transition were selected from the measurement and integrated. The first transition at $\approx 32\,\text{keV}$ peaked at $\approx 350\,\text{mV·ns}$ (black), while the second transition at $\approx 9\,\text{keV}$ peaked at $\approx 120\,\text{mV·ns}$ (red). Thhe spectrum is taken from [Ros14a].

each other. This can be explained by the high non-uniform light collection efficiency, which is limited by the usage of only one PMT together with a non-optimized PTFE reflector geometry and the range or energy deposition of the particles.

A calculation of the light yield ratio of electronic recoils R_e, which is the ratio of the measured light yields (pe/keV) of the 9.4 keV transition and the 32.2 keV transition, as used in [Apr12c], gives a value of $R_e \approx 1.4$, compared to $R_e = 1.052 \pm 0.005$, measured in liquid xenon and presented in the same work [Apr12c]. The origin of this discrepancy is very likely caused by imperfections of the light collection efficiency in combination with the particle ranges and the location of the energy deposition for the two transitions (see figure 5.7). The former assumption is also reflected in the large width of the distributions. Concerning the second argument, the density and thus the particle and energy deposit is very different in liquid xenon used in reference [Apr12c] with respect to gaseous xenon used in this work. An improvement of the uniformity of the light yield as function of energy might be achieved by using data-quality cuts but has not been investigated here.

Finally, these measurements demonstrated, that the mixing of xenon with radioactive ^{83m}Kr and the detection is working properly, although the results, presented here, indeed demonstrate, that the detectors are currently not feasible for spectroscopic applications. Never-

theless, they have been designed for the ^{83m}Kr tracer method to just count the number of events and, therefore, they can be used to investigate the separation performance of cryogenic distillation systems, presented in the chapters 6 and 7.6.

5.3 Krypton detection in xenon using RGMS

To give a complete summary of all techniques, that are used for the characterization of the Phase-1 distillation column, the RGMS system, developed at Max Planck Institut für Kernphysik in Heidelberg will be introduced very briefly. The system has been presented in more detail in [Lin13] and [Lin14]. This summary is based on these works.

The mass spectroscopic system (RGMS) has been developed in order to detect trace amounts of natural krypton in xenon down to the sub-ppt level. The projected detection limit has been determined in [Lin14] to be $^{nat}\mathrm{Kr/Xe} = 8\,\mathrm{ppq}$[13]$= 0.008\,\mathrm{ppt}$, feasible for the requirements of the XENON1T experiment.

As already mentioned in chapter 5.1, commercial mass separation techniques are usually not feasible to measure concentration in the sub-ppt regime. Therefore, an enrichment or separation needs to be implemented to separate the bulk of xenon in any sample beforehand. To achieve the detection limit, the colleagues in Heidelberg use the technique of gas-chromatography in combination with a custom sector field mass spectrometer. In figure 5.15 the flowchart of the gas-chromatographic section is shown. The sample is injected and forced with a helium carrier gas through the columns T2 and T3, which are filled with a special adsorbent, cooled with liquid ethanol to $-80°$C. While T2 is used to perform the separation of krypton and xenon, T3 is the storage for the krypton for a regulated release into the mass spectrometer section. The separation takes place due to the different interaction strength of krypton and xenon with the adsorbent. Another column T1, filled with a different adsorbent, cooled down to liquid nitrogen temperature is used to clean the helium carrier gas from krypton, in order to avoid any contamination of the sample. In addition, the setup is constructed, according to UHV standards from clean borosilicate glass and stainless steel, bake-able up to $\approx 120°$C to guarantee the cleanliness of the measurement.

The sample is extracted from the column T3 by cryogenic pumping with a cold finger into the mass spectrometer section, shown in figure 5.16 and injected into the ion source, where the atoms are ionized. In the following the ions are focused and accelerated by electric fields through a variable magnetic dipole field, to separate the single compositions of the sample. Finally the ions are detected in a combined detector, consisting of a Faraday cup and a secondary electron multiplier (SEM).

Since the setup is not portable, the sample drawing and storage is of particular interest. The collection of ultra-clean xenon from a stationary system, like XENON100, the Phase-1 column or XENON1T later on, without contaminating the sample is one of the advantages for the measurement. In addition, a leak-tight storage has to be provided, to avoid contaminations during the shipping process. At MPIK, pipettes have been constructed, using four stainless steel below sealed valves, welded together in series (see figure 5.17).

[13] $1\,\mathrm{ppq} = 1 \cdot 10^{-15}\,\mathrm{mol/mol}$

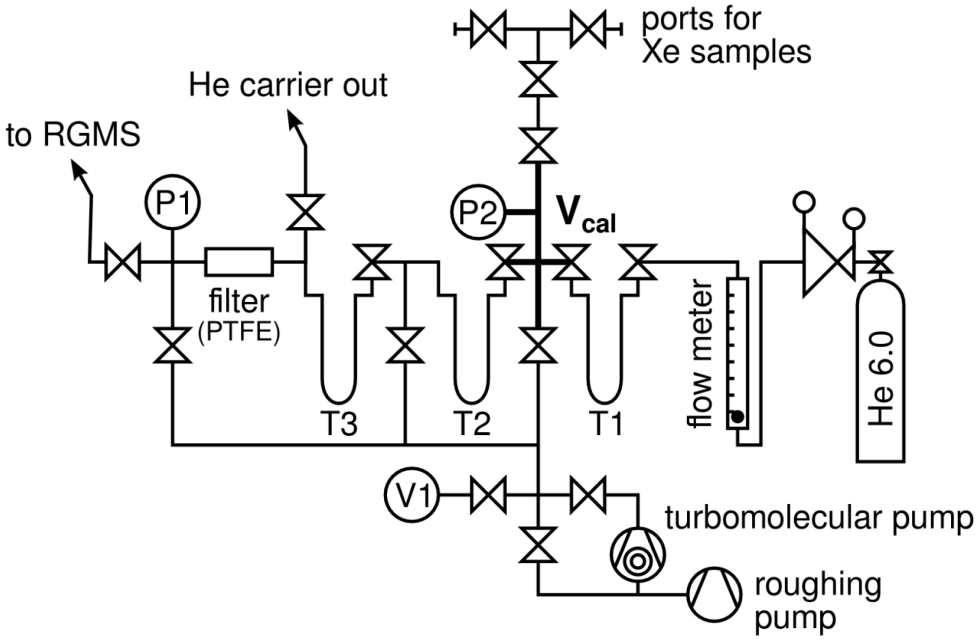

Figure 5.15: **Flowchart of the gas-chromatographic system.** The flowchart illustrates the sample treatment, based on gas-chromatography. Krypton and xenon are separated in cryogenic adsorbent columns T2 and T3 in order to reach the sub-ppt sensitivity. Helium is used as carrier-gas to flush the sample through the columns. The krypton enriched sample is than transfered to the sector field mass spectrometer. The picture is taken from [Lin14].

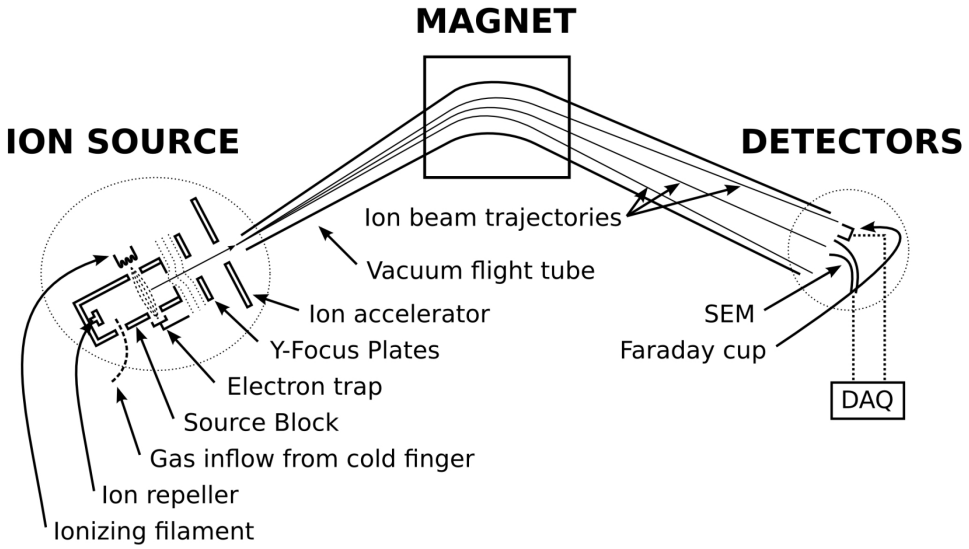

Figure 5.16: **Schematic view on the mass spectrometer.** In this picture, the sector field mass spectrometer is introduced. The sample is injected to the ion source, ionized and separated in the magnetic sector field, before the ions are detected in the detector section. The picture is taken from [Lin14].

Figure 5.17: **Pipette for sample retrieving.** The pipettes, used from MPIK to collect the samples are made from four stainless-steel bellow valves, welded together inside a row. The volume between two valves is used as sample volume. Photo provided by Dominik Stolzenburg, MPIK.

The volume between two valves is used to store the sample, leading to three volumes with $\approx 10\,\mathrm{cm}^3$ storage space, which is more than enough, since each measurement consumes only $\approx 1\,\mathrm{cm}^3$ of sample gas. The volume in the middle is shielded by the two other volumes against the atmosphere, to minimize the probability of contamination. For samples with the highest purity, extensive baking and pumping procedures have to be fulfilled before the sample is acquired. Finally, the pipettes are connected to the RGMS system with metal sealed VCR or Conflat connections.

The RGMS system has been used to characterize the Phase-1 column. The distillation conditions, together with the preparation of the sample retrieve and the results are presented in chapter 7.4.

Performance tests of the pre-separation station using ^{83m}Kr tracer

6

The construction of the distillation column was started with the first condensing station. The construction and the distillation tests are also published in [Ros15] and different section from the paper are used in this thesis as well. The distillation station, equipped with gaseous and liquid outlets is than used to run the first distillation tests using the ^{83m}Kr tracer method in order to check he feasibility of distillation for very low concentrations. A ^{83}Rb source of $\sim 1\,\mathrm{MBq}$ activity has been used. Although nearly all $^{83\mathrm{m}}$Kr particles should emanate from the beads [Ven05], a more conservative emanation efficiency of $\epsilon = 70\%$ has been assumed, in order to take the source production tolerances as well as the unknown emanation characteristics into gaseous xenon into account. As consequence, a $^{83\mathrm{m}}$Kr particle flux of ≈ 550000 atoms per second can be mixed into the xenon gas. A flow rate of 5 slpm of xenon, (which was the default flow rate during the measurements) is equal to a particle flux of $\approx 2 \cdot 10^{21}$ xenon atoms per seconds, which corresponds to a concentration of

$$^{83\mathrm{m}}\mathrm{Kr/Xe} \approx 0.3 \cdot 10^{-15} = 0.3\,\mathrm{ppq} \ll 0.5\,\mathrm{ppt}. \tag{6.0.1}$$

For the measurements, presented in this work, the xenon has been circulated in a closed loop, which allows for permanent emanation and enrichment of $^{83\mathrm{m}}$Kr in the xenon, achieving an equilibrium state between particle production and the radioactive decay. Hence, the $^{83\mathrm{m}}$Kr concentration is higher for a continuously open ^{83}Rb source and due to the continuous recirculation. The activity in equilibrium for a two-decay chain is given by:

$$\mathrm{A_{Kr}(t)} = \mathrm{A_{Rb}(t_0)} \cdot \cdot \frac{\lambda_{\mathrm{Kr}}}{\lambda_{\mathrm{Kr}} - \lambda_{\mathrm{Rb}}} \cdot \left(\mathrm{e}^{-\lambda_{\mathrm{Rb}} \cdot \mathrm{t}} - \mathrm{e}^{-\lambda_{\mathrm{Kr}} \cdot \mathrm{t}}\right) \tag{6.0.2}$$

For the decay constant of $^{83\mathrm{m}}$Kr which is much higher than the decay constant of ^{83}Rb $\lambda_{\mathrm{Kr}} = 1.05 \cdot 10^{-4}\mathrm{s}^{-1} >> \lambda_{\mathrm{Rb}} = 9.3 \cdot 10^{-8}\mathrm{s}^{-1}$ and expecting experimental times much smaller than the half-life of ^{83}Rb one can write:

$$\mathrm{A_{Kr}(t)} \approx \mathrm{A_{Rb}(t_0)} \cdot \epsilon \cdot \left(1 - \mathrm{e}^{-\lambda_{\mathrm{Kr}} \cdot \mathrm{t}}\right) \tag{6.0.3}$$

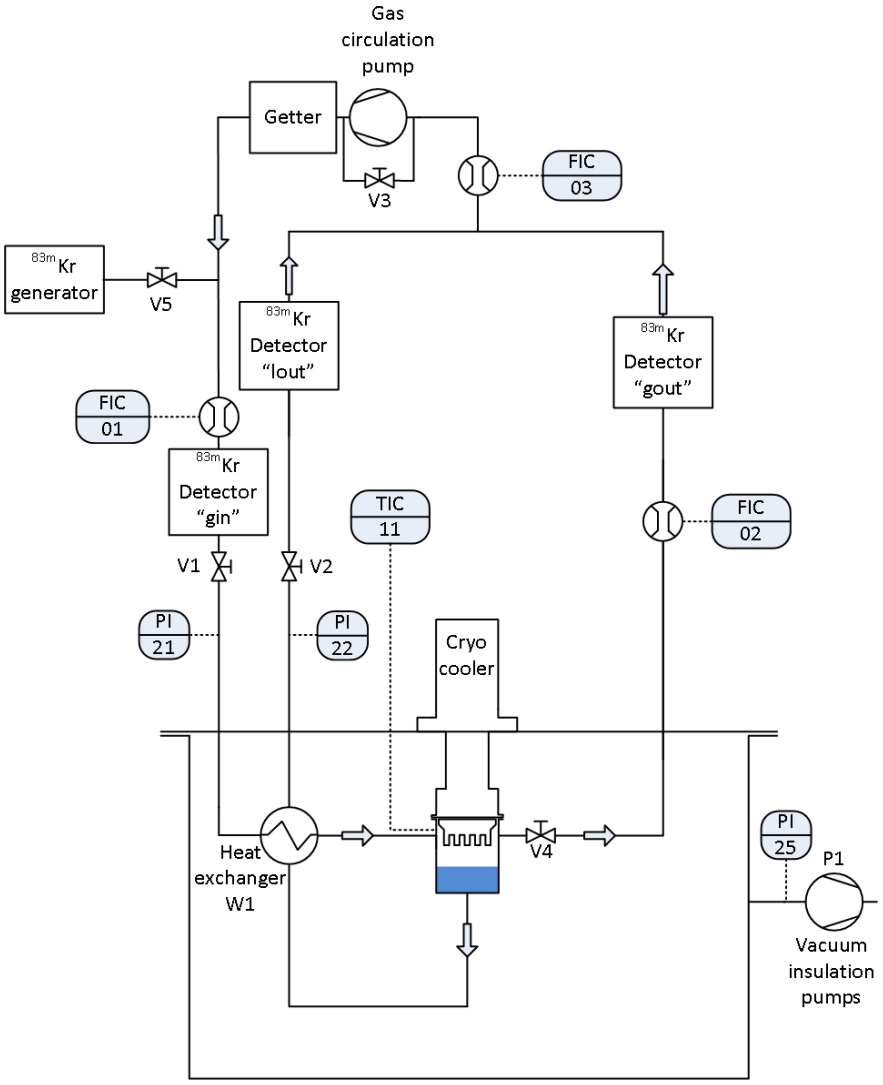

Figure 6.1: **Flow chart of the system.** The xenon is circulating through a closed loop, that contains the distillation setup, the different ^{83m}Kr decay detectors and the ^{83m}Kr generator. The flow is driven with a membrane pump through a hot getter to remove electronegative impurities (e.g. water) from the xenon. For the process control, the pressure is measured with several capacitive manometers (pressure index: PI21, PI22) while the flows are measured or even controlled with different flow controllers (Flow index control: FIC01-FIC03). The temperature in the distillation chamber is controlled using a silicon diode temperature sensor (temperature index control: TIC11).

For a measurement time of e.g. $t = 6\,h$ and an activity of the ^{83}Rb of $A_{Rb}(t_0) \approx 1\,MBq$ the number of radioactive ^{83m}Kr atoms can be calculated to $N_{^{83m}Kr} \approx 4.6 \cdot 10^9$, giving an average concentration for a xenon reservoir of 100 sl to be $^{83m}Kr/Xe = 1.7 \cdot 10^{-15} = 1.7\,ppq$. During the distillation process, the concentration inside the system varies, with an expected enhancement in the gaseous phase, which will be shown in the following section.

In summary, it is possible to investigate the distillation performance of any distillation setup

for xenon and krypton in the sub-ppt region using the doping method with ^{83m}Kr, since the detectors are able to measure the decay at such low concentrations. Furthermore, it allows for the first time to verify directly the assumption, that krypton isotopes of low abundance (here ^{83m}Kr as a model for ^{85}Kr) is effectively separated by cryogenic distillation like the other krypton isotopes with higher natural abundance like ^{84}Kr.

6.1 Experimental setup

The setup is designed as a closed loop with the single distillation stage as the key component (see figure 6.1). The circulation of the gas is forced by a membrane pump (KNF, type N143AN.12E) through a hot metal-based getter (SAES, type PS4-MT50-R), that removes electronegative impurities from the xenon.

The gas is passing the ^{83m}Kr generator that is attached to the system with the valve V5 before it is entering the distillation chamber. The flow is regulated with the flow controller, called FIC01 (MKS, type 1479B) while the pressure at the inlet is measured with the pressure gauge PI21 (Swagelok, type PTU-S-AC9-31AD). The distillation stage is made of a stainless steel vessel (316L) and a copper block (OFHC), where cooling fins have been milled to the copper to provide a large surface area for the liquefaction of the xenon (see figures 6.1 and 6.2). The copper itself is used as gasket to seal the vessel. This condenser station is connected to a cryo-cooler (Oerlikon-Leybold Vacuum, type CP50), that provides ~ 100 W of cooling power at -98°C. The temperature is measured with a silicon diode and kept constant by a heater cartridge, connected to a temperature controller (Lakeshore, model 336). The distillation unit is equipped with two outputs, one in the bottom of the stainless steel vessel, where the liquid can be extracted and one at the top of the vessel to extract xenon gas from above the liquid surface. While the liquid output is connected to a plate heat exchanger to evaporate the xenon, the gaseous xenon is guided directly out of the vacuum chamber. Both outputs and the input are monitored by ^{83m}Kr decay detectors (labeled “gin“, “gout“ and “lout“) and pressure sensors. Since the gaseous and the liquid outlet are connected outside the vacuum vessel, the pressure in these lines is expected to be equal and measured with PI22. In addition, the amount of xenon that is exhausted from the gas-phase is regulated by a flow controller, labeled as FIC02 (MKS, type 1479B). The third flow controller FIC03 is part of the circulation system and was fully opened for these measurements in order to avoid over-regulation of the system.

6.2 Performance measurements of the single-stage distillation setup

In order to understand the relation between the measured signal rates and the ^{83m}Kr particle flux, different aspects have to be taken into account including a detector calibration. Finally the separation factors can be calculated. These considerations are presented in the following:

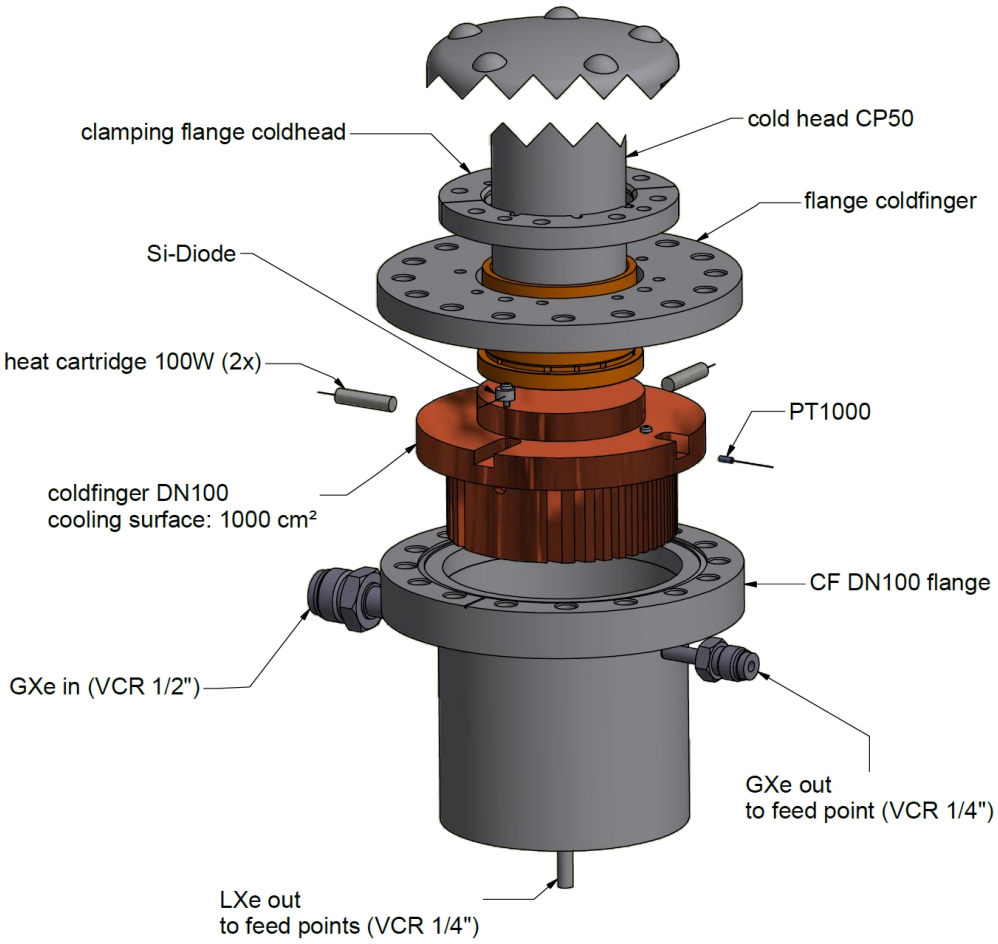

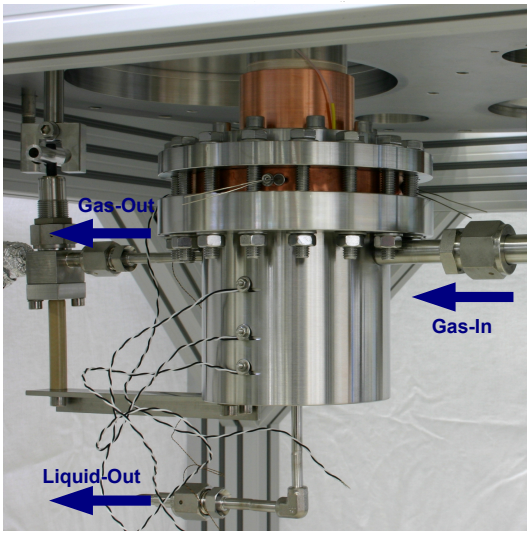

Figure 6.2: **Distillation stage.** Top: CAD drawing of the distillation stage made from a stainless steel vessel and a copper cooling block. Bottom: Distillation stage mounted inside the vacuum insulation vessel.

For the calculation, the different concentrations of ^{83m}Kr in the xenon at the three detectors (gin, gout, lout) are named as c_{gin}, c_{gout} and c_{lout}, the flow rates of the xenon as q_{gin}, q_{gout}, q_{lout} and the pressures at the detectors as p_{gin}, p_{gout}, p_{lout}, with $p_{gout} = p_{lout}$.

The detected event rate r_i (with $i = gin,\ gout,\ lout$) is a function of the ^{83m}Kr concentration c_i at each detector and can, therefore, be written as [Ros14a]:

$$r_i = \frac{n_i \cdot c_i \cdot V_{det,i}}{\tau} \tag{6.2.1}$$

With τ being the lifetime of the ^{83m}Kr (τ=9500 s), n_i being the total particle density and $V_{det,i}$ being a effective detector volume, that takes the different detector efficiencies into account.

The total particle density n_i can be expressed by the pressure and the temperature p_i and T_i together with the respective values n_0, p_0, T_0, V_0 at normal conditions by the law of ideal gas (with $p_0 = 1013\,\text{mbar} \approx 1\,\text{bar}$, $V_0 = 22.4\,\text{l}$ and $T_0 = 273.15\,\text{K}$, $n_0 = \frac{N_A}{V_0} \cdot 1\,\text{mol} = \frac{p_0}{k_B T_0}$):

$$n_i = \frac{p_i}{T_i} \cdot \frac{n_0 T_0}{p_0} \tag{6.2.2}$$

Giving the following expression for the rates:

$$r_i = p_i \cdot c_i \cdot V_{det,i} \cdot \frac{1}{\tau} \cdot \frac{n_0}{p_0} \cdot \frac{T_0}{T_i} \tag{6.2.3}$$

The determination of the absolute detector efficiencies is not necessary for the description of the separation performance. The knowledge of the relative detector efficiencies of the two output detectors relative to each other and to the input detector is necessary, as it will be shown later-on. These relative detector efficiencies can be obtained in a direct measurement, as presented in the next section.

6.2.1 Determination of the relative detector efficiencies

In order to determine the relative efficiencies, the system has been filled with xenon gas at room temperature, while the cryo-cooler was turned off to avoid any liquefaction of xenon. The gas is circulating through the system at a flow rate of 5 slpm entering the warm distillation chamber, where the flow is divided between the gas-out line and the liquid-out line before the gas is fed back to the system. As consequence, a constant gas flow along with a constant temperature and almost constant pressure (the latter one checked by the pressure sensors PI21 and PI22) at all three detectors is achieved. Since the system is operated in continuous circulation, the pressure between in- and outlet varies in the range of 10 mbar, which will be corrected for in the calculation).

In order to measure the background level of the detectors before, the valve (V5) to the ^{83m}Kr generator has been opened only after some time of circulation (t$\approx$35 min) so that

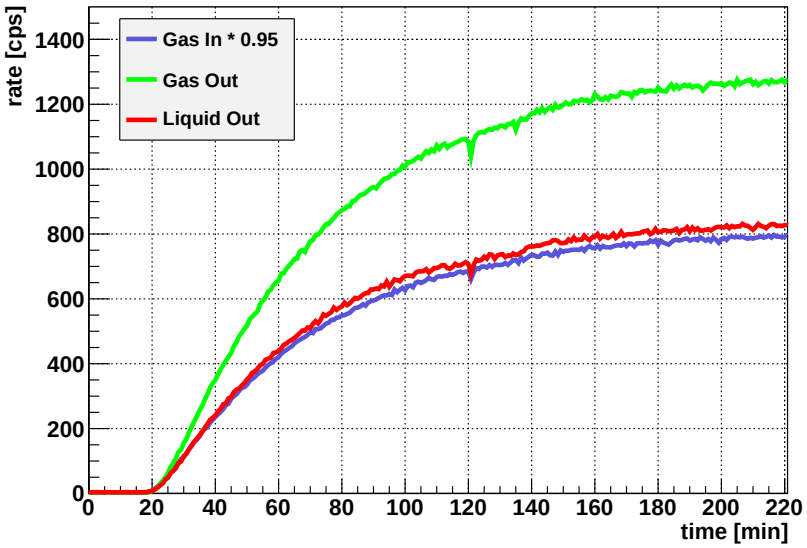

Figure 6.3: **Calibration of the ^{83m}Kr decay detectors.** The calibration has been performed by circulating xenon at room temperature through the system. After opening the valve (V5) to the ^{83m}Kr generator ($t \approx 20$ min) the rate increases on all detectors up to a saturation value, which indicates, that the krypton is distributed inside the circuit with an equal concentration. The efficiency in the gas-in and the liquid-out detector are very similar. Hence, the rate in the gas-in detector has been artificially multiplied by a factor 0.95 in order to make it distinguishable in the plot.

the ^{83m}Kr is mixed to the xenon. As shown in figure 6.3, the rates on all three detectors are increasing to a saturation value, defined by the ^{83}Rb source activity, the decay constant λ_{Kr} of ^{83m}Kr, as shown in equation 6.0.3, and the total amount of xenon gas in the system. This saturation indicates that the ^{83m}Kr atoms are distributed in the system equally after some time. Using equation 6.2.3 for equal concentrations c_i and temperature T_i at all three detectors, the relative correction factors ν_g and ν_l are defined as:

$$\nu_g = \frac{V_{det,gout}}{V_{det,gin}} = \frac{r_{gout}}{r_{gin}} \cdot \frac{p_{gin}}{p_{gout}} = 1.522 \qquad (\pm 0.1\%) \tag{6.2.4}$$

$$\nu_l = \frac{V_{det,lout}}{V_{det,gin}} = \frac{r_{lout}}{r_{gin}} \cdot \frac{p_{gin}}{p_{lout}} = 1.021 \qquad (\pm 0.1\%) \tag{6.2.5}$$

Both factors, ν_g and ν_l are visualized in figure 6.4, while their values have been determined by applying a constant fit after the system has been stabilized. As presented in the figures 6.3 and 6.4, the efficiency between the gin and the gout detectors varies by more than 50%, while the efficiency between gin and lout detectors only varies by $\approx 2\%$. This observation can be explained by the dependence of the PMT gain on the applied voltage. All three PMTs are supplied with +800 V and the same discriminator threshold is used, without correcting the

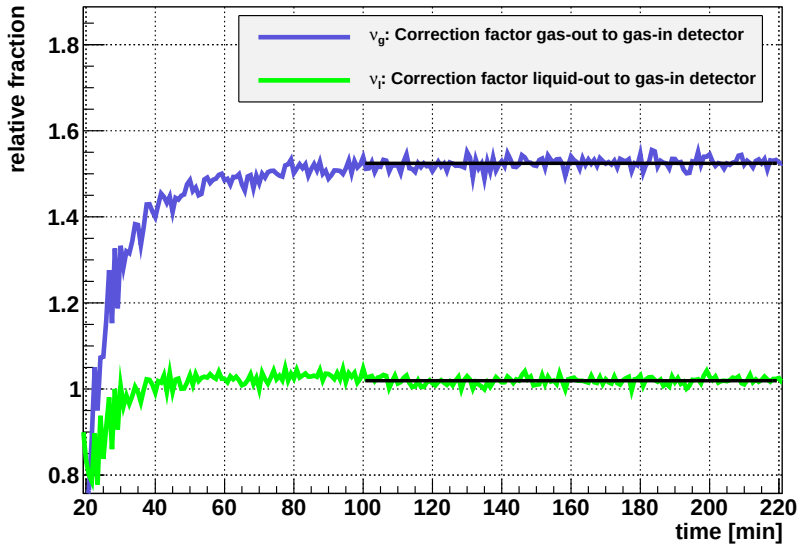

Figure 6.4: **Calculation of the relative correction factors.** The correction factors for the gas-out and the liquid-out detectors are determined to $\nu_g = 1.522\,(\pm 0.1\%)$ and $\nu_l = 1.021\,(\pm 0.1\%)$ relative to the gas-in detector, as defined in equations 6.2.5. The constant fits are obtained after the system comes to an equilibrium (t=150 min).

different gains of the individual PMTs (type R8520-06-AL, Hamamatsu, Japan). Differences of up to a factor 6 in the gain during calibration measurements of different PMTs for the same voltage and threshold have been observed.

6.2.2 Filling with liquid xenon and performance tests

After the calibration has been performed, the system has been cooled down to -98°C and the distillation chamber has been filled with liquid xenon to generate a two phase filling. The amount of xenon in this reservoir has been varied for different measurements between $\sim$180 ml liquid xenon ($\sim$98 sl) and $\sim$370 ml ($\sim$200 sl). During the normal operation, the xenon is pre-cooled in the heat exchanger (W1) and enters the condensing station, where the xenon gets liquefied at the copper surface, dropping into the reservoir. The flow rate in the gas-in line is regulated by the flow controller FIC01 to a set-point of 5 slpm. It has been turned out, that the flow controller for the in-gas has an offset of 10%, leading to a reduced inlet flow of $\approx$ 4.5 *slpm*. In the beginning, a small flow rate below 1.0 slpm has been applied via FIC02 at the gaseous output, while the difference between gas-in flow rate and gaseous out flow rate is extracted at the liquid-out port to guarantee a constant liquid level in the vessel. Due to the circulation inside the closed loop, the amount of in-going and out-going particles has to be the same. The non-zero flow rate at the gas-out line was necessary in almost all measurements for stable operation of the system after the filling and strongly depends on the amount of xenon in the chamber. As indicated in figure 6.6, the pressure in

the in-gas is measured to be higher than 3 bar. From literature, the vapor pressure for xenon at −98°C has been stated as 1.75 bar [Nis14a]. The pressure in the system is going down for an increased flow-rate in the gas-out line but in these measurements, the predicted vapor pressure has never been reached, which has different reasons: The distillation process is not only separating krypton from xenon, but also other light and therefore more volatile noble gases like argon or helium, which are also present in trace amounts in commercial xenon gas as krypton. These light gases are collected in the gas phase inside the condensing chamber. Although the concentration is rather low they prohibit a proper heat exchange from the cooling fins with the xenon gas (so called blanketing effect). As consequence, the pressure in the chamber is increased and the system gets unstable. A small gaseous out flow rate takes the light gases out, breaking the blanket and enhancing the heat exchange with the xenon. Higher flow rates in the gas-out line leads to an even better heat transfer, followed by a decrease in pressure that is observed. It is not possible to extract the light gases completely from this setup because of the closed loop system and even with increased circulation speed they remain partly in the chamber and affect the heat transfer. Furthermore, the sensor PI21 is located in front of the distillation chamber measuring the pressure in the gas-in line with the flow driven by the pump, not directly above the liquid phase (the vapor pressure is valid for a closed, static system). Hence, the pressure is expected to be slightly higher due to the flow dynamics.

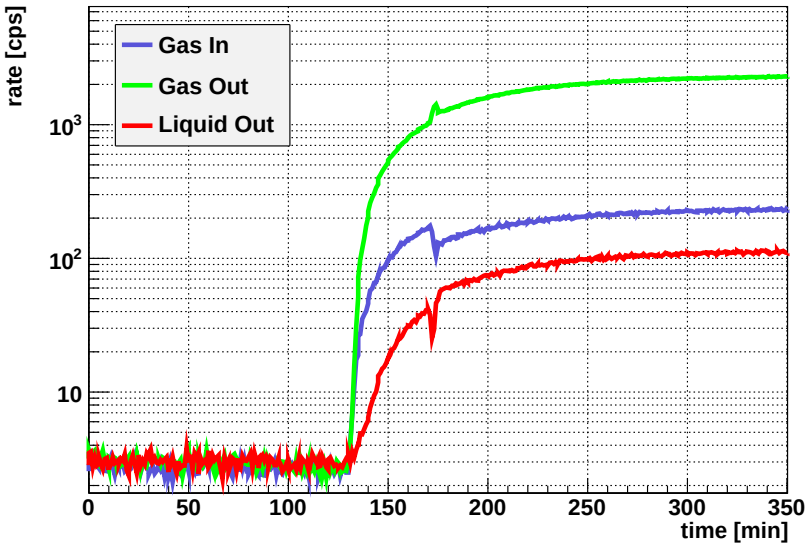

Figure 6.5: **Event rates, measured by the three ^{83m}Kr detectors.** This measurement has been performed with a liquid load of 370 ml xenon and an initial flow rate of 1.0 slpm in the gas-out line. At $t = 175$ min the flow rate in the gas-out line has been changed to 0.5 slpm causing the instability in the rates.

After the system is filled and reached equilibrium, V5 is opened and the ^{83m}Kr is emanating into the system. In the following, the rates in the detectors are increasing, detecting the ^{83m}Kr decay in the xenon. The measurement, presented in figure 6.5, has been performed with about 370 ml liquid xenon and started with a flow rate of 1.0 slpm at the gas-out line,

which has been increased later on. The flow rate in the gas-in line is kept constant all the time at 5 slpm. The valve V5 controlling the ^{83m}Kr injection has been opened at t$\approx$ 130 min. The rates indicate that the separation in the chamber takes place as expected, since the rate in the gas-out detector is getting the highest one. This is expected, because ^{83m}Kr, as the more volatile component, prefers the gaseous phase.

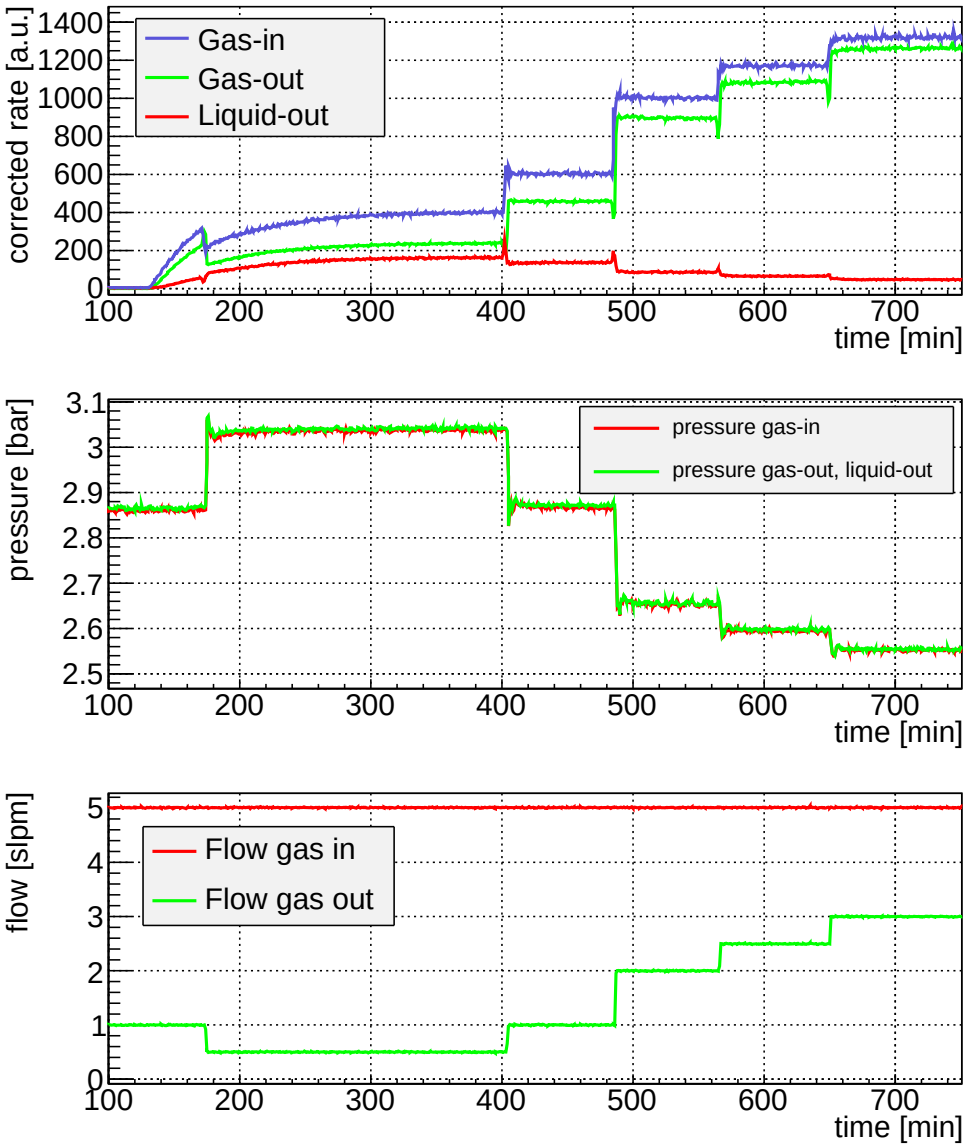

Figure 6.6: **Rates on ^{83m}Kr decay detectors together with important system parameters.** This plot shows different control variables from the system and the rates at the ^{83m}Kr detectors for one example measurement with a liquid load of 370 ml xenon. Top: Corrected rates at the three detectors, normalized by flow, pressure and detector efficiency. Middle: Pressures at the inlet (PI21) and the both outlet lines (PI22). Bottom: Flows at the inlet (FIC01) and the gas-out line (FIC02).

While the rates at the gin and the gout detector are following the same time behavior due to the fact that the krypton is traveling in the same state of matter, the rate on the lout detector behaves different: It starts increasing after some offset time and shows a different shape. This indicates, that the ^{83m}Kr stays longer in the liquid phase, which can be explained by the higher density of this phase. Therefore, a correction on the residence time of the ^{83m}Kr in the liquid phase is of crucial importance, which will be presented later on.

After some mixing time of the ^{83m}Kr, the performance of the distillation stage for different ratios of flow rates in the liquid and the gas-out are investigated, by changing the flow rate at the gas-out, using FIC02, in several steps of 0.5 slpm (see figure 6.6). Between each step, a measurement time of $\sim$90 min has been chosen to let the system stabilize. As consequence of the different flows, the rates on the ^{83m}Kr decay detectors are changing due to the different separation performance.

In order to calculate a separation factor from the single stage, the particle flow of ^{83m}Kr in the liquid-out and gas-out line relative to the inlet has to be determined. In general, the total particle flow $\dot{N}$ can be expressed by using the ideal gas law as:

$$\dot{N} = \frac{N}{t} = \frac{\nu \cdot N_A}{t} = \frac{pV}{t}\frac{1}{k_B T} = q\frac{1}{k_B T} \tag{6.2.6}$$

With ν being the number of moles and $q = pV/t$ being the gas flux. This is valid for the total amount of particles, krypton and xenon together, circulating through the system. For the ^{83m}Kr particle flux, equation 6.2.6 has to be multiplied with the concentration c of ^{83m}Kr in the xenon:

$$c\dot{N} = \frac{cq}{k_B T} \tag{6.2.7}$$

Since the rate r_i on each detector is related to the concentration c_i of ^{83m}Kr and the gas density n_i in the detector volume, as shown in equation 6.2.3, the concentration can be expressed by:

$$c_i = \frac{r_i \cdot \tau \cdot p_0 \cdot T_i}{V_{det,i} \cdot p_i \cdot n_0 \cdot T_0} \tag{6.2.8}$$

Combining equations 6.2.7 and 6.2.8, the relation between the ^{83m}Kr particle flux and the detected rate is given by:

$$(c\dot{N})_i = \frac{c_i q_i}{k_B T_i} = \frac{r_i \cdot q_i}{p_i} \cdot \frac{\tau}{V_{det,i}} \cdot \underbrace{\frac{p_0 \cdot T_i}{n_0 \cdot T_0 \cdot k_B T_i}}_{=1} \tag{6.2.9}$$

$$= \frac{r_i \cdot q_i}{p_i} \cdot \frac{\tau}{V_{det,i}} \tag{6.2.10}$$

In the next step, the ratio between the outgoing ^{83m}Kr particles at the gas-outlet and the ingoing particles at the gas-inlet can be calculated:

$$f_g = \frac{\dot{N}(^{83m}Kr)_{gout}}{\dot{N}(^{83m}Kr)_{gin}} = \frac{(c \cdot \dot{N})_{gout}}{(c \cdot \dot{N})_{gin}} \tag{6.2.11}$$

$$= \frac{r_{gout} \cdot q_{gout} \cdot p_{gin}}{r_{gin} \cdot q_{gin} \cdot p_{gout}} \cdot \underbrace{\frac{V_{det,gin}}{V_{det,gout}}}_{=1/\nu_g} \tag{6.2.12}$$

The same should be valid for the ratio between the outgoing ^{83m}Kr particles at the liquid-out and the ingoing particles at the inlet:

$$f_l = \frac{\dot{N}(^{83m}Kr)_{lout}}{\dot{N}(^{83m}Kr)_{gin}} = \frac{(c \cdot \dot{N})_{lout}}{(c \cdot \dot{N})_{gin}} \tag{6.2.13}$$

$$= \frac{r_{lout} \cdot q_{lout} \cdot p_{gin}}{r_{gin} \cdot q_{gin} \cdot p_{lout}} \cdot \underbrace{\frac{V_{det,gin}}{V_{det,lout}}}_{=1/\nu_l} \tag{6.2.14}$$

Due to particle conservation, the sum of f_l and f_g should be matching to $f_l + f_g = 1$, but one has to take also the radioactive decay of the ^{83m}Kr into account. While the liquid phase is of much higher density compared to the gas phase, the residence time of ^{83m}Kr compared to the decay constant is not negligible. Especially for small flow rates on the gas-out line, this effect drastically influences the mass balance and therefore, the rate, measured on the liquid out detector has to be corrected for this. To get r_{lout} out of the measured rate r'_{lout} one can use the law of a radioactive decay:

$$r'_{lout} = r_{lout} \cdot e^{-\frac{\tau_{\mathrm{lout}}}{\tau}} \tag{6.2.15}$$

With τ_{lout} being this residence time, which can be estimated by different approaches which are discussed in the following. Furthermore, it is known, that the accuracy of the mass-flow controllers, also including device offsets, is limited. Therefore, additional factors $K_{q_{gout}}$ and $K_{q_{lout}}$ which are constant fit parameters have been added to the formulas 6.2.12 and 6.2.14 which allows to correct the mass-balance for these errors:

$$f_g = \frac{r_{gout} \cdot q_{gout} \cdot p_{gin}}{r_{gin} \cdot q_{gin} \cdot p_{gout}} \cdot \frac{1}{\nu_g} \cdot K_{q_{gout}} \tag{6.2.16}$$

$$f_l = \frac{r'_{lout} \cdot q_{lout} \cdot p_{gin}}{r_{gin} \cdot q_{gin} \cdot p_{lout}} \cdot \frac{1}{\nu_l} \cdot K_{q_{lout}} \cdot e^{\frac{\tau_{\mathrm{lout}}}{\tau}} \tag{6.2.17}$$

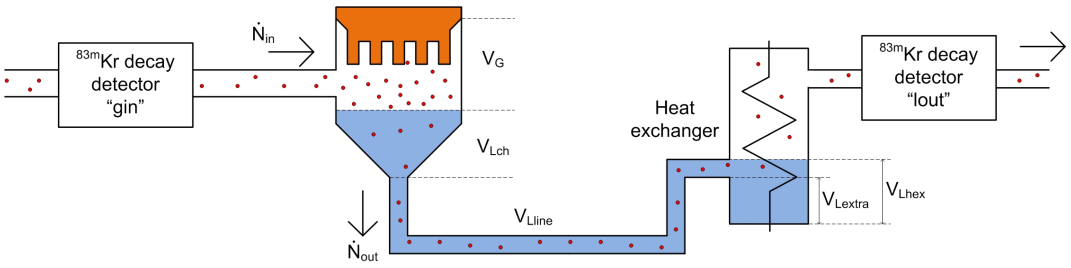

Figure 6.7: **^{83m}Kr particle flow in the distillation chamber.** This simplified scheme of the condensing chamber illustrates the ^{83m}Kr flow, expected for the distillation chamber, with a liquid-out line only. The traveling time of the krypton particles through the liquid is essential because of the radioactive decay.

6.2.3 Measurement of the residence time correction factor

One measurement has been performed under special conditions and can be used to estimate the residence time of the krypton in a certain liquid xenon volume under the given conditions. After the initial filling with ~ 180 ml, the pressure in the system was still low enough to start the measurement with a completely closed gas-out line (FIC02 = 0 slpm). When opening V5 to inject the ^{83m}Kr, the rate at the gas-in detector increases, while it takes a few minutes until the liquid-out detector measures the first ^{83m}Kr decays.

This measurement can be used to model the krypton-particle flux in the liquid xenon. In figure 6.7 a simplified scheme for this measurement is shown, having only a liquid-out line. In blue the liquid xenon is marked, while the ^{83m}Kr is indicated by red dots.

To describe the ^{83m}Kr particle flux $\dot{N}(t)$ some assumptions are made:

- **Liquid level is constant during the measurement:** This can be confirmed in equilibrium from the pressure stability in the system. A changing liquid level would cause pressure fluctuations during the measurement. Additionally, the trapping of xenon on other spots than the condensing chamber and the heat exchanger is avoided by the construction of the system.
- **Rapid liquid-gas interchange:** The liquid-gas interchange is expected to be connected to the surface area of the liquid xenon and therefore, related to the amount of xenon in the vessel. Filling only the liquid-out line and the heat exchanger (compare figure 6.7, $V_{Lchamber} = 0$) would drastically reduce the liquid surface area and prohibits a fast liquid-gas interchange. The influence on the separation efficiency will be investigated.
- **Instantly concentration equilibrium in the liquid volume V_L:** The fast equalization of the concentration is assumed.

Because of the last point we expect the liquid outflow q_{lout} to possess the uniform krypton concentration of the liquid volume V_L with a typical exchange time

$$t_{lout} := \frac{V_L}{q_{lout}} \tag{6.2.18}$$

In average a ^{83m}Kr atoms stay for a *residence time* t_{lout} in the liquid volume V_L, for which we will have to correct the decay losses.

By the special mounting and the construction of the heat exchanger there is additionally an extra volume V_{Lextra} which is filled by LXe in the beginning of the operation (compare figure 6.7) and which does not take part in the liquid xenon flow and thus in the krypton exchange. This volume does not have the constant krypton concentration of the liquid xenon in the distillation chamber V_{Lch}, the liquid out line V_{Lline} or the heat exchanger V_{Lhex} (all together described by the volume $V_L = V_{Lch} + V_{Lline} + V_{Lhexr}$). Neglecting this extra volume the residence time can be estimated from the amount of xenon in the liquid phase, e.g. $V_L \approx 100\,\mathrm{sl}$, divided by the circulation speed of 5 slpm to $\tau_{lout} = V_L/q_{lout} \approx 20\,\mathrm{min}$ for a pure liquid-out flow. The measurement shows a shorter residence time because of the extra volume as it will be described in the following.

The time behavior of the ^{83m}Kr atoms N(t) in the liquid xenon volume V_L is defined by the flux of incoming ^{83m}Kr atoms $\dot{\mathrm{N}}_{\mathrm{gin}}(\mathrm{t})$, the outgoing krypton particle flux $\dot{\mathrm{N}}_{\mathrm{lout}}(\mathrm{t}) = \mathrm{N}(\mathrm{t})/\tau_{\mathrm{lout}}$ and the losses from decays $\mathrm{N}(\mathrm{t})/\tau$ (with N(t) the number of ^{83m}Kr atoms in the liquid volume V_L):

$$\dot{\mathrm{N}}(\mathrm{t}) = \frac{\mathrm{dN(t)}}{\mathrm{dt}} = \dot{\mathrm{N}}_{\mathrm{gin}}(\mathrm{t}) - \frac{\mathrm{N(t)}}{\tau} - \frac{\mathrm{N(t)}}{\tau_{\mathrm{lout}}} \tag{6.2.19}$$

$$= \dot{\mathrm{N}}_{\mathrm{gin}}(\mathrm{t}) - \frac{\mathrm{N(t)}}{\tau_1} \tag{6.2.20}$$

with $\tau_1 = \tau \cdot \tau_{\mathrm{lout}}/(\tau + \tau_{\mathrm{lout}})$.

The ^{83m}Kr particle flux at the inlet is directly related to the rate $\mathrm{r_{gin}}$ at the ^{83m}Kr decay detector as already mentioned by equation 6.2.10: $\dot{N}_{\mathrm{gin}}(\mathrm{t}) \propto r_{\mathrm{gin}}$, while the same is valid for the liquid-out detector as well: $\dot{N}_{\mathrm{lout}}(\mathrm{t}) \propto r_{\mathrm{lout}}$. As in equation 6.2.18 the outgoing ^{83m}Kr rate $\dot{\mathrm{N}}_{\mathrm{lout}}$ depends on the number of atoms N(t) in the volume V and the exchange time τ_{lout}:

$$\mathrm{N(t)} = \dot{\mathrm{N}}_{\mathrm{lout}} \cdot \tau_{\mathrm{lout}} = \mathrm{A}^{\mathrm{lout}}_{\mathrm{p,q,V}} \cdot \tau_{\mathrm{lout}} \cdot \mathrm{r_{lout}} \tag{6.2.21}$$

$$\longrightarrow \dot{\mathrm{N}}(\mathrm{t}) = \mathrm{A}^{\mathrm{lout}}_{\mathrm{p,q,V}} \cdot \tau_{\mathrm{lout}} \cdot \frac{d\mathrm{r_{lout}}}{d\mathrm{t}} \tag{6.2.22}$$

with $\mathrm{A}^{\mathrm{lout}}_{\mathrm{p,q,V}} = (\mathrm{q_{lout}} \cdot \tau)/(\mathrm{p_{lout}} \cdot \mathrm{V_{det,lout}})$ being the proportional constant, see equation 6.2.10. Finally, the equations 6.2.20 and 6.2.22 can be set equal to receive the relation between the detector rates:

$$\mathrm{A}^{\mathrm{lout}}_{\mathrm{p,q,V}} \cdot \tau_{\mathrm{lout}} \cdot \frac{d\mathrm{r_{lout}}}{d\mathrm{t}} = \mathrm{A}^{\mathrm{gin}}_{\mathrm{p,q,V}} \cdot \mathrm{r_{gin}} - \mathrm{A}^{\mathrm{lout}}_{\mathrm{p,q,V}} \cdot \frac{\tau_{\mathrm{lout}}}{\tau_1} \cdot \mathrm{r_{lout}} \tag{6.2.23}$$

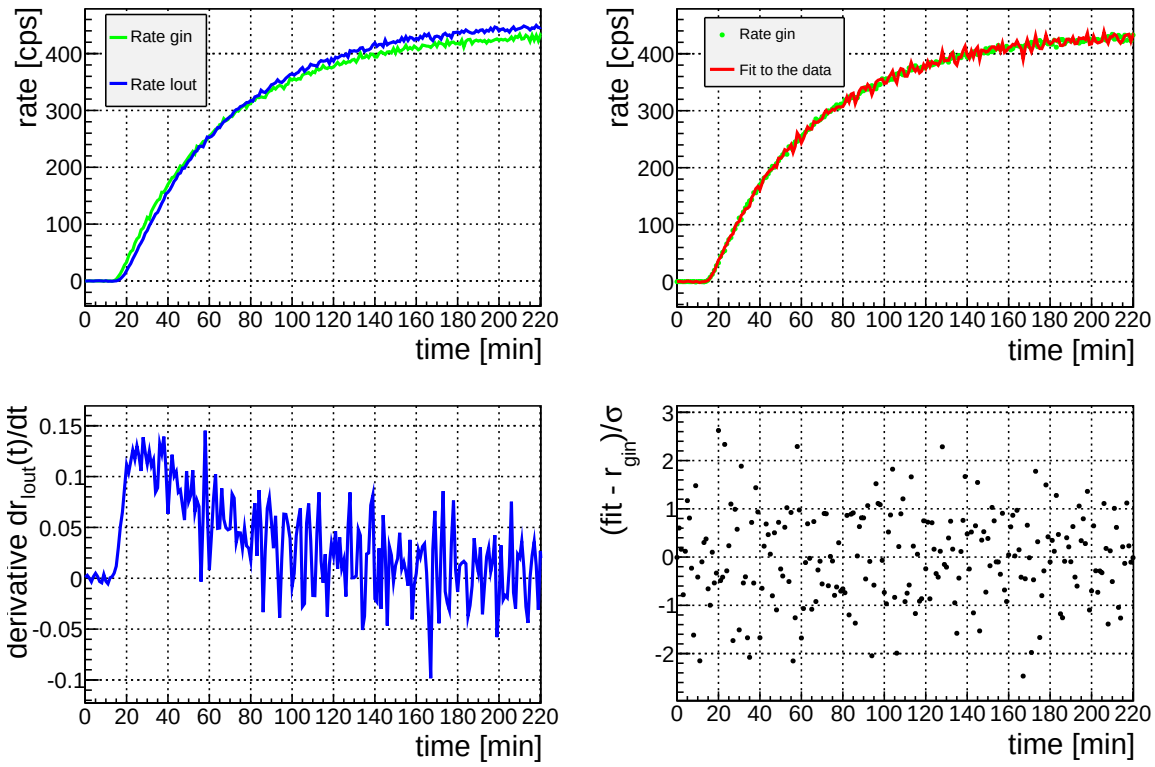

Figure 6.8: **Fitting of the residence time** τ_{lout} to the data. Left top: rates in the gas in detector $r_{gin}(t)$ and in the liquid out detector $r_{lout}(t)$, bottom left: numerically calculated derivative $\dot{r}_{\mathrm{lout}}(t)$. Right top: fit of the rate in the in gas detector $r_{gin}(t)$ with equation 6.2.24, right bottom: residues of this fit.

$$\mathrm{r_{gin}(t)} = \frac{\mathrm{A^{lout}_{p,q,V}}}{\mathrm{A^{gin}_{p,q,V}}} \cdot K_{q_{lout}} \cdot \left(\tau_{\mathrm{lout}} \cdot \dot{\mathrm{r}}_{\mathrm{lout}}(\mathrm{t}) + \frac{\tau_{\mathrm{lout}}}{\tau_1} \cdot \mathrm{r_{lout}(t)} \right) \tag{6.2.24}$$

Again the factor $K_{q_{lout}}$ has been added in order to compensate the error from the mass-flow controller as described before. Furthermore, it follows that $\tau_{\mathrm{lout}}/\tau_1 = (\tau + \tau_{\mathrm{lout}})/\tau \approx 1$ since $\tau = 9500\,s \gg \tau_{\mathrm{lout}} = \mathcal{O}(200s)$. Equation 6.2.24 relates the rate in the gas in detector $\mathrm{r_{gin}(t)}$ with the rate in the liquid-out detector $\mathrm{r_{lout}(t)}$ and its time derivative. Fitting the sum of $\mathrm{r_{lout}}$ and $\tau_1 \cdot \dot{\mathrm{r}}_{\mathrm{lout}}(\mathrm{t})$ allows to determine τ_{lout} by the fit. Using a χ^2 minimization implemented in the ROOT framework [ROO15] $\mathrm{r_{gin}(t)}$ is fitted as function of the liquid-out rate $\mathrm{r_{lout}(t)}$ and its derivative with the residence time τ_{lout} as free parameter. This is shown in figure 6.8 together with the residuals. The residence time is determined to $\tau_{lout} = (197 \pm 8)\,\mathrm{s}$ ($\approx 3.3\,\mathrm{min}$), with $K_{q_{lout}} = 0.98$. The reduced χ^2 of $\chi^2_{Red} = 0.86$ at $N_{dof} = 238$ has been achieved for the fit.

As already mentioned, this type of measurement has only been performed with the smallest liquid xenon amount and the residence time of 3.3 min is only valid under the operating conditions. For the changing flow rates in the gout line, the residence time might change slightly due to the changing pressure conditions in the chamber. Therefore, a second approach has

been used, in oder to take these changes as well as the different liquid xenon inventories into account. By taking the effective volume as free fit parameter to obtain the mass balance, the residence time can be calculated.

6.2.4 Determination of the residence time from the mass balance

To estimate the effective volume and therefore, to achieve a decay correction in the liquid-out line for all measurements with changing liquid xenon reservoir, the formula 6.2.17 for f_l can be modified (using also equation 6.2.15), including the effective volume V_{lout} as free parameter which is related to the residence time $V_{lout} = \tau_{lout} \cdot q_{lout}$:

$$f_l = \frac{(c \cdot \dot{N})_{lout}}{(c \cdot \dot{N})_{gin}} \tag{6.2.25}$$

$$= \frac{r_{lout} \cdot q_{lout} \cdot p_{gin}}{r_{gin} \cdot q_{gin} \cdot p_{lout}} \cdot 1/\nu_l \cdot e^{V_{lout}/(q_{lout} \cdot \tau_{dec})} \tag{6.2.26}$$

Additionally, the sum of the liquid fraction and the gaseous fraction is constrained in the fit to be one, according to the ^{83m}Kr particle balance: $f_l + f_g = 1$.

The same dataset, which is presented in figure 6.8, is used but instead of fitting the initial start up to 240 min, the second method uses the equilibrium concentration of ^{83m}Kr (reached at t=170 min ($\approx$10.000 s)) and the complete dataset with the different flow fractions. The result is shown in figure 6.9. The fit routine calculated the effective volume to $V_{lout} = (27.8 \pm 0.9)$ sl $\approx$ 15 ml liquid xenon, corresponding to a residence time of $\tau_{lout} \approx 5.5$ min for 5 slpm. A reduced χ^2 of $\chi^2_{Red} = 1.05$ at $N_{dof} = 2097$ has been achieved for the fit. The error on the calculation is coming from the uncertainties of the different flow and pressure sensors as well as from the uncertainties in the rates of the different ^{83m}Kr decay detectors and the error propagation, causing this result. For comparison, the data can be fitted also using an effective volume of $V_{lout} = 0$ sl, which is shown in figure 6.10. Neglecting the radioactive decay of the ^{83m}Kr leads directly to a miss-balance in the particle flow. The sum $f_g + f_l < 1$ is obtained since the decaying particles are not included in the description. The reduced χ^2 is calculated to $\chi^2_{Red} = 1.82$. Alternatively, the expected effective volume of $V_{lout} = 100$ sl ($\tau_{lout} \approx 20$ min for 5 slpm) can be used as a check, which is shown in figure 6.11. The particle flow in the liquid-out line is over-estimated since the decay correction is to big. For this fit, a reduced χ^2 of $\chi^2_{Red} = 2.4$ has been achieved.

Using this approach of fitting the effective volume for a second measurement of the same filling level, is giving $V_{lout} = (19.5 \pm 0.8)$ sl $\approx$ 10 ml liquid xenon, corresponding to a residence time of $\tau_{lout} \approx 3.9$ min for 5 slpm with $\chi^2_{Red} = 1.18$ at $N_{dof} = 2597$. Although the system parameter, like pressure and temperature where identical, a discrepancy of about 30% indicates, that the method is limited in the reproducibility. Nevertheless, comparing these residence times, determined by the two methods ($\approx$3.3 min, $\approx$5.5 min, $\approx$3.9 min) with the original expectation value of $\approx$20 min, estimated in chapter 6.2.3, showed, that indeed the concentration equilibrium is reached on a much shorter time scale of a few minutes. The

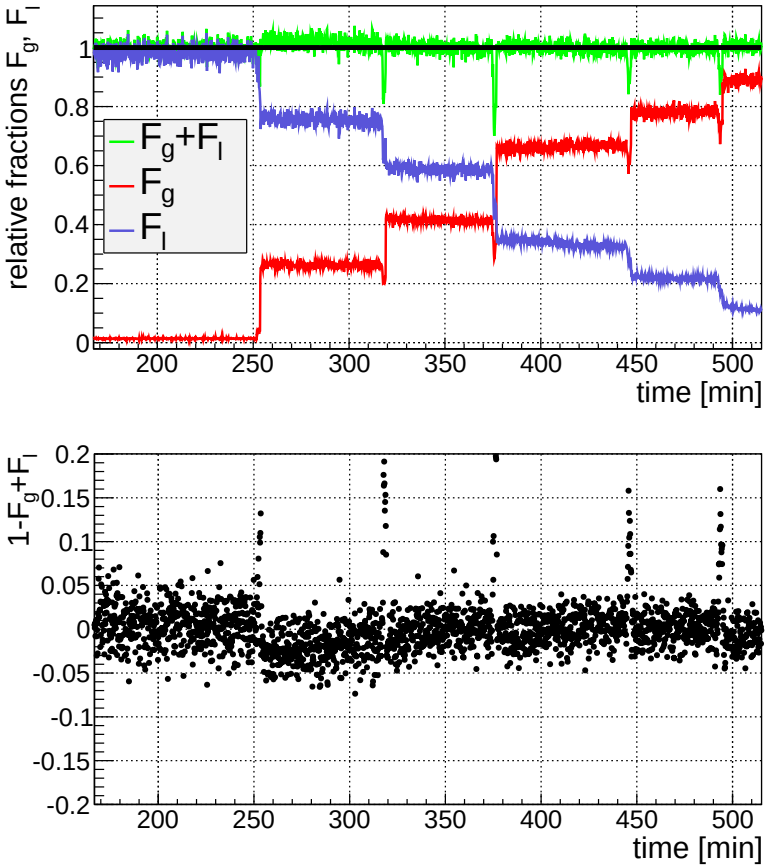

Figure 6.9: **Relative ^{83m}Kr particle flux from fitting the effective volume.** Top: the relative fraction f_l and f_g together with the sum of both, fitted with the effective volume as free parameter. Bottom: Difference between the total particle flux $f_l + f_g$ and the idealized mass-balance which demands $f_l + f_g = 1$.

reason for the short residence times is very likely caused by the distribution of liquid xenon inside the system. As shown in figure 6.7, a fraction of liquid xenon is stored in the heat exchanger inside a dead volume and does not influence the ^{83m}Kr flux. Hence, the residence time is shorter.

6.3 Conclusion

With the second method, all data files have been fitted, which is shown in figure 6.12. The different effective volumes are collected in tabular 6.1. The values for the correction factors $K_{q_{lout}}$ and $K_{q_{gout}}$ are expected to be almost the same for all measurements, since they are related the the uncertainties in the different sensors. Hence, they have been restricted in the fit to a certain margin of $0.95 < K_{q_{lout}}, K_{q_{gout}} < 1.04$. For the effective volume one can expect, that with increasing the xenon reservoir also the effective volume V_{lout} is increasing, which would lead to longer residence times. For a inventory of 98 sl an average effective

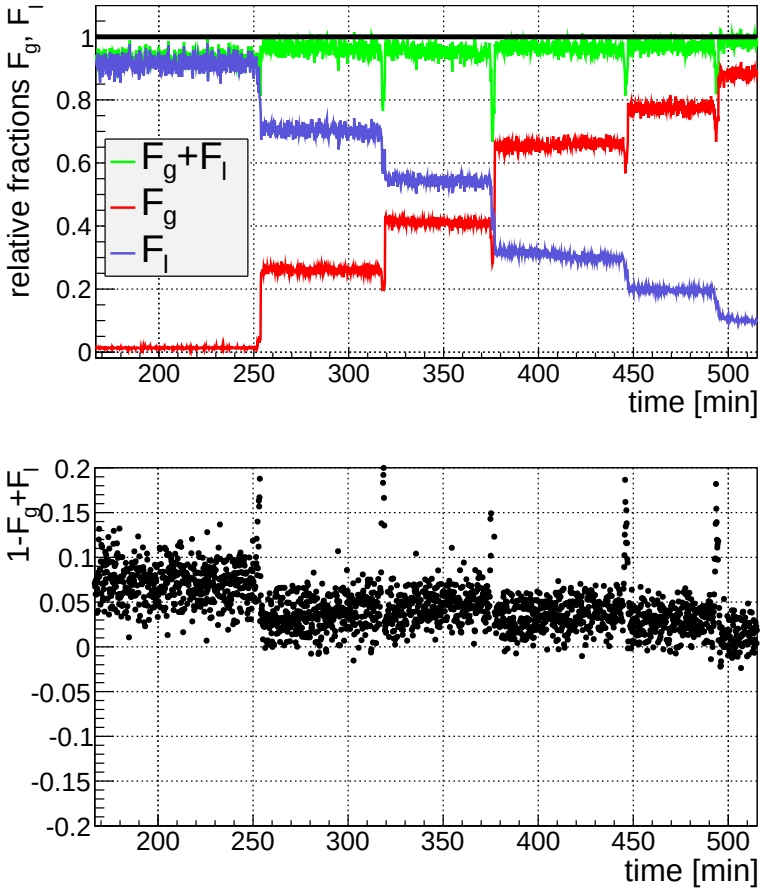

Figure 6.10: **Relative ^{83m}Kr particle flux for a fixed effective volume of $V_{lout} = 0\,sl$.** Top: the relative fraction f_l and f_g together with the sum of both, fitted with the effective volume of $V_{lout} = 0\,sl$. Bottom: Difference between the total particle flux $f_l + f_g$ and the idealized mass-balance which demands $f_l + f_g = 1$.

volume, calculated from the two measurements results in $\overline{V}_{lout} = (23.2 \pm 4.1)\,sl$[14]. For an inventory of 127 sl an average effective volume of $\overline{V}_{lout} = (60.0 \pm 20.2)\,sl$[15] is calculated from the two measurements, being higher as expected. But, the final measurement at 198 sl gives a shorter residence time with an effective volume of $V_{lout} = (45.0 \pm 3)\,sl$, being in contradiction to the expectation stated before. In addition, the differences in the single effective volumes indicate, that the reliability of the procedure is in general limited. The reason for this behavior might be related to the system conditions. As already mentioned before, the stability of the system at high xenon inventories is limited which is also reflected in the fit errors, being larger for higher inventories. Furthermore, the very high values of the reduced χ^2 for the larger inventories indicate that the model for this regime is not complete. Eventually, additional processes might also influence the krypton transport, e.g.

[14]The uncertainties of the average has been enhanced by the $\sqrt{\chi^2}$ of this match of the two values to get a realistic uncertainty

[15]The uncertainties of this average has also been enhanced by the $\sqrt{\chi^2}$ to get a realistic uncertainty

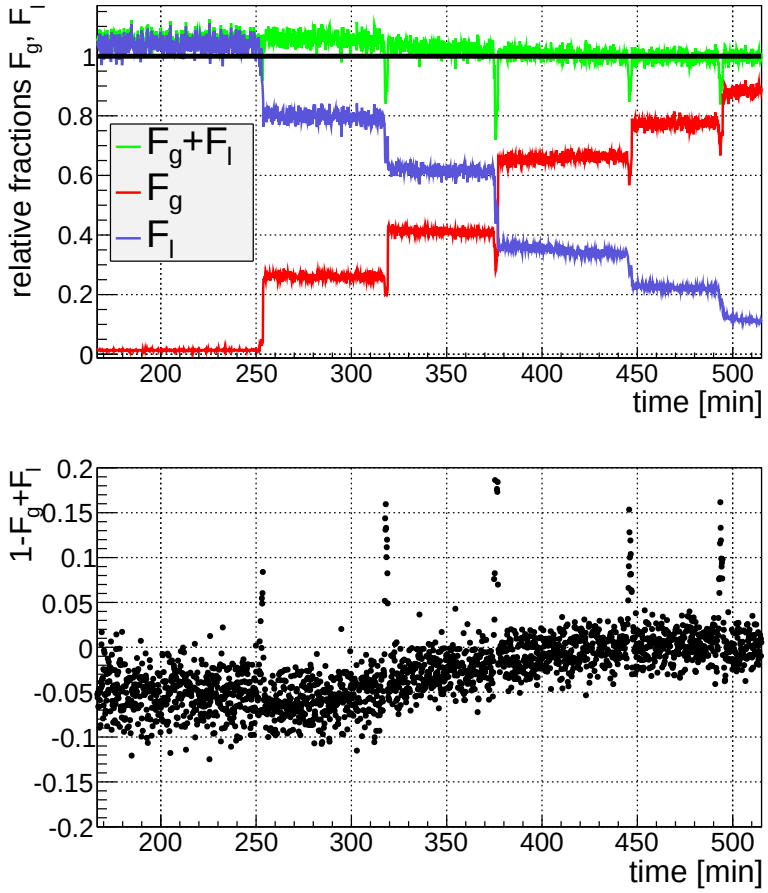

Figure 6.11: **Relative ^{83m}Kr particle flux for a fixed effective volume of $V_{lout} = 0$ sl.** Top: the relative fraction f_l and f_g together with the sum of both, fitted with the effective volume of $V_{lout} = 100$ sl. Bottom: Difference between the total particle flux $f_l + f_g$ and the idealized mass-balance which demands $f_l + f_g = 1$.

the instabilities could cause turbulences which lead to an inhomogeneous particle transport through the liquid xenon which have to be investigated in order to perform an accurate description.

Despite these short comings, a separation factor S can be defined as the fraction

$$S := f_g/f_l = \frac{(c \cdot \dot{N})_{gout}}{(c \cdot \dot{N})_{lout}}. \tag{6.3.1}$$

Which is describing the enhancement in the gaseous phase, related to the liquid phase. Using equation 4.2.2 for the ratio of the concentrations and equation 6.2.6 to exchange the particle flow at constant temperatures, the expectation for the separation factor can be calculated to

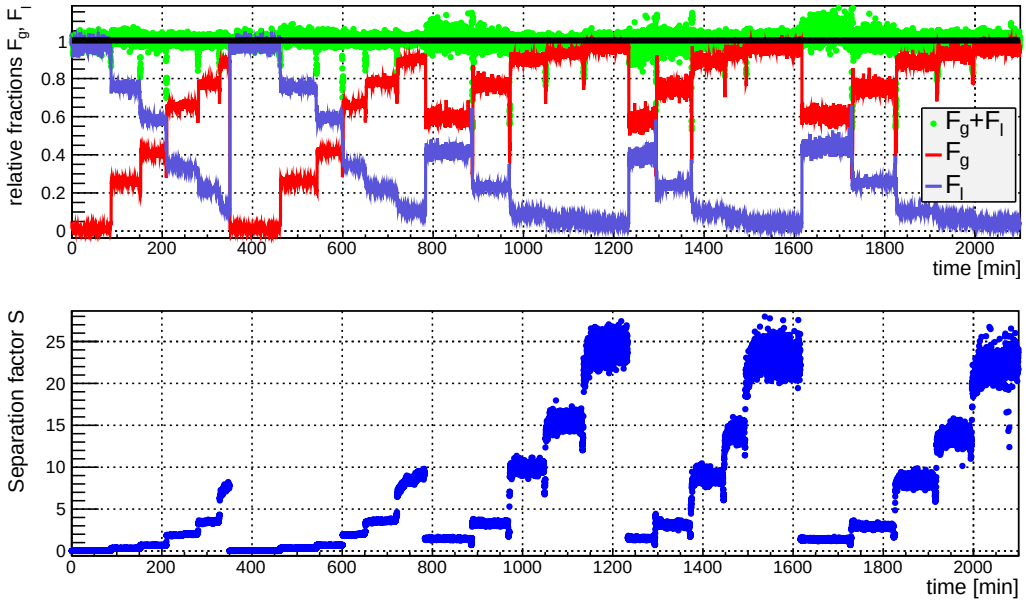

Figure 6.12: **Fit to all measurements.** This plot shows all five measurement connected in series. Top: relative fractions f_g and f_l for the different measurements together with its sum. Bottom: separation factor S, determined from different measurements.

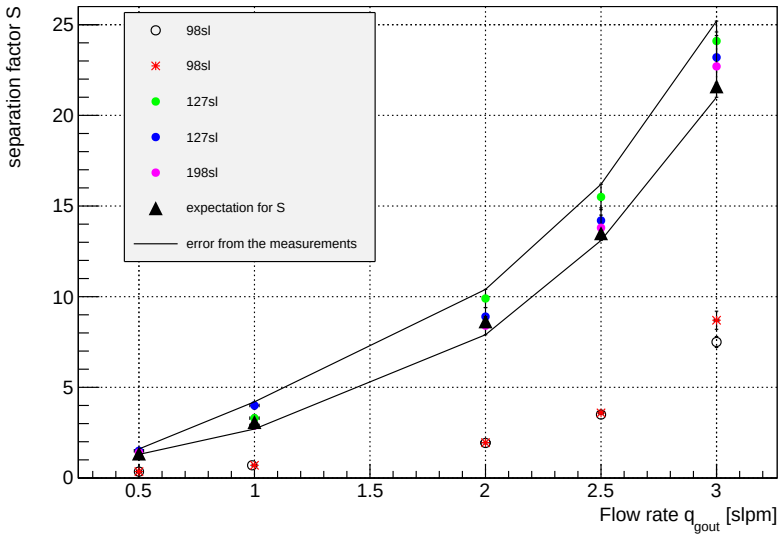

Figure 6.13: **Separation factors for different flow rates and xenon inventories.** This plot shows the averaged separation factors, presented in figure 6.12, as function of the gas out flow for different filling levels, together with the expectation from equation 6.3.2 including the uncertainties of the flow determination. The error on the data points has been calculated from the standard deviation.

Table 6.1: **Results from fitting the different data sets.** The effective volumes V_{lout} for different measurements are collected together with the correction factors $K_{q_{lout}}$ and $K_{q_{gout}}$.

Inventory [sl]	V_{lout} [sl]	$K_{q_{lout}}$	$K_{q_{gout}}$	χ^2_{Red}
98	27.8 ± 0.9	0.990 ± 0.001	1.0150 ± 0.0001	1.05
98	19.5 ± 0.8	0.990 ± 0.003	1.0139 ± 0.0004	1.18
127	24.8 ± 7	0.9625 ± 0.0001	1.0135 ± 0.0003	8.6
127	71.5 ± 4	0.9870 ± 0.0001	1.0001 ± 0.0001	2.5
198	45.0 ± 3	0.980 ± 0.001	1.0010 ± 0.0003	4.9

$$S = \alpha \cdot \frac{q_{gout}}{q_{gin} - q_{gout}}. \tag{6.3.2}$$

In total five measurements with different liquid xenon inventories are presented in series. The first two measurements have been performed with a total xenon inventory of ≈ 98 sl, before the amount of xenon is increased to ≈ 127 sl (measurement 3 and 4) and finally to ≈ 198 sl (measurement number 5). Obviously, the separation performance depends on the inventory in the system and the flow rate in the gas-out line. For a better comparison, the separation factor S has been extracted from the data and is summarized for the different flow-rates in the gaseous outlet q_{gout} in figure 6.13. The error on the separation factor is calculated as the standard deviation from the mean value. While measurements with 98 sl show much smaller separation factors than for an inventory of 127 sl, there is no significant difference between 127 sl and 198 sl, which are also in agreement with the expectation values according to equation 6.3.2. The measurement at the lowest inventories indicate that the separation for this level is not sufficient. The dependency on the filling level might be related to the insufficient surface area of the liquid xenon in the distillation chamber: $V_{Lch} \approx 0$. In order to achieve a good separation, a sufficiently large liquid/gaseous xenon interface seems to be required requesting $V_{Lch} > 0$. For 98 sl of xenon it is possible, that the majority of the liquid is stored in the extra volume of the heat exchanger at its bottom. Increasing the liquid reservoir V_L would fill also liquid xenon into the chamber $V_{Lch} > 0$ providing a sufficiently large gaseous/liquid xenon interface giving rise to the expected separation according to equation 6.3.2. Comparing the measured separation factors with the expectation values shows good agreement for the two larger inventories within the uncertainties of the measurements.

It has been demonstrated, that the separation of krypton and xenon is possible also for very low concentrations well below the ppt level of krypton in xenon and that the krypton concentrations in the gaseous and liquid phases follow the ratio of the vapor pressures at these very low krypton concentration. Hence, the cryogenic distillation, especially used as a multi-stage distillation system is feasible for achieving the purity, needed at the XENON1T experiment. The single stage distillation station will be used as input condensing station for the Phase-1 column and due to its construction, which allows to use it as separation station, it is called pre-separator in the following descriptions.

Construction and commissioning of the Phase-1 distillation column

7

In this chapter, the mechanical construction of the Phase-1 column is reviewed before the initial operation and commissioning phase will be introduced. The stability of the different operation modes are presented together with the determination of separation characteristics using the different methods inserted in chapter 5.

7.1 Setup of the Phase-1 column

The fabrication of the single components has been performed for the most parts in the mechanical workshop of the Institut für Kernphysik in Münster. Additionally, a mobile orbital welding station (Orbitec) has been used, which allowed to do the complete gas routing (gas lines of half and quarter inch diameter) directly in the lab next to the column in order to guarantee proper fitting of the parts and to achieve extreme leak-tightness in the weld-seems, as requested in chapter 4.1. An example for orbital welding is given in figure 7.1. The gas-routing lines have been welded by hand to the vacuum insulation flange while the lines have been equipped with proper fittings, using the orbital welder.

The pre-separator, already introduced in chapter 6 has been directly used for the Phase-1 column without any changes. It is still mounted in the same location at the main vacuum flange, while only the inner piping has been changed. Together with the pre-separator, the reboiler vessel is mounted in the bottom of the column following the initial design (see figure 4.9). In figure 7.2 the reboiler, mounted to the main flange is shown.

The four threaded rods hold the reboiler in place and are constructed in a way, which allows to manipulate the horizontal orientation of the reboiler. Since the package material is mounted on top of the reboiler it allows to adjust the vertical alignment of the package tube by using the rods. This is of crucial importance to guarantee a good orientation, which prohibits that the liquid xenon is leaving the package material and rinses against the wall.

The package tube, consisting of the four segments, was mounted in the clean-room of the institute to avoid any contamination of the tube with dust particles. The piece of package

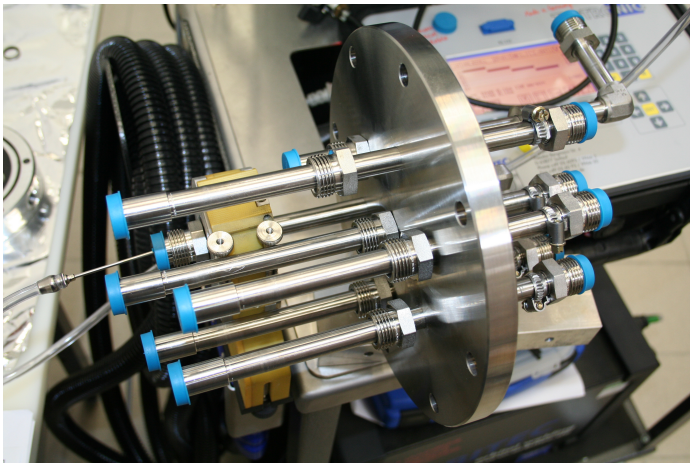

Figure 7.1: **Orbital-welding of the gas-piping.** The picture shows the welding of fittings to the half-inch pipe of the gas distribution flange. The lines inside the vacuum insulation flange are used to guide the xenon inside the distillation column and to extract the purified liquid. Additional lines for diagnostics are also foreseen.

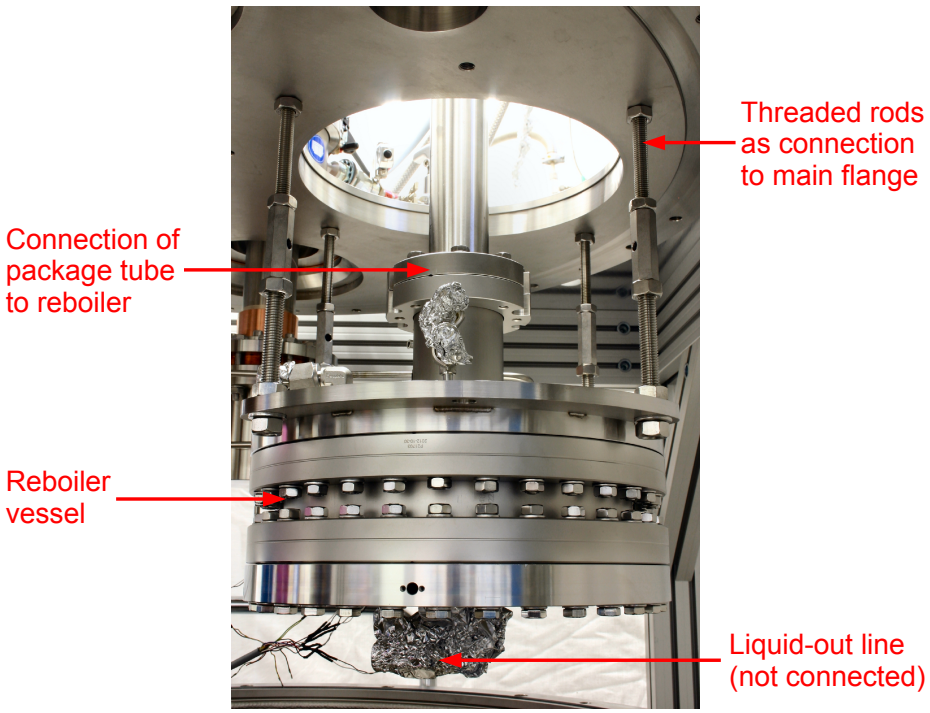

Figure 7.2: **Reboiler vessel mounted to the main flange.** The reboiler, consisting of a CF-250 distance flange is mounted with threaded rods to the main flange in the bottom of the column.

material are surrounded by a metal stripe with tiny fins, that are bended (see figure 7.3, top-left picture) in order to hold the pieces in place inside the tube and to collect the liquid, that is rinsed on the surface of the tube to conduct it to the inside. The segments are connected with three distance flanges, which are equipped with the liquid-feed and analysis

ports. Furthermore, the distance flanges have a funnel shape to collect the liquid coming from the segment above to guide it to the following segment. Finally, the package tube is mounted to the reboiler vessel and a silicon insulated heating tape, which is supposed to be vacuum compatible, has been wrapped around and fixed with steel metal clamps.

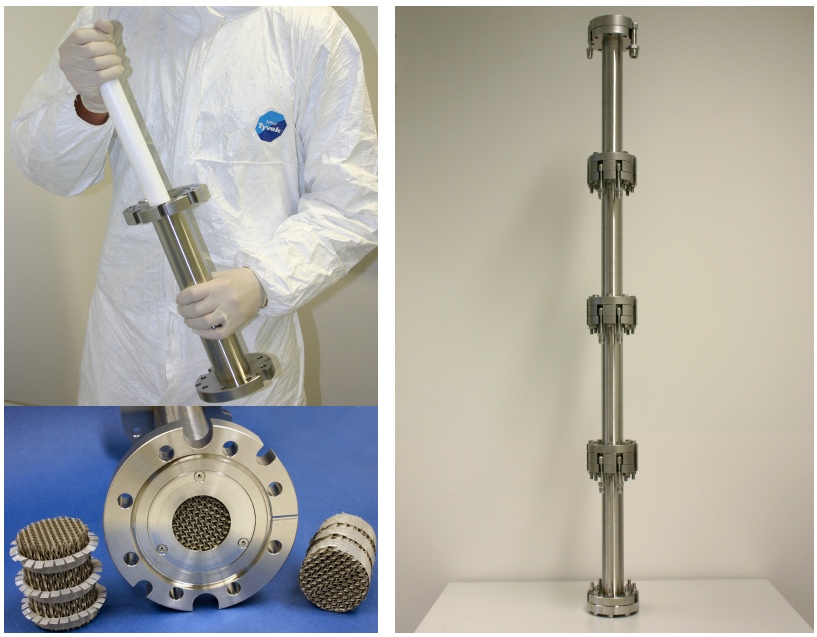

Figure 7.3: **Mounting of the package tube.** Top-left: Package material, with bended fins and filled in the package tube. Bottom-left: The package material is pressed to the pipe with a clean PTFE-rod. Right: Phase-1 package tube, made from four segments, finally mounted inside the clean-room.

The condensing station at the top is designed very similar to the pre-separator, using the copper cooling block as sealing but is of larger diameter. The funnel shaped condensing chamber has a liquid outlet to the package equipped with a DN63-CF flange. In figure 7.4 the mounting of these parts are shown. For additional the liquid nitrogen cooling, a copper tube has been bent around a copper block, which acts as connection between cold-head and condensing chamber. For good thermal contact, the copper tubed has been soldered to the copper. The liquid nitrogen can be injected over dedicated vacuum feed-troughs. At the bottom, the top-condenser is equipped with a funnel shape and a DN63-CF flange to provide the connection to the package material. This connection is done with a stainless steel bellow, in order to guaranty a certain flexibility. This is important for the reduction of mechanical stress due to the thermal shrinking and stretching during the cool down or baking[16] processes.

The manipulation of the gas-routing inside the vacuum insulation vessel was of particular importance. As already pointed out, several valves inside the insulation vacuum vessel, allow to influence the xenon flow from outside the vessel. Especially the different valves to

[16]Using the coefficient of linear thermal expansion of stainless steel (alloy 316L in the temperature range between +20°C and +100°C) $\alpha_{316L} = 16.0 \cdot 10^{-6}\,\mathrm{K}^{-1}$ [Thy11], the thermal expansion for a 1 m-package tube during baking to +100°C can be estimated to $\Delta L = \alpha_{316L} \cdot L_0 \cdot \Delta T = 1.3\,\mathrm{mm}$.

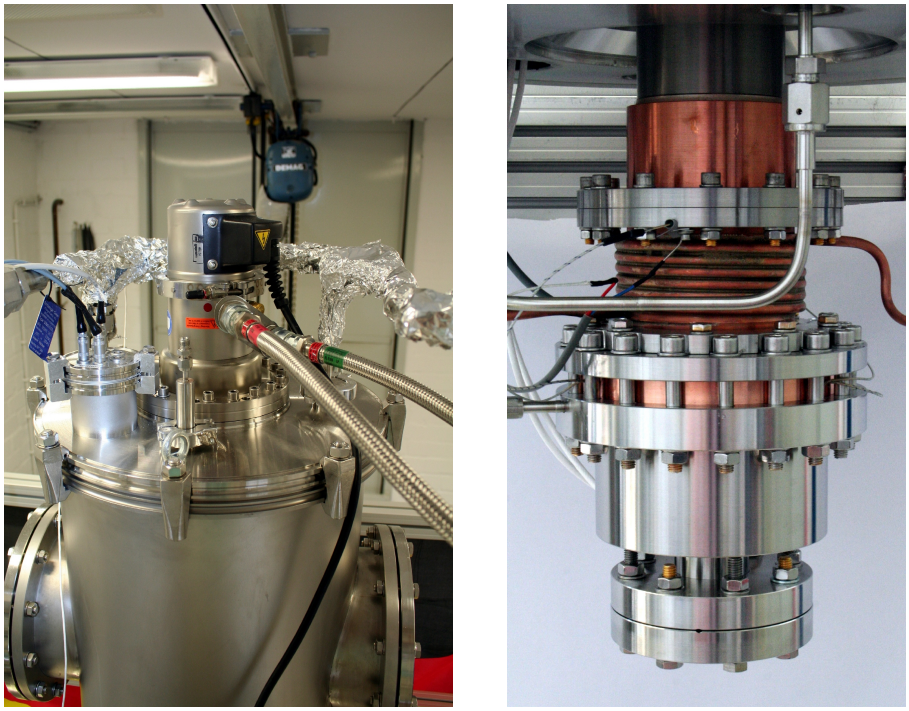

Figure 7.4: **Mounting of the top-condenser.** Left: Top condenser mounted to the vacuum insulation vessel of the Phase-1 column. Right: Top-condenser, consisting of stainless steel vessel and copper block, connected to the cold-head via special clamping flanges and liquid nitrogen copper cooling block in between.

control the liquid-in feeds are of great interest. Since commercial available cold valves are very expensive, custom cold-valves have been designed using standard bellow-sealed valves (Swagelok, SS-4BG-V51) and turn them by a fork shaped transmission (see figure 7.5, left picture), sealed with fluorine-elastomer gaskets in the feed-through to the atmosphere. It was tested, that the valves can be operated at lower temperatures than specified by the manufacturer. Due to its construction, it is possible to detach the fork shape transmission from the valve to avoid thermal bridges to the outside.

In order to control the valve position, a potentiometer readout has been designed using gear-wheels to transform the valve turnings into a changing residence of a potentiometer (see figure 7.5, right picture).

7.2 Design of the control interface

The design of the control system (Slow Control, SC) is of particular importance for the regulation of the column. Beside displaying the different sensor outputs, it has to allow the regulation of the different control variables, to store the SC data and it has to be equipped with a dedicated alarm system. For the Phase-1 column, the scheme of the SC system is presented in figure 7.6.

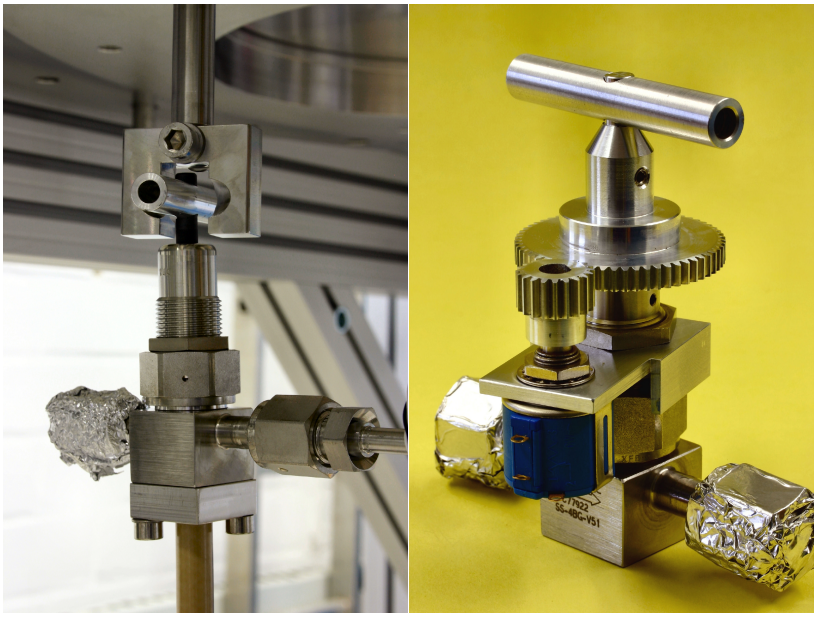

Figure 7.5: **Design of a custom cold valve.** Left: Cold valve mounted inside the column. The fork shaped transmission allows to turn the valve from the outside. Right: Potentiometer readout mounted to a valve. The readout of the resistance allows to monitor the position (open/close).

Key component of the system is the Compact Rio controller (National Instruments, type NI-9074). It is of the same type than used for the purification system, already introduced in chapter 3.1. The different modules allow to read-out the different pressure and flow sensors directly (Analog Input Module NI-CRIO-9205) and by using a custom-made constant current source, it also allows to measure the temperature at the PT1000 sensors as voltage drop for the changing resistance. An analog output module produce the auxiliary voltages that are needed to adjust the flow at the three flow controllers (set-point voltages). Similar to the purification system, one Ethernet port is used for communication with a temperature controller (Lakeshore, model 336) and the other port for communication with the lab-PC for programming, data-storage and as alarm system. The Lakeshore is used to measure the temperature at the different silicon diodes, one at each condensing station and one at the reboiler. It also regulates the temperature at the pre-separator with its internal 100 W-power source. Additionally, it allows to regulate the heating power at the top-condenser and the reboiler by controlling the associated power sources via analog voltages.

The SC program is designed to control the system in different operation modes. As it will be explained in the next chapter, different use-cases have to be considered (cooling, filling, distillation, recuperation) which are distinguished by different control parameters. For example, during the filling process, the temperature at the top condenser is regulated actively, in order to not freeze the xenon, while in the distillation mode, the pressure in the system is regulated by heating at the reboiler which leads automatically to constant temperature at the top-condenser without the need to regulate it actively. The different cases are implemented, providing several PID algorithms for the different operation modes. The SC data is transfered to the Lab-PC and stored on the on-board drive in ASCI format. Regularly

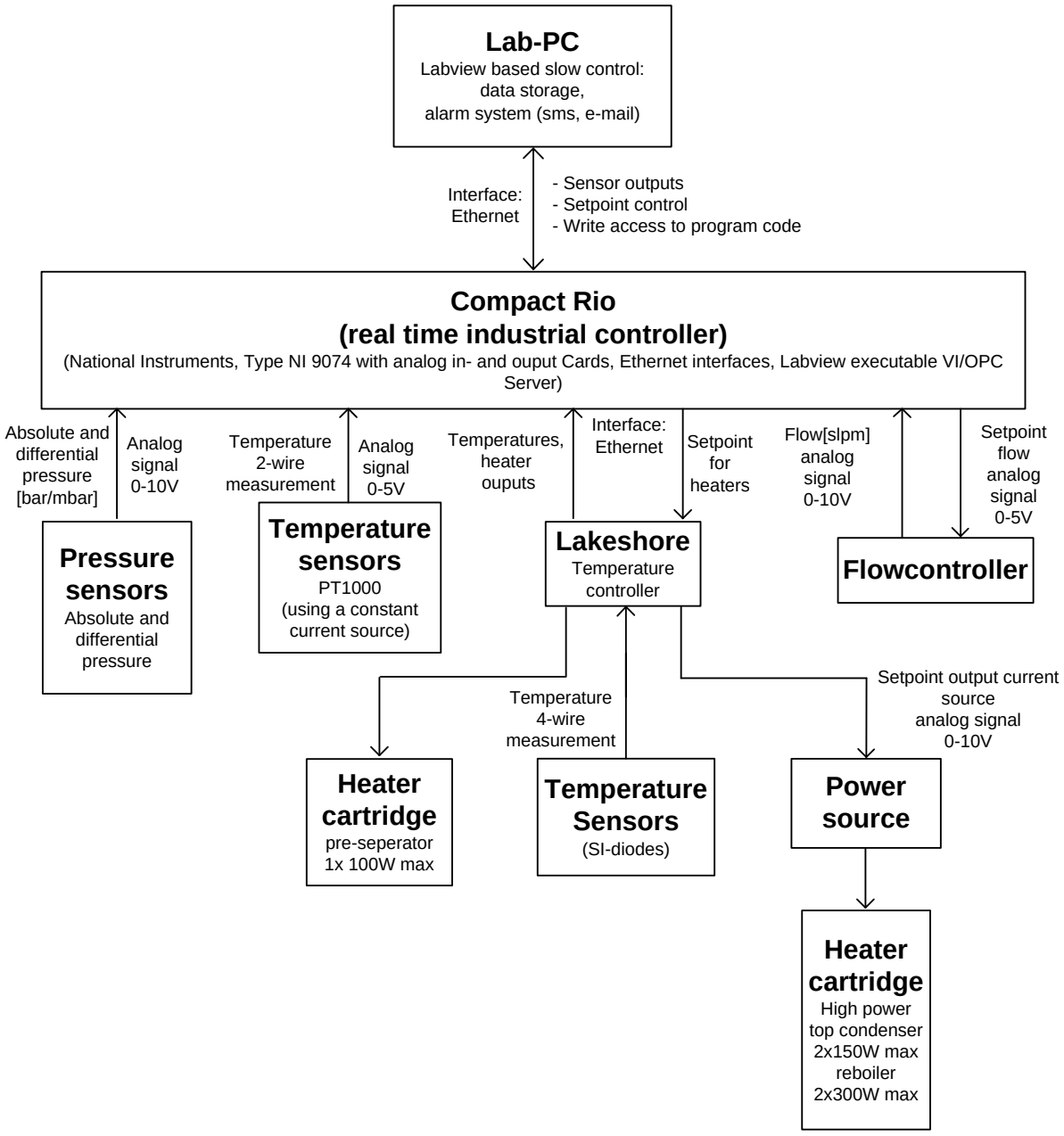

Figure 7.6: **Chart of the slow control system.** The chart shows the architecture of the SC system, developed for the Phase-1 column. The different sensors and devices are read-out and controlled by a Compact Rio system, using a Labview based software.

backups with the dedicated server ensure the securing of the data. Additionally, the values are read by the alarm program, checking whether actual values of crucial parameters, e.g. pressure inside the column or different temperatures, are within the pre-defined ranges. In case of an alarm, e-mails as well as SMS are sent to the operators, allowing for short reaction times.

7.3 Initial operation and commissioning

The Phase-1 column reached a final height of about three meter. As already shown in figure 3.1, the column has been connected to the gas purification system, which allows to supply the column with xenon and to perform the distillation tests. The off-gas has been collected in an additional bottle, mounted next to the column and using the principle of cryogenic pumping by immersing the bottle into liquid nitrogen, as already presented in chapter 3.1. Furthermore, the RGA-2 setup is mounted to the analysis line. The complete setup is shown in figure 7.7.

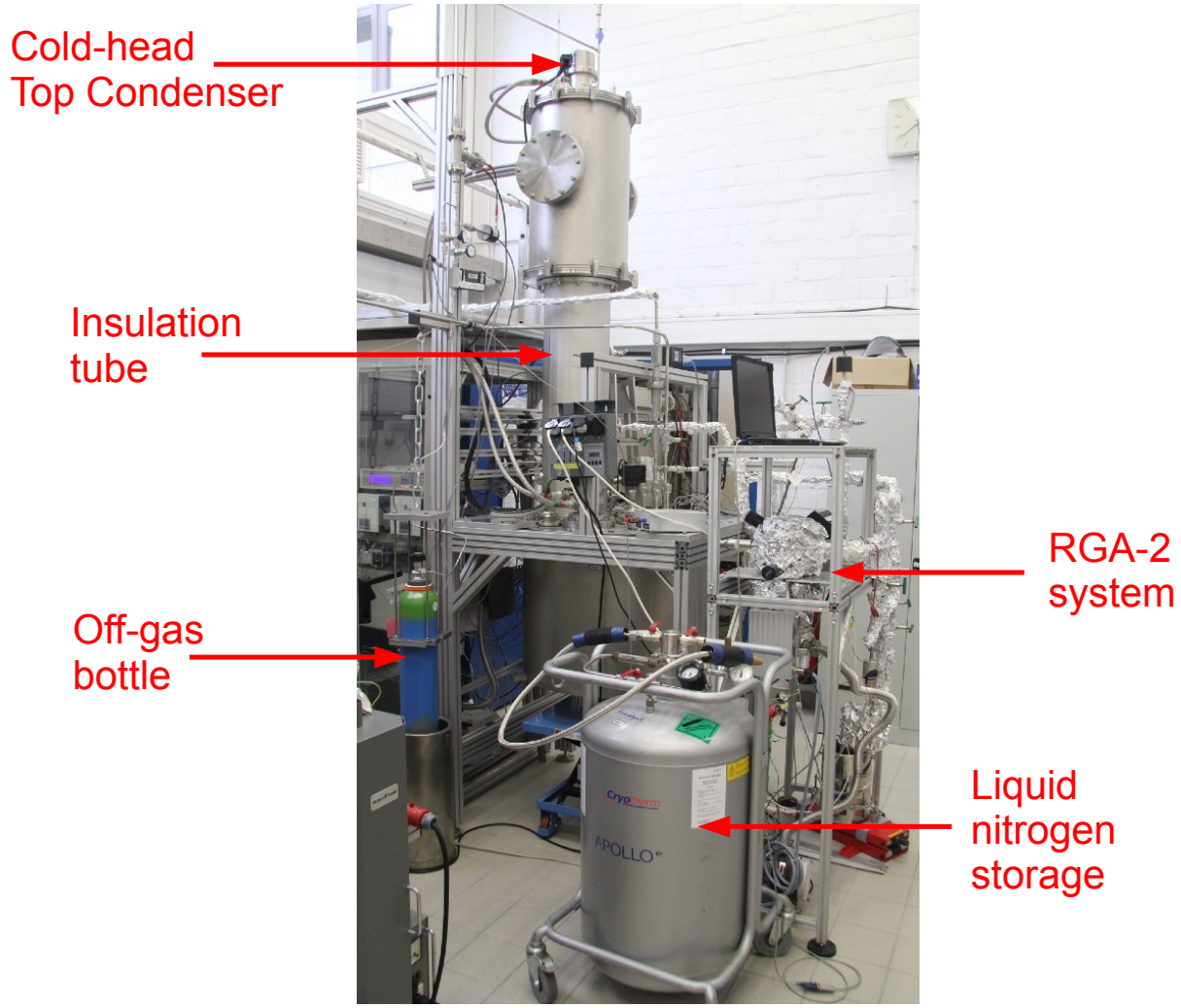

Figure 7.7: **Phase-1 distillation column.** This picture shows the Phase-1 distillation column, equipped with one meter package material. In front of the column the RGA-2 setup is mounted next to liquid nitrogen dewar.

Before the first distillation test is started, the system has been evacuated, using the RGA-2 as pumping station for the inner part of the system and the implemented vacuum system to produce the insulation vacuum of $\approx 1 \cdot 10^{-5}$ mbar. Simultaneously, the package tube has been baked, by the implemented heating tape to $\approx +100°C$, in order to remove impurities

(mainly water), sticked to the surfaces of the package material. Subsequently, first test on the cooling power of the cold-head mounted to the top condenser have been performed. The cooling power was measured by regulating the indicated temperature, TIC12 (figure 4.7) to a pre-defined set-point value. This is realized, by a PID algorithm, implemented to the control software, which controls the heating power at the cartridges (compare scheme of the control system in figure 7.6). The cooling power has been measured to $\approx 205\,\mathrm{W}$ at $\mathrm{T} = -98°\mathrm{C}$ for the empty system without xenon. The stability of the set-point temperature can be used to qualify the stability of the cold-head. Since the PID regulation is designed to control the heaters, based on a constant cooling power, any drastic changes in the temperature is directly coupled to the cold-head performance, expecting that the heater control is working properly.

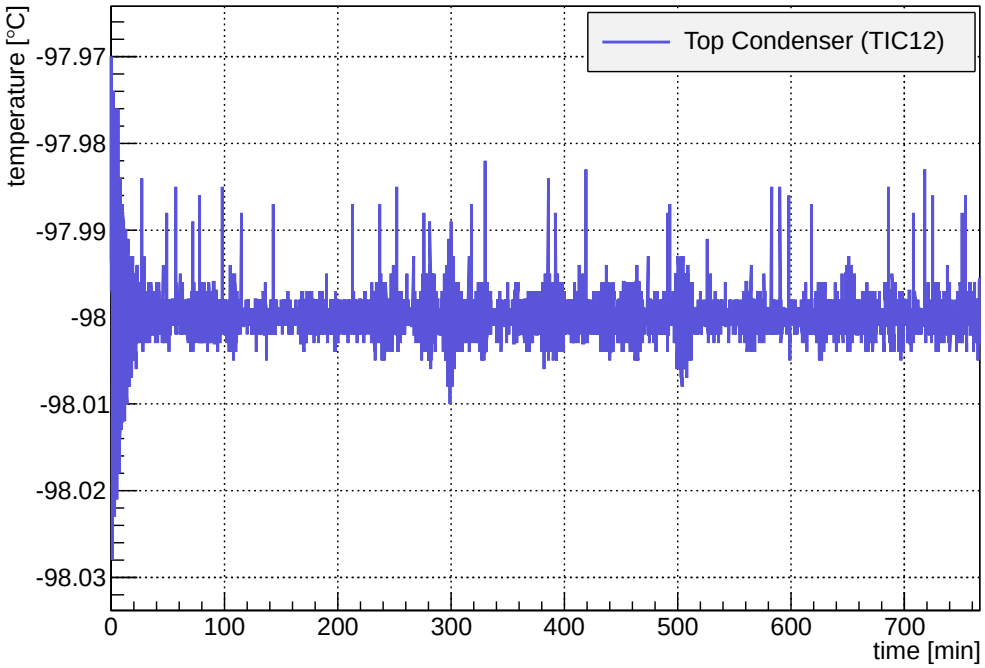

Figure 7.8: **Cooling test of the top condenser.** The plot shows the evolution of the temperature at the top condenser in a cooling and stability test of about 12.6 h at a set-point temperature of $\mathrm{T_{Set}} = -98°\mathrm{C}$. The initial 30 min are dominated by the running-in characteristics of the PID regulation.

In figure 7.8, the measured temperature at the top condenser is shown. Over ≈ 12.6 hours of measurement time, the temperature is found to be stable at $\mathrm{T_{Meas}} = (-97.999 \pm 0.002)°\mathrm{C}$. The error has been calculated as standard deviation started after 300 min, to not consider the initial running-in of the PID circuit. The span between maximal measured temperature and minimal measured temperature has been determined to be 0.03°C only. The fluctuations in the power output has been recorded to be less than 0.5% with a span between maximum power and minimum power of $\approx 5.5\,\mathrm{W}$.

Although the cold-head fulfills the requirements for the cooling power, calculated in chapter

4, a substantial loss of $\approx 50\,\mathrm{W}$ in cooling power compared to the specifications from the company has been confirmed. The losses are very likely caused by heat bridges due to the connection of the top condenser with the package tube and also by the connection of the liquid nitrogen supply line. Furthermore, the heat radiation from the walls is not negligible and in addition, the cold-head works as a cryogenic vacuum pump, decreasing the pressure in the insulation vessel by about one order of magnitude to $\approx 8 \cdot 10^{-7}\,\mathrm{mbar}$.

Cool-down and filling of the Phase-1 column

After pumping, baking and leak checking, the column is filled with 2.5-3.0 bar of xenon. After turning-on the top condenser and reaching the condensation point (a set-point temperature of $T_{Set} = -98°\mathrm{C}$ is chosen), the xenon gets liquefied and is rinsing down the column. The evaporation of the xenon on the warm surface leads to a progressive cool down of the system. Due to the passive cooling, it takes several hours before additional xenon can be filled to the system, in order to avoid overpressure in the system . In figure 7.9, a cooling down procedure is shown. The column has been filled to a pressure of 2.7 bar before the cold-head at the top-condenser was turned on at $t = 12\,\mathrm{min}$ to the set-point value. When reaching the liquid xenon temperature, the column is cooled down by the evaporation of liquid xenon droplets at the surface. At some point the temperature in the package is only decreasing very slowly along the tube and additional xenon has to be added in order to ensure a proper cooling of the whole tube, shown in figure 7.10. The cooling time between between figure 7.9 and figure 7.10 was four days, indicating, that in deed a certain amount of xenon is needed to cool down the whole setup and to keep it cold over time. After filling additional xenon, the temperature in the package and also in the reboiler goes down faster than before. Finally after finishing the initial cooling by adding xenon three times, the filling of the reboiler can be started.

In the reboiler, the purified xenon is collected and the increasing height of the liquid level inside the vessel during the filling can be controlled with two different techniques. A differential pressure measurement allows to monitor the relative changes of the liquid level with high accuracy, while an array of PT1000 sensors allows to control the level at discrete locations independently.

In figure 7.11, the construction for the leveling with PT1000 sensors is shown. In total four sensors are mounted to a stainless steel rod and fixed to a CF-40 feed-through flange, where the sensors are connected. The flange is mounted to the top of the reboiler, whereat the PT1000 sensors, inside the reboiler show a visible temperature drop when they are in contact with the liquid xenon (see figure 7.13, middle). The sensors are sealed with a special ceramic and equipped with PTFE isolated cables in order to keep the xenon clean. Although this technique gives only a rough estimation on the height of the liquid level, it is a redundant system beside the differential pressure measurement, which is used to stabilize the mass-balance of the column. The working principle is shown is figure 7.12. The hydrostatic pressure p_{Hyd} is directly connected to the height h of the liquid xenon inside the reboiler.

$$p_{\mathrm{Hyd}} = \rho_{\mathrm{LXe}} \cdot g \cdot h \qquad \rightarrow \qquad h = \frac{p_{\mathrm{Hyd}}}{\rho_{\mathrm{LXe}} \cdot g} \tag{7.3.1}$$

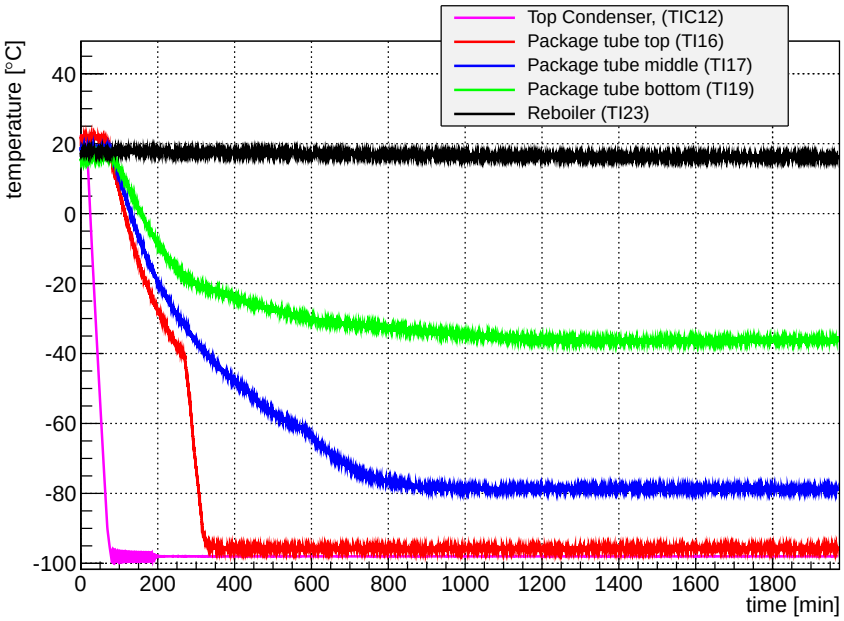

Figure 7.9: **Pre-cooling of the Phase-1 column.** After injecting xenon to the column, reaching a pressure of 2.7 bar, the cold-head has been turned on and regulated to $T_{Set} = -98°C$. The package tube is slowly cooling down for several hours by liquid xenon droplets.

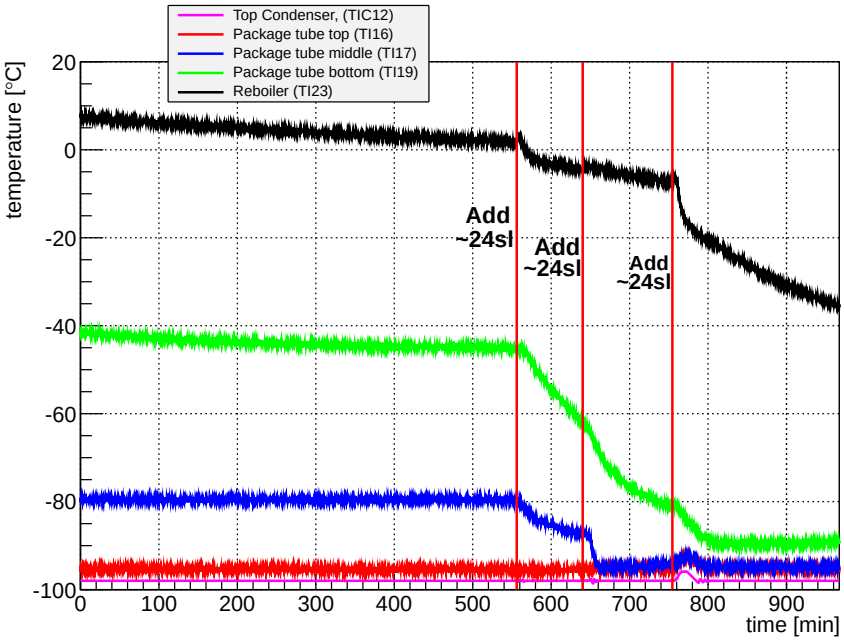

Figure 7.10: **Filling of the Phase-1 column.** After injecting additional xenon in three steps (about 3×24 sl) to the column, the cooling of the package proceeds before the filling of the reboiler is started

Figure 7.11: **Level control using PT1000 sensors.** Four temperature sensors are mounted with a stainless steel rod to a CF-40 feed-through flange, that is connected to the reboiler. The contact with liquid xenon leed to a visible drop in temperature.

The measurement of p_{Hyd} is technical realized by two stainless steel tubes of quarter inch diameter, welded to the top of the reboiler vessel. While one line stays in the gas phase, the other one goes almost all the way down to the bottom of the reboiler. When the liquid level is increasing it is also filling up the long pipe.

By measuring the pressure difference p_{Diff} using a capacitive manometer (MKS, type 121A Baratron with a range of 100 mbar and an accuracy of $\pm 0.5\%$ of reading), the hydrostatic pressure p_{Hyd} of the liquid xenon level and finally the height h of the liquid level in the reboiler can be determined ($p_{\mathrm{Diff}} = p_{\mathrm{Hyd}}$).

In figure 7.13 the signals at the PT1000 sensors (TI23-TI26) and the differential pressure sensor (Δp27) during a filling of the reboiler are presented. The filling starts with 4 slpm before the flow rate is increased to 5 slpm. After $t \approx 20$ min, the differential pressure starts to increase, which indicates that the liquid level hit the quarter inch pipe. The first PT1000 sensor (TI26) is reached after $t \approx 50$ min, showing a drastic temperature drop, directly going down to liquid xenon temperature and staying constant. The second PT1000 sensor (TI25) is reaching liquid xenon temperature after $t \approx 95$ min. The distance between the two sensors is $h \approx 1$ cm. The difference in the hydrostatic pressure between $t \approx 50$ min and $t \approx 95$ min has been measured to $p_{\mathrm{Hyd}} = 2.4$ mbar. In comparison, the hydrostatic pressure for a liquid xenon column of 1 cm height is calculated to $p_{\mathrm{Hyd}} \approx 2.8$ mbar for a liquid xenon density of 2870.2 kg/m^3 at the given conditions. Since the resolution for the PT1000 readout

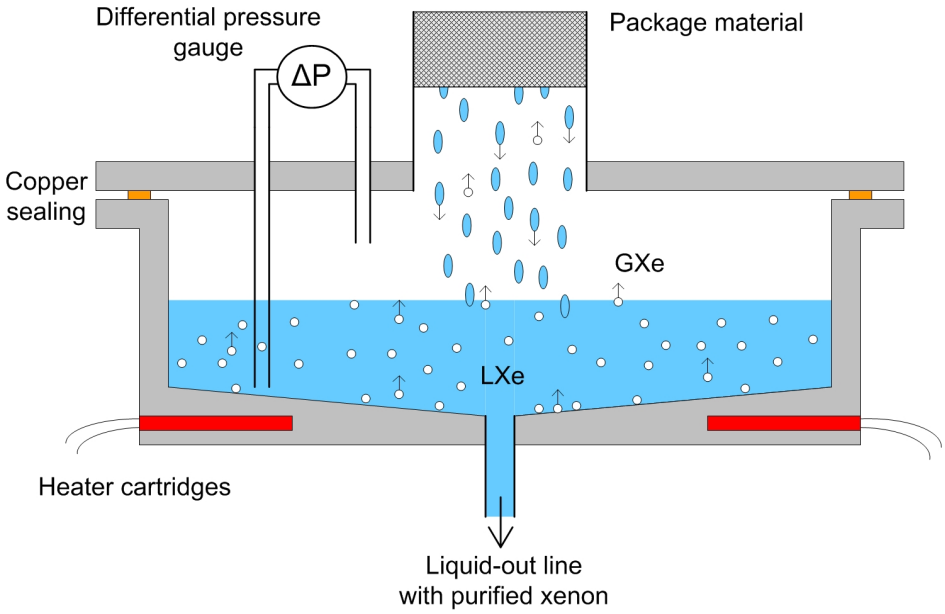

Figure 7.12: **Level control using differential pressure measurement.** The hydrostatic pressure, to quantify the height of the liquid is determined by measuring the differential pressure between the two gas lines. One is immersed in the liquid, while the other is sorter and open to the gas phase above the liquid.

and the knowledge about the sensor position are limited, the accuracy of this estimation is also limited as well. Nevertheless, it shows, that the differential pressure measurement gives feasible values and additionally the PT1000 sensors allow for a rough observation of the liquid level. During the filling, the hydrostatic pressure further increased to $p_{\mathrm{Hyd}} = (6.7 \pm 0.1)\,\mathrm{mbar}$ (equal to $h = (23.9 \pm 0.4)\,\mathrm{mm}$) until the filling was stopped. The error on the level metering is calculated from the standard deviation of the fluctuation. The minimal change in the level of $\approx 0.4\,\mathrm{mm}$, is showing that monitoring relative changes in the liquid level on the millimeter scale is possible and allow for proper control of the mass-balance as it will be discussed later in the chapter.

During the filling process, the system has been run in the similar operation mode than used for the cooling test, where the temperature at the top condenser is regulated to be constant. For the distillation mode the working condition is changed in the slow control to regulate the system in order to achieve a constant pressure in the column. The pressure is the most important regulation parameter during the distillation. Hence, it is measured with a high accuracy capacitive manometer (MKS, Baratron 121A) instead of using a less precise Swagelok device. For the regulation, the heaters at the top-condenser are turned off and the cold-head is providing full cooling power, while the heater at the reboiler are turned on in order to evaporate the xenon in the vessel. The up-streaming gas hits the top-condenser and the temperature is stabilizing automatically. A PID algorithm regulates the heating power in the bottom while the column pressure is the regulation parameter. For the different distillation tests the set- point value is chosen to be around 2 bar, as foreseen in the design of the column.

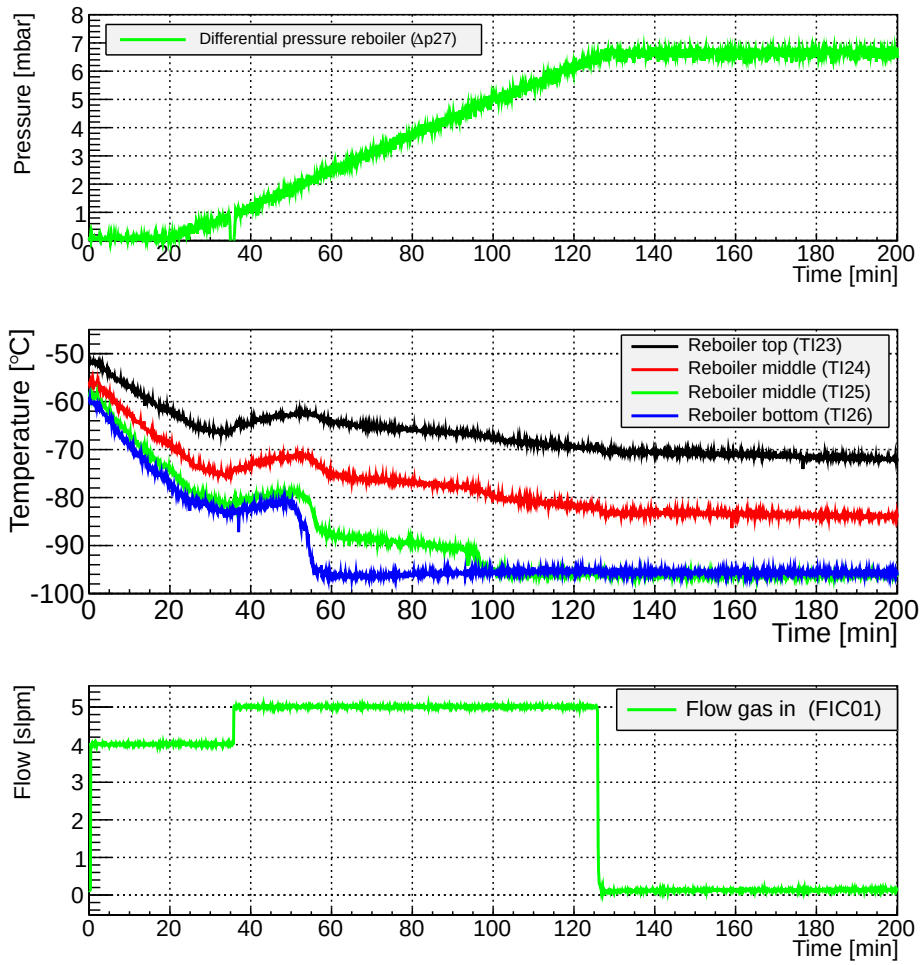

Figure 7.13: **Filling of the reboiler vessel.** The filling of the reboiler with liquid xenon is directly observed with the differential pressure sensor (Top) and the PT1000 level control (middle). The height of the liquid xenon level can be estimated: A hydrostatic pressure of ≈ 6.7 mbar is equal to a height of 2.4 cm. The filling rate was 4-5 slpm (Bottom).

Filling of the pre-separator

Before the distillation can be started, the pre-separator has to be filled, providing a liquid xenon reservoir for the pure liquid xenon feed. Usually a volume of ≈ 200 sl has been chosen. This value has been selected due to the experience, made with the separation tests with the single stage distillation setup, presented in chapter 6. For the filling, the temperature at the cold-head has been set to a fixed temperature and all valves to the package tube are closed. Filling with 5 slpm leads to a filling-time of 40 min to achieve the desired amount of xenon.

7.4 Thermodynamic stability of the distillation process

The preparation of the column, including cleaning, cooling and filling procedure is taking several days before the distillation can be started. For the performance studies of the Phase-1 column, the gas purification system, presented in chapter 3 is used as gas routing system, as already indicated in figure 3.1. The xenon is stored in aluminum cylinders, then cleaned by the getter and injected to the column, while the products (liquid-out and off-gas) are collected in dedicated storage bottles using cryogenic pumping.

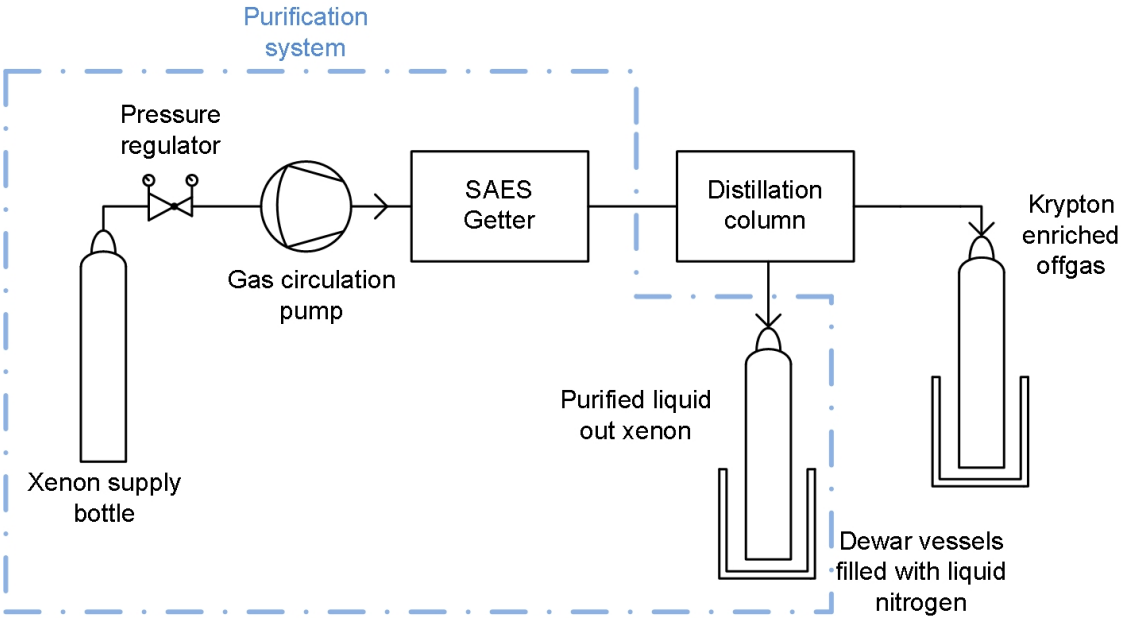

Figure 7.14: **Simplified scheme of a distillation test.** The xenon stored in the storage bottle is guided to the column after passing the purification system (getter). The processed xenon is again stored in dedicated aluminum bottles by cryogenic pumping.

A simplified scheme, neglecting pressure sensors and flow controllers, is shown in figure 7.14. Using the getter in front of the column has the advantage that the xenon is cleaned from electronegative contaminations, e.g. nitrogen or oxygen that might influence the distillation process. To achieve a proper performance of the getter, a pure xenon inlet (99.9995%) has to be provided. For very dirty xenon, the getter has to be bypassed.

Different distillation tests have been performed in order to investigate the optimal procedure for the handling of the Phase-1 column and to understand the characteristics of the system. One distillation will be presented in the following, taking place for about 11 hours of continuous distillation, processing about 30 kg of xenon. In order to start the distillation, the following sequence has to be executed before:

1. **Preparing of the gas bottles:**

   a) Cool down: Filling of the dewar vessels with liquid nitrogen to cool down the liquid-out and the off-gas storage bottles. It takes 15-30 min until an aluminum

bottle with a volume of 50ℓ is cooled down, depending on the initial xenon content of the bottle.

b) After the cooling, the valves to the gas bottles are opened. For the feeding bottle, the pressure regulator is set to an output pressure of 3-4 bar, which is feasible for the gas system. The pressure sensors at the different locations allow to monitor the pressure at the bottles. During the distillation it is of crucial importance to refilling the dewar vessel with liquid nitrogen.

2. **Preparing the gas system:** The valves in the gas system (compare figure 3.1 in chapter 3.1) are arranged in order to inject the xenon (in-gas), PV1, PV15 and MV17 have been opened, while PV17 has been closed. During the distillation, the TPC was bypassed using PV3, PV4 and PV5. The valves to the off-gas bottle are opened as well, while all the flow controllers remain closed.

3. **Start the circulation:** The distillation is started by opening the flow controller at the in-gas (FIC01) to a small flow rate of 4 slpm. In the next step the desired feeding valve (LF1-LF3, GV1) is carefully opened before the off-gas flow controller is opened to the design value (usually FIC03 = 0.1 slpm). The flow controller at the liquid-out (FIC02) line is adjusted slowly to achieve a proper mass-balance.

4. **Adjusting to design values:** After initial stability has been reached, the flow rates are adjusted to higher values e.g. FIC01 = 8.5 slpm and FIC03 = 8.2 − 8.7 slpm to match with the design criteria. The feeding valve (LF1-LF3, GF1) usually also has to be adjusted to achieve the mass-balance. The different characteristics for the start-up and the stable distillation are explained in more detail in the following.

During the distillation test, presented in the following, the pressure set-point is set to 1.9 bar, while a pure liquid feed at the middle port LF2 is used. In figure 7.16 the first 200 min, which is the initial starting, of the distillation is shown. The xenon is injected to the column via FIC01, which is set to 4 slpm in the beginning to avoid large fluctuation and grant shorter regulation time. The opening of the feeding valve is the critical moment. The liquid is pushed from the pre-separator by an overpressure above the liquid surface through the pipe and into the package tube, causing instabilities in the system until the pressure regulation has adapted to the new conditions. The amount of xenon transfered from the pre-separator into the package is regulated by the conductance of the feeding valve and is directly related to the pressure inside the pre-separator and in the column. It is opened in several steps in order to achieve a balance between the in-gas flow rate and the transfer speed to the package to preserve a constant liquid level inside the pre-separator. Since the flow in the feeding line can not be measured, the stability of the pre-separator level indicates, whether the flow rate to the package is matching. Unfortunately, there are only PT1000 sensors, mounted on the outside of the vessel to estimate the filling level. These sensors are in thermal contact with the steel and are supposed to measure the height of the liquid xenon indirectly. Since the precision is very limited, the liquid level inside the reboiler can be used to estimate the proper feeding rate. For the Phase-2 column an improvement for the level indicator in the pre-separator is foreseen. By implementing an additional differential pressure gauge, similar to the one used at the reboiler for level-control, the precision is enhanced and the regulation can be improved.

The right valve position has to be adapted for the different distillation tests and depends on the column pressure, the location of the feeding port and the pressure inside the pre-separator. After opening the liquid feed, FIC02 is slowly increased to extract the liquid xenon from the reboiler. This directly effects the liquid level in the reboiler, as shown in figure 7.15. When the flow controller to the bottle is opened, the liquid is sucked out to the heat-exchanger (HE1) where the xenon is evaporated. Hence, the liquid level inside the reboiler is decreased causing a fast drop in the hydrostatic pressure from $p_{\mathrm{Hyd}} = 7\,\mathrm{mbar}$ down to $p_{\mathrm{Hyd}} = 6.5\,\mathrm{mbar}$. An observed double peak structure is just cause by the system instability. These structures appear usually during the start-up or when the liquid xenon transfer between pre-separator and package tube is disturbed (pressure difference to low or other instabilities). Finally, the pressure inside the column is stabilizing, which continues over several hours before the oscillation is damped.

The period of the oscillation of $T_{Osc} = 60\,\mathrm{min}$ depends on the characteristics of the PID regulation, which is related to the thermal properties of the system (xenon inventory, design of reboiler vessel and amount of material that is heated). Different PID values have been tested in order to find initial values for the startup. The amplitude of the oscillation after 3 h is measured to be less than 40 mbar, comparable low in contrast to the beginning. The injection of xenon to the package tube naturally affects the pressure regulation of the system. Instabilities of several 100 mbar can be observed. After about 40 min, the final flow rate of 8.5 slpm in the in-gas is achieved and is maintained for 11.1 h. The evolution of the pressures of the complete run is shown in figure 7.16. The differential pressure in the reboiler is used to stabilize the mass-balance of the system. While the flow rate at the in-gas and the off-gas lines are constant, the flow rate at the liquid- out line is varied for stabilization of the reboiler level. After 350 min the liquid stays almost constant at an average hydrostatic pressure of $p_{\mathrm{Hyd}} = (6.0 \pm 0.1)\,\mathrm{mbar}$ ($h \approx 22\,\mathrm{mm}$). In order to quantify the stability, a linear fit as been applied to the data with a slope calculated to $\approx -3 \cdot 10^{-5}\,\mathrm{mbar/min}$. The measured change in the liquid level is only -0.2% during the last 5 h of the test, indicating very good stability of the mass-balance in the system.

The absolute pressure inside the column PI24 is further stabilizing to PI24 = $(1.900 \pm 0.006)\,\mathrm{bar}$, matching the set-point and showing excellent stability (also determined from the last 5 h). Additionally to the differential pressure at the reboiler, a second sensor is used, in order to measure the differential pressure along the package tube. In the distillation test, the differential pressure has been measured to $(1.0 \pm 0.1)\,\mathrm{mbar}$. As already pointed out, the operation regime should be chosen below the flood point to achieve a proper mass-flow along the package. During the presented distillation test, the maximal possible cooling and heating powers have already been provided. Therefore, we are below the flood-point, being in a good operation regime. The company Sulzer recommended a pressure drop for the EX package of 1 mbar/m for the best performance, whereas we achieved a value of $\approx 0.9\,\mathrm{mbar/m}$ with the Phase-1 column. Reaching the flooding point would lead to a sudden increase in differential pressure along the tube.

The average heating power in the reboiler for this distillation can be investigated in order to compare them with the design criteria. With $P_{Reb}^{Meas} = (151.4 \pm 0.8)\,\mathrm{W}$, indicated by the power source, the heating power is a little bit higher than the design value of $P_{Reb}^{Des} = 148.2\,\mathrm{W}$, calculated in chapter 4.3. Using this value, the actual reflux ratio R_{Meas} is calculated.

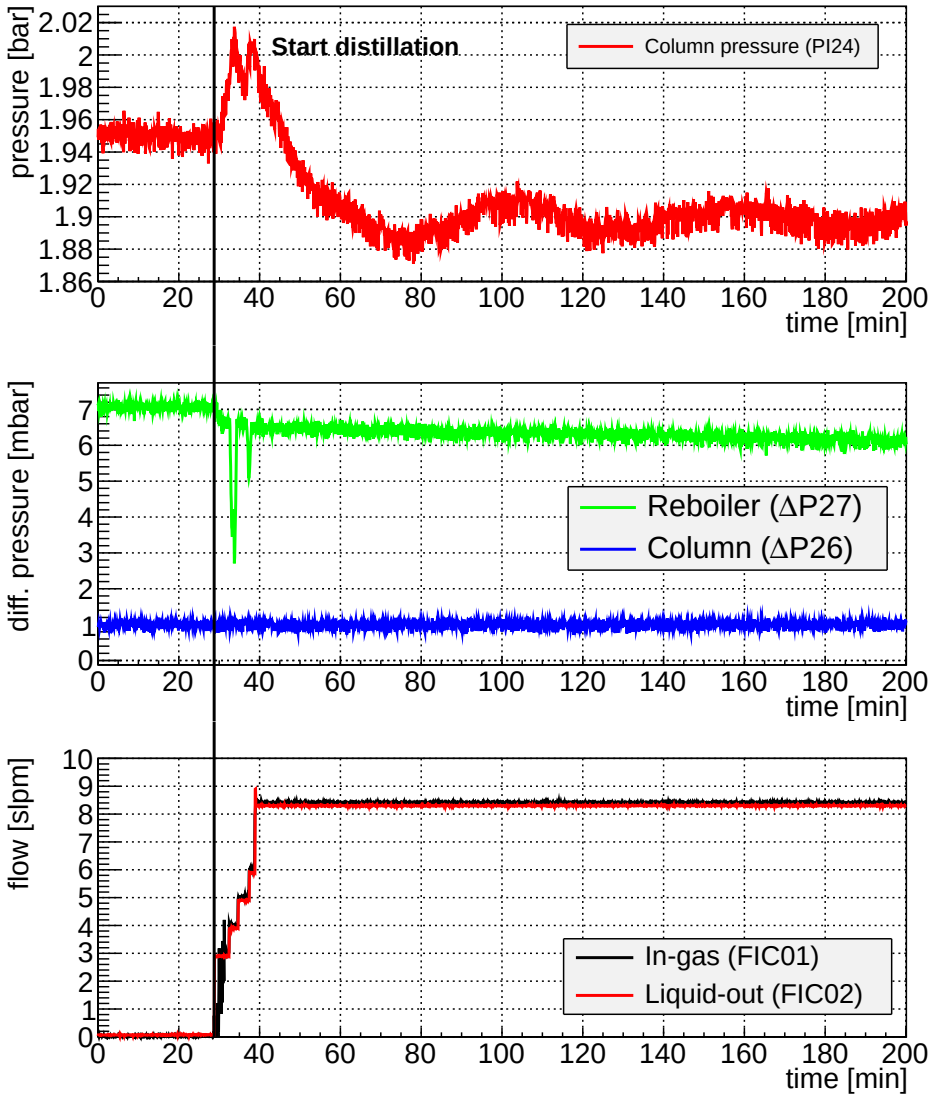

Figure 7.15: **Starting of a distillation test.** These plots show the differential pressure in the reboiler in combination with the column pressure and the flow rates for the initial start-up of a distillation test.

For a pure liquid feed, the flow rate of up-streaming gas from the stripping section V' is equal to the flow rate V in the rectifying section, hence, related to the heating power of the reboiler (see equation 4.3.2). Using the enthalpy between gaseous and liquid xenon of $\Delta h_{\nu,Xe} = 92.5\,\mathrm{kJ/kg}$, the up-streaming flow is calculated to

$$V = V' = \frac{P_{Reb}}{h_{\nu,Xe}} = 5.9\,\mathrm{kg/h} \tag{7.4.1}$$

By using equation 4.2.6 and $L = V - D$ the reflux ratio is given by the measured values for $V = 5.9\,\mathrm{kg/h}$ and the off-gas flow rate of D. The latter one has been set to a slightly higher value of $D = 0.032\,\mathrm{kg/h}$ (1.1% of $3\,\mathrm{kg/h}$) than foreseen in the design report:

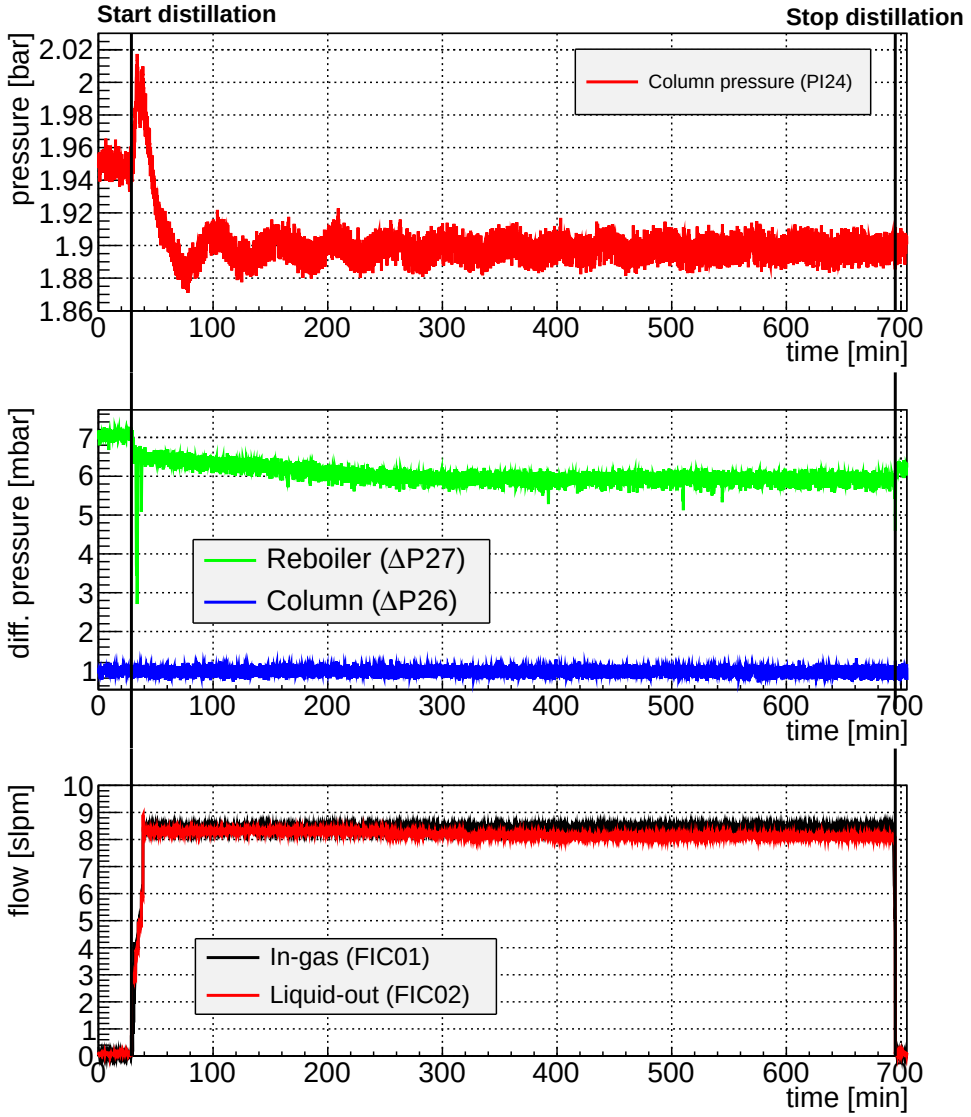

Figure 7.16: **Distillation run of 11.1 h under the designated flow rates.** These plots show the column pressure in combination with the differential pressures in the reboiler and along the package tube. The flow rates for the initial start-up in the in-gas and liquid-out line indicate the status of the system.

$$R_{Meas} = \frac{L}{D} = \frac{V - D}{D} = \frac{V' - D}{D} = \frac{V'}{D} - 1 \approx 183 < 191 \tag{7.4.2}$$

The achieved reflux ratio R_{Meas} is slightly smaller than the original design value, but still much larger than the minimal reflux ratio $R_{min} = 9.1$ calculated in chapter 4.2. The reduced reflux ratio is caused by the enhanced off-gas flow rate.

Nevertheless, the applied heating power of 151.4 W comparing with ≈ 200 W, measured for an evacuated column, indicated, that ≈ 49 W of cooling power is lost. Since the column is thermodynamically coupled to the cold-head with the xenon, the losses from heat radiation

of the package tube are enhanced in comparison to an evacuated column. The amount of thermal leakage due to heat radiation for a one meter package tube can be estimated by using the general Stefan-Boltzmann law for the heat flow I and modify it for the geometry of the system [Jou06]:

$$I = \epsilon \cdot A \cdot \sigma \cdot T^4 \qquad \rightarrow \qquad I = C_S \cdot A_c \cdot (T_w^4 - T_c^4) \tag{7.4.3}$$

and

$$C_S = \frac{\sigma}{\frac{1}{\epsilon_c} + \frac{A_c}{A_w}(\frac{1}{\epsilon_w} + 1)} \tag{7.4.4}$$

with $\epsilon_c = \epsilon_w = 0.16$ being the emissivity of polished stainless steel [Bar01] at the cold surface (A_c) of the package tube with the temperature T_c and of the vacuum insulation surface A_w at the temperature T_w. For the package tube housed inside the insulation vacuum vessel, the model of two cylinders is used, with a length of 1.2 m each.

The area of the package tube is estimated from the tube diameter $d_P \approx 50\,\text{mm}$, while the area of the insulation tube is calculated for an inner diameter of $d_T \approx 300\,\text{mm}$. As a result, the heat loss from radiation is estimated to $I \approx 10\,\text{W}$, which is about 20% of the losses during operation. It has to be noted, that the formulas 7.4.3 and 7.4.4 are only valid for simple, concentric geometries. Additional losses are related to edge disturbances, heat bridges by cables and feed- and analysis pipes as well as the influence of the reboiler vessel together with its holding screws in the bottom and the bellow in the top.

Finally, the thermodynamic performance of the pre-separator is presented in figure 7.17. The temperature at the silicon diode has been measured to TIC11 = (-98.80 ± 0.03)°C and only shows fluctuations during the start and the end of the distillation on a time scale of $\approx 20\,\text{min}$. The power at the heater cartridge before the distillation has started, was measured to $(91.8 \pm 0.3)\,\text{W}$. After turning on the distillation, the heating power is reduced due to the incoming xenon, which is liquefied at this stage. During the measurement the average heating power is measured to be $(84.7 \pm 0.6)\,\text{W}$ and only slightly decreasing with time by $\approx 2.5\,\text{mW/min}$. Conclusively, the additional power, provided by the cold-head to liquefy the xenon can be calculated to $\approx 7.1\,\text{W}$. From the actual average in-gas flow rate of 8.4 slpm and the pressure in the in-gas line of $\approx 2.2\,\text{bar}$, the required heating power for a saturated liquid feed can be calculated to $\approx 87\,\text{W}$ (following the relations, presented in chapter 4.3). The discrepancy can be explained by the performance of the heat exchanger. While the liquid xenon, extracted from the reboiler is evaporated, the incoming xenon is liquefied. By comparing the measured power difference with the expected value, the efficiency of the heat exchanger has been calculated to $\epsilon_{HE} = 92\%$. This high efficiency is possible because of the operation mode and the construction of the system. Inside the heat exchanger, the heat transfer is performed at an equilibrium temperature arising from the two xenon streams. In order to provide an efficient heat transfer which enables the phase transition, the boiling points of xenon at different pressures are used. The collection of liquid xenon by cryogenic pumping produces a lower pressure in the liquid-out line compared to the in-gas line ($\Delta p_{In/Liq} = 0.2\,\text{bar}$). Due to the pressure difference, the boiling temperatures also varies

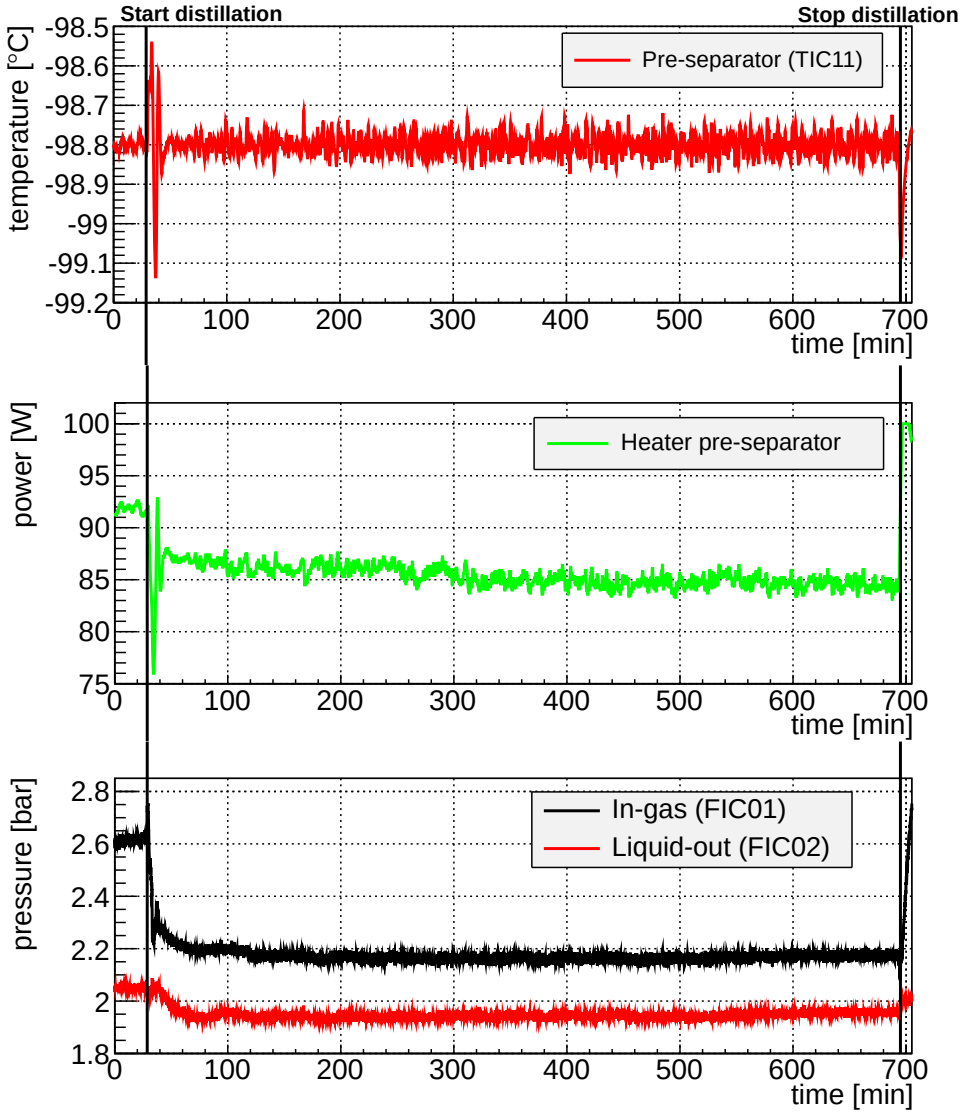

Figure 7.17: **Pre-separator performance for distillation run of 11.1 h.** These plots show the cold-head temperature at the pre-separator (top) and the related heating power (middle) and the associated pressures in the in-gas and liquid-out line. The pressures are connected due to the heat exchanger, which is important for efficient operation.

between −93.5°C for the in-gas xenon and −95.8°C for the xenon in the liquid-out line. This temperature difference allows to liquefy the incoming xenon and evaporate the out-streaming xenon with high efficiency.

The advantages of this design are manifold. The extraction with the heat exchanger makes additional heating of the liquid-out line unnecessary. It prohibits the liquid xenon line outside the insulation vacuum vessel from freezing and furthermore, it allows to inject the xenon with even higher flow rates than foreseen in the design. The thermodynamic stability of a distillation test with high flow rate is presented in the following.

7.4.1 Distillation with high flow rates

Due to the high efficiency of the heat exchanger, one distillation test with the Phase-1 column has been performed in order to investigate the thermodynamic stability for higher flow rates. This is presented in figure 7.18. The measurement is started from a distillation with an established flow rate of FIC01=8 slpm before the process speed is increased to 10 slpm for a short time and further enhanced to 12 slpm. This condition is kept for more than two hours, in order to stabilize the system. As one can see, the liquid level in the reboiler is decreasing over time, indicating that the xenon transfer from the pre-separator into the package is not working sufficiently and further adjustment on the feeding valves was necessary.

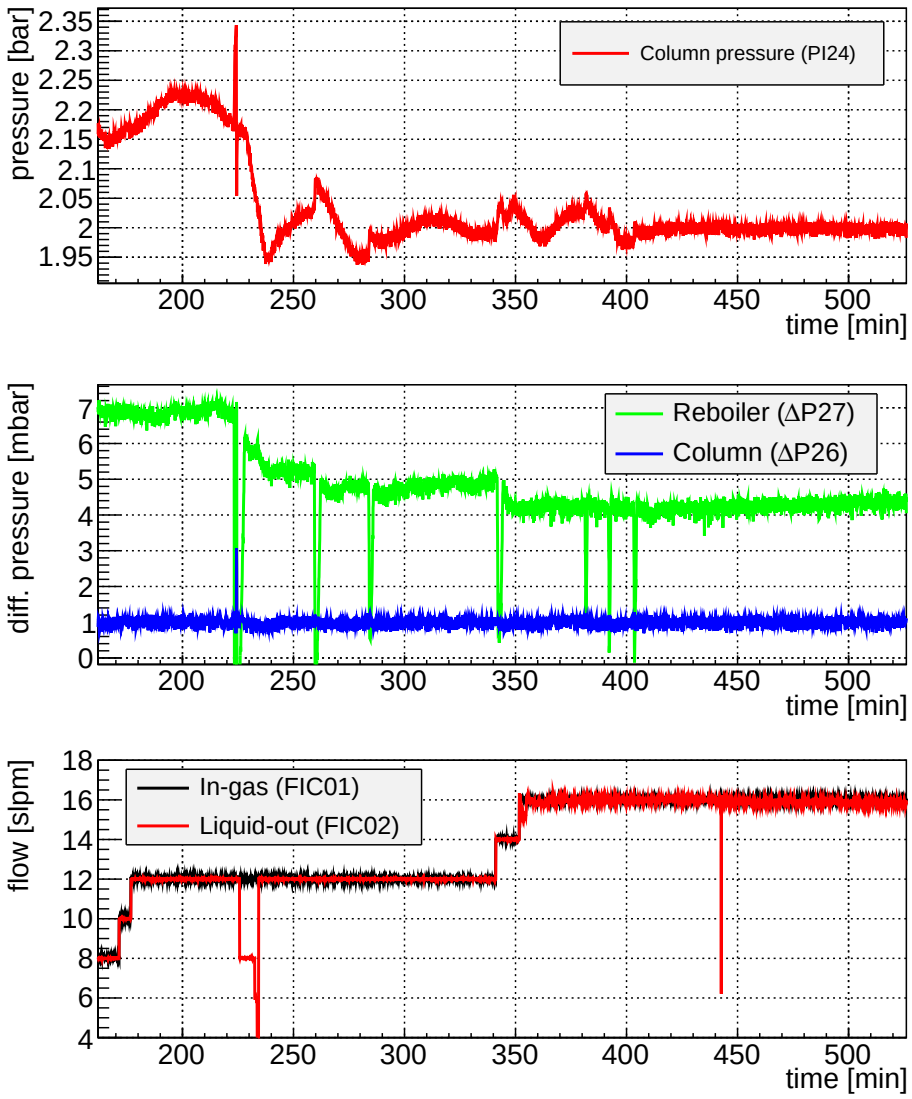

Figure 7.18: **Distillation at very high flow rates up to 16 slpm.** The plots are showing the pressure inside the column together with the differential pressures in the reboiler and along the package tube. It further shows, that process speeds of up to 16 slpm have been tested to be stable.

This distillation run is performed using the middle liquid feed (LF2) but in addition using the gaseous feed (GF1) as well. The reason for also using the gaseous feed is an increase in the inlet pressure at the pre-separator, presented in figure 7.19. In order to stabilize the pressure at a more convenient level, the gaseous out-line of the pre-separator was slightly opened (around $t = 230\,\text{min}$, allowing for a certain amount of gas streaming to the top of the column. The reason for the pressure increase is the "blanketing effect", which was already introduced in chapter 6 and explained in more detail in the next chapter 7.4.2. After finding the proper configuration, the system has been stabilized at 16 slpm, with a short intermediate step at 14 slpm.

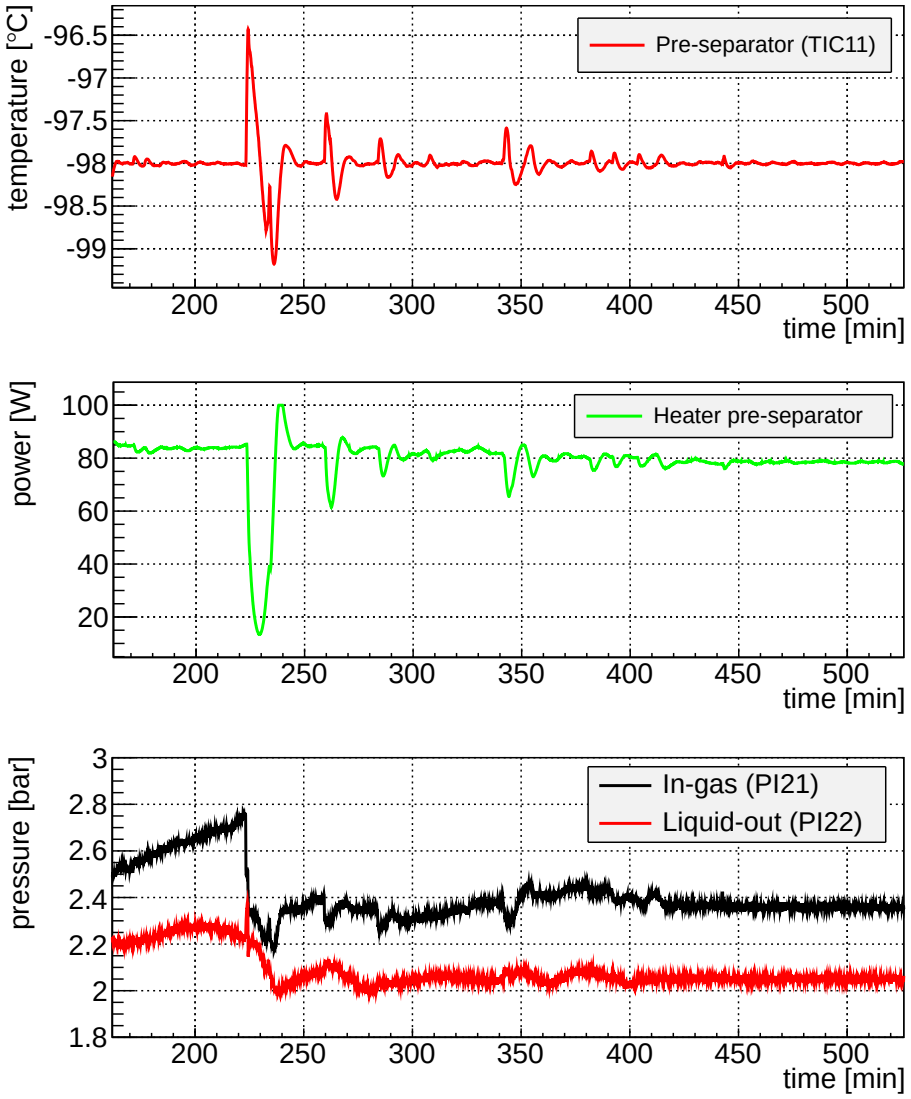

Figure 7.19: **Pre-separator performance under high flow rates up to 16 slpm.** The plots are showing the temperature (top) and the heater power (middle) at the pre-separator together with the pressures in the in-gas and liquid-out lines (bottom) during the distillation with high flow rates. The distillation has been performed with a mixed feed of liquid (LF2) and gaseous (GF1) xenon.

The system operated stable for about $\approx 2\,\mathrm{h}$ before the xenon reservoir in the supply bottle was emptied. Higher flow rates than 16 slpm have been tested to be not stable due to the cryo-pumping capability of the gas bottle, connected to the liquid-out line. The cooling of the bottle, already filled with $\approx 30\,\mathrm{kg}$ xenon was not sufficient to provide a higher collection rate.

From the flow rates and the heating power, the internal flows and the reflux ratios can be calculated. The in-gas flow rate has been measured to $\mathrm{q_{FIC01}} = (16.0 \pm 0.2)\,\mathrm{slpm}$ ($\approx 5.2\,\mathrm{kg/h}$ for an inlet pressure of 2.38 bar), where the uncertainty consists of the accuracy of the device $\Delta q_{FIC01,sys} = 0.1\,\mathrm{slpm}$ and a statistical fluctuation, calculated as standard deviation $\Delta q_{FIC01,stat} = 0.1\,\mathrm{slpm}$. The measured heating power under these conditions was $P_{Reb}^{Meas} = (144.5 \pm 0.7)\,\mathrm{W}$, leading to $V' = 5.6\,\mathrm{kg/h}$. Being lower compared to the distillation process at 8.4 slpm, which was a pure liquid feed. The heating power is expected to be reduced because of the injected gaseous xenon through GF1. This can be estimated by comparing the heating power in the reboiler for the low flow distillation, with the power at the high flow distillation and the participating gas streams: For the high flow distillation, the vapor stream in the rectifying section can be written as the sum of the vapor stream from the stripping section and the amount of gaseous xenon from GF1: $V = V' + q_{GV1}$ (For the low flow distillation $V = V'$). From the difference in power between the two distillation tests $\Delta P_{Reb} = 151.4\,W - 144.5\,W = 6.9\,\mathrm{W}$ to flow rate via GF1 is calculated to $q_{GV1} = 0.27\,\mathrm{kg/h}$. This can be compared to the estimation coming from conductivity measurements performed in [Mur14]. From the potentiometer readout it has been measured, that the valve position was at $\approx 2.5\%$ of fully open (which is equal to 53.4Ω). This corresponds to a conductivity of $\approx 0.01\,\ell/\mathrm{s}$ and a mass flow of $0.45\,\mathrm{kg/h}$ (for a gaseous xenon density of $12.7\,\mathrm{kg/m^3}$). The discrepancy is in fully agreement with the limited precision of the conductance measurement in the low-flow regime.

Finally the reflux ratio can be calculated to $R_{meas} = (V - D)/D = 182$ with $D = 0.032\,\mathrm{kg/h}$, also being close to the design value. The high flow performance does not influence the reflux ratio in the rectifying section. It only changes the reflux ratio in the stripping section. According to equation 4.2.9, the liquid flow in the liquid-line $B = 5.1\,\mathrm{kg/h}$ and the stream $L' = 10.8\,\mathrm{kg/h}$ changed, giving a reflux ratio of $R' = 2.1$ compared to $R' = 3.0$ of the standard operation.

The maximal achievable process flow rate in this example was only limited by the pumping capability of the cooled bottle. The heater at the pre-separator was still heating at $(79 \pm 1)\,\mathrm{W}$, giving that the cold-head only needs to provide $\approx 13.5\,\mathrm{W}$ of cooling power for the liquefaction process. For 16 slpm, a calculated power of $\approx 166\,\mathrm{W}$ is needed, giving an efficiency of $\approx 92\%$, confirming the result from the distillation under the design conditions. The flow controllers FIC01 and FIC02 are limited to a maximum flow of 20 slpm being the ultimate flow rate of the Phase-1 setup without exchanging the flow controllers.

7.4.2 The blanketing effect

As already mentioned in chapter 6 and 7.4.1 the performance of the distillation system depends on the purity of the injected xenon. The contaminations inside the xenon can

drastically influence the heat transfer and prohibits a stable operation. This is shown in a distillation test, presented in figure 7.20, using off-gas from former distillation tests and distill it again.

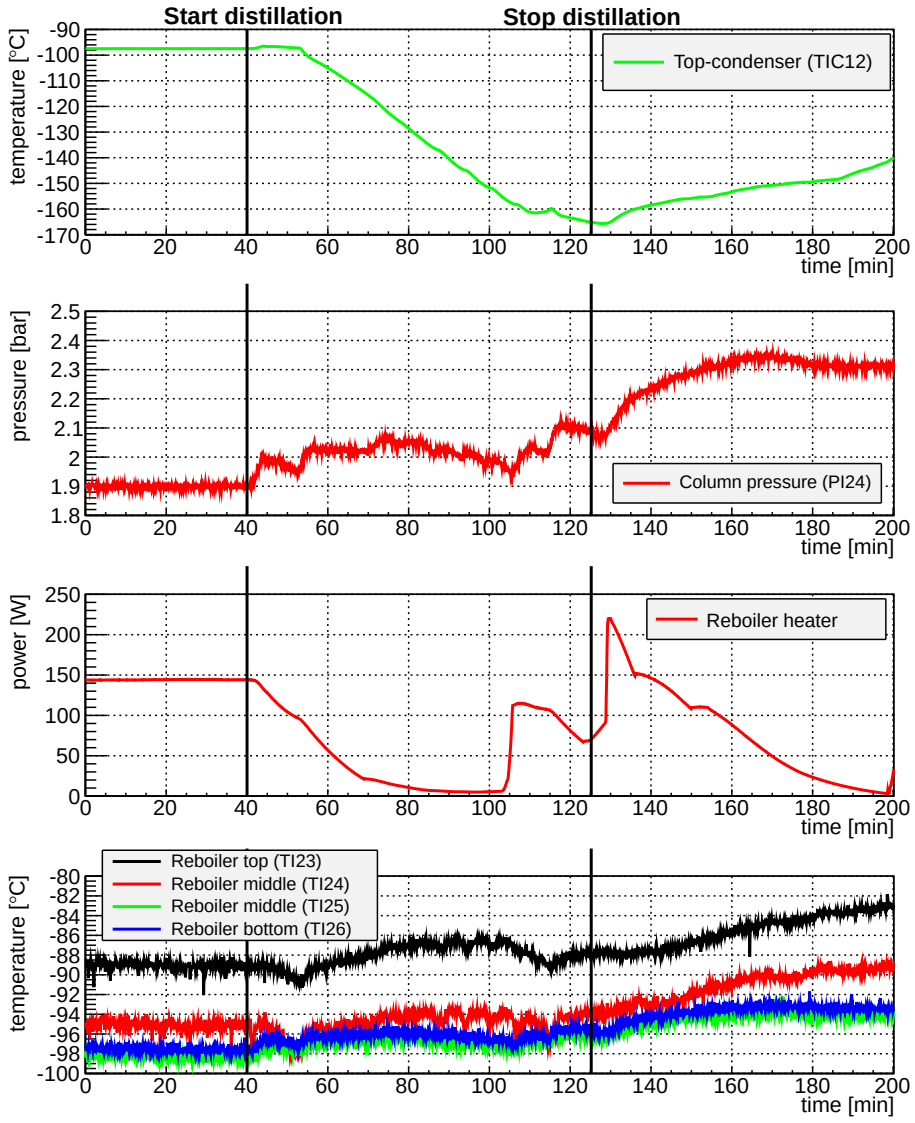

Figure 7.20: **Distillation of highly contaminated xenon.** This distillation test has been performed with xenon, spoiled with helium and argon. The temperature at the top-condenser (top) as well as the pressure inside the column and the heating power in the reboiler are shown (middle) together with the temperatures, measured at the package tube (bottom).

After starting the distillation process, it takes a few minutes until the temperature at the top condenser drastically decreases, while the pressure in the system slightly increases (after $t \approx 55\,\text{min}$). Hence, the heating power, provided at the reboiler is decreasing with time, in order to regulate the pressure in the system to the set-point value. At $t \approx 105\,\text{min}$, the pressure set-point of the system has increased, causing also an increase in heating power in the reboiler. Apparently, the cooling power from the cold-head at the top-condenser is not

transfered to the xenon properly, leading to a decrease in the temperature and prohibit a proper mass-transfer along the column. Investigations on the impurities in the xenon at the in-gas, liquid-out and the off-gas line indicated, that this distillation run was spoiled with high concentrations of light noble gases helium and argon, which effect the stability. By using the RGA-1 system with cold-trap, a mass-spectrum of the components in the mass- range of 1 amu to 41 amu has been measured. The spectra for the in-gas and the liquid-out sample are shown in figure 7.21. The measured intensity has been normalized to the pressure in the analyzing chamber in order to make the measurements more comparable. The intensity in the helium peak in the in-gas sample was measured to $I_{\text{He, in-gas}} = 2.9{\cdot}10^{-2}$ amps/mbar, being almost three orders of magnitude higher (reduction factor of ≈ 820) than the intensity in the liquid-out sample for the same mass $I_{\text{He, in-gas}} = 3.5 \cdot 10^{-5}$ amps/mbar. For the argon peak, the intensity in the in-gas sample was measured to $I_{\text{Ar, in-gas}} = 1.2 \cdot 10^{-3}$ amps/mbar, being about two orders of magnitude higher (a reduction factor of ≈ 195) than the intensity in the liquid-out sample for the same mass $I_{\text{Ar, in-gas}} = 6.4 \cdot 10^{-6}$ amps/mbar. The measurement of the off-gas sample was not comparable with the other measurements and are not shown. The contaminations produce a higher vapor pressure in the LN_2 cold-trap of the RGA-system than expected from xenon ($\approx 1 \cdot 10^{-1}$ mbar compared to $\approx 2 \cdot 10^{-3}$ mbar) and also prohibit the usage of the electron multiplier to measure the mass-range, since the current limit exceeded. Nevertheless, these measurements show directly the reduction for light noble gases by cryogenic distillation. Since the calibration for both RGA setups has been performed only for krypton, the absolute concentrations for helium and argon as well as the detection limits are unknown. Consequently, the reduction has been demonstrated, but the reduction factor can not be estimated from this measurement.

In contrary to helium and argon, the calibration for krypton has been performed and the separation performance of the Phase-1 column is investigated in the following chapter 7.6. Although the temperature is still to high to liquefy or freeze these lighter components, their influence is obviously non-negligible and xenon with a high concentration of light noble gases prohibit a stable operation of the Phase-1 column. In order to achieve a steady process, different features have to be used or implemented. For medium levels of impurities (e.g. 10 ppm), a combination of gaseous and liquid feed can be used to stabilize the pressure in the pre-separator as already performed in different measurements (compare previous chapter 7.4.1). Since the impurities are enriched in the gas-phase, opening the valve GF1 allows to directly guide these impurities to the top-condenser and to extract them to the off-gas. This is also feasible for long-term distillations, where the light gases are enriched in the pre-separator during the operation. For very high concentrations of impurities the construction of the system has to be modified to process these gases. A modification of both condensing-stations at the top condenser and the pre-separator is necessary by adding additional gas-out lines at the very top of the vessels. This construction provides a more effective collection of the light gases for a more direct release to the off-gas bottle. In addition a second flow controller at the off-gas line is foreseen, mounted in parallel to the existing one, in order to allow for higher off-gas flow rates. The enhancement of the off-gas flow rate allows for faster collection of the light noble gases and a better heat transfer to the xenon due to turbulences. Under normal operation with rather clean xenon, this additional flow controller is closed and only used for high contaminated xenon. The modifications are implemented during the upgrade to the Phase-2 column [Mur18].

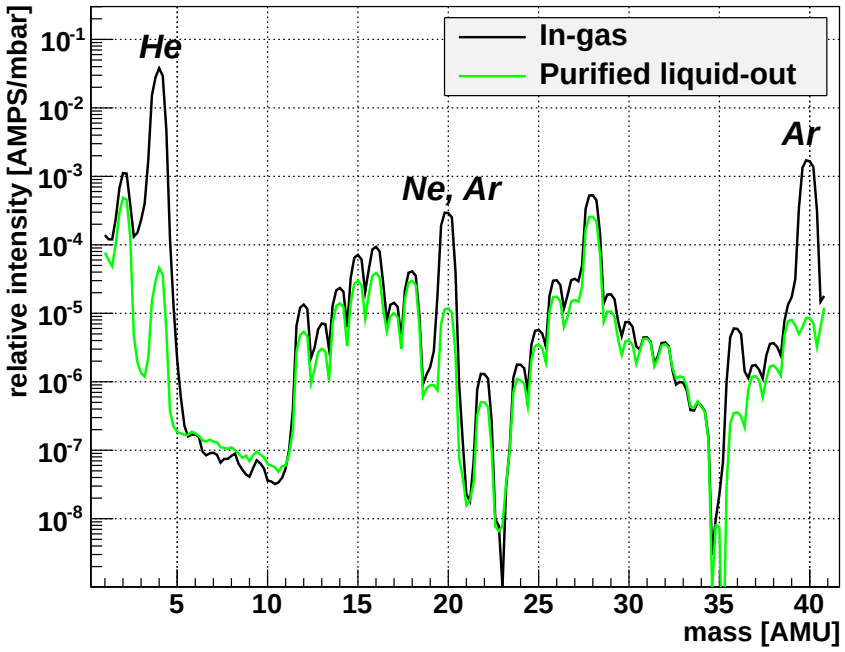

Figure 7.21: **Mass-spectrum of contaminated xenon before and after the distillation.** The mass-spectra, measured with the RGA-1 system in the mass-range 1-41 amu, show the performance of the distillation for light noble gases argon and helium. The intensity of the characteristic lines (argon also appears at mass 20 as double ionized atom Ar^{2+}) in the purified liquid-out is drastically reduced compared to the intensity in the in-gas sample.

7.4.3 Increase of the cooling power using liquid nitrogen

The usage of liquid nitrogen to provide the cooling power was originally implemented in order to have a back-up system in case of a failure in the cryo-cooler and, more importantly, to procure additional cooling power in case, that it is needed to achieve a good separation. Since the cold-head is feasible to reach the design goal for a pure liquid feed, the LN_2 cooling has not been used for the distillation runs. It was only tested using an almost empty column in order to proof the functionality and how much cooling power can be provided. Figure 7.22 shows the scheme of the supply with liquid nitrogen. A portable liquid nitrogen dewar (Cryotherm, type Apollo100) with a volume of 100ℓ is connected to the inlet with a flexible metal tube. The liquid nitrogen is pushed inside the copper coil by the overpressure inside the dewar vessel. At the outlet of the coil, a motor driven valve allows to regulate the flow of gaseous boiling nitrogen remotely, which directly influences the applied cooling power.

An additional hand valve was mounted, in order to have a redundant system for the emergency case that the motor valve is not working properly. The regulation valve is a custom construction consisting of a standard bellow-sealed valve (SS-4BG-V51, Swagelok) combined with a motor drive (Maxon motors). The mounting of the regulation valve is shown in figure 7.23. The control software has been designed to return the valve status in percentage of

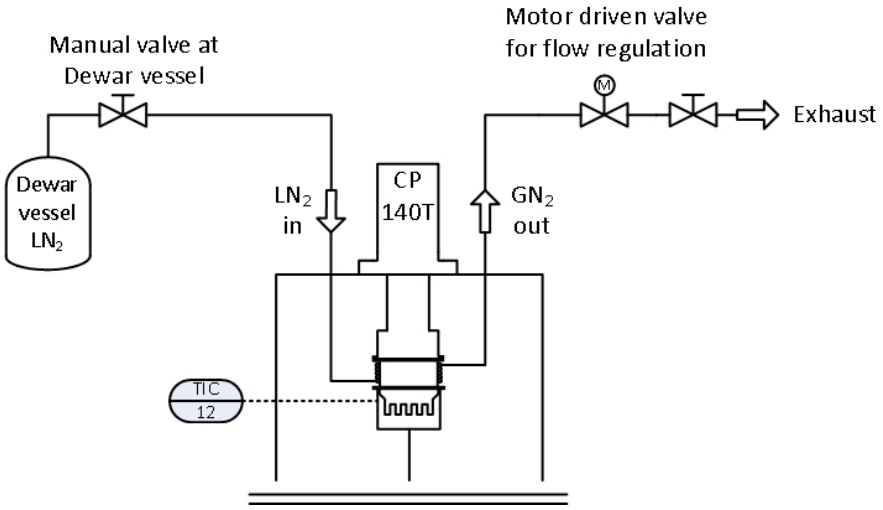

Figure 7.22: **Flow chart of the cooling test with liquid nitrogen supply.** The liquid nitrogen is stored in a 100ℓ portable dewar vessel and connected with a flexible tube to the column. With the overpressure in the vessel the liquid nitrogen is pushed into the copper coil, while the amount of boil-off nitrogen is regulated by a motor driven valve.

rotation. Therefore, 20% of rotation is not equal to 20% of conductance. Since the absolute flow rate of boil-off nitrogen is of minor interest, this notation is used during this test.

Figure 7.23: **Nitrogen flow control with a motor-valve.** The motor driven valve (small picture, left) is connected via a stainless steel tube of quarter inch diameter to the outlet of the cooling line and allows to regulate the flow rate of the boil-off nitrogen to control the applied cooling power.

The test has been started with an initial temperature of $T = -98°C$. After the cryo-cooler was turned off, the valve to the dewar was opened and the regulation at the valve was set to a fixed value in order to measure the cooling power at a given set-point temperature for different valve positions.

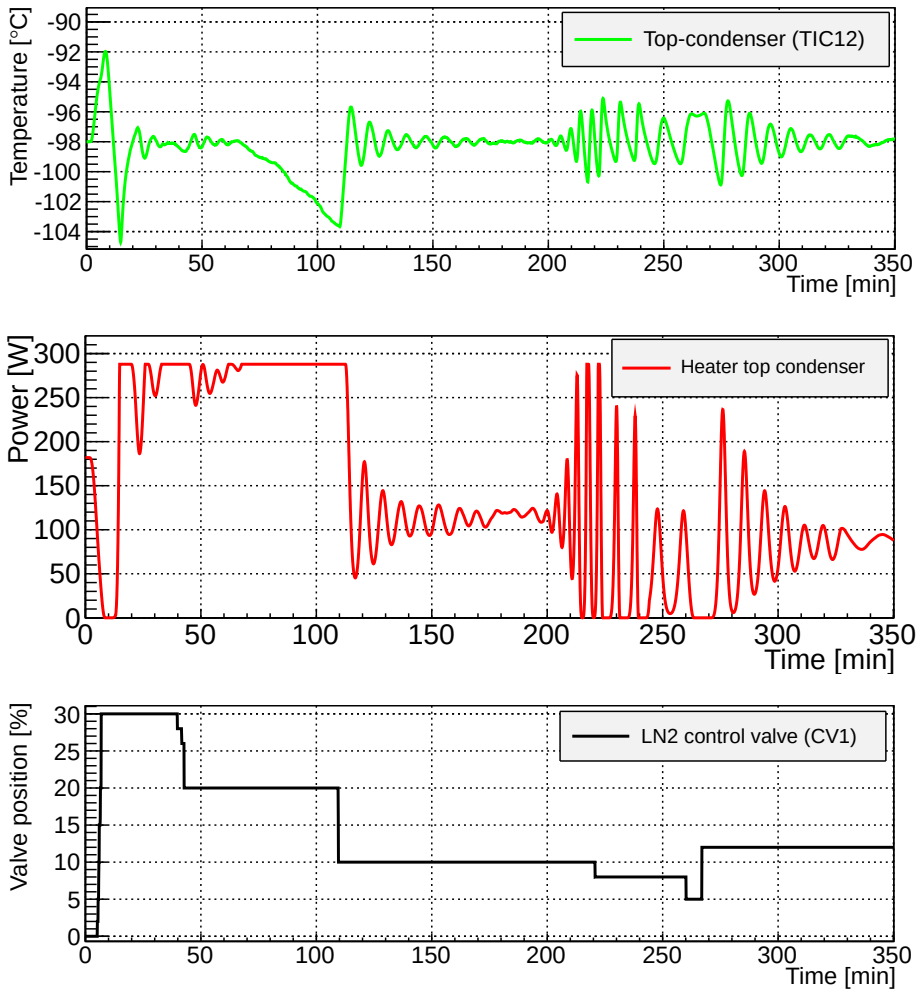

Figure 7.24: **Cooling test with liquid nitrogen supply.** In these plots, the temperature at the top condenser (top) is shown together with the applied heating power (middle). The valve position is indicated as percentage of turning (bottom).

The data is presented in figure 7.24. In the beginning, when the valve was regulated at 30% the cooling power was going up to the edge of the heating capability of 290 W and it was decided to reduce the amount of boil-off nitrogen to 20% in the next step. In the scope of this measurement, the temperature at the top-condenser starts to decrease while the heater was regulated to the maximum achievable power. With this valve configuration it is possible to give more than 290 W cooling power to the system. In the next step, the valve was regulated down to 10%, which was shortly stabilized($\approx$15 min) to a heating power of 120 W before a strong oscillation in the regulation appeared. Different valve positions were not helping to stabilize the system again. The instability in the system was caused by the liquid nitrogen supply. Since the overpressure inside the dewar vessel fluctuates during the extraction of the liquid, the flow rate is not constant over time. Consequently, the cooling power gets unstable

and the PID regulation can not compensate for this, leading to large fluctuations.

The cooling test with liquid nitrogen showed, that it is possible to supply the Phase-1 column with much more cooling power than the cryo-cooler. For the stabilization of the system it is of crucial importance to produce a constant liquid nitrogen flow. This can be achieved by pressure controlled gaseous nitrogen injected above the liquid surface in the dewar vessel. The regulation with the motor drive worked during the measurement very well, but long-term investigations have to be performed, whether the construction is feasible for continuous operation. Due to the cold temperatures at the nitrogen outlet, the pipes and valves got frozen and after some time, the temperature and the frozen ice might damage the electronics of the motor drive or blockade the valve.

7.5 Summary on the thermodynamic stability and the implications for XENON1T

During numerous distillation tests, a procedure has been developed, which allows the user to start a thermodynamically stable operation at the desired process speed of 3 kg/h, feasible for the XENON1T experiment [Ros14b]. The regulation on the system pressure is of crucial importance for the performance of the system. It has been observed, that a more precise level-control for the pre-separator is necessary in order to improve the regulation of the amount of xenon which is injected to the package tube. An upgrade has been performed for the Phase-2 column [Mur18], by using a differential pressure sensor at the pre-separator for leveling purpose similar to the level control in the reboiler. The measurements of the heating power showed, that it is reaching the design goal and allows for very high reflux ratios. The differential pressure along the column would even allow for higher fluxes inside the package tube, since the flood point is not reached yet. To achieve this, additional cooling power with liquid nitrogen could be set up.

Due to the very efficient heat exchanger, it has been tested, whether higher flow rates than the original design value of 3 kg/h can be processed. It has been shown, that thermodynamically stable flow rates of more than 5 kg/h can be achieved. The observed limitations were given by the cooling power of the collection bottles and the ranges of the flow controller in the inlet and the purified outlet but not by the system itself.

In addition, the impact of impurities on the distillation process has been observed. The contamination with light noble gases helium and argon prohibits a proper heat transfer between the cooling stations and the xenon. Hence, the performance of the system is spoiled and modifications on the cooling stations have been implemented for the Phase-2 setup [Mur18], in order to allow also for processing highly contaminated xenon. Since argon and helium are also reduced by the distillation, it is feasible to use the Phase-2 setup even to clean much dirtier xenon gas than planned in the original design.

7.6 Separation Efficiency of the Phase-1 column

In this section, the separation performance is investigated, using the different techniques, described in chapter 5. The absolute concentration of natural krypton is measured for the injected xenon as well as for the products in order to determine the reduction factor using the Coldtrap-MS and the RGMS technique. The dynamic of the process is investigated with the ^{83m}Kr tracer method, which is compared with a model for the krypton particle flux. The different techniques also allow to obtain the HETP value of the package material for a xenon-krypton mixture.

7.6.1 Measurement of the column performance using coldtrap-MS

From careful calibration studies, presented in [Fie14], it has been shown, that the sensitivity (S) of both coldtrap-MS systems (RGA-1 and RGA-2) is rather limited:

$$\begin{aligned} \mathrm{S}_{\mathrm{RGA-1}}(^{84}\mathrm{Kr}) &= (206 \pm 35)\,\mathrm{ppt} \\ \mathrm{S}_{\mathrm{RGA-1}}(^{86}\mathrm{Kr}) &= (318 \pm 58)\,\mathrm{ppt} \end{aligned} \tag{7.6.1}$$

$$\begin{aligned} \mathrm{S}_{\mathrm{RGA-2}}(^{84}\mathrm{Kr}) &= (67 \pm 12)\,\mathrm{ppt} \\ \mathrm{S}_{\mathrm{RGA-2}}(^{86}\mathrm{Kr}) &= (191 \pm 35)\,\mathrm{ppt} \end{aligned} \tag{7.6.2}$$

The sensitivity limits (1σ) for the two most abundant krypton isotopes are valid for a natural mixture of krypton isotopes (see table 7.1) and have been calculated to be different due to the different natural abundances of the isotopes and the varying background in the mass-over-charge ratios. Although the sensitivities are much higher than the design goal of the column ($^{\mathrm{nat}}\mathrm{Kr/Xe} < 0.5\,\mathrm{ppt}$) the technique is feasible for initial investigations. Beside of the determination of the reduction factor using the RGA-1 system, the concentration profile along the column has been measured with the RGA-2 system.

Table 7.1: **Natural abundance of the krypton isotopes.** The natural abundance of the most common krypton isotopes is given [Nis15].

Isotope	Mass	Abundance
^{78}Kr	77.920400	0.35%
^{80}Kr	79.916380	2.25%
^{82}Kr	81.913482	011.6%
^{83}Kr	82.914135	11.5%
^{84}Kr	83.911507	57.0%
^{86}Kr	85.910616	17.3%

Measurement of the reduction factor with coldtrap-MS

The average concentration of krypton in the storage bottles in Münster has been determined to be $^{nat}Kr/Xe \approx 0.2\,ppb$, using the RGA-2 system with its higher sensitivity. Thus, any distillation test using this gas batch will not allow to investigate the separation, since the krypton concentration is already below the limit of the RGA-1 system. Consequently, the xenon has been doped with natural krypton to achieve higher inlet concentrations. A small mixing volume of $V_{Mix} \approx 30\,ml$ was connected to the gas-bottle rack and has been filled with $p \approx 10\,mbar$ of krypton coming from a gas-storage bottle, roughly estimated to achieve a doping in the ppb range related to the amount of xenon in the storage bottle. The krypton is mixed with the xenon by expanding the xenon from a storage bottle to the mixing volume and cryo-pumping the mixture back in the bottle. Since the pressure and the absolute volume are not measured precisely, the absolute concentration is determined with the RGA- 1 system during the distillation run. In figure 7.25, the time evolution of the current in the RGA-1 is shown. The distillation has been performed with a process speed of $FIC01 = 8.5\,slpm$ and $FIC03 = 0.1\,slpm$, using a combined filling mode of liquid and gaseous flow at LF2 and GF1. The xenon is injected to the RGA-1 system at $t = 285\,s$ with the butterfly valve (BV) closed to 15° during the initial start-up and further closed to 0° at $t = 358\,s$. After the sample passes the cold-trap and reaches the analyzing chamber, the current in the RGA is increasing for the different mass-over-charge value of the different krypton isotopes. Comparing the intensities with the natural abundances of the different isotopes (see table 7.1) shows good agreement. Only ^{78}Kr shows different behavior, since some background component and its low abundance spoil the result.

For the determination of the concentration, the current at the analyzer I(t) is corrected for the inlet flow from the sample volume (Vol-1 + Vol-2, see figure 5.1), which is measured as the pressure-drop with time for a fixed volume [Fie14]:

$$I_c(t) = I(t) \cdot \frac{q_n}{q_{in}(t)} \qquad \text{with} \qquad q_{in}(t) = V\frac{dp}{dt} \tag{7.6.3}$$

q_n is the average flow during typical measurements, introduced for the flow normalization. The calibration of the system has been performed for a fully closed butterfly valve (BV = 0°), which leads to the region of interest. For the subsequent analysis, one has to distinguish between samples with high krypton concentrations ($^{nat}Kr/Xe > 100\,ppb$) in contrast to samples with very low concentrations ($^{nat}Kr/Xe < 1\,ppb$). In the latter case, the signal-to background ratio is much worse and these data-sets are treated differently. For the high-concentration sample, the corrected intensity $I_c(t)$ is averaged over the region of interest (e.g. in figure 7.25 between 370 s and 400 s), giving the absolute concentration by applied a linear function $k(^{84}Kr,^{86}Kr)$ between the concentration and the corrected intensity of the two most abundant isotopes ^{84}Kr and ^{86}Kr [Fie14]:

$$\bar{I}_c = k(^{84}Kr,^{86}Kr) \cdot c_{Kr} \quad \longrightarrow \quad c_{Kr} = \frac{\bar{I}_c}{k(^{84}Kr,^{86}Kr)} \tag{7.6.4}$$

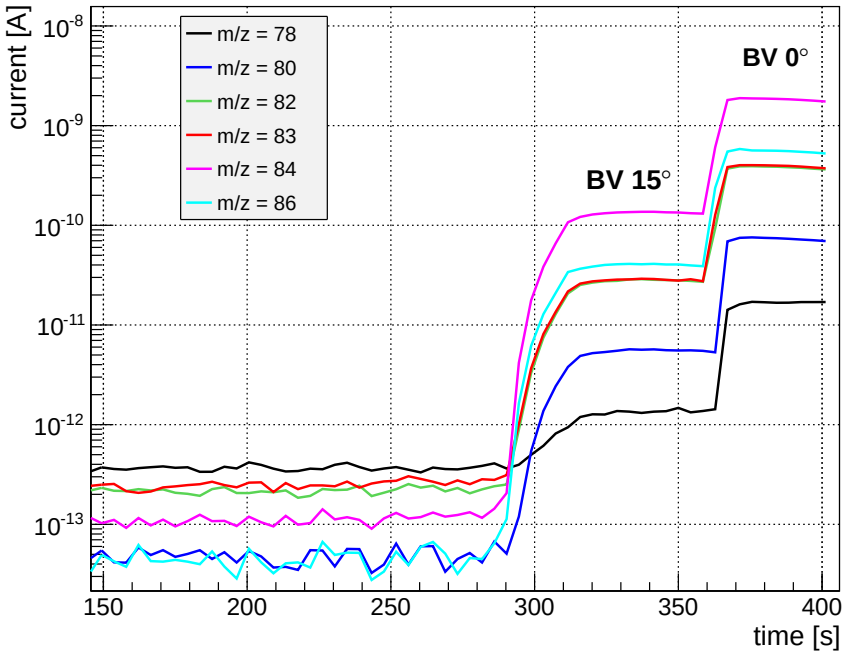

Figure 7.25: **Measurement of the natural krypton isotopes in the injected xenon.** The plot shows the time evolution of the different krypton isotopes during a coldtrap-MS measurement of the in-gas during a distillation test. After the sample gas is injected at t = 285 s with a butterfly position of 15° before it is closed to 0° at t = 358 s. The distillation has been performed at the 10.02.2014 with a process speed of 8.5 slpm injected via LF2 and GF1.

The background effects are neglected in this model, since they are at least three orders of magnitudes lower than the intensities. For additional cross-check, the measured abundance of the different krypton isotopes can be compared to the literature in order to verify the krypton signals. For the low concentration regime, the background can not be neglected, especially when the measured signals are close to the sensitivity limit. Comparable to measurements with high concentration, the intensity in the different masses is increasing when injecting sample gas. This can be seen in figure 7.26, which shows a measurement of the purified liquid-out during the same distillation test, presented in figure 7.25. The sample is injected after $t \approx 185$ s, resulting to an increase in the signals, but being much smaller in intensity and not showing the correct relative abundance in the isotopic composition. Hence, the concentration in the liquid- out sample is very close to the sensitivity limit or even lower. For the analysis of the low concentration sample, a linear fit $\gamma(t)$ is applied to the time evolution of the intensities of the most abundant isotopes ^{84}Kr and ^{86}Kr, including a background component I_B:

$$\gamma(t) = I_{in}(t) \cdot \frac{q_n}{q_{in}(t)} + I_B \tag{7.6.5}$$

In the transit region between low and high concentrations, between 1 ppb and 100 ppb, the

two methods give comparable results, as it has been tested during the calibration campaign, presented in [Fie14].

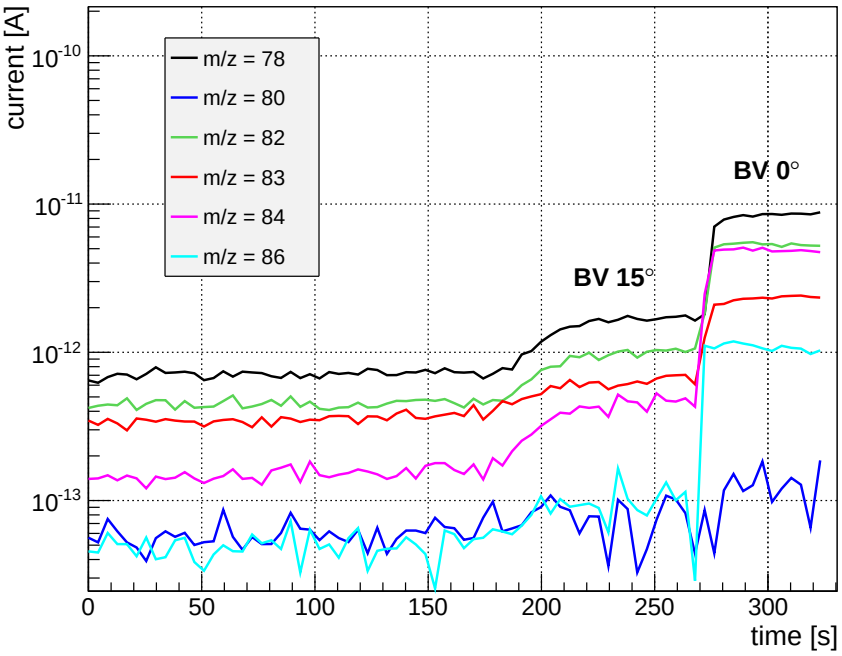

Figure 7.26: **Measurement of the natural krypton isotopes in the purified liquid-out line.** This plot shows a measurement with the RGA-1 system of the purified xenon from the distillation test at the 10.02.2014, performed with a process speed of 8.5 slpm injected via LF2 and GF1.

For the two measurements, presented in the figure 7.25 and figure 7.26, the krypton concentration in the in-gas sample has been determined using the high concentration method to:

$$\begin{aligned} &\text{In-gas sample } {}^{84}\text{Kr}: \quad {}^{\text{nat}}\text{Kr/Xe} = (123.34 \pm 54.50)\,\text{ppb} \\ &\text{In-gas sample } {}^{86}\text{Kr}: \quad {}^{\text{nat}}\text{Kr/Xe} = (126.51 \pm 55.98)\,\text{ppb} \end{aligned} \tag{7.6.6}$$

The errors for the in-gas sample are very large, which is related to the limited measurement time leading to high statistical errors. For the concentration in the liquid-out sample, using the low concentration analysis, no signals are observed compare to the background. Hence, only the limits of sensitivity of the RGA-1 system for the two isotopes are given (already presented in equation 7.6.1) in order to quantify the concentration in the liquid-out sample:

$$\begin{aligned} &\text{Liq-out sample } {}^{84}\text{Kr}: \quad {}^{\text{nat}}\text{Kr/Xe} < (206 \pm 35)\,\text{ppt} \\ &\text{Liq-out sample } {}^{86}\text{Kr}: \quad {}^{\text{nat}}\text{Kr/Xe} < (318 \pm 58)\,\text{ppt} \end{aligned} \tag{7.6.7}$$

Consequently, the reduction factor (see equation 2.5.2) in this distillation test using doped xenon gas can be calculated from the ^{84}Kr isotope to be $F_{Red} > 597 \pm 285$. The error has been calculated from gauss error propagation. Additional measurements have been performed and all the results for the ^{84}Kr isotope are collected in tabular 7.2. As indicated, all the samples taken from the liquid-out line show lower concentrations of natural krypton than measurable by the RGA-1 system, although the different distillation tests have been performed with artificially doped xenon. Three measurements show a reduction factors of $F_{Red} > 165$, demonstrating the separation process inside the column.

Table 7.2: **Results from coldtrap-MS measurements for different distillation runs.** The separation performance was tested using xenon gas, artificially doped with krypton. All measurements, using only the signals from ^{84}Kr, show that the krypton concentration in the purified liquid-out is below the sensitivity limit of the RGA-1 system for the ^{84}Kr isotope. In most of the cases no off-gas sample was taken or the sample was contaminated (marked "cont.").

Date	Distillation conditions	c_{Kr}(in-gas) (ppb)	c_{Kr}(liq-out) (ppt)	c_{Kr}(off-gas) (ppm)	Reduction factor F_{Red}
10.02.14	$q_{in} = 8.4$ slpm $q_{off} = 0.1$ slpm LF2 + GF1	123 ± 55	$< 206 \pm 35$	-	$> 597 \pm 285$
18.02.14	$q_{in} = 16$ slpm $q_{off} = 0.1$ slpm LF2 + GF1	18 ± 13	$< 206 \pm 35$	cont.	$> 89 \pm 64$
04.03.14	$q_{in} = 8.5$ slpm $q_{off} = 0.1$ slpm LF2	102 ± 34	$< 206 \pm 35$	-	$> 495 \pm 185$
06.03.14	$q_{in} = 8.5$ slpm $q_{off} = 0.1$ slpm LF2 + GF1	45 ± 8	$< 206 \pm 35$	3.7 ± 1.9	$> 219 \pm 53$

It has been turned out that the measurements of the off-gas samples are less significant, since the contaminations with other light noble gases influences the freezing processes in the cold-trap (blanketing, compare section 7.4.2) and prohibit proper measurements in most of the cases. Furthermore, as indicated by the measurement from the 06.03.2014, the accuracy of the system for very high concentrations does not allow for quantitative analysis of the separation process. For very small concentrations (<1 ppt) in the liquid-out sample, the relative changes in the off-gas sample is less than 1%, far below the achieved accuracy.

Generally, for measuring the reduction factor, either a higher doping is needed (which is realized for the Phase-2 setup) or instead, improving the sensitivity of the RGA systems. A third option would be to use a different measurement system to determine the concentration, which is the RGMS, already introduced in chapter 5. The sample drawing and the results for the Phase-1 system are presented in the following in chapter 7.6.2.

Measurement of the concentration profile using the RGA-2 system

As already mentioned before, the RGA-2 system is connected and allows for analyzing gas samples from the different analysis ports from bottom (AV-1) to the top (AV-3) and even to extract off-gas samples. Two sets of measurements have been performed using doped xenon gas at the 04.03.14 and the 06.03.14, at which the measured concentrations for the in-gas and liquid-out, using the RGA-1 system, are given in tabular 7.2.

The different samples have been extracted and analyzed subsequently, starting with the port AV-1, which is expected to show the lowest concentration and continue with the next higher concentration. This procedure avoids contaminations of the following sample with residual krypton in the extraction lines and the measurement chamber. In figure 7.27, the time evolution of the measurement from the 04.03.2014 is shown, taken at a process speed of 8.5 slpm and a pure liquid feed at LF2. The signals are almost all background-dominated, expect for the most abundant isotope, ^{84}Kr, which gives a concentration of $c_{Kr}(\text{AV-1}) = (0.32 \pm 0.10)$ ppb, using the low-doping fit method and the calibration of the RGA-2 system, introduced before.

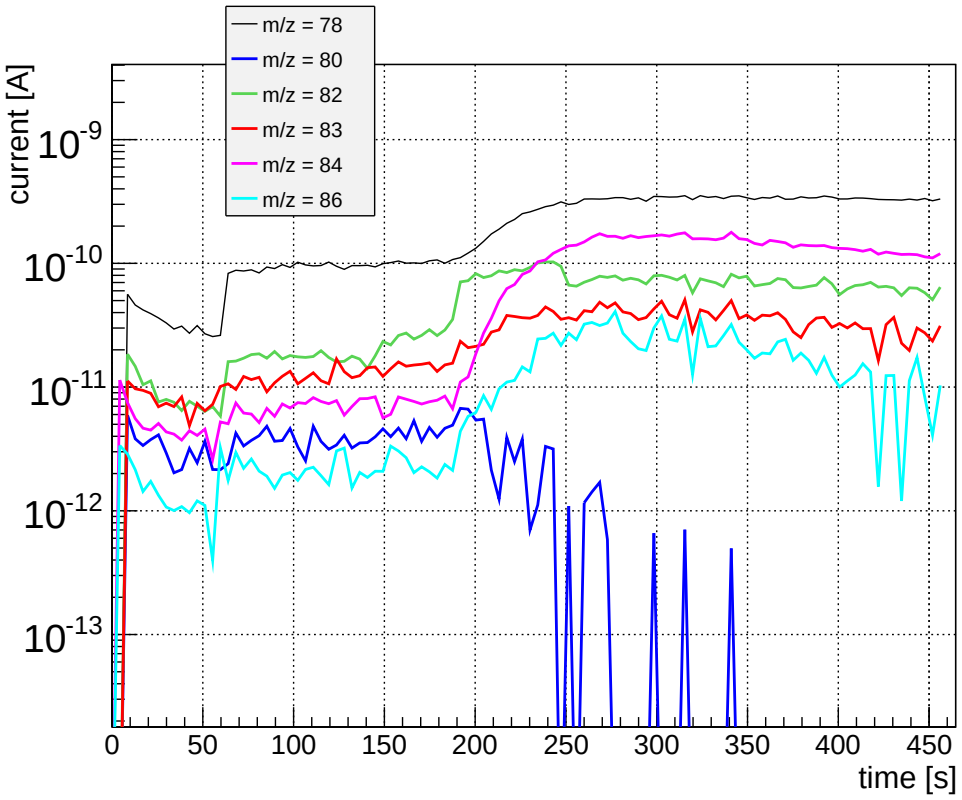

Figure 7.27: **Measurement of the natural krypton at the AV-1 port.** Using the RGA-2 system, it is possible to extract gas batches from the different analysis-port. In this plot a sample from AV-1 port is measured, extracted during a distillation test at the 04.03.2014, performed with a process speed of 8.5 slpm injected via LF2.

The second sample, from the AV-2 port has been taken after warming up the cold-trap and evacuate the whole sample from the AV-1 port by the turbo-pump of the RGA-2 system. After reaching a sufficient pressure level below the detection limit of the gauge at the main chamber ($p_{min} = 1.3 \cdot 10^{-8}$ mbar), the system was ready for the next measurement. The AV-2 port is next to the feeding port LF-2 which has been used for this test and allows to compare the feeding concentration with concentration of krypton injected to the package tube. The measurement, presented in figure 7.28, shows a significant dip in the time-evolution of the signals around t = 240 s, which is very likely caused by the flow dynamics inside the RGA-2 system. This effect has been observed in different calibration measurements but is not reproducible and still under investigation. The calibration measurements showed that the result is not influenced. The concentration has been determined to $c_{Kr}(\text{AV-2}) = (112 \pm 15)$ppb, averaged over the results from the ^{84}Kr isotope and the ^{86}Kr isotope. From the RGA-1 system, the inlet concentration has been measured to $c_{Kr}(\text{in-gas}, ^{84}\text{Kr}) = (102 \pm 34)$ppb, matching in the range of the errors with the concentration, measured at the AV-2 port. The time difference, between the measurement of in-gas sample and the AV-2 sample was about four hours, assuming that the concentration in the in-gas stays stable over time.

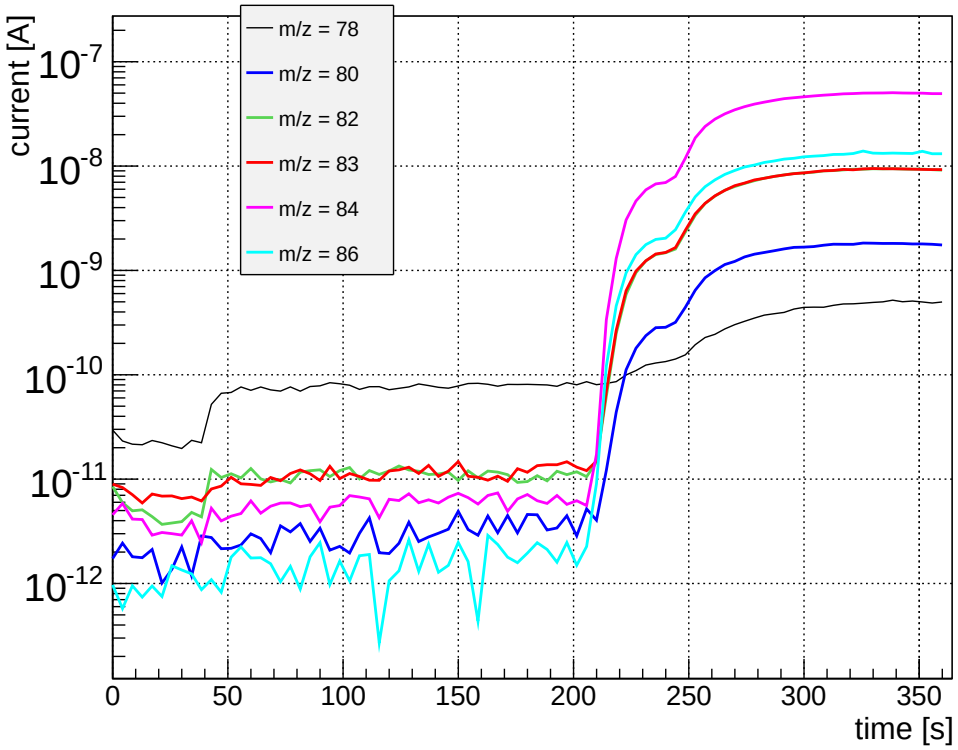

Figure 7.28: **Measurement of the natural krypton at the AV-2 port.** This plot shows the time-evolution of the measurement using a sample from the AV-2 port, extracted during a distillation test at the 04.03.2014, performed with a process speed of 8.5 slpm injected via LF2.

Finally, the sample, drawn from the AV-3 port has been analyzed and is presented in figure 7.29. In contrary to the measurement of the AV-2 sample, this time the signals are smoothly

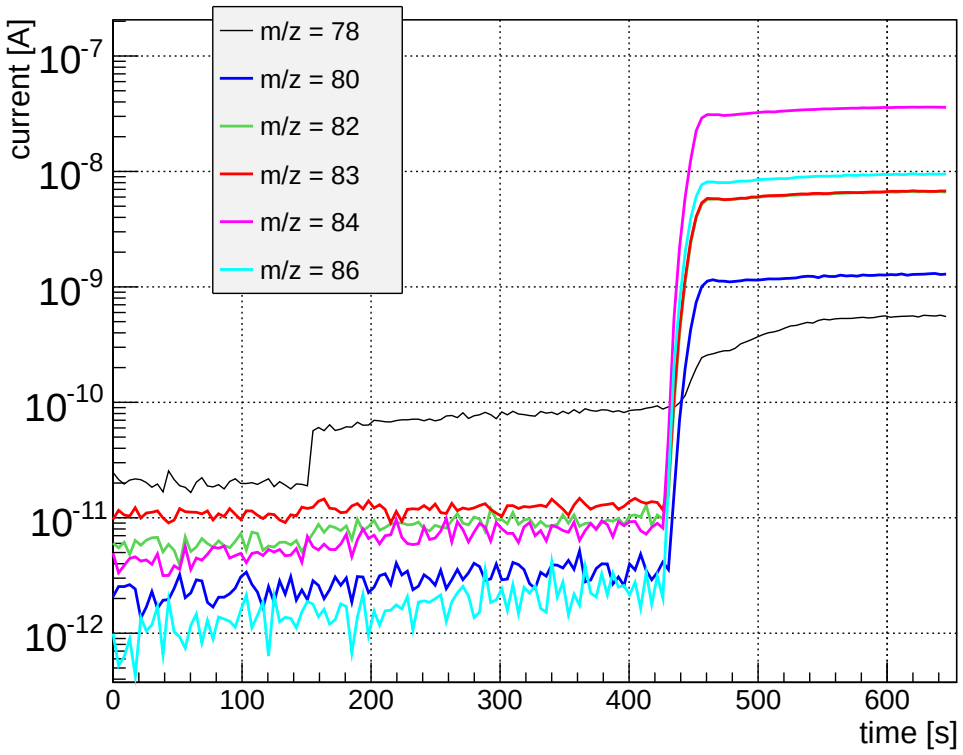

Figure 7.29: **Measurement of the natural krypton at the AV-3 port.** This plot shows the time-evolution of the measurement using a sample from the AV-3 port, extracted during a distillation test at the 04.03.2014, performed with a process speed of 8.5 slpm injected via LF2.

increasing and do not follow the observed step-wise behavior than for the AV-2 sample. The concentration has been measured to c(Kr) = (92 ± 19) ppb calculated as the average of the values from the ^{84}Kr and the ^{84}Kr isotope signals.

A second profile has been taken on the 06.03.2014, using the feeding ports LF2 and GF1 at a process speed of 8.5 slpm. The results from both profiles is collected in tabular 7.3 and are compared also to the related measurement of the in-gas concentration. Qualitatively it is shown, that the concentration, determined for the in-gas, is matching within the range of accuracy to the concentration at the feeding port LF2 for the liquid feed for the measurement at the 04.03.2014. The measurement at the AV-1 port shows the reduced krypton concentration as it is expected for the more volatile component being enriched in the top. For the operating parameters, the actual McCabe-Thiele diagram can be drawn, which is shown in figure 7.30 and allows to determine the HETP value. In order to achieve the same concentration, measured at the AV-1 port, the McCabe-Thiele diagram predicts three theoretical stages. The amount of package material between AV-1 and AV-2 is fixed to 27.5 cm by the design of the segments, giving an HETP value of HETP = 9.2 cm/stage. Furthermore, it is measured that the concentration in the AV-3 port is the same as in the AV-2 port (within the range of the accuracy) and that the krypton together with other light gases is enriched

in the off-gas sample. Since the sample was contaminated with very high concentrations of impurities, the pressure in the main chamber was raised to value, critical for the RGA. In addition, the current in the ion detector of the RGA was raised due to the high concentration of krypton in the sample (related to the doping). In order to reduce the gas load and prevent the device from damaging, the butterfly valve has been opened successively up to 20°. Consequently the intensity in the signals did not reach their maximum. Hence, only a lower limit of $^{nat}Kr/Xe > 1\,ppm$ can be set at the moment, since the calibration has not been preformed for different butterfly positions.

In summary, the measured profiles indicate the separation of krypton and xenon giving also an estimation on the HETP value of HETP = 9.2 cm/stage. It has been observed, that the sample extraction is complicated. In order to not disturb the distillation process only small flow rates are allowed during the extraction. The different AV-ports are equipped with bellow sealed valves, which are not constructed to regulate tiny flow rates. The sample drawing is performed by careful turning the AV-valves open and monitor the pressure in the sample volume.

Table 7.3: **Results from concentration profile measured coldtrap-MS.** The results from the in-gas sample are measured with the RGA-1 system and are also presented in tabular 7.2, using the ^{84}Kr isotope only. The other samples are measured with the RGA-2 system, where the concentration in the AV-1 sample is also related to the ^{84}Kr only since it has the better sensitivity. In contrary, the batches from the AV-2, AV-3 and the off-gas port are calculated as the average of the signals for the ^{84}Kr and the ^{86}Kr isotope.

Sample	04.03.2013 LF2	06.03.2014 LF2&GF1
in-gas (ppb)	102 ± 34	45 ± 8
AV-1 (ppb)	0.32 ± 0.10	$< 0.067 \pm 0.012$
AV-2 (ppb)	112 ± 21	-
AV-3 (ppb)	92 ± 19	51 ± 10
off-gas (ppb)	-	>1000

It happened that the valve of the AV-3 port was accidentally opened too much and the sample was extracted very fast which might lead to incorrect results. An improvement can be implemented by taking the samples using either capillaries or low-conductance orifices.

The latter solution will be realized in the Phase-2 column to procure a better sample preparation.

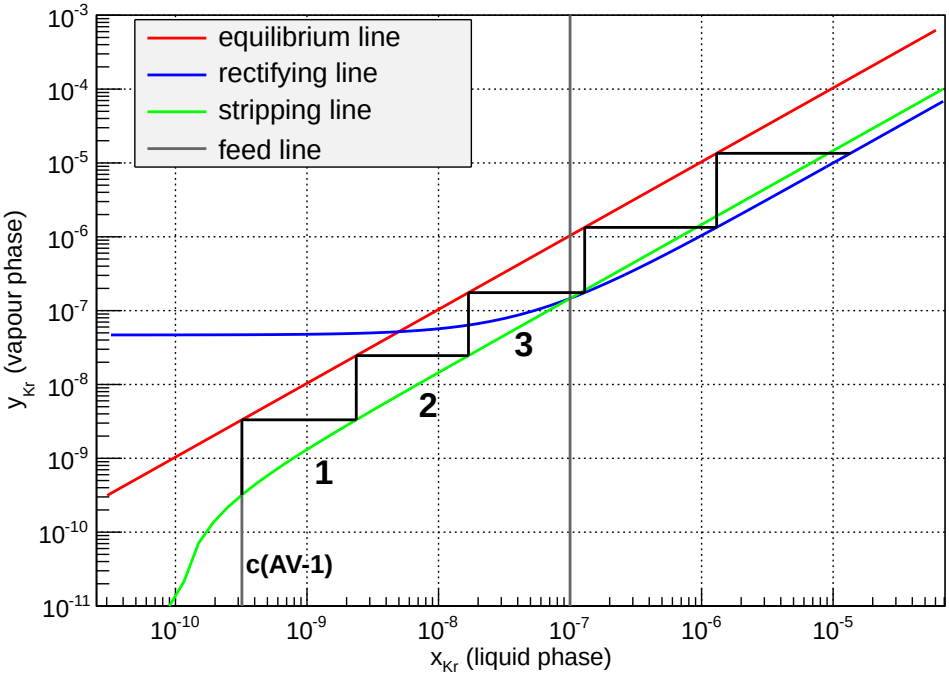

Figure 7.30: **McCabe-Thiele diagram for the distillation run of the 04.03.2014.** The McCabe-Thiele diagram uses an input concentration of $c_{in} \approx 100$ ppb from artificially doped xenon and is calculated down to concentration, measured at the AV-1 port at the 04.03.14. The distillation process has been performed with a process speed of 8.5 slpm injected via LF2.

7.6.2 Measurements of the column performance using RGMS

Since the limitations on the sensitivity of the RGA systems prohibits the final determination of the separation efficiency the RGMS system, already presented in chapter 5, is used. The following measurement campaign was done in collaboration with Dominik Stolzenburg from MPIK in Heidelberg, who also used the results for his master thesis [Sto14]. The cooperation with Heidelberg had the intention to characterize the Phase-1 distillation system, but also to test the RGMS system with ultra-clean xenon, which was not available before.

The distillation was performed with xenon gas with an unknown krypton concentration. The process gas was distilled several times and re-mixed with dirty xenon beforehand. The process speed was chosen to FIC01=8.5 slpm using a pure liquid feed at LF2. In total six pipettes have been mounted to the different ports of the system, three provided by the Münster group (labeled PM-1 to PM-3) and three provided by the Heidelberg group (PH-1 to PH-3). Since PH1 and PH2 (already presented in figure 5.17) have been measured for internal background rates several times, it has been decided to use them for storing the in-gas

sample and the cleaned liquid-out sample. PH3 and PM-1 to PM-3 are used for collecting samples from the three analysis ports and the off-gas line. The pipettes from Münster are constructed very similar to the once from Heidelberg (see figure 7.31), but instead of welding the valves together they are connected with VCR connectors.

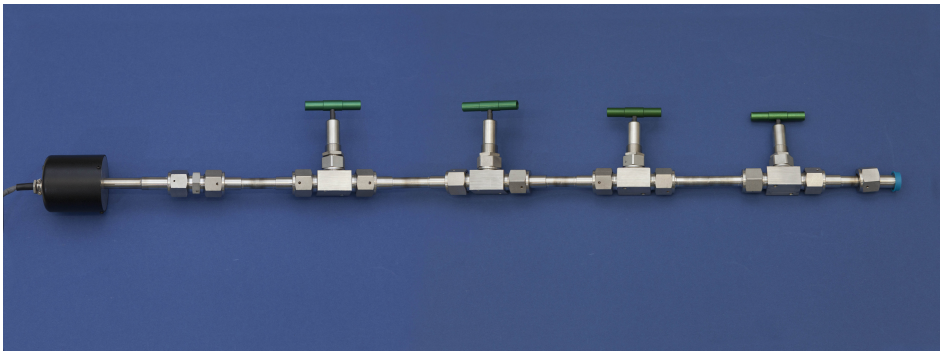

Figure 7.31: **Pipettes for sample taking and storage.** The pipettes used by the Münster group is made from stainless-steel bellow sealed valves connected with VCR tubing. In this picture the pipette is equipped with a absolute pressure gauge, which is used during the calibration of the RGA systems.

The pipettes are connected to the distillation column via the RGA-1 and the RGA-2 system, which directly allow to draw the samples after the cleaning procedure. The pipettes have been pumped using the turbo-pumps of the two RGA systems allowing for oil-free evacuation of the vessels. During the pumping, the pipettes have been baked to T = +200°C for two days in order to avoid any contamination of the samples. After finishing the cleaning, the distillation has been started and stabilized for about six hours before the samples have been taken. The off-line analysis with the RGMS gave a concentration of $^{nat}Kr/Xe = (136 \pm 22)$ ppt for the in-gas sample, by measuring 3 times the different sample volumes. The purified liquid-out sample in the different chambers of the pipettes was measured six times, giving an upper limit on the concentration of

$$^{nat}Kr/Xe < 0.026\,\text{ppt} = 26\,\text{ppq with 90\% confidence level.} \tag{7.6.8}$$

With these measurements it has been demonstrated for the first time, that the distillation is feasible to clean xenon from krypton to the sub-ppt regime. Furthermore, the goal for the XENON1T experiment, $^{nat}Kr/Xe < 0.5$ ppt has been outreached by a factor of ≈ 20. In table 7.4, the achieved concentration is compared to other experiments, demonstrating a so far unreached level of purity. The careful design and the accurate construction, including ultra-high vacuum standards, as well as the stable operation, enabled by precise measurement of the process variables (pressures, flow rates and temperatures) leaded to this result.

Finally, the reduction factor factor of the Phase-1 column can be calculated from the values to $F_{Red} > 3846$ at 90% confidence level, being at least a factor of 3.8 higher than the column used at XENON100 [Abe09].

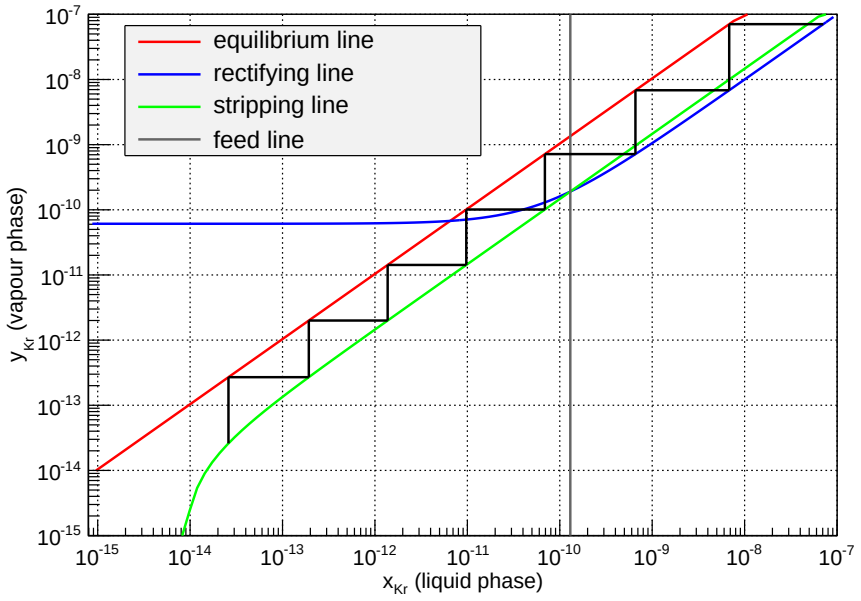

Figure 7.32: **McCabe-Thiele diagram under measured conditions.** The distillation for an input concentration of ^{nat}Kr/Xe = (136 ± 22) ppt and a liquid out concentration of ^{nat}Kr/Xe = 0.026 ppt gives the McCabe-Thiele diagram, that is showed in this figure. It has been drawn for the related operation parameters with FIC01=8.5 slpm, a fraction of 1.1% in the off-gas flow rate and a reflux ratio of $R = 180$.

Table 7.4: **Krypton concentration in different experiments.** This table compares the achieved concentrations of natural krypton in xenon and its removal technique. Values collected from [Xia14], [Ake14], [Lin14], [Abe13].

Experiment	Technology	^{nat}Kr/Xe [ppt]
XENON100	cryogenic distillation	0.95 ± 0.16
XMASS	cryogenic distillation	2.7
LUX	gas charcoal chromatography	4
PandaX	-[17]	83
XENON1T Phase-1 column	cryogenic distillation	< 0.026

Furthermore, the measured separation efficiency together with the system parameters allows to actualize the McCabe-Thiele diagram in order to estimate the HETP value. The average heating power in the reboiler was measured to $P_{Reb}^{Meas} = (153.5 \pm 1.9)$ W (being in good agreement with the heating power of $P_{Reb}^{Meas} = (151.4 \pm 0.8)$ W measured in chapter 7.4), while the corresponding reflux ratio has been calculated to $R = 180$. With the measured concentrations in the in-gas and liquid-out sample, the McCabe-Thiele diagram for a liquid

[17] In the first dark matter search of PandaX [Xia14], no purification for krypton is claimed. But a cryogenic distillation column has been designed and constructed for the next stage of PandaX stating purities of ^{nat}Kr/Xe ∼ 1 ppt [Wan14].

feed is drawn and shown in figure 7.32. It has been calculated, that at least 7 theoretical stages are necessary in order to achieve the observed separation. With 110 cm of package material, the HETP value is calculated to HETP $\approx$ 15.7 cm.

7.6.3 Determination of the HETP value using the ^{83m}Kr tracer method

Beside the determination of the separation efficiency by measuring the ^{nat}Kr content in the in- and outlets, also the dynamics of the process is investigated using the ^{83m}Kr tracer method. Similar to the setup, presented in chapter 6, the ^{83m}Kr generator is put at the in-gas line of the column and the inlet as well as both outlet lines are monitored with the ^{83m}Kr decay detectors, introduced in chapter 5. The detector calibration has been performed with a warm column, very similar to the procedure presented for the single stage setup in chapter 6. The xenon was circulated through the warm column in a closed loop, splitting the xenon flux to pass the off-gas detector as well as the liquid-out detector. In total five calibration measurements have been performed. Three of them while the detectors have been mounted to the Phase-1 column and two additional measurements with the detectors mounted in series to the gas circulation system several month later. The latter two measurements have been performed in order to investigate the calibration on a long-term scale. For all the measurements the same voltage and threshold settings on all detectors are used. The results are collected in tabular 7.5.

Table 7.5: **Results from calibration measurements of the ^{83m}Kr detectors.** The relative efficiencies of the off-gas and liquid-out detector have been determined relative to the in-gas detector. Three calibrations have been performed with the detectors mounted to the Phase-1 column during the commissioning phase, while two additional calibrations have been performed afterwards at the purification system.

Date	$V_{det,\ gas\text{-}in}/V_{det,\ gas\text{-}out}$	$V_{det,\ gas\text{-}in}/V_{det,\ gas\text{-}out}$	Mode
28.11.2013	1.796 ± 0.003	0.66 ± 0.01	Phase-1 column
08.01.2014	2.07 ± 0.01	0.598 ± 0.001	Phase-1 column
02.04.2014	2.20 ± 0.01	0.570 ± 0.001	Phase-1 column
09.12.2014	2.304 ± 0.002	0.294 ± 0.001	Purification system
04.02.2015	2.299 ± 0.002	0.284 ± 0.001	Purification system

As expected, the ^{83m}Kr decay detectors are changing their sensitivity over time which can be explained by drifts or aging of the single components on the PMT-bases and of the photomultiplier itself. For the measurements during the commissioning of the Phase-1 column, average calibration factors can be used, calculated as the mean values obtained from the three calibrations at the Phase-1 column:

$$\frac{V_{det,gas-in}}{V_{det,gas-out}} = 2.0 \pm 0.2 \qquad \text{and} \qquad \frac{V_{det,gas-in}}{V_{det,liq-out}} = 0.61 \pm 0.05 \tag{7.6.9}$$

The obtained values are not comparable to the calculated efficiencies presented in chapter 6, since the detectors have been slightly modified, implementing tight steel meshes in the gas-stream as shatter protection and more important, improve the cabling in the detectors. Additional calibrations have been performed during the commissioning of the Phase-2 column, using different thresholds and will be presented in [Mur18].

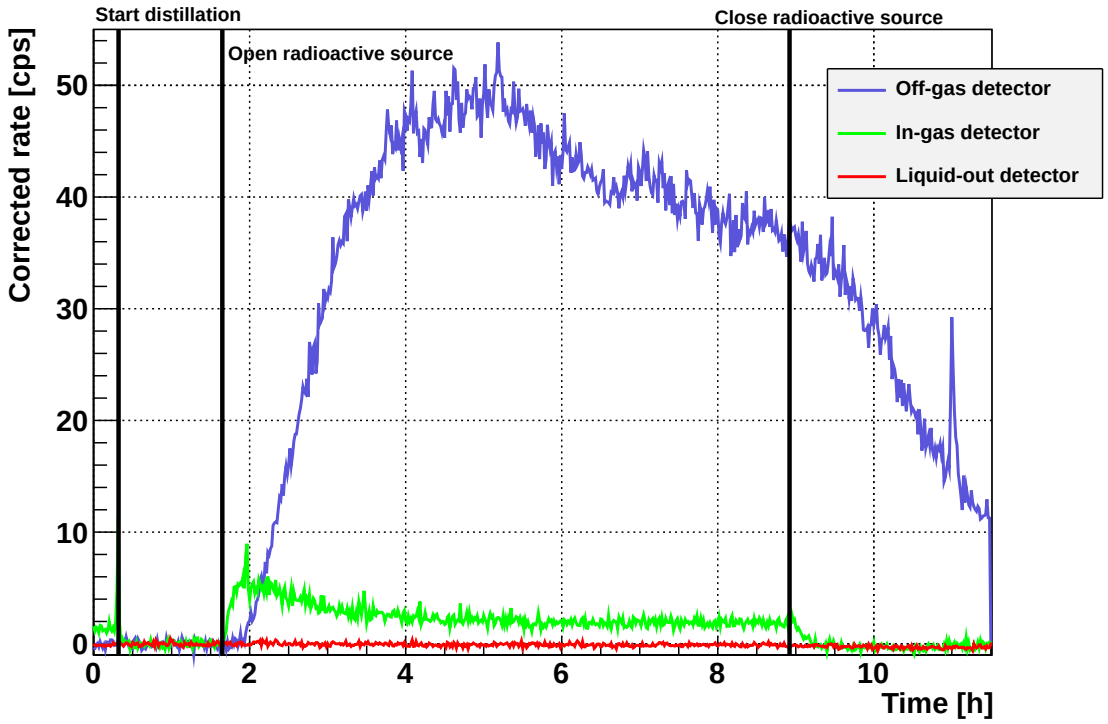

Figure 7.33: **Rates of the ^{83m}Kr decay detectors.** The distillation test has been performed at 8.5 slpm with an off-gas flow rate of 1.1%. After t $\approx$ 1.6 h the valve to the ^{83m}Kr generator is opened and the decay of the radioactive krypton is detected by the three sensors. The enhancement in the rate at the off-gas detector while the liquid-out detector is constant in the background rate indicates that a separation takes place. The rates have been corrected for background and relative efficiencies (see equation 7.6.9) of the outlet detectors relative to the inlet detector.

Figure 7.33 shows the event rates in an example of a measurement, which has been performed under the operating conditions, presented in the figures 7.16 and 7.17. The event rates have been corrected by subtracting the background rates of the different detectors and additionally the relative detector efficiencies have been taken into account. After the distillation is started, the system has been stabilized for about t $\approx$ 1.6 h before the valve to the ^{83m}Kr generator is opened.

The rate in the in-gas detector is increasing almost immediately before it peaked very fast after t $\approx$ 2 h and levels down slowly to an almost constant value, which has been fitted to be $R^{Meas}_{in-gas} = (1.90 \pm 0.03)$ cps (background corrected), before the valve is closed again after

$t = 9\,h$. The shape of the curve is related to the accumulation of the radioactive krypton in the volume above the zeolite beads. The amount of krypton is enriched, being in equilibrium with the production rate of ^{83}Rb and its decay rate. After opening the valve, the collected ^{83m}Kr is released in a short time. Later only the constant flux from the ^{83}Rb decay is emanated, leading to the constant event rate in the in-gas detector. The reason for these low rates compared to the much higher rates in chapter 6 is the missing recirculation of the ^{83m}Kr. During the distillation test, the xenon is passing the source and the in-gas detector only one before it is fed into the column and extracted afterwards. The xenon is finally stored in the dedicated bottles and not feed back to the inlet. Therefore, the radioactive krypton is not enriched with time and only the ^{83m}Kr atoms from the source are detected. Comparing this with equation 6.0.1, which is valid for this operation mode, directly proves that the detection on the sub-ppt scale is possible, although the efficiency is limited.

While the rate in the liquid-out line stays at the background level, the rate in the off-gas line is enhanced due to the separation characteristics of the column. The slowly increasing rate in the off-gas detector peaked at a maximum rate of $R^{Meas}_{off\text{-}gas} = (50 \pm 7)\,cps$ (background corrected) and is decreasing, following the same behavior, than the in-gas rate but on a longer time scale. The flattening out is not observed, since the ^{83m}Kr flux is stopped which already indicates very long time scales until an equilibrium is reached. A reduction factor can not be determined directly due to the low rate in the in-gas detector and the background signal in the liquid-out detector. Nevertheless, the rates in the in-gas and off-gas detector can be used in order to model the dynamics inside the column, which is presented in the following.

In figure 7.34, a simplified scheme of our distillation column is shown. The ^{83m}Kr is indicated by red dots, while areas, filled with liquid xenon are colored in blue. The system has been divided in four segments, that are individually influencing the ^{83m}Kr particle flow and therefore, are described separately. The number of ^{83m}Kr particles in the different parts is varying due to particle transport, separation and dilution processes. For this model, two different mechanisms are distinguished: The delay and the time-wise broadening of the ^{83m}Kr particle flux. The first one is also important because of the short half life of the ^{83m}Kr of $T_{1/2} = 1.8\,h$, producing severe losses. The different segments are separated like the following:

1. **Pre-separator:** The particle flow in the pre-separator has already been presented in chapter 6 and is only briefly reviewed for a pure liquid feed. Since the liquefaction in this stage can be interpreted as first distillation step (depending whether the gaseous phase is extracted) and due to the liquid reservoir (high particle number due to high density) the pre-separator produces a broadening in the particle number with a time constant τ_1.

2. **Feed line:** The feed line is only a transport section for the particles in the liquid phase from the pre-separator inside the column with a certain velocity. Therefore, it produces a delay, which is called Δt_1.

3. **Column:** In the column the separation process takes place. The incoming particles are transported along the package material with a certain velocity, causing a delay which is called Δt_2. Furthermore, the phase-transitions (separation) on the different

(theoretical) distillation stages in combination with the high reflux ratio produce a broadening in the krypton number with a time constant τ_2.

4. **Off-gas line:** The off-gas line is again a transport section for particles in the gas phase (at room temperature) with a certain velocity. This also produces a delay, called Δt_3.

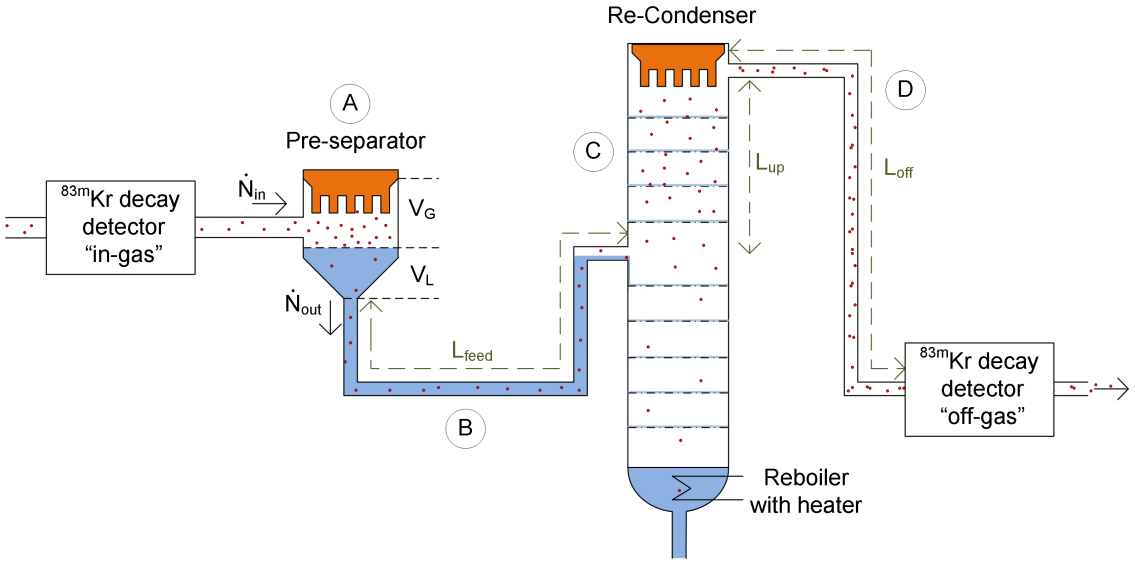

Figure 7.34: **Scheme of the krypton particle flow inside the distillation column.** This scheme shows the different segments of the distillation column that influence the flux of the ^{83m}Kr atoms. In blue, the liquid xenon distribution is illustrated, while the red dots are indicating the ^{83m}Kr.

In the following, the different ^{83m}Kr particle flows for the single segments are explained in more detail. As already mentioned before, one has to take into account, that the liquid-out line, containing the purified xenon is also equipped with a ^{83m}Kr decay detector. Since we do not see an increased rate above the background during the distillation tests, this sensor is neglected in this model.

Dynamics in the pre-separator

As already pointed out in chapter 6, the rate in the in-gas detector $r_{gin}(t)$ is related to the outgoing rate $r_{lout}(t)$ in the liquid line of the pre-separator (see equation 6.2.24):

$$r_{gin}(t) = \frac{A^{lout}_{p,q,V}}{A^{gin}_{p,q,V}} \cdot \left(\tau_{lout} \cdot \dot{r}_{lout}(t) + \frac{\tau_{lout}}{\tau_1} \cdot r_{lout}(t) \right)$$

Since the outgoing rate from the pre-separator is not measured (which leads to $A^{lout}_{p,q,V} = A^{gin}_{p,q,V}$), the differential equation has to be treated differently in the following description of the dynamics. The general form of an approach to solve an inhomogeneous differential equation of the type $\dot{u}(t) + a(t)u(t) = f(t)$ is given by:

$$u(t) = e^{-\int_{t_0}^{t} a(\xi)d\xi} \cdot \{\int_{t_0}^{t} f(\xi) \cdot e^{\int_{t_0}^{\xi} a(\eta)d\eta} d\xi + u_0\} \tag{7.6.10}$$

In our case the function $a(t) = 1/\tau_1$ is a constant yielding $e^{-\int_{t_0}^{t} a(\xi)d\xi} = e^{-(t-t_0)/\tau_1}$ and $e^{\int_{t_0}^{\xi} a(\eta)d\eta} = e^{(\xi-t_0)/\tau_1}$. Solving the second integral over ξ and using the initial condition that $t_0 = 0$ and $r_{lout}(0) = 0 = r_{gin}(0)$ (neglecting a background rate) leads to the following result for the output:

$$r_{lout}(t) = e^{-\frac{t}{\tau_1}} \cdot \{\int_0^t \frac{r_{gin}(\xi)}{\tau_{lout}} \cdot e^{\frac{\xi}{\tau_1}} d\xi\} = \int_0^t \frac{r_{gin}(\xi)}{\tau_{lout}} \cdot e^{-\frac{(t-\xi)}{\tau_1}} d\xi \tag{7.6.11}$$

$$\longrightarrow r_{lout}(t) = r_{gin}(t) \otimes e^{-\frac{t}{\tau_1}} \cdot \frac{1}{\tau_{lout}} \tag{7.6.12}$$

This corresponds to a convolution of the in-gas rate with an exponential damping which is than a function of the broadening time τ_1.

For example, a simplified Θ-function $r_{gin}(t) = a \cdot \Theta(t)$ would give a typical charging curve:

$$r_{gin}(t) = a \cdot \Theta(t) \longrightarrow r_{lout}(t) = \frac{a \cdot \tau_1}{\tau_{out}} \cdot (1 - e^{-\frac{t}{\tau_1}}) \tag{7.6.13}$$

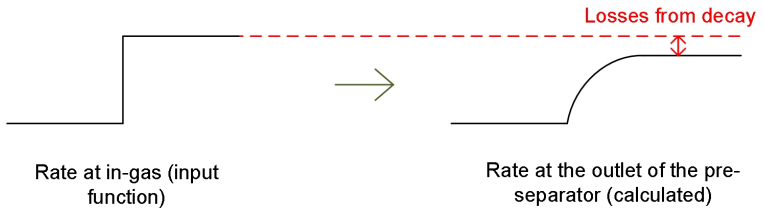

Figure 7.35: **Response of the pre-separator for an idealized in-gas function.** An idealized step-function for the in-gas rate $r_{gin}(t) = a \cdot \Theta(t)$ would lead in this model to a charging curve with a characteristic time τ_1 and a broadening in the krypton particle flux at the liquid outlet of the pre-separator. In addition the decay of the ^{83m}Kr has to be considered (see equation 7.6.27).

Apparently, the in-gas rate does not follow an idealized step-function (see figure 7.33) but the measured rate is used as input parameter later on.

Section B: Feed line

The transport of the particles between pre-separator and column is done in the liquid phase as requested from the design and demonstrated in chapter 7.4, neglecting evaporation in the feed line. Therefore, the delay time is given by the ratio of the tube length L_{feed} and the liquid velocity u_{feed}: $\Delta t_1 = L_{feed}/u_{feed}$. For a pure liquid feed the flow rate through the line

is equal to the feeding rate $\dot{F}$. The flow rate and the particle velocity in the liquid u_L are connected over the density ρ_L and the surface area A of the tube:

$$\dot{F} = j_L \cdot A = u_L \cdot \rho_L \cdot A \tag{7.6.14}$$

with j_L being the particle flux in the liquid. The feeding line is of quarter inch outer diameter and an inner diameter of 4.57 mm, giving a surface area of $A = 0.17\,cm^2$. Using a liquid xenon density of $\rho_L = 2873.2\,kg/m^3$ and a flow rate of $\dot{F} = 3\,kg/h$ gives a particle velocity of $u_L = 1.8\,cm/s$. One has to take into account, that the tube length varies, depending on the feeding port. For the LF-2 port, the length is determined to $L_{feed} \approx 1.5\,m$, which allows to calculate the transport time to $\Delta t_1 = 83.3\,s$.

Section C: Dynamics inside the column

In this model, the gas dynamics of the ^{83m}Kr inside the column is mainly producing a delay and a broadening. A simplified scheme is shown in figure 7.36. The delay Δt_2 can be seen as the time, that ^{83m}Kr atom travels along the package tube. We use the general approach from literature, that the package material can been seen as a series of theoretical distillation stages with a certain, unknown HETP value.

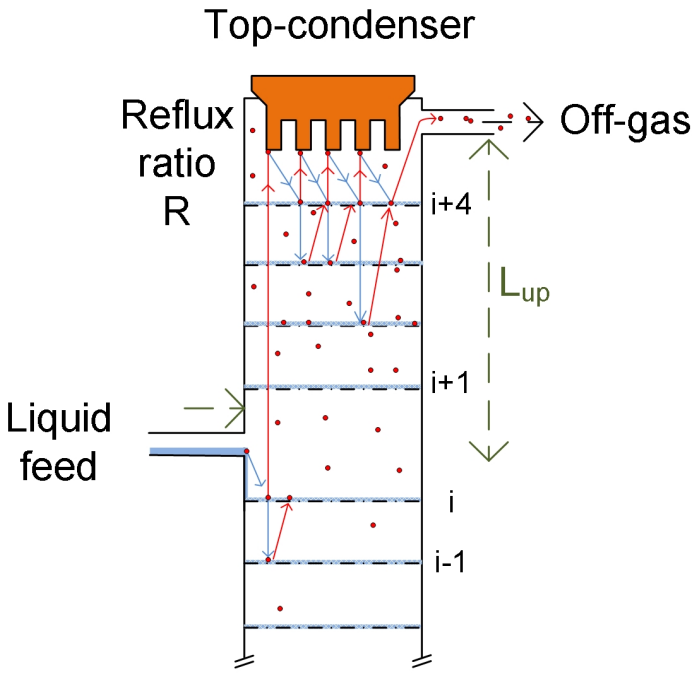

Figure 7.36: **Dynamics inside the column.** In this model the general approach is used, that the package column can be divided in discrete theoretical plates. On each plate the krypton atoms (red) have a certain probability to change from liquid to gas phase (red arrows) or vice versa (blue arrows).

When reaching the next theoretical stage, an incoming krypton particle, solved in the liquid xenon can either change into the gas phase with a certain probability P_{Gas} (in figure 7.36 indicated by red arrows) or it stays in the liquid phase (blue arrows) with the probability P_{Liq} (with $P_{\mathrm{Gas}} + P_{\mathrm{Liq}} = 1$). The probabilities can be related to the volatility by using the definition of the equilibrium line in the McCabe-Thiele method (compare equation 4.2.12):

$$y_{Kr} = \frac{\alpha \cdot x_{Kr}}{1 + (\alpha - 1) \cdot x_{Kr}} \approx \alpha \cdot x_{Kr} \qquad \text{for} \qquad (\alpha - 1) \cdot x_{Kr} \ll 1.$$

One can deduce, that the probability can be defined in the same manor and is therefore:

$$P_{\mathrm{Gas}} = \alpha \cdot P_{\mathrm{Liq}} \qquad \Longrightarrow \qquad P_{\mathrm{Gas}} = \frac{\alpha}{\alpha + 1} \qquad \text{and} \qquad P_{\mathrm{Liq}} = \frac{1}{\alpha + 1} \tag{7.6.15}$$

Due to the volatility of $\alpha \approx 10$, krypton prefers to change into the gas-phase: $P_{\mathrm{Gas}} > P_{\mathrm{Liq}}$. This is valid for each theoretical stage.

In our model we assume, that the injected krypton atom is changing into the gas phase with high probability of $\approx$91% at the first theoretical stage (i, see figure 7.36) which is in contact with the feed port. The probability is even $\approx$98.5% at the next lower stage (i-1). The majority of upstreaming krypton can reach the top-condenser without changing to the liquid, e.g. compare figure 7.36 with five theoretical stages, the probability is calculated to $P_{\mathrm{Gas}}^{Tot} = \prod_{i=0}^{4} P_{\mathrm{i,Gas}} \approx 62\%$. The contribution to the delay time therefore depends on the gas velocity $\mathrm{u_G}$ and the length of the package material $\mathrm{L_{up}}$ with $\mathrm{L_{up}/u_G}$. Additionally, at each of the theoretical stage, the number of stages $\mathrm{i_{Tot}}$ can be calculated by the amount of package material and the HETP value $\mathrm{i_{Tot} = L_{up}/HETP}$, the $^{83\mathrm{m}}$Kr can change in the liquid phase with the probability $P_{\mathrm{Liq}} = 1/(\alpha + 1)$. In such a case, the $^{83\mathrm{m}}$Kr atom goes one theoretical stage down as liquid with the velocity $\mathrm{u_L}$ and gaseously up again with the velocity $\mathrm{u_G}$. The probability for one liquefaction step during the up-streaming is calculated to $\approx$26% (expecting five possible stages). Additional liquefaction steps are neglected here for the first modeling and the delay time $\Delta \mathrm{t_2}$ can be expressed like the following

$$\Delta \mathrm{t_2} = \frac{\mathrm{L_{up}}}{\mathrm{u_G}} + \underbrace{\frac{\mathrm{L_{up}}}{\mathrm{HETP}}}_{=\mathrm{i_{Tot}}} \cdot P_{\mathrm{Liq}} \cdot \left(\frac{\mathrm{HETP}}{\mathrm{u_G}} + \frac{\mathrm{HETP}}{\mathrm{u_L}}\right) = \frac{\mathrm{L_{up}}}{\mathrm{u_G}} + \frac{\mathrm{L_{up}}}{\alpha + 1} \cdot \left(\frac{1}{\mathrm{u_G}} + \frac{1}{\mathrm{u_L}}\right) \tag{7.6.16}$$

The velocities of the gaseous and the liquid xenon can be estimated from the operation parameters of the system. Between feed-point and top-condenser, the flow rate of liquid xenon going down and gaseous xenon going up is almost equal, due to the high reflux ratio ($\dot{D} \ll \dot{V}$):

$$\dot{L} = \dot{V} - \dot{D} \rightarrow \dot{L} \approx \dot{V} \tag{7.6.17}$$

As already mentioned in equation 7.6.14, the flow rate $\dot{L}$ of streaming liquid xenon is related to the particle velocity u_L over the density ρ_L. This is also valid for the liquid inside the

package material and furthermore, the same is valid for the gas stream inside the tube as well:

$$\dot{V} = j_G \cdot A = u_G \cdot \rho_G \cdot A \tag{7.6.18}$$

which, therefore, leads to the relation between between the two velocities using 7.6.17:

$$\rightarrow u_G \cdot \rho_G = u_L \cdot \rho_L \tag{7.6.19}$$

During the distillation process under standard conditions, presented in chapter 7.4, a heating power of $P_{Reb}^{Meas} = (151.4 \pm 0.8)\,\mathrm{W}$ was measured, leading to a gas stream $\dot{V} = 5.9\,\mathrm{kg/hr}$ (reflux ratio $R = 183$):

$$u_G = \frac{\dot{V}}{\rho_G \cdot A} = 6.1\,\mathrm{cm/s} \tag{7.6.20}$$

with the cross-section area of the tube $A = \pi \cdot r_{pack}^2 \cdot (1-\epsilon) = \pi \cdot (0.0225\,\mathrm{m})^2 \cdot (1-0.05).\epsilon$ is a geometrical correction factor and takes into account that the gas can not stream freely due to the structure of the package material. The voidage depends on the type of package and is specified by the manufacturer. The gas density during the process is $\rho_G = 17.8\,\mathrm{kg/m^3}$ (at $\mathrm{p_{column}} = 1.9\,\mathrm{bar}$ and $\mathrm{T_{column}} = -96°\mathrm{C}$).

To determine the particle velocity in the liquid, the amount of material inside the package (liquid load) has to be estimated. The fraction of liquid inside the package can be estimated from the initial filling. The total inventory after filling is measured by the flow controller during the filling process to be $\approx 925\,\mathrm{sl}$ and is distributed inside the system as following:

- **230 sl in the pre-separator:** Determined with the flow-controller during the filling procedure.
- **630 sl in the reboiler and the heat exchanger:** Determined from the hydrostatic level meter and geometric assumptions of the liquid-out pipe.
- **As consequence: 65 sl collected inside the package tube:** The amount of liquid xenon, stored in the different pipes (liquid-out and feeding pipe), is rather unknown. Hence, the estimation is very limited in accuracy.

Using a gas density of $\rho_{G,standard} = 5.5 \cdot 10^{-3}\,\mathrm{kg/l}$ and the value of $\approx 65\,\mathrm{sl}$, the mass can be calculated to $m_{\mathrm{pack}} = 0.35\,\mathrm{kg}$. The volume of the package tube, including the package material is about:

$$V_{pack} = L_{Tot} \cdot \pi \cdot r_{pack}^2 \cdot (1-\epsilon) = 1.8 \cdot 10^{-3}\,\mathrm{m^3}. \tag{7.6.21}$$

Therefore the liquid density inside the column can be estimated, expecting a homogeneous distribution of liquid along the tube: $\rho_L = 195\,\mathrm{kg/m^3}$. With this the liquid velocity is calculated to:

$$u_L = u_G \cdot \frac{\rho_G}{\rho_L} = 0.061\,\mathrm{m/s} \cdot \frac{17.8\mathrm{kg/m^3}}{195\mathrm{kg/m^3}} = 0.56\mathrm{cm/s} \tag{7.6.22}$$

being much smaller than the gas velocity as expected. These velocities can be seen as average flow velocities of a forced flow in a certain direction along the package material. The diffusion motion of the single atoms in all directions is averaged out.

Using the velocities for gaseous and liquid xenon, the delay time Δt_2 is calculated for the LF2 feed ($L_{up} = 55\,\mathrm{cm}$) to:

$$\Delta t_2 = \frac{L_{up}}{u_G} + \frac{L_{up}}{\alpha + 1} \cdot \left(\frac{1}{u_G} + \frac{1}{u_L}\right) \approx 20\,\mathrm{s} << \tau = 2.64\,\mathrm{h}$$

Hence, the delay for the ^{83m}Kr flux along the tube is small compared to the average lifetime of the isotope. Furthermore it emphasizes that the krypton concentration is only enriched in the top, and the last stages in the package tube. This is in agreement with the observation from the RGA-2 measurements of the concentration profile, which does not show the enhanced concentration in the AV3-port related to the AV-2 port but shows the high concentration in the off-gas sample.

For the ^{83m}Kr dynamics, the more severe effect related on the amount of radioactive krypton is related to the residence time inside the column which is expressed by the broadening time τ_2. To calculate the response time τ_2, one has to determine the average time, a krypton particle is "trapped" in the column. To understand this trapping, the reflux ratio R of the overhead product in the rectifying section is important, as it has been defined in chapter 4.2:

$$R = \frac{\dot{L}}{\dot{D}} \qquad \text{with} \qquad \dot{L} = \dot{V} - \dot{D}$$

where $\dot{V}$ is the flow rate of the upstreaming vapor. As already demonstrated, the Phase-1 system is operated at a very high reflux ratio of $R = 183$, thus, only a small fraction of gas is extracted compared to the down streaming liquid. The reflux ratio is used to define an escape probability. A ^{83m}Kr atom, reaching the top of the column, needs in average $(R+1)$ trials before it can escape into the off-gas line. Therefore, the probability for trapping P_{trap} can be seen as $P_{trap} = R/(R+1)$ and the escape probability as $P_{esc} = 1 - P_{trap} = 1/(R+1)$. With a very high probability $P_{trap} = 99.5\%$ (for $R = 183$), the ^{83m}Kr stays inside the column, gets liquefied at the top-condenser with the probability P_{Liq} and goes down the package with the velocity u_L. In figure 7.36 this is indicated by the blue arrows from the top condenser to the next lower theoretical stage. After reaching this stage, the ^{83m}Kr is either changing into the gas phase with the probability P_{Gas} (indicated by red arrows) and streaming up with the velocity u_G or it stays in the liquid phase and travels down a second theoretical stage. As already mentioned before, the krypton is preferring the gaseous phase going up to the top very fast.

The residence time τ_2 depends on P_{Liq} taking the liquefaction process at the top-condenser into account. It also depends on the average number of attempts N_R for a ^{83m}Kr atom to escape through the off-gas line. One can write:

$$\begin{aligned}\tau_2 &= N_R \cdot (1 + P_{\mathrm{Liq}}) \cdot \mathrm{HETP} \cdot (\frac{1}{\mathrm{u_G}} + \frac{1}{\mathrm{u_L}}) \\ &= N_R \cdot (1 + \frac{1}{\alpha + 1}) \cdot \mathrm{HETP} \cdot (\frac{1}{\mathrm{u_G}} + \frac{1}{\mathrm{u_L}})\end{aligned} \tag{7.6.23}$$

As already mentioned, the number of stages, which the down going krypton can pass is limited. Therefore, only two theoretical stages are used in this model. Additional stages only make a small contribution.

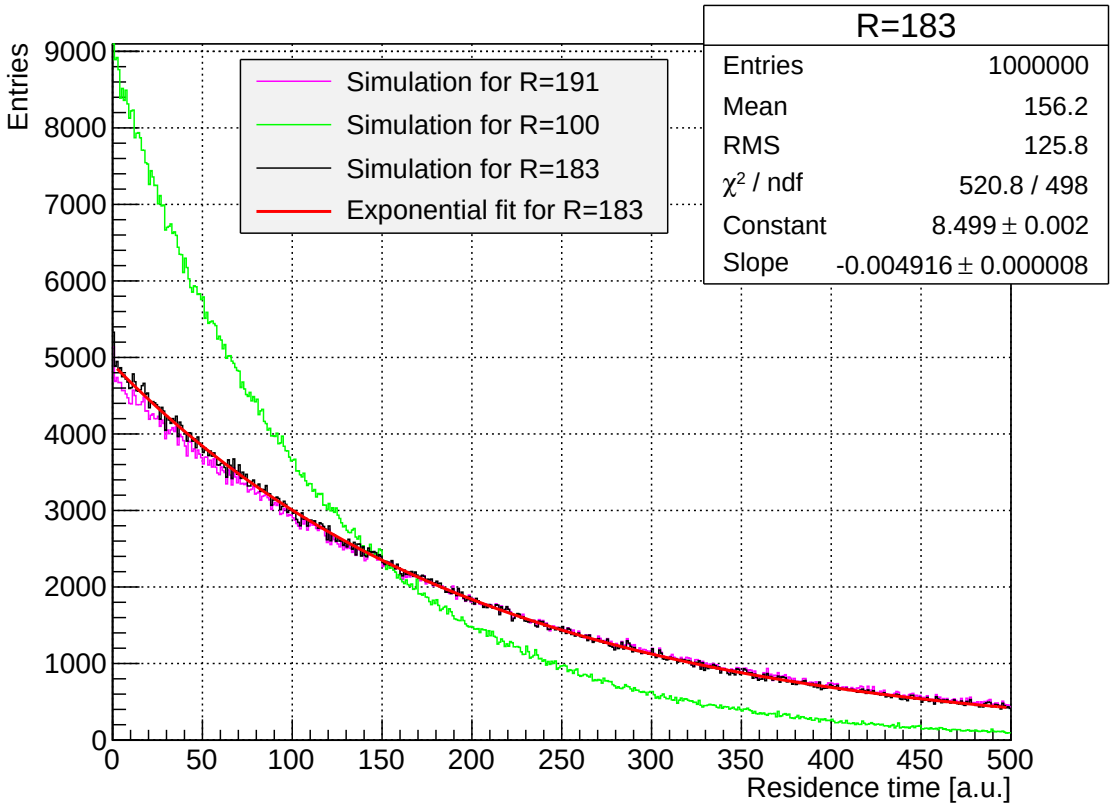

Figure 7.37: **Simulation on the residence time behavior of ^{83m}Kr in the package tube.** This histogram shows the krypton residence time for different reflux ratios using an event generator with 1000000 Krypton atoms. In this simple model, $N_R \cdot (1 + P_{\mathrm{Liq}}) >> 1$.

Since the HETP value is unknown, the residence time of krypton particles is simulated in order to estimate the characteristics of the trapping process and to estimate N_R. The number of escape tries, which can be seen as number of phase transition steps is estimated, neglecting

particle velocities and HETP value. By using a random number generator together with the probability for the trapping P_{trap} and the liquefaction P_{Liq}, the average number of steps is modeled. This shown is in figure 7.37, where the behavior of the residence time for different reflux ratios R is plotted. The residence time is following an exponential decrease, while the reflux ratio influence the average residence time as expected. Smaller reflux ratios decrease the trapping time. For the actual operating parameters with $R = 183$, the distribution has been fitted with an exponential function, with a reduced χ^2 for $1 \cdot 10^6$ simulated krypton atoms of $\chi^2 = 1.05$, giving $\langle N_R \; rangle = 184 \approx R$.

The rate $r_{\text{out-column}}(\mathrm{t})$ is proportional to the number of $^{83\mathrm{m}}$Kr leaving the column at the top and flushed into the off-gas line (which is labeled in figure 7.34 as section D). Hence, the amount of injected $^{83\mathrm{m}}$Kr from the pre-separator is further broadened in the top of the column by an additional exponential function with the constant τ_2:

$$r_{\mathrm{out\,column}}(\mathrm{t}) = \underbrace{(r_{in}(\mathrm{t}) \otimes \frac{1}{\tau_{\mathrm{out}}} \cdot e^{-\frac{\mathrm{t}}{\tau_1}})}_{\text{injected from pre-separator}} \otimes e^{-\frac{t}{\tau_2}} \tag{7.6.24}$$

By using the associative law for convolutions: $(f \otimes g) \otimes h = f \otimes (g \otimes h)$ the calculation can be simplified for the fit program by convolute the two exponential functions first, which can analytically be solved:

$$\alpha_1 \cdot e^{-t \cdot \alpha_1} \otimes \alpha_2 \cdot e^{-t \cdot \alpha_2} = (e^{-t \cdot \alpha_2} - e^{-t \cdot \alpha_1}) \frac{\alpha_1 \cdot \alpha_2}{\alpha_1 - \alpha_2} \tag{7.6.25}$$

With $\alpha_1 = 1/\tau_1$ and $\alpha_2 = 1/\tau_2$.

Section D: Off-gas line

The krypton enriched xenon is collected in the top and guided on a very tiny flow rate of $\approx$ 0.1 slpm through the $^{83\mathrm{m}}$Kr decay detectors into the off-gas bottle. The off-gas line consist of two lines in parallel, mounted to the top-condenser, which allow to extract the off-gas at two different heights. One line is made from a quarter inch tube, with a length of $\approx$ 1 m (volume $V_{1/4,out} = 0.02\,\ell$), and the second one is made from half inch tubing with a length of $\approx$ 0.9 m (volume $V_{1/2,out} = 0.08\,\ell$). Both lines are connected together outside the vacuum vessel to a half inch tube with a length of $\approx$3 m (volume of 0.25 ℓ), guiding the gas to the detector and afterwards to the bottle, while the flow after the detector is regulated by the flow controller.

The pressure in the line is equal to the column pressure, measured to be in average $\approx$ 2 bar(a) - slightly changing for different distillation runs. Using the pressure and the calculated total volume inside the pipes of $V_{Tot} \approx 0.35\,\ell$ in relation to the flow rate of $\dot{D} = 0.1$ slpm ≈ 1.69 mbarℓ/s the time delay can be calculated to $\Delta \mathrm{t}_3 \approx 379$ s

The gas velocity in the half-inch tube can be calculated by using the flow rate $\dot{D} = 0.1$ slpm (=0.036 kg/h at 20°C and a line pressure of 2 bar(a)), the area cross-section of the tube $A = 82\,\mathrm{mm}^2$ and the density $\rho_{\mathrm{Xe,20°C}} = 10.9\,\mathrm{kg/m}^3$ of the xenon at given operating conditions:

$$u_{G,Offgas} = \frac{\dot{D}}{\rho_{Xe,20°C} \cdot A} = 11.2\,mm/s \tag{7.6.26}$$

Fitting the model to the data

The information from the different sections can be summed up, to fit the detected rate on the ^{83m}Kr decay detector in the off-gas line, using the in-gas rate as an input function.

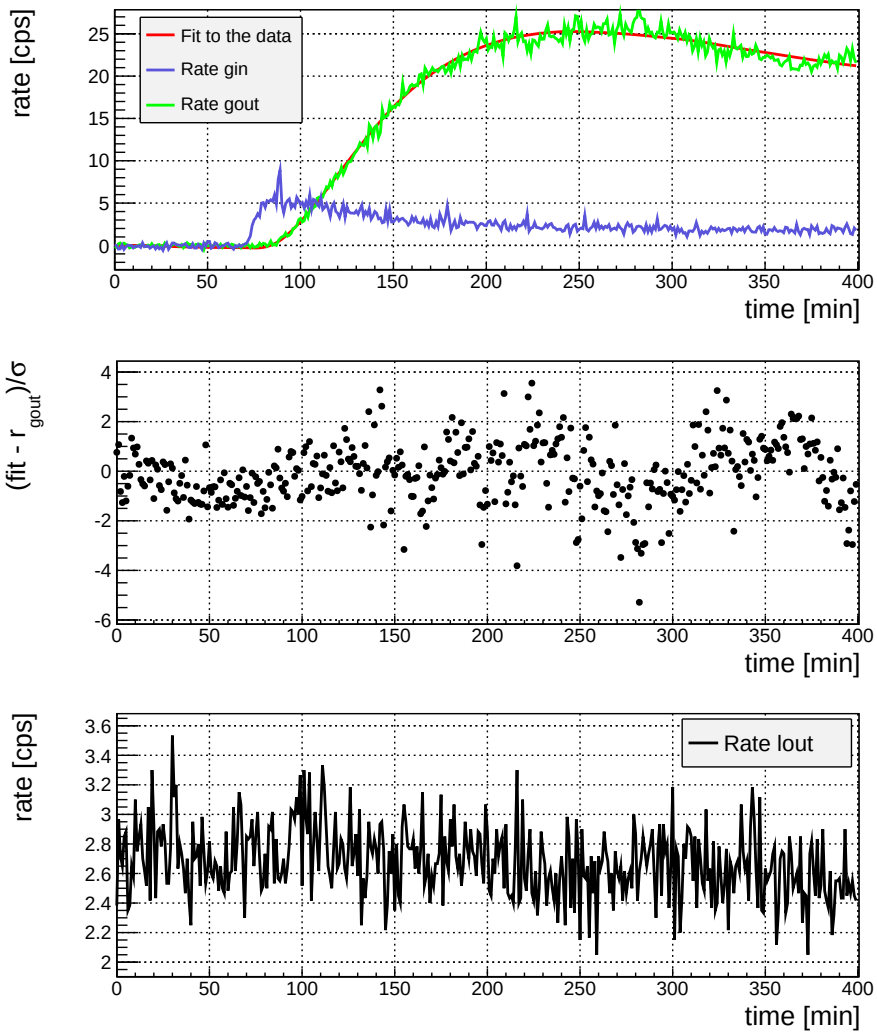

Figure 7.38: **Modeling of the ^{83m}Kr atom dynamic during distillation.** This plot shows the time evolution of a ^{83m}Kr measurement, performed with the Phase-1 column in a liquid feed only distillation via LF-2 at 8.5 slpm (15.01.2014). Top: Rates at the in-gas and the off-gas detector together with the fit to the off-gas rate. Middle: Residues of the fit function versus the measured rate in the off-gas. Bottom: Event rate in the liquid-out detector (without background subtraction).

The final formula is looking like:

$$r_{\text{off-gas}}(\text{t}) = r_{\text{outcolumn}}(\text{t}) \cdot B_{qp} \cdot exp(-\frac{\tau_1 + \tau_2 + \Delta t_{Tot}}{\tau}) \tag{7.6.27}$$

with the delays $\Delta t_{Tot} = \Delta t_1 + \Delta t_2 + \Delta t_3 \approx 480\,\text{s}$ and $B_{q,p}$ being an amplitude, related to the pressure and the flow rates in the different lines and is a free fit parameter. The expectation value is given by the flow and pressure conditions in the in- and off-gas lines $B_{q,p} = q_{in} \cdot p_{off}/(q_{off} \cdot p_{in})$.

One measurement with the Phase-1 column from the 15.01.2014 is shown in figure 7.38 at a process speed of 8.5 slpm and a pure liquid feed at LF2. The fit has been performed with a reduced χ^2 of $\chi^2_{Red} = 1.13$ at $N_{dof} = 394$, leading to an HETP value of HETP $= (15.28 \pm 0.01)\,\text{cm/stage}$ with a residence time for the pre-separator of $\tau_1 = (3185 \pm 7)\,\text{s}$ and an amplitude $B_{q,p} = 48.1 \pm 0.1$. The expected amplitude is calculated from the different flows and pressures to be $B^{calc}_{q,p} = (65.6 \pm 2.3)$ whereat the error is calculated from the Gauss error propagation from the accuracies of the senors. As one can see, the measured amplitude is not matching the expectation value. This is very likely caused by the quality of the in-gas measurement. As one can see, the measured rate, determined in equilibrium is very low $r_{in} = 1.9\,Hz$ compared to a background rate of $r^{Back}_{in} = 2.9\,Hz$. Hence, the precision in the in-gas is limited and might lead to the discrepancy. An additional measurement has been performed at the 17.01.14, using again the pure liquid feed at LF2 but with increased in-gas flow rate of 12 slpm. The measurement is shown in figure 7.39. The fit has been performed with a reduced χ^2 of $\chi^2_{Red} = 1.3$ at $N_{dof} = 326$, leading to an HETP value of HETP $= (12.6 \pm 0.3)\,\text{cm/stage}$ with a residence time for the pre-separator of $\tau_1 = (2364 \pm 14)\,\text{s}$ and an amplitude $B_{q,p} = 35.3 \pm 0.3$ (expected $B^{calc}_{q,p} = (117 \pm 13)$. The rate in the inlet is measured to $r_{in} = 1.7\,Hz$, which is reduced by about 10% compared to the previous measurement, while the flow rate changed by 50%. Since the krypton emanation rate is constant during the measurement time, it is reasonable, that the rate decreases due to the higher mass-flow passing the source. In addition, the residence time τ_1 which is related to the pre-separator decreases due to the higher mass-flow at the fixed volume of the pre-separator. In tabular 7.6, the results from the different measurements are collected.

Table 7.6: **Results from modeling the ^{83m}Kr results.** The fit parameters together with the achieved χ^2_{Red} values have been collected for different measurements with varying conditions.

	15.01.14 LF2, 8.5 slpm	17.01.14 LF2, 12.0 slpm	20.02.2014 LF1, 8.5 slpm	06.03.14 LF2+GF1, 8.5 slpm
HETP	15.28 ± 0.01	12.6 ± 0.3	24.3 ± 7.6	11.67 ± 0.01
τ_1	3185 ± 7	2364 ± 14	762.4 ± 0.1	1921 ± 3
$B_{q,p}$	48.1 ± 0.1	35.3 ± 0.3	119.2 ± 0.1	45.6 ± 0.1
χ^2_{Red}	1.13	1.3	0.8	0.82
N_{dof}	394	326	246	246

In total four measurements have been made under different conditions. Only the measurement from the 20.02. using the LF-1 port does not match with the other. It shows a much

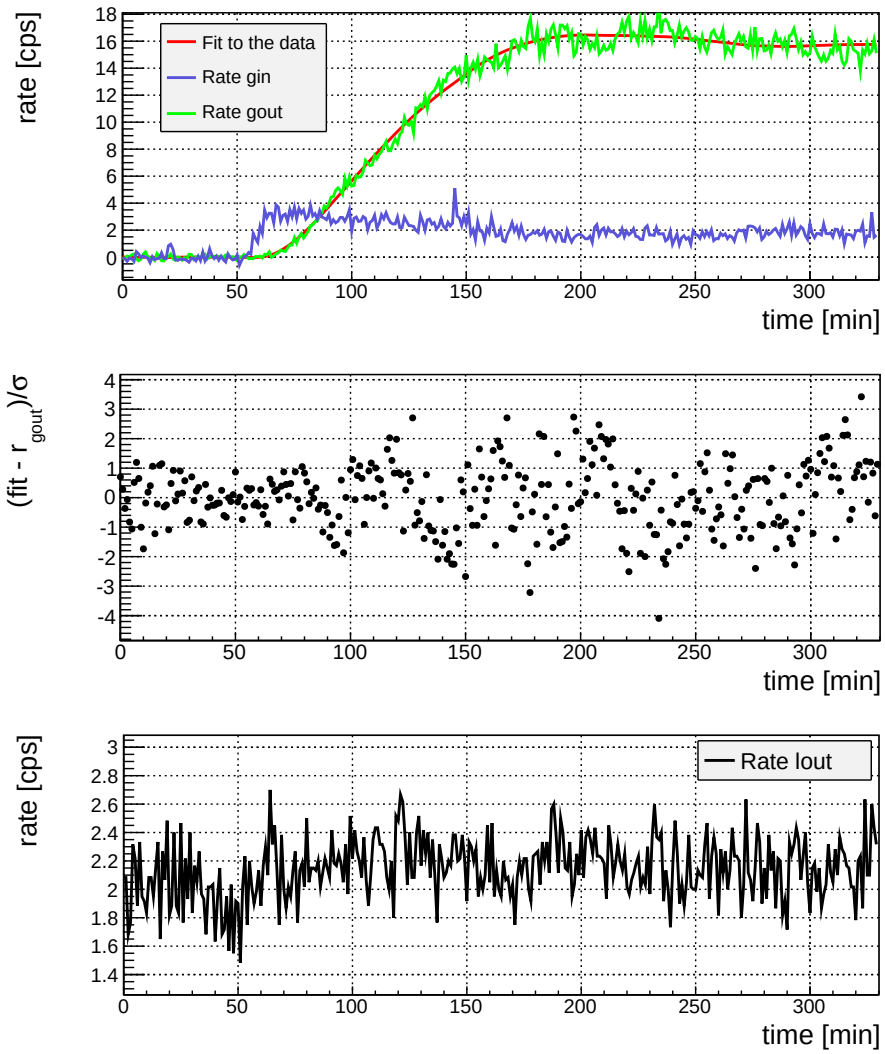

Figure 7.39: **Modeling of the ^{83m}Kr atom dynamic during distillation.** This plot shows the time evolution of a ^{83m}Kr measurement, performed with the Phase-1 column in a liquid feed only distillation via LF-2 at 12.0 slpm (17.01.2014). Top: Rates at the in-gas and the off-gas detector together with the fit to the off-gas rate. Middle: Residues of the fit function versus the measured rate in the off-gas. Bottom: Event rate in the liquid-out detector (not background corrected).

shorter residence time and higher amplitude. The reason for this is unknown, since the distillation was performed very stable. Only the inventory of the pre-separator is unknown which might explain the different behavior if the level inside would be low compared to previous measurement. Due to the limited precision and reproducibility, a detailed error-analysis has been postponed. The HETP values, obtained with this method from the different measurements are of the same order than measured with the RGA-2 and the RGMS system and larger than stated by the company but for different gases.

To summarize, a model of the ^{83m}Kr has been developed, which fits nicely the krypton particle flux at the off-gas outlet by using the in-gas ^{83m}Kr flux. The application of the model on the Phase-1 column allowed to estimate the HETP values for different operation modes, which match to the values measured with RGMS and RGA techniques. Uncertainties are given by the filling level of the pre-separator which influences the residence time and on the distribution of krypton along the package tube. Furthermore, the in-gas rate in the decay detectors was close to background, also limiting the precision.

8 Summary and outlook

Several astronomical observations in the last 80 years indicate, that the matter content in the universe is dominated by non-baryonic dark matter. Different models from particle physics predict new, yet undiscovered particles that interacts very weak with ordinary matter and could explain the gravitational effects that are observed. The field of direct dark matter detection, searching for interaction of dark matter with ordinary matter, is growing in the recent years leading to large and very sensitive earth-bound detectors which are beginning to probe the parameter space, that is favored by different theories, e.g. by super-symmetric enhancements of the standard model of particle physics.

The dual-phase xenon TPC, used by different experiments around the worlds, is the leading technology for direct dark matter search, producing the most stringent limit on the spin-independent WIMP-nucleon cross sections in recent years. The XENON collaboration is running the XENON100 experiment, being the most sensitive experiment until autumn 2013 with a spin-independent WIMP-nucleon cross section of $\sigma_{SI} = 2 \times 10^{-45}$ cm^2 at 90% confidence level at a WIMP mass of 55 GeV/c^2. Currently, the LUX experiment, also using a dual-phase xenon TPC, set the best limit with a minimum at 33 GeV/c^2 and a spin-independent cross section of $\sigma_{SI} = 7.6 \times 10^{-46}$ cm^2 with 90% confidence level. The upcoming XENON1T experiment aims for even higher sensitivity to reach a cross section of $\sigma_{SI} \approx 2 \times 10^{-47}$cm^2 after two years operation for a fiducial mass of 1 ton liquid xenon.

In order to achieve the desired sensitivity for the XENON1T experiment, the xenon has to be cleaned from electronegative impurities, which influences light and charge propagation in the liquid xenon. Additionally, the xenon has to be purified from intrinsic radioactive contaminations, especially from ^{85}Kr, which contributes to the background in the dark matter search.

For the XENON1T experiment a new gas circulation system has to be designed, cleaning the xenon by using hot metal getters at very high flow rates up to 100 slpm, or even beyond. A demonstrator setup has been designed and constructed for studying of the proper components in order to fulfill the requirements of a leak-tight, redundant and remotely controllable system to clean the xenon from electronegative impurities to concentrations less than 1 ppb. A high flow metal getter has been tested with this setup together with an ultra-sensitive moisture analyzer, which allows to monitor the water content in the xenon down to 0.2 ppb. It has been demonstrated, that the metal getters are well suited to achieve high purities of $H_2O/Xe < 0.2$ ppb, verified with the moisture analyzer and allow for high flow rates of

$\approx$ 80 slpm with a moderate pressure drop of $\Delta p = 1$ bar. Furthermore, this technique has been used successfully for the venting of the main-spectrometer of the KATRIN experiment with ultra-clean argon in order to allow for maintenance of the spectrometer during its commissioning phase. Finally, a new type of gas circulation pump (QDrive) has been tested to investigate its characteristics. The QDrive has been tested to be a stable and reliable pump, showing maximal fluctuations of 0.6 slpm at a flow rate of 54.1 slpm on a 51 h time scale. Although different voltage and frequency settings have been tested, it was not possible to reach the design goal of 100 slpm.

The experience, made with demonstrator setup of the gas system allowed to find the proper components and to construct the XENON1T gas system, which is designed to use at least two pumps and getters in parallel in order to achieve the desired flow rate, but to profit from the stability the leak-tightness of the QDrive pumps. The system has been already shipped to the Gran Sasso underground lab and will be implemented into the XENON1T system.

In contrary to the electronegative impurities, the radioactive krypton can not be removed with metal getters. Instead, the technique of cryogenic distillation is one feasible approach. Since the total amount of $\approx$3.3 tons of xenon has to be purified for the XENON1T experiment down to a so far unrivaled concentration of $^{nat}Kr/Xe < 0.5$ ppt a new custom distillation column has been constructed. It is designed for a process speed of 3 kg/h at a xenon recovery of 99%. The technical lay-out of the new column has been done in accordance to standard distillation facilities known from industry and science, combined with the experience made with a commercial column at the XENON100 experiment and requirements in leak-tightness and cleanliness known from ultra-high vacuum applications. Furthermore, accurate process control using several sensors for pressures, flow-rates and temperature has been addressed. Finally, the design and the commissioning of the different setups has been done in collaboration with Dr. Ion Cristescu, cryogenic distillation expert from the Tritium-Laboratory Karlsruhe (TLK) at the KIT.

The design of multi-stage distillation plants is usually done by the well-known Mccabe-Thiele approach, which allows to calculate the number of distillation stages, needed to achieve a certain purity. For the technical realization it has been decided to built a package column, using structured package material in order to provide a large surface for the phase-transition. The number of theoretical stages is than transfered in the height of the package material by the HETP value, defining the total height of the column. For the XENON1T experiment, so far unreached concentrations of krypton in xenon are necessary. The McCabe-Thiele method is usually applied for higher concentrations in the mixture and question rises, whether the model is still valid. Additionally the HETP value for the special package material and a krypton-xenon mixture is not measured yet, leading to uncertainties in the final column height. Hence, the project has been split in different phases to investigate the feasibility of cryogenic distillation for the desired concentration regime and to construct a new distillation system for the XENON1T experiment. In the first step, the distillation of krypton and xenon in a single stage distillation set-up is investigated. By using a novel tracer method with radioactive ^{83m}Kr in xenon and its detection with custom PMT-based detectors it was possible to study the dynamics of the separation process for tiny concentration in the ppt-range and even below. As it has been demonstrated, the separation also effects the radioactive krypton for tiny concentrations. In the dynamic mode, separation factors up

to $S = 24$ have been achieved for the single stage, also indicating that the multi-stage distillation approach is needed to achieve reduction factors up to $F_{Red} \approx 10^5$. In a second step a package column has been designed and constructed, using about 1 m package material and is called the Phase-1 column. It allows to study the separation performance and to answer the open questions on the HETP value. The injected xenon is liquefied in the pre-separator and injected to the package tube. Since the pre-separator is equipped with a liquid and gaseous out line a first separation can be realized, which is important for processing high contaminated xenon. Inside the package tube, the main separation takes place, providing a huge surface on the stainless steel structure package material from the company Sulzer. While the liquid xenon is rinsing down the package, the evaporating xenon, coming from the reboiler is streaming up to be condensed at the top condenser. Hence, a multi-stage distillation (rectification) with partial reflux is realized. The important control parameter for the process are the incoming and outgoing flow rates as well as the system pressure. In order to achieve a stable mass-balance, the inlet flow as well as the off-gas flow are set to a constant value, while the purified liquid-out flow rate is regulated. The pressure inside the column is regulated by controlling the heating power in the reboiler, which is important to achieve a stable distillation process. It has been shown that the Phase-1 column is working thermodynamically stable and matches the design criteria of 3 kg/h at 1% xenon recovery [Ros14b]. Furthermore, the efficiency of the heat exchanger of >90% allows for even higher flow rates which has been tested up to 5 k/h. It has been turned out, that light noble gases influence the heat transfer inside the system. Hence, the Phase-1 column was not able to process xenon samples with high concentrations of helium and argon.

The separation performance of the system has been tested using three different approaches. The RGA systems with coldtrap-enhanced sensitivity allowed for the first separation tests and gave reduction factors of $F_{Red} > 150$. Furthermore, the measurements of the concentration profile with the RGA-2 system gave a HETP value of HETP = 9.2 cm/stage from comparing the concentrations on the AV-1 and AV-2 port with the classic McCabe-Thiele approach. It also gives first hints that the concentration enhancement of krypton in xenon is mainly taking place at the very end of the column. In order to measure the final reduction factor, the more sensitive RGMS system, developed at MPIK in Heidelberg, is used. After careful sample preparation to avoid any contamination, samples from different locations have been drawn during a distillation run and have been analyzed in the Heidelberg setup. It gave a concentration of $^{nat}Kr/Xe = (136 \pm 22)$ ppt for the in-gas sample. The purified liquid-out sample has been measured to:

$$^{nat}Kr/Xe < 0.026\,\text{ppt} = 26\,\text{ppq with 90\% confidence level.} \tag{8.0.1}$$

The concentration, being at least 20 times lower than the XENON1T requirement (which is $^{nat}Kr/Xe < 0.5$ ppt), is even feasible for the dark matter experiments coming after XENON1T, e.g. XENONnT or Darwin. It has been demonstrated, that reaching the sup-ppt scale is possible and that leak-tightness and cleanliness together with stable operation of the device regarding the pressure and the mass-flows is of crucial importance for a successful distillation. The separation factor has been determined to $F_{Red} > 3846$ at 90% confidence level, being at least a factor of 3.8 higher than the column used at XENON100 [Abe09] and reaching for

the first time concentrations of less than 0.1 ppt, which is of crucial importance for direct dark matter search experiments as XENON, LUX, PandaX or XMASS.

Finally, the dynamics of the system has been investigated using the ^{83m}Kr tracer method and develloping a dynamic model, based on probabilistic propagation of krypton in xenon. It has been used to determine the HETP value for different working conditions to be between HETP = 11 cm/stage and HETP = 24 cm/stage being in good agreement with the values obtained from the RGMS and the RGA-2 system. The limitations of the method lay in the low count rate at the in-gas line and the missing information on the liquid load inside the pre-separator, which will be improved.

For the next stage of the development the column is enlarged to the Phase-2 system. Although the final concentration requirement is more than fulfilled, it has been decided to include some upgrades to enhance the performance and the diagnostics. In order to reach the calculated numbers of theoretical stages and a certain safety margin, the amount of package material is enhanced to about 3 m. This guaranties a proper separation performance also for long-term operation over several weeks, which were not tested due to the limited xenon inventory. Furthermore, both condensing stations will be modified by adding extra gas lines to increase the collection of lighter gases. Together with an additional flow controller in the off-gas line it allows also to process samples with higher concentrations of impurities. In addition a new differential pressure sensor will be implemented to observe the liquid level inside the pre-separation which will help to stabilize the system much faster by achieving a proper mass- balance. Finally, a fourth ^{83m}Kr decay detector will be implemented and used to measure the ^{83m}Kr atom concentrations at the different analysis ports. Using a much stronger source will also help to understand the dynamics and the separation process much better. The Phase-2 column is supposed to fulfill all requirements for the XENON1T experiment.

Bibliography

[Aad13] G. Aad *et al.*, (ATLAS collaboration), *Search for Dark Matter Candidates and Large Extra Dimensions in Events with a Photon and Missing Transverse Momentum in pp Collision Data at $\sqrt{s} = 7$ TeV with the ATLAS Detector*, Phys. Rev. Lett. **110** (2013) 011802.

[Abe09] K. Abe *et al.*, *Distillation of Liquid Xenon to Remove Krypton*, Astrop. Phys. **31** (2009) p. 290-296, arXiv:0809.4413 [physics.ins-det].

[Abe13] K. Abe *et al.*, *XMASS detector*, Nucl. Inst. Meth. A **716** (2013) p. 78-85, arXiv:1301.2815 [physics.ins-det].

[Acc14] L. Accardo *et al.*, (AMS Collaboration), *High Statistics Measurement of the Positron Fraction in Primary Cosmic Rays of 0.5-500 GeV with the Alpha Magnetic Spectrometer on the International Space Station*, Phys. Rev. Lett. **113** (2014) 121101.

[Ade14] P.A.R. Ade *et al.*, (Planck Collaboration), *Planck 2013 results. I. Overview of products and scientific results*, Astron. & Astroph. **571** (2014) A1, arXiv:1303.5062v2 [astro-ph.CO].

[Agn13] R. Agnese *et al.*, (CDMS collaboration), *Silicon Detector Dark Matter Results from the Final Exposure of CDMS II*, Phys. Rev. Lett. **111** (2013) 251301.

[Agu13] M. Aguilar *et al.*, (AMS collaboration), *First Result from the Alpha Magnetic Spectrometer on the International Space Station: Precision Measurement of the Positron Fraction in Primary Cosmic Rays of 0.5â350 GeV*, Phys. Rev. Lett. **110** (2013) 141102.

[Ake14] D.S. Akerib *et al.*, (LUX Collaboration), *First results from the LUX dark matter experiment at the Sanford Underground Research Facility*, Phys. Rev. Lett. **112** (2014) 091303, arXiv:1310.8214 [astro-ph.CO].

[Alc00] C. Alcock *et al.*, *The MACHO Project: Microlensing Results from 5.7 Years of LMC Observations*, Astrophys. J. **542** (2000) 281, arXiv:astro-ph/0001272v1.

[Ale13] T. Alexander *et al.*, (DarkSide-50 Collaboration), *DarkSide search for Dark Matter*, JINST **8** (2013) C11021.

[Alm10] J. Alme *et al.*, (Alice collaboration), *The ALICE TPC, a large 3-dimensional tracking device with fast readout for ultra-high multiplicity events*, Nucl. Instrum. Meth. A **622** (2010) 316, arXiv:1001.1950 [physics.ins-det].

[Ang14] G. Angloher *et al.*, (CRESST collaboration), *Results on low mass WIMPs using an upgraded CRESST-II detector*, Eur. Phys. J. C **74** (2014) 3184, arXiv:1407.3146 [astro-ph.CO].

[Apr10a] E. Aprile and T. Doke, *Liquid Xenon Detectors for Particle Physics and Astrophysics*, Rev. Mod. Phys. **82** (2010) p.2053-2097, arXiv:0910.4956v1 [physics.ins-det].

[Apr10b] E. Aprile *et al.*, (XENON Collaboration), *XENON1T at LNGS - Technical Design Report, October 2010*, (2010), http://www.bo.infn.it/xenon/docs/tdr2010.pdf.

[Apr10c] E. Aprile *et al.*, (XENON Collaboration), *First Dark Matter Results from the XENON100 Experiment*, Phys. Rev. Lett. **105** (2010) 31302, arXiv:1005.0380 [astro-ph.CO].

[Apr11] E. Aprile *et al.*, (XENON100 Collaboration), *Study of the electromagnetic background in the XENON100 experiment*, Phys. Rev. D **83** (2011) 082001, arXiv:1101.3866 [astro-ph.IM].

[Apr12a] E. Aprile *et al.*, (XENON Collaboration), *The XENON100 Dark Matter Experiment*, Astropart. Phys. **35** (2012) p 573-90, arXiv:1107.2155v2 [astro-ph.IM].

[Apr12b] E. Aprile, (XENON Collaboration), *The XENON1T Dark Matter Search Experiment*, (2012) arXiv:1206.6288v1 [astro-ph.IM].

[Apr12c] E. Aprile *et al.*, *Measurement of the scintillation yield of low-energy electrons in liquid xenon*, Rev. Sci. Instrum. **86** (2012) 112004, arXiv:1209.3658 [astro-ph.IM].

[Apr13a] E. Aprile *et al.*, (XENON Collaboration), *Dark Matter Results from 225 Live Days of XENON100 Data*, Phys. Rev. Lett. **109** (2013) 181301, arXiv:1207.5988v2 [astro-ph.CO].

[Apr13b] E. Aprile *et al.*, (XENON Collaboration), *Limits on Spin-Dependent WIMP-Nucleon Cross Sections from 225 Live Days of XENON100 Data*, Phys. Rev. Lett. **111** (2013) 021301, arXiv:1301.6620v2 [astro-ph.CO].

[Apr13c] E. Aprile *et al.*, (XENON collaboration), *The neutron background of the XENON100 dark matter search experiment*, J. Phys. G: Nucl. Part. Phys. **40** (2013) 115201.

[Apr13d] E. Aprile, T. Yoon, A. Loose, L. W. Goetzke, and T. Zelevinsky, *An atom trap trace analysis system for measuring krypton contamination in xenon dark matter detectors*, Rev. Sci. Instrum. **84** (2013) 093105, arXiv:1305.6510 [physics.atom-ph].

[Apr14a] E. Aprile *et al.*, (XENON Collaboration), *First axion results from the XENON100 experiment*, Phys. Rev. D **90** (2014) 062009, arXiv:1404.1455 [astro-ph.CO].

[Apr14b] E. Aprile *et al.*, (XENON Collaboration), *Conceptual design and simulation of a water Cherenkov muon veto for the XENON1T experiment*, JINST **9** (2014) P11006, arXiv:1406.2374 [astro-ph.IM].

[Ari11] M. Arik *et al.*, (CAST collaboration), *Search for Sub-eV Mass Solar Axions by the CERN Axion Solar Telescope with ^{3}He Buffer Gas*, Phys. Rev. Lett. **107** (2011) 261302.

[Ari12] K. Arisaka *et al.*, *Studies of a three-stage dark matter and neutrino observatory based on multi-ton combinations of liquid xenon and liquid argon detectors*, Astrop. Phys. **36** (2012) p.93-122.

[Ase00] V.N. Aseev *et al.*, *Energy loss of 18 keV electrons in-gaseous T_2 and quench condensed D_2 films*, Eur. Phys. J. D **10** (2000) 39.

[Asz04] S. J. Asztalos *et al.*, (ADMX collaboration), *Improved rf cavity search for halo axions S. J. Asztalos*, Phys. Rev D **69** (2004) 011101

[Atr05] V. Atrazhev *et al.*, *Electron Transport Coefficients in Liquid Xenon*, ICDL 2005. 2005 IEEE International Conference on Dielectric Liquids, pp. 329â332.

[Bak76] G. Bakale, U. Sowada, W.F. Schmidt, *Effect of an Electric Field on Electron Attachment to SF6, N20, and O2in Liquid Argon and Xenon*, J. Phys. Chem. **80** (1976) 23.

[Bar01] BARTEC Messtechnik und Sensorik, *Technische Information: Emissionsfaktor-Tabelle*, (2001) http://www.bartec.de/homepage/deu/downloads/produkte/19_temperatur/Ti_Tabelle_Emission_d.pdf

[Beg91] K.G. Begeman, A.H. Broeils and R.H. Sanders, *Extended rotation curves of spiral galaxies: dark haloes and modified dynamics*, Mon. Not. R. astr. Soc. **249** (1991) p. 523-537.

[Bel13] Bellini G *et al.*, (BoreXino Collaboration), *SOX: Short distance neutrino Oscillations with BoreXino* (2013), arXiv:1304.7721 [physics.ins-det].

[Ber05] G. Bertone, D. Hopper and J. Silk, *Particle dark matter: evidence, candidates and constraints*, Phys. Rep. **405** (2005) p. 279â390.

[Bor03] B. Bornschein, J. Bonn, L. Bornschein, E.W. Otten and C. Weinheimer, *Self-charging of quench condensed tritium films*, J. Low Temp. Phys. **131** (2003) 69.

[Bro13] E. Brown *et al.*, *In situ measurements of Krypton in Xenon gas with a quadrupole mass spectrometer following a cold-trap at a temporarily reduced pumping speed*, JINST **8** (2013) P02011, arXiv:1212.5136 [physics.ins-det].

[Bro15] Brown E, *et al.*expected 2015, Paper on dual phase time projection chamber in Münster, in preparation.

[Bul14] E. Bulbul, M. Markevitch, A. Foster, R. K. Smith, M. Loewenstein, S. W. Randall, *Detection of An Unidentified Emission Line in the Stacked X-ray spectrum of Galaxy Clusters*, Astrophys. J. **789** (2014) 13, arXiv:1402.2301 [astro-ph.CO].

[Cha12] Chart, Inc, 2S132C-X GAS PUMP Operation Manual (2012).

[Dob11] A. Dobi, C. Davis, C. Hall, T. Langford, S. Slutsky, and Y.R. Yen, *Detection of krypton in xenon for dark matter applications*, Nucl. Inst. and Meth. in Phys. Res. A **665** (2011) 1â6, arXiv:1103.2714 [astro-ph.IM].

[Dod93] S. Dodelson and L.M. Widrow, *Sterile Neutrinos as Dark Matter*, Phys. Rev. Lett. **72** (1993) 17-20.

[Dre13] G. Drexlin, V. Hannen, S. Mertens, and C. Weinheimer, *Current Direct Neutrino Mass Experiments*, Adv. in High Energy Phys. Vol **2013** (2013), Article ID 293986.

[Erh14] M. Erhard *et al.*, *High-voltage monitoring with a solenoid retarding spectrometer at the KATRIN experiment*, JINST **9** (2014) P06022,

[Esm13] A. Esmaili, E. Kemp, O.L.G. Peres and Z. Tabrizi, *Probing light sterile neutrinos in medium baseline reactor experiments*, Phys. Rev. D **88** (2013) 073012, arXiv:1308.6218 [hep-ph].

[Exo14a] J.B. Albert *et al.*, (Exo Collaboration), *Improved measurement of the* $2\nu\beta\beta$ *half-life of* ^{136}Xe *with the EXO-200 detector*, Phys. Rev. C **89** (2014) 015502, arXiv:1306.6106 [nucl-ex]

[Exo14b] J.B. Albert *et al.*, (Exo Collaboration), *Search for Majorana neutrinos with the first two years of EXO-200 data*, Nature **510** (2014) p.229, arXiv:1402.6956 [nucl-ex].

[Fen10] J.L. Feng, *Dark matter candidates from particle physics and methods of detection*, Annu. Rev. Astron. Astrophys. **48** (2010) p. 495-545.

[Fie14] A. Fieguth, *Investigations of impurities in xenon gas with a cold-trap-enhanced quadrupole mass spectrometer*, Master thesis (2014), http://www.uni-muenster.de/Physik.KP/AGWeinheimer/Files/theses/Master_Alexander_Fieguth.pdf

[Fix09] D.J. Fixsen, *The temperature of the cosmic microwave background* Astrophys. J. **707** (2009) p 916-20.

[Fra11] F.M Fränkle, *KATRIN: an experiment to determine the neutrino mass*,(2011) arXiv:1110.0087 [physics.ins-det].

[Gru05] C. Grupen, *Astroparticle Physics* (2005), Springer Verlag.

[Han11] V. Hannen et al., *Limits on the release of Rb isotopes from a zeolite based* ^{83m}Kr *calibration source for the XENON project*, JINST **6** (2011) P10013, arXiv:1109.4270 [astro-ph.IM].

[Hub04] J.H. Hubbell and S.M. Seltzer, *Tables of X-Ray Mass Attenuation Coefficients and Mass Energy-Absorption Coefficients from 1 keV to 20 MeV for Elements Z = 1 to 92 and 48 Additional Substances of Dosimetric Interest*, http://www.nist.gov/pml/data/xraycoef/index.cfm (2004).

[Iup13] IUPAC Commission on Isotopic Abundances and Atomic Weights, (2013), http://www.chem.qmul.ac.uk/iupac/AtWt/

[Jou06] K. Justen, Ed., *Wutz Handbuch Vakuumtechnik - Theorie und Praxis*, 9. Auflage (2006), Friedr. Vieweg & Sohn Verlag, GWV Fachverlage GmbH, Wiesbaden, Deutschland

[Jun96] G. Jungman, M. Kamionkowski and K. Griest, *Supersymmetric dark matter*, Phys. Rep. **267** (1996) p. 195-373.

[Kas09] L.W. Kastens, S.B. Cahn, A. Manzur and D.N. McKinsey, *Calibration of a liquid xenon detector with* $^{83}Kr^{m}$, Phys. Rev. C **80** (2009) 045809, arXiv:0905.1766 [physics.ins-det].

[Kas10] L.W. Kastens, S. Bedikian, S.B. Cahn, A. Manzur and D.N. McKinsey, *A* $^{83}Kr^{m}$ *source for use in low-background liquid xenon time projection chambers*, JINST **5** (2010) P05006, arXiv:0912.2337 [physics.ins-det].

[Kat04] J. Angrik *et al.*, (KATRIN collaboration), *KATRIN Design Report 2004*, (2004) http://www-ik.fzk.de/ katrin/publications/documents/DesignReport2004-12Jan2005.pdf

[Kay08] B. Kayser, *Neutrino mass, mixing and flavor change.* Particle data group booklet (2008), Chapter 13.

[Ket12] H. Kettling, *Trace Gas Analysis of Krypton for the XENON Dark Matter Project*, Diploma thesis (2012), http://www.uni-muenster.de/Physik.KP/AGWeinheimer/Files/theses/Diplom_Hans_Kettling.pdf.

[Kom09] E. Komatsu *et al.*, (WMAP collaboration), *Five-year Wilkinson microwave anisotropy probe observations: cosmological interpretation*, Astrophy. J. Suppl. Ser. **180** (2009) 330, arXiv:0803.0547 [astro-ph].

[Leo10] D.S. Leonard, A. Dobi, C. Hall, L.J. Kaufman, T. Langford, S. Slutskya and Y.R. Yen, *A simple high-sensitivity technique for purity analysis of xenon gas*, Nucl. Inst. and Meth. in Phys. Res. A 621 (2010) p.678â684, arXiv:1002.2742 [physics.ins-det].

[Lev14] C. Levy, *Light Propagation and Reflection off Teflon in Liquid Xenon Detectors for the XENON100 and XENON1T Dark Matter Experiment*, PHD thesis (2014), http://repositorium.uni-muenster.de/document/miami/42495273-2cc7-4632-99af-accf074921e7/diss_levy.pdf

[Loh07] B. Lohrenegel, Einführung in the thermischen Trennverfahren, (2007), Oldenborg Wissenschaftsverlag GmbH.

[Loh07a] B. Lohrenegel, Einführung in the thermischen Trennverfahren, (2007), Oldenborg Wissenschaftsverlag GmbH, p. 30.

[Loh07b] B. Lohrenegel, Einführung in the thermischen Trennverfahren, (2007), Oldenborg Wissenschaftsverlag GmbH, p. 216.

[Lid06] D.R. Lide, *CRC handbook of chemistry and physics* 87th edition (2006-2007), CRC press, U.S.A.

[Lin13] S. Lindemann, *Intrinsic* ^{85}Kr *and* ^{222}Rn *Backgrounds in the XENON Dark Matter Search*, PHD thesis 2013, p. 161, http://hdl.handle.net/11858/00-001M-0000-0014-BD64-D

[Lin14] S. Lindemann and H. Simgen, *Krypton assay in xenon at the ppq level using a gas chromatographic system and mass spectrometer*, Eur. Phys. J. C **74** (2014) 2746, arXiv:1308.4806 [physics.ins-det].

[Man10] A. Manalaysay *et al.*, *Spatially uniform calibration of a liquid xenon detector at low energies using* ^{83m}Kr, Phys. Rev. D **81** (2010) 073303, arXiv:0908.0616 [astro-ph.IM].

[McC05] W.L. McCabe, J.C. Smith and P. Harriott, *UNIT OPERATIONS OF CHEMICAL ENGINEERING*, 7th edition (2005), McGraw-Hill international edition.

[Men13] W. Menn *et al.*, (PAMELA collaboration), *The PAMELA space experiment*, Adv. in Space Res. **51** (2013) p.209-218.

[Mer15] S. Mertens *et al.*, *Sensitivity of Next-Generation Tritium Beta-Decay Experiments for keV-Scale Sterile Neutrinos* arXiv:1409.0920v2 [physics.ins-det], submitted to JCAP

[Mit14] V.A. Mitsou, 2014, *Overview of searches for dark matter at the LHC*, arXiv:1402.3673 [hep-ex].

[MKS06] MKS Instruments, *Datasheet Type 1579 DIGITAL MASS FLOW CONTROLLER FOR HIGH FLOW RATES*, http://www.mksinst.com/docs/UR/1579DS.pdf (2006).

[Moc11] E. Mocchiutti *et al.*, (PAMELA collaboration), *Results from PAMELA*, Nucl. Phys. B (Proc. Suppl.) *217* (2011) p.243â248.

[Mur14] M. Murra, *Set up and test of a cryogenic distillation column for the XENON1T experiment*, Master thesis (2014), http://www.uni-muenster.de/Physik.KP/AGWeinheimer/Files/theses/Master_Michael_Murra.pdf

[Mur18] M. Murra, phd thesis about the Phase-2 distillation column, expected for 2018.

[Nis14a] National Institute of Standard and Technology, U.S. Department of Commerce, (2014), *Thermophysical Properties of Fluid Systems*, http://webbook.nist.gov/chemistry/fluid/

[Nis14b] ESTAR program, provided by the National Institute of Standards and Technology (NIST) U.S. Department of Commerce (2014): http://physics.nist.gov/PhysRefData/Star/Text/ESTAR.html

[Nis15] National Institute of Standard and Technology, U.S. Department of Commerce, (2015), *Handbook of basic atomic spectroscopic data*, http://physics.nist.gov/PhysRefData/Handbook/Tables/kryptontable1.htm

[Nob78] "The Nobel Prize in Physics 1978". Nobelprize.org. Nobel Media AB 2013. Web. 22 Jun 2014. <http://www.nobelprize.org/nobel_prizes/physics/laureates/1978/>

[Nuc14] Nuclear Chart, Brookhaven National Laboratory (2014), http://www.nndc.bnl.gov/chart/.

[Oli14] K.A. Olive *et al.*, (Particle Data Group), *Reviews: 28. COSMIC RAYS* Chin. Phys. C **38** (2014) 090001.

[Pic92] A. Picard *et al.*, *Precision measurement of the conversion electron spectrum of* ^{83m}Kr*with a solenoid retarding spectrometer*, Z. Physik **A342** (1992) 71.

[Pla61] R.L. Platzman, *Total ionization in-gases by high-energy particles: An appraisal of our understanding*, Int. J. Appl. Radiat. Isot. **10** (1961) 116.

[Pla14] G. Plante on behalf of the XENON Collaboration *The Multi-Ton XENON Program at the Gran Sasso Laboratory*, (2014), Dark Matter 2014 - UCLA, http://www.pa.ucla.edu/sites/default/files/webform/plante-dm2014-20140228.pdf

[Pri00] J.R Primack and M.A.K. Gross, *Hot dark matter in cosmology* (2000), arXiv:astro-ph/0007165v1.

[Rob91] R.G.H. Robertson, T.J. Bowles, G.J. Stephenson, Jr., D.L. Wark, J.F. Wilkerson, and D.A. Knapp, *Limit on $\bar{\nu}_e$ mass from observation of the β decay of molecular tritium*, Phys. Rev. Lett. **67** (1991) 957.

[ROO15] ROOT data analysis framework, CERN, https://root.cern.ch/drupal/ ©1995-2015

[Ros14a] S. Rosendahl *et al.*, *A novel ^{83m}Krtracer method for characterizing xenon gas and cryogenic distillation systems*, *JINST* **9** (2014) P10010, arXiv:1407.3981 [astro-ph.IM]

[Ros14b] S. Rosendahl *et al.*, *A cryogenic distillation column for the XENON1T experiment*, *J. Phys. Conf. Ser.* **564** (2014) 012006.

[Ros15] S. Rosendahl *et al.*, 2015, *Determination of the separation efficiencies of a single-stage cryogenic distillation setup to remove krypton out of xenon by using a ^{83m}Kr tracer method*, submitted to Review of Scientific Instruments.

[Rub78] V.C. Rubin, W.K Ford Jr. and N. Thonnard, *Extended rotation curves of high-luminosity spiral galaxies. IV. Systematic dynamical properties Sa→Sc*, Astrophys. J. **225** (1978) L107-L111.

[SAE10] SAES Pure Gas, Inc, *Heated Getter Gas Purifiers*, (2010) http://www.saespuregas.com/

[Sch12] M. Schlack, *Calibration Methods for a Distillation Column for the XENON1T Dark Matter Experiment*, Bachelor thesis (2012), http://www.uni-muenster.de/Physik.KP/AGWeinheimer/Files/theses/Bachelor_Martin_Schlak.pdf

[Sch15] S. Schneider, *Thesis in preparation*, Master thesis in preparation, expected 2015.

[Sel12] M. Selvi, 2012, internal Note on the krypton background

[Sil10] C. Silva et al., *Reflectance of polytetrafluoroethylene for xenon scintillation light*, J. Appl. Phys. **107** (2010) 064902, arXiv:0910.1056 [physics.ins-det].

[Sin14] B. Singh and J. Chen, *Nuclear Data Sheets* **116** (2014) 1, http://www.nndc.bnl.gov/chart/.

[Sle12] M. Slezák, D. Venos, O. Lebeda and T. Trojek, *Precise energy of the 9.4 keV gamma transition observed in the 83Rb decay*, Eur. Phys. J. A **48** (2012) 12.

[Ste13] N. Steinbrink, V. Hannen, E.L. Martin, R.G.H. Robertson, M. Zacher and C. Weinheimer, *Neutrino mass sensitivity by MAC-E-Filter based time-of-flight spectroscopy with the example of KATRIN*, New J. Phys. **15** (2013) 113020, arXiv:1308.0532 [physics.ins-det]

[Sto14] D. Stolzenburg, *On the krypton background in the Xenon100 and Xenon1T dark matter search experiments*, Master thesis (2014), http://pubman.mpdl.mpg.de/pubman/faces/viewItemOverviewPage.jsp?itemId=escidoc:2057509:2

[Tak83] T. Takahashi, S. Himi, M. Suzuki, J. Ruan and S. Kubota, *Emission spectra from Ar-Xe, Ar-Kr, Ar-N_2, Ar-CH_4, Ar-CO_2 and Xe-N_2 gas scintillation proportional counters*, Nucl. Instrum. Meth. **205** (1983) 591.

[Thy11] THYSSENKRUPP MATERIALS INTERNATIONAL GMBH, Werkstoffdatenblatt, Werkstoff-Nr. 1.4404, 2011, http://www.edelstahl-service-center.de/tl_files/ThyssenKrupp/PDF/Datenblaetter/1.4404.pdf

[Tig06] Tiger Optics LCC, *HALO+ Trace Gas Analyzer, Instruction Manual, M7103 Series, Revision G*, (2006).

[Tur90] M.S. Turner, *Windows on the axion*, PHYSICS REPORTS (Review Section of Physics Letters) **197**, No. 2 (1990) p.67â97. North-Holland.

[Ven05] D. Venos, A. Spalek, O. Lebeda and M. Fiser, *^{83m}Kr radioactive source based on ^{83}Rb trapped in cation-exchange paper or in zeolite*, Appl. Radiat. Isotopes **63** (2005) 323.

[Ven06] D. Venos, O. Dragoun, A. Špalek and M. Vobecký, *Precise energy of the weak 32-keV gamma transition observed in Kr-83m decay*, Nucl. Instrum. Meth. A **560** (2006) 352.

[Wan14] Z. Wang *et al.*, *Design and construction of a cryogenic distillation device for removal of krypton for liquid xenon dark matter detectors*, Rev. Scient. Inst. **85** (2014) 015116.

[Wol14] J. Wolf *et al.*, 2014, *Commissioning of the vacuum system of the KATRIN Main Spectrometer* prepared for JINST, expected to be published in 2015.

[Xia14] M.J. Xiao *et al.*, 2014 *First dark matter search results from the PandaX-I experiment*, Sci China-Phys Mech Astron, **57** (11): 2024-2030

[Zbo13] M. Zboril *et al.*, *Ultra-stable implanted ^{83}Rb/^{83m}Kr electron sources for the energy scale monitoring in the KATRIN experiment*, *JINST* **8** (2013) P03009, arXiv:1212.5016 [physics.ins-det].

[Zio05] K. Zioutas *et al.*, (CAST collaboration), *First Results from the CERN Axion Solar Telescope*, Phys. rev. Lett. **94** (2005) 121301.

[Zwi33] F. Zwicki, *Die Rotverschiebung von extragalaktischen Nebeln*, Helvetica Physica Acta, **Vol. 6** (1933), p.110-127.

Danksagung

Ich möchte mich ganz herzlich bei Prof. Dr. Christian Weinheimer für die Möglichkeit bedanken in diesem Forschungsgebiet meine Dissertation anzufertigen und ebenso für die Betreuung während dieser Zeit. Weiterhin möchte ich mich bei Prof. Dr. Alfons Khoukaz bedanken, der sich freundlicherweise als zweiter Gutachter zur Verfügung gestellt hat.

Weiterhin gilt mein Dank Herrn Georg Bourichter und seinen Mitarbeitern aus der mechanischen Werkstatt für ihre großartige Arbeit bei der Fertigung der verschiedensten Bauteile die wir uns gewünscht haben sowie Herrn Roland Berendes und seinen Mitarbeitern aus der Elektronikwerkstatt für die tatkräftige Unterstützung bei allen Problemen der Mess- und Regeltechnik. Ich möchte mich auch ganz herzlich bei den Mitgliedern der Arbeitsgruppe Weinheimer bedanken für die Unterstützung, die vielfältige Diskussionen und dem hervorragenden Betriebsklima. Insbesondere ist hier auch noch das ganze XENON-Team, inklusive aller ehemaligen Mitglieder zu nennen - zusammen haben wir ein großes, leeres Labor mit Leben gefüllt und einpaar coole Sachen gebaut und wichtige Experimente gemacht die hoffentlich dazu beitragen in nicht allzu ferner Zukunft die dunkle Materie nachzuweisen.

I would also like to thank Dr. Ion Cristescu from the Tritium Laboratory in Karlsruhe. His advices during all the phases of the development of the distillation column were of crucial importance for the success of the project.

Schließlich möchte ich mich auch bei meinen Freunden und bei meiner Famile für die ganze moralische Unterstützung und den Rückhalt während des Studiums und in der Zeit meiner Doktorarbeit bedanken.